Experimental and numerical study of nanoparticles for potential energy applications

Song, Pengxiang

Experimental and Numerical Study of Nanoparticles for Potential Energy Applications

Thesis by

Pengxiang Song

School of Engineering and Materials Science

Queen Mary, University of London

A thesis submitted for the degree of Doctor of Philosophy at University of London

July 2010

Declaration:

I hereby declare that this thesis entitled 'Experimental and Numerical Study of Nanoparticles for Potential Energy Applications' to the University of London, and the research to which it refers, are the product of my own work, and that any words or ideas and the figures from the work of other people, published in books and papers or otherwise, are fully acknowledged in accordance with the standard referencing.

Pengxiang Song

Signature: _____

Date: _____

Preface

The work presented in this dissertation was undertaken at the School of Engineering and Material Science, Queen Mary, University of London, between October 2006 and February 2010. This dissertation is the result of my own work and includes nothing which is the outcome of work done in collaboration except where specifically indicated in the text. Neither the present dissertation, nor any part thereof, has been submitted previously for a degree to this or any other university. The main text of this dissertation-chapters one through eight-including appendix, bibliography, tables, and equations contains approximately 53,400 words. Additionally 100 equations, 92 figures and 10 tables are included.

Some of the works in this dissertation have been published:

1. **Song, P.**, Wen, D., Guo, Z. X. and Korakianitis, T. (2008). Oxidation investigation of nickel nanoparticles, *Physical Chemistry Chemical Physics*, **10**: 5057-5065.

2. **Song, P.** and Wen, D. (2009). Experimental investigation of the oxidation of Tin nanoparticles, *Journal of Physical Chemistry C*, **113**: 13470-1347.

3. **Song, P.** and Wen, D. (2010). Molecular dynamics simulation of the sintering of metallic nanoparticles, *Journal of Nanoparticle Research*, **12**: 823-829.

4. **Song, P.** and Wen, D. (2010). Surface melting and sintering of metallic nanoparticles, *Journal of Nanoscience and Nanotechnology*, **10:** 1166.

5. **Song, P.** and Wen, D. (2010). Molecular dynamics simulation of a core-shell structured metallic nanoparticle, *Journal of Physical Chemistry C*, **114**: 8688-8696.

Abstract

This thesis investigates both experimentally and numerically the oxidation, sintering, melting and solidification processes of different nanoparticles under various thermodynamic scenarios, with a background for energy applications. Two sets of main techniques are adopted in this work, which are isoconvensional kinetic analysis and molecular dynamics simulation. Based on the techniques of simultaneous Thermogravimetric Analysis (TGA) and Differential Scanning Calorimetry (DSC), for first time the isoconvensional kinetic analysis is applied to study the oxidation of nickel and tin nanoparticles. This method is demonstrated capable of modelling one-step nanoscale oxidation and revealing underling kinetic mechanisms. Moreover, some distinct features of nanoparticle oxidation compared with their bulk counterparts are found such as melting depression, oxidation kinetic change in the vicinity of Curie point of nickel and pressure-related two-step oxidation of tin nanoparticles. The detailed study from Molecular Dynamics (MD) simulation establishes a three-stage sintering process of two nickel nanoparticles, which is unable to be described by bulk continuum-level models. MD is applied to study the interaction between nickel and aluminium and its consequent thermo-mechanical and structural property evolution in a nickel-coating aluminium particle in a heating and cooling cycle. The simulation successfully predicts the atomic diffusion during melting and the formation of glass and crystal phases, and allows for the estimation of interior core-shell pressure. Reactive MD is then applied to simulate the oxidation of silicon nanoparticles. It predicts well the exothermal reaction process and experimentally reveals the oxygen exchange process.

Keywords: melting, cooling, oxidation, sintering, molecular dynamics, TGA, DSC, nickel, tin, aluminium, silicon, functional, energetic nanoparticle

Acknowledgment

I would like to thank my supervisor Dr. Dongsheng Wen for his continued guidance and encouragement, without which this thesis would not have been possible. I also thank my co-supervisors, Prof. Zheng Xiao Guo of University College, London and Prof. Theodosios Korakianitis of Queen Mary, University of London for their stimulating discussions with me.

I would like to extend my thanks to Dr. Steve Plimpton, one of the primary developers of LAMMPS at Sandia National Laboratory, USA for inspirational discussions via several electronic mails. I am also grateful to Prof. Dennis C. Rapaport of Department of Physics, Bar-Ilan University, Israel; Dr. Wei Cai of Department of Mechanical Engineering, Stanford University, USA; Dr. Aidan Thompson of Sandia National Laboratory, USA; Dr. Adri van Duin of Pennsylvania State University, USA and Dr. Leandro Martínez of State University of Campinas, Brazil for their helpful discussions.

All of this work has been done at computers or in laboratories, so I am thankful to those people who help me in all those computational and experimental works. Special thanks are due to my office colleagues for various help and Dr. Zofia Luklinska of NanoVision Centre, Queen Mary, University of London for her patient assistance on my microscopic observation.

My funding from 'Interdisciplinary Research Scholarship' from the School of Engineering and Material Science, Queen Mary, University of London is gratefully acknowledged and appreciated.

Finally, I would like thank my family, who have always been incredibly supportive whenever I need help. Without their love and blessing, this work could never have been accomplished.

Contents

List of Figures

List of Tables

Important Nomenclature

Roman symbols

c	concentration
d	diameter
D	diffusion coefficient
e	elementary charge, $1.602176487(40)\times10^{-19}$ coulombs
E_a	activation energy
j	mass flux
k_0	pre-exponential factor

k_B	Boltzmann constant, 1.38×10^{-23} m^2 kg s^{-2} K^{-1}
k_p	rate constant
l	atomic bond length
L	oxide thickness
m	mass
M	molecular weight
H_m	latent heat of melting of nanoparticle
H_0	enthalpy of melting of bulk material
p	momentum of atom
P	pressure
r_{ij}	distance between the atoms i and j
R	gas constant, 8.314472 KJ/mol
R_c	nearest-neighbour atomic distance
R_g	gyration radius
R_K	kinetic front radius
R_o	oxygen front radius

R_S	surface radius
t	time
T	temperature
T_m	melting point of nanoparticle
T_0	melting point of bulk material
U	internal energy, total energy
v	velocity of atom
V	volume
x	the fraction of metal that has been oxidized
z	relative volume expansion from metal to oxide
Z	numbers of elementary charge per particle

Greek symbols

α	conversion ratio
β	heating rate
θ_c	Curie point
κ	dielectric constant

μ	mobility of the species
ρ	density
σ	surface tensions

Abbreviations

AES	Auger electron spectroscopy
AFM	Atomic force microscope
BCC	Body-centered cubic
BET	Brunauer-Emmett-Teller (absorption theory)
BO	Bond order
CG	Conjugate gradient (optimization method)
CRH	Constant rates of heating
DFT	Density functional theory
DMA	Differential mobility analyzer
DSC	Differential scanning calorimetry
DTA	Differential thermogravimetric analysis
EAM	Embedded-Atom-Method (potential)

EDS	Energy dispersive X-ray spectroscopy
FCC	Face-centered cubic
FF	Force field
FS	Finnis-Sinclair (potential)
G-B	Ginstling-Brounshtein (kinetic model)
GDOES	Glow discharge optical emission spectrometry
HA	Honeycutt-Andersen (pair analysis)
HCP	Hexagonal close-packed
HRTEM	High-resolution transmission electron microscopy
KCE	Kinetic compensation effect
K-F	Koch-Friedlander (model of sintering)
KMC	Kinetic Monte Carlo
L-J	Lennard-Jones (potential)
MD	Molecular Dynamics
MEAM	Modified-Embedded-Atom-Method (potential)
MSD	Mean square displacement

NPT	Isothermal–isobaric ensemble
NVE	Microcanonical ensemble
NVT	Canonical ensemble
PDF	Powder Diffraction File
QC	Quantum chemistry
QM/MM	Quantum mechanics/Molecular mechanics
RDF	Radial distribution functions
RMSD	Root mean square displacement
SAXS	Small angle X-ray scattering
SEM	Scanning electron microscope
SD	steepest descent (optimization method)
SHS	Self-propagating high-temperature synthesis
SPMS	Single particle mass spectroscopy
STM	Scanning tunnelling microscope
TB	Tight binding (potential)
TEM	Transmission electron microscopy

TGA	Thermogravimetric analysis
XPS	X-ray photoelectron spectroscopy
XRD	X-ray diffraction

Chapter 1

Introduction

1.1 Nanotechnology and Energy

The modern concept of nanoscience and nanotechnology is generally credited to Professor Richard Feynman who gave a seminal talk in 1959, 'There is plenty of room at the bottom'. The prefix, nano, then becomes a common vocabulary word in research domain boosted by the development of experimental tools such as Atomic Force Microscope (AFM), Scanning Tunnelling Microscope (STM) and advanced simulation methods conducted on high-performance computers. Nanoscale materials are known to exhibit different physical, chemical, electrical, and optical properties compared to their counterparts at the macroscale.

As fundamentally most of the energy conversion, energetic reaction and storage processes occur at atomic or molecular level, it is natural to adopt nanotechnology to solve today's big issue: the energy challenge, *i.e.* the challenge to secure our clean energy future under the scenario of a sharp increase in energy demand *vs.* the depletion of fossil fuels together with increasing concerns about carbon emission and global warming. The motivation of today's energy research in respect of material approach is double sided: find alternative cleaner energy sources and conversion processes to secure our future energy supply and find new materials for converting or collecting the harmful emissions to tackle the climate change. The use of nanotechnology is a potential solution to contribute both sides in various energy applications including photovoltaic cells, hydrogen (storage, transport and distribution), carbon capture and storage, fuel cells, heat transfer and combustion applications, hot rock drilling system, power transmission, catalysing chemical processes, as well as improving the efficiency of oil and natural gas systems, and solar and renewable energy

systems (James Baker III Institute for Public Policy of Rice University, 2005).

In many scenarios of nanotechnology, nanoparticles are ubiquitous, in useful forms or in harmful forms. Nanoparticle is referred to any solid material whose length scale typically in the range of one to several hundred 10^{-9} m. Due to their unique physical, chemical and thermal properties associated with their large specific surface area, nanoparticles have been found extensive applications in many energy related fields as catalyst, nanocomposites or energetic materials. Compared to their counterparts at macroscale, theses nanoparticles are shown to have increased reactivity (Guczi, 2005), increased catalytic activity (Schlogl and Abd Hamid, 2004), superparamagnetic behaviour (Gupta *et al.*, 2004), superplasticity (Xu *et al.*, 2004), lower melting temperatures (Mei and Lu, 2007), and lower sintering temperatures (Koparde and Cummings, 2005).

Metallic nanoparticles, compared with the corresponding bulk materials, have distinct mechanical, electrical, optical, magnetic, chemical, and catalytic properties and have been the subjects of extensive experimental and theoretical studies. Understanding the thermodynamics of nanoparticles is a key step for the bottom-up approach for nanodesign and nanomachining. The utilization of metallic nanoparticles in combustion and energetic materials communities advances the application of future fuels, propellants, pyrotechnics, explosives and reactive materials with nanoscale features or ingredients (Yetter *et al.*, 2009). Some nanostructured composite particles, *i.e.* mixtures of nanosized reactant particles, undergo exothermic reactions after being activated, possessing features such as high burn rates and high temperature accompanied by low volume expansion, which have wide range of defense and commercial applications (Zhao *et al.*, 2006, 2007a, 2007b). Some metallic nanoparticles including iron and nickel are also potential candidates of oxygen carriers to improve the efficiency of Chemical-Looping Combustion (CLC), which is a promising environmental-friendly

combustion technology in which the separation of CO_2 is easy (Song and Wen, 2009). Theoretically metallic nanoparticles can be used to improve the efficiency in CO_2 capture and storage in O_2-related combustion (Adanez *et al.*, 2004; Cho *et al.*, 2004). Recently some energetic nanomaterials such as aluminium, iron and silicon have been proposed as an alternative secondary energy carrier where the fundamental scientific challenge is to understand and control the oxidation, ignition and combustion process of these energetic nanoparticles (Wen *et al.*, EPSRC Project: EP/F027281/1, 2007). In many of these applications, proposed materials need to be nano-structured or functionalized with one or two other materials, in order to utilize the distinct properties of both materials at both nano and macro-scales. These nanostructured functional particles do not only improve conventional properties of energy materials related to their bulk counterparts but also promote other novel applications such as future fuel for outer space exploration and self-propagating high-temperature synthesis (SHS) of materials.

Meanwhile nanoparticles are not always beneficial. Uncontrolled nanoparticle agglomeration and sintering may result in mal-functioning products. Particulate matters emission from power plants and combustion engines is a potential health threat (Neeft *et al.*, 1996), whereas our current understandings on the health effect of these nanoparticles are not comprehensive (Gwinn and Vallyathan, 2006).

A better understanding of these nanoparticles associated phenomena requires a fundamental study at individual particle level. Among different scenarios of production, storage, application and prevention management, metallic nanoparticles are usually exposed to oxidative and unstable thermal environment, where particle sintering and oxidation may occur. The subsequent morphological, structural and thermodynamic properties of nanoparticles are crucial to their functional performance and environmental impact.

Various methods are employed to investigate the characteristics of metallic nanoparticles both experimentally and computationally. Simultaneous Thermogravimetric Analysis and Differential Scanning Calorimetry (TGA/DSC) is an experimental technique able to record sensitive weight change and simultaneous heat released or absorbed for a small amount of powder undergoing thermal-related physical and chemical processes. The experiment can be conducted under computer-programmed heating/cooling mode in a desired gas flow. As a core technique of modern thermal analysis, it is proved to be a sound method to investigate thermal-activated properties of particle samples. However, there is quite little work relating information obtained from TGA/DSC to oxidation mechanisms of nanometallic particles. A comprehensive modelling based on data from TGA/DSC experiments, in assistance of several experimental techniques, such as X-ray diffraction (XRD), scanning electron microscope (SEM), transmission electron microscopy (TEM), and energy dispersive X-ray spectroscopy (EDS) in regard to oxidation mechanism will be one of the main aims of this study.

When the effort comes to the quantitive simulation of the properties that macroscopic models fail to predict, molecular dynamics (MD) simulation is employed. MD is a well established simulation method to investigate the multi-body system at molecular level. Particularly MD has been developed as a successful technique to simulate metal materials over last three decades, especially since the development of Embedded-Atom-Method (EAM) (Daw and Baskes, 1983). Since the very first MD simulation, done by Alder and Wainwright in 1957, containing 108 hard sphere particles under a simple potential, along with tremendous growth of computation capability in the past three decades, a wide range of materials and phenomena consisting of hundreds to billions of atoms lasting femtosecond to microsecond can be fully simulated (Vashishta *et al.*, 2003; Kadau *et al.*, 2006). A moderate simulation dealing with tens of thousand atoms can be conveniently performed in a personal computer today. The sintering process of nickel

nanoparticles and thermal response of a Ni/Al bimetallic nanoparticle are simulated by MD to investigate the dynamics and interactions at individual nanoparticle level under non-reactive conditions. A reactive MD simulation dealing with oxidation reaction of a silicon nanoparticle will be conducted as an extension of MD technique and a benchmark of potential mesoscale oxidation study.

1.2 Outline of the Dissertation

This dissertation aims to conduct a fundamental study of metallic nanoparticles associated thermal phenomena that include heating, cooling, and thermal oxidation and sintering from both experimental and numerical aspects. Specifically, the main objectives of this dissertation are:

To investigate the oxidation of metallic nanoparticles (Ni and Sn) in use of simultaneous TGA/DSC technique and various characterization means and experimental tools.

To model the oxidation of metallic nanoparticles (Ni and Sn) based on the iso-conversion method so that the oxidation kinetic mechanism and reactivity of oxidation in terms of activation energy and the reaction model are determined.

To simulate the behaviours of nickel nanoparticles in use of non-reactive MD with respect to revealing the heating and diffusion features of nanoparticle interaction.

To simulate the thermal-mechanical behaviours of aluminium-nickel core-shell nanoparticle during the heating and solidification processes including glass transition and crystallization in use of non-reactive MD.

To apply the reactive MD to silicon clusters undergoing oxidation, simulating the energy released and bond evolution during the oxidation process.

The dissertation is organized into eight chapters. After the introduction in **Chapter 1**, the development of theory describing oxidation of metals and related experimental technique are reviewed in **Chapter 2**. This chapter also includes the extension of oxidation from planar film to spherical shape, which is followed by a detailed review on the isoconversional method that is used in this work. The isothermal and non-isothermal oxidations of nickel nanoparticles investigations are reviewed in **Chapter 3**. The experimental study begins with the oxidation of nickel nanoparticles, an one-step oxidation, as the benchmark of the isoconversional method. **Chapter 4** describes a two-step oxidation process of tin nanoparticles using the same methodology. The isothermal study helps to establish a clear reaction picture under non-isothermal conditions. **Chapter 5** makes an effort on simulating a particular morphology change of nanoparticle: sintering. The chapter begins with a review of the principle of MD technique, its application to the nanoparticle sintering process and the limitation of conventional theories. A detailed study using EAM on two non-equal sized nickel nanoparticles is the presented. The melting of nickel nanoparticles are also discussed and related to the sintering situation. **Chapter 5** validated MD by revealing the distinct features during sintering at nanoscale. In **Chapter 6**, a nickel coating aluminium nanoparticle is simulated under heating and cooling processes by MD. The thermo-mechanical properties and structural evolution of the core-shell structured particle is revealed. The successful MD simulation on structural evolution of the nanoparticle leads to a simulation on oxidation in use of reactive MD. **Chapter 7** concentrates on a reactive MD simulation of the oxidation of a small silicon nanoparticle. The computational results are compared to some published simulation and experiments studies on oxidation of silicon materials. Finally, the conclusions of the present study are summarized in **Chapter 8**. On the basis

of the insight gained and the problems faced, future works are also recommended in the final chapter.

Chapter 2

Theory and Experiment of Oxidation of Metallic Nanoparticles

2.1 General Theory of Oxidation of Metal

A general theoretical frame of oxidation of metals has been established in the 1940s (Mott, 1947). The formed oxides are considered to be typical ionic crystals exhibiting a common mechanism of diffusion and electrical conductivity. Therefore the mechanisms of oxidation may occur by one or more of the following processes: (i) outward diffusion of metal ions and electrons; (ii) migration of oxygen ions toward the metal oxide interface and outward movement of electrons; (iii) simultaneous combination of first and/or second situations by a counter current motion of metal ions and electrons outward and oxygen ions inward (Hauffe, 1965; Atkinson, 1985; Franchy, 2000).

The oxidation occurs supportively by bulk diffusion through the oxide film with the diffusion coefficients and motilities being specific to the system. Various species can move through an oxide, *e.g.* ions, electrons and their coupled holes, neutral atoms or molecules and impurities. The growth of the oxide films on a metal is limited by a transport of ions and charge-compensating electrons through the oxide layer, assisted by a built-in electric field. Defects and impurities are likely to act as the channels for this transportation. In these cases, the electrons are readily transported by hopping conduction, and ion transport should be rate-determining. The so-called built-in electric field, E, which is due to the difference of conductivities between electrons and ions in oxide, has affected the

diffusion currents and thus the oxidation rate (Hauffe, 1965; Kofstad, 1966; Fromhold, 1980; Atkinson, 1985; Franchy , 2000).

2.1.1 Isothermal model for planar metal

The oxidation theory was initially applied to isothermal oxidation for planar metals, where the thickness of metal was expressed as a function of time. For the ionic species through oxide film in a low defect density, Wanger (1933) proposed his renowned linear diffusion relationship for planar oxide as

$$J_i = -D_i \frac{\delta C_i(x,t)}{\delta x} + \mu_i E C_i(x,t) \tag{2.1}$$

where J_i is the flux of species i, E is the electric field, C_i is its concentration and μ_i is the mobility of the charged species related to the diffusion coefficient D_i by the Einstein relationship $Z_i e D_i = \mu_i k_B T$, where Z_i is numbers of elementary charge per particle, e is elementary charge. The integration of Wanger equation (**Equation 2.1**) for planar oxide gives the classical parabolic growth law describing the oxide thickness, L, with time, t:

$$L(t)^2 - L(0)^2 = k_p t \tag{2.2}$$

where the parabolic rate constant is k_p, different in cases of thin film and thick film. Copper, iron, cobalt, and nickel are examples of metals that grow oxide films of parabolic type on their surfaces at room temperatures (Hauffe, 1965; Fromhold, 1980; Franchy, 2000).

The Wanger equation (**Equation 2.1**) is well applicable to thick oxide films. For thin films, the parabolic law is limited as cation diffusion is assisted by an electrical field due to difference in electron concentration between the boundaries of the oxide layer. Cabrera and Mott (1948) considered this case

of thin film, and derived a parabolic rate law for oxidation limited by cation diffusion in the bulk oxide

$$L^2 = 4\Omega D_i n_c t \tag{2.3}$$

where Ω is the oxide volume per metal ion, n_c the concentration of ions at the metal-oxide interface, and D_i the diffusion coefficient for ions. The concentration of metal ions at the gas-oxide interface was assumed to be zero.

Cabrera and Mott (1948) also found a criterion to distinguish this parabolic growth based on bulk oxide control from other modes of growth based on interface control. A critical thickness, L_{cr} was introduced for the space charge region in the oxide by the contact of metal or semiconductor

$$L_{cr} = e^2 \sqrt{\frac{\kappa k_B T}{8\pi n_c}} \tag{2.4}$$

where κ is the dielectric constant of the oxide and n_c the concentration of dissolved ions. Parabolic growth is essentially driven by the concentration gradient of ions in thick oxides. Franchy (2000) pointed out that there is another threshold thickness, L_{th} written as

$$L_{th} = \frac{qaV}{k_B T} \tag{2.5}$$

where $q = Z_i e$, and a is the ionic jump distance. If the value of oxide thickness L falls within the range of $L_{th} < L < L_{cr}$, *i.e.* the condition $qaE << k_B T$ is satisfied, there is

$$\frac{dL}{dt} = \frac{n_c \mu_i V \Omega}{L} \tag{2.6}$$

The integration of **Equation 2.6** yields a parabolic law

$$L^2 = 2\Omega\mu_i n_c V t + const \tag{2.7}$$

Making use of the Einstein relationship, $Z_i e D_i = \mu_i k_B T$, **Equation 2.7** becomes

$$L^2 = 2Z_i n_c D_i \Omega \frac{eV}{k_B T} t + const \tag{2.8}$$

Equation 2.8 (thin film case) is clearly different from **Equation 2.3** (thick film case). Depending upon the boundary conditions, **Equation 2.7** can also lead to linear or cubic rate laws when it is integrated. The cubic rate law has also been explained in term of a transition state by Evans (1960). The rate of oxidation is controlled by the passage of oxygen inward or/and metal outward through a continuous, pseudomorphic layer next to the metal. In this kind of oxide growth of thin film the ions and electrons are considered to move across the oxide layer independently. The space charge due to the dissolved ions can be disregarded, and quasi-equilibrium of electrons is established between the metal and adsorbed oxygen. The thickness of films in this category is in the range of several hundred angstroms (Å) or less.

For metals such as aluminium, zinc, beryllium, and chromium, their oxide films whose growth mainly obey the logarithmic law, can be represented by the relation below (Atkinson, 1985),

$$L(t) = k_p \ln(mt + 1) \tag{2.9}$$

where k_p and m are constant characteristics for each metal. In the case of aluminium and beryllium, metals of fixed valence, the oxide films show a high electrical resistance that increases with increasing thickness of film and finally stops the flow of electrons from the metal to the oxide-gas surface. In

the case of zinc and chromium, their oxides show high electronic conductivity, but their ionic conductivity remains very low because of an excess of metal ions in their lattices (Hauffe, 1965). This creates a high space charge, preventing the diffusion of metal ions and interrupting film growth. Thus, in both cases, the logarithmic law rules.

For metals of group I in periodic table, the linear law holds, which generally yields porous and permeable films (Atkinson, 1985). When the rate of oxidation is constant for a given temperature, and it is not affected by the diffusion, the equation of oxide growth is

$$L(t) = k_p t \tag{2.10}$$

The rate of oxidation is controlled by the similar movement of oxygen and metal in cubic law. The oxide layer maintained constant thickness, being renewed as fast as it breaks down. The outer layer is broken by cracks, so that it is permeable to the passage of oxygen. Under such conditions the rate of oxidation for a given temperature remains constant.

2.1.2 Isothermal model for spherical metal

For the non-planar case, it is convenient to define the percentage of conversion, x, *i.e.* the fraction of metal that has been oxidized, which is a function of time, $x = x(t)$. Its time derivative is proportional to surface integral of the defect current density normal to the reaction interface (Karmhag, 2003).

$$\frac{dx(t)}{dt} = (C / zV)\int_{\text{interface}} \vec{J}_1 dA = CI_1 / zV \tag{2.11}$$

where V is the initial volume of metal particle, z is the relative volume expansion upon formation of oxide and C is a constant. For spherical symmetry there will be a uniform radial flow of current and the integral can

be easily evaluated. This integral is the total current, I_1, at the reaction interface, which must be the same when evaluated at any given radius in the oxide.

In analogy with the case of thin oxide film and non-linear field, non-planar case can be written as

$$CI_1(x) = 4\pi k_p (r_1(x) r_2(x) / L_{cr}) \sinh(L_{cr} / L(x)) \tag{2.12}$$

where r_1 is the radius of the metal core, and r_2 is the radius of the oxidized particle. These parameters can be computed from the initial metal core radius and oxide thickness, for each oxidation ratio.

Carter (1960) deduced the rate law particularly for nickel spherical particle using diffusion control model as follows, which shows a non-linear growth:

$$k_p t = \frac{z r_0^2}{2(z-1)} [z - (z-1)(1-x)^{2/3} - (1+(z-1)x^{2/3}] \tag{2.13}$$

where r_0 is the initial particle radius. Fromhold (1980) obtained the same equation and expressed k_p in forms of the mobility of diffusing species, their concentrations at interfaces and built-in voltage over the oxide film. Karmhag (2001) developed a simpler and rarely applied equation by just modifying the parabolic law of **Equation 2.2** into sphere geometry as

$$L(t)^2 - \frac{2}{3r_0} L(t)^3 = 2k_p t \tag{2.14}$$

If the oxide thickness L has a general time dependence and an Arrhenius temperature dependence given by

$$L = \exp(-E_a / k_B T) f(t) \tag{2.15}$$

The logarithm at a specific value of $L = L_i$ will give the following relation between two different isotherms at temperatures, T_1 and T_n

$$\ln f(t_n) = \ln f(t_1) - \left(\frac{E_a}{k_B T_1} - \frac{E_a}{k_B T_n} \right) \tag{2.16}$$

The two isotherms should fall onto a single curve in a double logarithmic plot since the translation $\ln f(t_n) - \ln f(t_1)$ only depends on temperature. The activation energy of the isothermal process can be determined by plotting the shift of the logarithms of the different isotherms $(\ln t_n - \ln t_1)$ against the inverse temperature $1/T_n$. This model has been used to predict the oxidation of a 20 nm sized nickel sample, activation energy of which is found as 1.34 eV, which is smaller than that of 1.5 eV and 1.9 eV for 5 μm and 150 μm Ni particles respectively (Karmhag, 1999a and 1999b). A more detailed isothermal study of nanoscale nickel oxidation referring to this model will appear in next chapter.

Actually, many metals follow more than one type of growth law, depending on the temperature range. Usually, at lower temperatures, the logarithmic law prevails, followed by the parabolic law at higher temperatures. At even higher temperatures, there may be a transition from the parabolic law to the linear law (Atkinson, 1985).

2.2 Isoconversional Method

All the models described before are essentially isothermal mode, usually a temporal relation of oxide growth in which kinetic parameters thermodynamically varying with temperature is fixed. For many processes of practical applications, for instance, combustion and catalysis, the reactants are usually placed in continuous heating environment and isothermal experiment is unable to predict the reaction environment

changing with increasing temperature. Isothermal method is also restricted within limited conversion ratio, for instance, nickel particles can only be oxidized to ~10% after 27 hours isothermal heating at 135 °C (Karmhag *et al.*, 2003). Therefore many interests of study turn to modelling non-isothermal situations, which are mainly considered in the framework of solid-state reaction kinetics.

In general the solid-state kinetic principle assumes that the rate of conversion, $d\alpha / dt$, is a linear function of a temperature-dependent rate constant, $k(T)$, and a temperature-independent function of the conversion ratio, $f(\alpha)$, as below (Ortega, 2001),

$$\frac{d\alpha}{dt} = k(T) f(\alpha) \tag{2.17}$$

where α is the oxidation ratio, defined as the ratio of oxidized fraction, x, to the maximum possible conversion fraction, x_{max}, $\alpha = x(t) / x_{\max}$, where $x_{\max} = x(t \to \infty)$. The reaction rate constant $k(T)$ is typically expressed by the general Arrhenius expression

$$k(T) = k_0 \exp[-E_a / k_B T] \tag{2.18}$$

where k_0, the pre-exponential factor, is assumed to be independent of temperature, E_a is the activation energy, T is the absolute temperature, and k_B is the Boltzmann constant. Combination of **Equations 2.17** and **2.18** gives

$$\frac{d\alpha}{dt} = k_0 f(\alpha) \exp^{-E_a / k_B T} \tag{2.19}$$

For iso-conversion process where the heating rate is a constant, $\beta = dT / dt$, the rate of conversion can be written as

$$\frac{d\alpha}{dT} = \frac{k_0}{\beta} f(\alpha) \exp^{-E_a / k_B T} \tag{2.20}$$

An integration of **Equation 2.20** from an initial temperature, T_0, corresponding to a degree of conversion, α_0, to a particular temperature, T_p, where $\alpha = \alpha_p$, gives

$$\int_{\alpha_0}^{\alpha_p} \frac{d\alpha}{f(\alpha)} = \frac{k_0}{\beta} \int_{T_0}^{T_p} \exp^{-E_z / k_B T} \, dT \tag{2.21}$$

If T_0 is low, it may be reasonably assumed thạt $\alpha_0 = 0$ and considering that there is no reaction between $T = 0$ and $T = T_0$:

$$\int_0^{\alpha_p} \frac{d\alpha}{f(\alpha)} = \frac{k_0}{\beta} \int_0^{T_p} \exp^{-E_a / k_B T} \, dT = \frac{k_0 E_a}{\beta k_B} \int_{y_p}^{\infty} \frac{\exp(-y)}{y^2} dy = \frac{k_0 E_a}{\beta k_B} p(y_p) = g(\alpha) \tag{2.22}$$

where $y = E_a / k_B T$, $y_p = E_a / k_B T_p$ and $p(y) = \int_y^{\infty} \frac{\exp(-y)}{y^2} dy$, which is the integral function of conversion ratio that has different formats depending on different approximations. As **Equation 2.22** is not analytically soluble, some approximations of $p(y)$ must have to be proposed (Doyle, 1965; Boswell, 1980; Mittemeijer, 1992; Ozawa, 1992; Graydon *et al.*, 1994; Starink, 1996). Some established methods based on both integral and differential manners of approximation are adopted in this work to calculate kinetics constants, as described in next section below.

2.2.1 Activation energy determination

The activation energy calculation varies according to the characteristics of the reactions due to different controlling features. Different methods deploying different approximations of $p(y)$ have been proposed to calculate kinetic parameters depending on both experimental conditions and mathematical treatment of data.

Kissinger method

The Kissinger integral method (Kissinger, 1957) involves no assumption of the reaction mechanism but based on one assumption of $y >> 1$. This can be reasonably justified for most of the solid state reactions as typical activation energy is in the range of 1-2 eV, which is much larger than the thermal energy of the carriers. The integral function can then be simplified as $p(y) \approx \exp(-y)/y^2$. Take this pure mathematical approximation into the **Equation 2.22**, the Kissinger method can be expressed as:

$$\int_0^{\alpha_p} \frac{d\alpha}{f(\alpha)} = \ln\frac{k_0 E_a}{k_B} + \ln\frac{1}{\beta y_p^2} - y_p \tag{2.23}$$

At a constant fraction transformed, α_p, this leads to

$$\ln\frac{\beta}{T_p^{\,2}} = -\frac{E_a}{k_B}\frac{1}{T_p} + C_1 \tag{2.24}$$

where C_1 is the integral constant $C_1 = \ln\frac{k_0 k_B}{E_a} - \ln\int_0^{\alpha_p}\frac{d\alpha}{f(\alpha)}$. The activation energy can be calculated by plotting a curve of $\ln T_p^{\,2}/\beta$ vs. $1/T_p$, which should result a straight line and the slope equals to E_a/k_B.

Flynn-Wall-Ozawa method

The Flynn-Wall-Ozawa method (Flynn and Wall, 1966; Ozawa, 1992) is based on the Doyle approximation (Doyle, 1965), which approximates the integral function as $\ln p(y) = -2.315 + 0.4567y$. The result of the integration form of **Equation 2.22** becomes

$$\ln \beta = -\frac{0.457E_a}{k_B}\frac{1}{T_p} + C_2 \tag{2.25}$$

where C_2 is the integral constant, $C_2 = \ln\frac{k_0 k_B}{E_a} - \ln\int_0^{\alpha_p}\frac{d\alpha}{f(\alpha)} - 2.315$. The method does not need the knowledge of reaction order to determine the activation energy. The activation energy for different conversion values can be derived by plotting $\ln\beta$ vs. $1/T$ curves at different conversion ratios.

Starink method

Starink (1996) adopted a more general expression of the conversion function

$$f(\alpha) = (1-\alpha)^p\left[\ln\frac{1}{1-\alpha}\right]^q \tag{2.26}$$

where p and q are constants that account for different reaction kinetics, *i.e.* $q = 0$ for any homogenous p-th order reaction kinetics. **Equation 2.24** is proposed to be a more general form of calculating the activation energy.

$$\ln\frac{\beta}{T_p^{1.8}} = -\frac{AE_a}{k_B}\frac{1}{T_f} + C_3 \tag{2.27}$$

where C_3 is the integral constant, $A = 1.007 - 1.2 \times 10^{-5} E_a$ with E_a in the unit of kJ/mol. The activation energy can be obtained through the slope of $\ln \beta / T_p^{1.8}$ versus $1/T_p$ curves.

ASTM method

A reference method for activation energy calculation from iso-conversion data is provided by ASTM standard E698-79 (1992). It is based on the Flynn-Wall-Ozawa method through assuming Arrhenius-type homogeneous reaction kinetics $d\alpha / dt = k(T)(1-\alpha)^n$. The activation energy is obtained by the slope of $-\ln \beta$ vs. $1/T$ curve. This method is also used in this work for comparison.

Friedman method

While all above methods are based on integration method, one differential method has been widely used (Friedman, 1969). The Friedman method is based on the intercomparsion of the rates of conversion $d\alpha/dT$ for a given degree of conversion α using different heating rates. By differentiating **Equation 2.20**, the equation below is obtained:

$$\ln(\beta \frac{d\alpha}{dT}) = -\frac{E_a}{k_B}\frac{1}{T} + \ln[k_0 f(\alpha)] \qquad (2.28)$$

For iso-conversion method where α = constant, a straight line should be found between $\ln(\beta \frac{d\alpha}{dT})$ and $1/T$ for different heating rates. The activation energy and the product $k_0 f(\alpha)$ can be obtained from the slope and the intercept of the straight line. The Friedman method does not involve any approximation and is mathematically exact. It requires both temperatures at

a fixed α and the conversion rate. The measurement of conversion rate is usually practically diffcult and source of error.

2.2.2 Reaction models determination

The temperature-independent function $f(\alpha)$, also under the name of 'reaction model function', reflects the intrinsic physical and chemical process whose analytical form is derived from multidisplinary backgrounds. $f(\alpha)$ in addition of activation energy reveals the fundamental kinetics of solid state reaction. The process of developing a diffusion-controlled reaction model function related to subsequent study in oxidation of nickel is present. For a homogeneous two-element reaction proceeding as $mA + nB = pC$, the general equation of reaction rate is

$$\frac{dc_c}{dt} = k(T)c_a^m c_b^n \tag{2.29}$$

where c_a, c_b and c_c denote the concerntration of reactants *a*, *b* and *c* as product, $k(T)$ is the rate constant which obeys Arrhenius relationship shown in **Equation 2.18** (Galwey, 2004). In case of heterogeneous solid-state reaction the concept of concentration is not valid anymore where reactants only have physical contact. The conversion ratio α is hence to be defined as an alternative parameter in equation. If the reactants are in form of spherical particles, the average radius before reaction is r_0. Therefore the reaction extent or conversion ratio is expressed as

$$\alpha = \left[\frac{r_0^3 - (r_0 - x)^3}{r_0^3}\right] = 1 - \left(\frac{1-x}{r_0}\right)^3 \tag{2.30}$$

If diffusion barrier in a solid state reaction can be neglected, and the reaction is under chemical kinetic control, the general equation is modified by induction of reaction cross-section, *S*

$$\frac{d\alpha}{dt} = k(T)S[f(\alpha)] \tag{2.31}$$

Regardless of geometric shape of reactant, the reaction cross-section is presumably constant during reaction. This model only works in the case that product volume change caused by reaction is relatively small and hence neglected.

Some examples of particulate solid-state reactions are quantitatively described by the reaction cross-section including $BaCO_3(s) + SiO_2(s) \rightarrow BaSiO_3(s) + CO_2(g)$ and $Na_2CO_3(s) + SiO_2(s) \rightarrow Na_2SiO_3(s) + CO_2(g)$ (Mitchell, 1969).

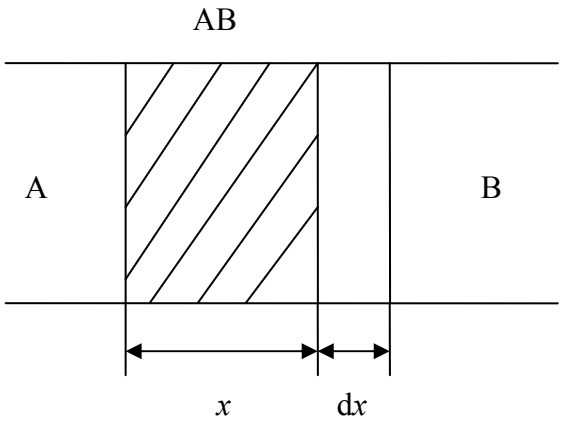

Figure 2.1: Schematic showing of planer layer diffusion

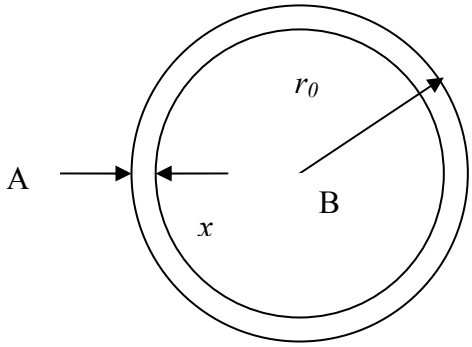

Figure 2.2: Schematic showing of spherical diffusion

Consider a reaction proceeding in planar contact of reactants ***A*** and ***B*** in **Figure 2.1**; two reactants approach each other at interface formed by the product ***AB***. For simplicity of description, it is assumed that the reactant ***A*** diffuses through the product layer whose thickness is x to react with ***B***, whereas assuming two-way diffusion gives similar results. From time t to $t+dt$, the mass through the unit area of cross-section of ***AB***, dm and c_0, the concentration of ***A*** at interface ***A***-***AB*** is represented by Fick's first law

$$\frac{dm}{dt} = D\frac{dc}{dx} \tag{2.32}$$

where D still represents diffusion coefficient. Rewriting dm in ρ, the density of ***AB***, and m_{AB}, the mole mass of ***AB***, it has $dm = \rho(dx/m_{AB})$. When the diffusion is stastic, the concentration profile along x is represented as

$$\frac{dc}{dx} = \frac{c_0}{x}; \qquad \frac{dx}{dt} = \frac{m_{AB}Dc_0}{\rho x} \tag{2.33}$$

The boundary condition is $x = 0\big|_{t=0}$. Integrating **Equation 2.33** gives

$$x^2 = \frac{2m_{AB}Dc_0t}{\rho} = Kt \tag{2.34}$$

In case of spherical sphere, illustrated in **Figure 2.2**, considering **Equation 2.30**, **Equation 2.34** becomes

$$x^2 = r_0^2[1-(1-\alpha)^{1/3}]^2 = Kt \tag{2.35}$$

Put the constant r_0^2 on the right side of equation, the renowned Jander equation (1927) is obtained:

$$g(\alpha) = [1-(1-\alpha)^{1/3}]^2 = \frac{Kt}{r_0^2} = K_J t \tag{2.36}$$

Ginstling and Brounshtein (1950) proposed that in the situation of diffusion control where ***A*** diffuses much faster than ***B*** and is consumed immediately in reaction with ***B*** at interface ***AB***-***B***, the concentration of ***A*** remains as zero, and at interface ***A***-***AB***, the diffusive component ***A*** has constant concentration c_0. Based on this it was developed that the thickness x has the relationship with the time

$$x^2(1-\frac{2x}{3r_0}) = 2K_0 t \tag{2.37}$$

Replacing x in **Equation 2.37** by **Equation 2.30** gives

$$g(\alpha) = 1-\frac{2}{3}\alpha-(1-\alpha)^{2/3} = K_G t \tag{2.38}$$

It is worth mentioning that Carter's model, *i.e.* **Equation 2.13**, is a modification of Ginstling-Brounshtein (G-B) model by introducing radius of reaction front (Ginstling and Brounshtein, 1950; Carter, 1960). The form of $f(\alpha)$ or $g(\alpha)$ is not only derived from reaction kinetic analysis but also from broader backgrounds *e.g.* statistical consideration for nucleation and formation of new phase. Kolmogorov-Johnson-Mehl-Avrami model obtained from analysis of statistics theory assisted by Arrenenius equation, in solid state reaction kinetics which is usually under the name of Avrami-Erofeev model (Kolmogorov, 1937; Johnson and Mehl, 1939; Avrami, 1939, 1940, 1941; Erofeev, 1960) is widely used in crystallization kinetics, polymers and depositions in surface science, ecological systems and even cosmology (Jun *et al.*, 2005). Some established reaction model functions are listed in **Table 2.1** (Bezjak *et al.*, 2002).

Table 2.1: Reaction models of solid state reaction

Model	$f(\alpha)$	$g(\alpha)$
Power law	$4\alpha^{3/4}$	$\alpha^{1/4}$
Power law	$3\alpha^{2/3}$	$\alpha^{1/3}$
Power law	$2\alpha^{1/2}$	$\alpha^{1/2}$
Power law	$\frac{2}{3}\alpha^{-1/2}$	$\alpha^{3/2}$
1st homogeneous	$1-\alpha$	$-\ln(1-\alpha)$
2nd homogeneous	$(1-\alpha)^2$	$(1-\alpha)^{-1}-1$
3rd homogeneous	$(1-\alpha)^3$	$\frac{1}{2}[(1-\alpha)^{-2}-1]$
4th homogeneous	$(1-\alpha)^4$	$\frac{1}{3}[(1-\alpha)^{-3}-1]$
Avrami-Erofeev	$4(1-\alpha)[-\ln(1-\alpha)]^{3/4}$	$[-\ln(1-\alpha)]^{1/4}$
Avrami-Erofeev	$3(1-\alpha)[-\ln(1-\alpha)]^{2/3}$	$[-\ln(1-\alpha)]^{1/3}$
Avrami-Erofeev	$2(1-\alpha)[-\ln(1-\alpha)]^{1/2}$	$[-\ln(1-\alpha)]^{1/2}$
One-Dimension symmetry	$\frac{1}{2}\alpha$	α^2
Two-Dimension symmetry	$[-\ln(1-\alpha)]^{-1}$	$(1-\alpha)[\ln(1-\alpha)]+\alpha$
Jander (three-dimension with constant diameter)	$\frac{3}{2}(1-\alpha)^{2/3}[1-(1-\alpha)^{1/3}]^{-1}$	$[1-(1-\alpha)^{1/3}]^2$
G-B (three-dimension with changing diameter)	$\frac{3}{2}[(1-\alpha)^{1/3}-1]^{-1}$	$(1-2\alpha/3)-(1-\alpha)^{2/3}$
Contracting sphere	$3(1-\alpha)^{2/3}$	$1-(1-\alpha)^{1/3}$
Contracting cylinder	$2(1-\alpha)^{1/2}$	$1-(1-\alpha)^{1/2}$

The thermo-activated physical processes are well described by the Arrhenius approach including nucleation and diffusion in which energy barrier must be overcome (Le Claire, 1975; Raghavan, 1975). The energy distribution presumably obeys Boltzmann statistics. However, the Arrenius-like equations can be further extended and show wider validity in condense matter physics from Fermi-Dirac statistics for electrons system to Bose-Einstein statistics for phonons (McCallum, 1970; Galwey, 1995).

2.3 Experimental Methods

As discussed in the previous section 2.1, the kinetic process of oxidation, *i.e.* the derived reactivity as function of time and temperature with respect to oxidation can be well established based on described models once the temporal oxide content and corresponding thermodynamic parameters and geometry details are known. This also requires the details of size, structure, and composition of reactants obtained from experiment. Generally there are two ways to estimate the oxidation contents: measurement of oxide thickness, depth, and volume, coverage etc. in direct or indirect manners and measurement of oxidation conversion extent without instant information of geometric details of reactants. The direct measurement mainly relies on the *in-situ* equipment such as high-resolution transmission electron microscopy (HRTEM), scanning electron microscopy (SEM), energy dispersive X-ray spectroscopy (EDS), AFM and STM (Kolarik *et al.*, 1992; Urban *et al.*, 1997; Chien *et al.*, 2001). High temperature and pressure mode equipments must be auxiliary if the oxidation occurs at elevated temperature, pressure or continuous heating condition. Glow discharge optical emission spectrometry (GDOES) is a recent technique for the quantitative measurement of depth-profiling of solids, which has been applied to oxidation of nanoscale material (Dosbaeva *et al.*, 2010). Interpretations of various instant images obtained from charge-coupled device (CCD) can be processed pixel by pixel and thus the geometry details can accurately calculated. Moreover, sample structure, lattice parameters, chemical composition and morphology of the samples are able to be derived (Urban *et al.*, 1997). Indirect measurement of

oxide growth refers to the *in-situ* conductance measurement. While the formed oxide is usually an insulator and the substrate metal is a conductor, the measured conductance is caused by the conductivity of residual substrate metal. When the oxidation is finished, the conductance should be decreased or dramatically changed consequently. Although the direct and indirect measurements are straightforward, the limitation is obvious: only regular objects with uniform shape, *e.g.* planar surface, individual sphere, single column etc. are suitable for this technique. For powder sample with multiple particles packing together, it is difficult to directly measure the overall oxidation. Instead, oxidation conversion extent is preferred in this kind of situation. A widely used conventional technique, TGA is used in this study. Single particle mass spectroscopy (SPMS) is recently developed (Mahadevan *et al.*, 2002) which allows for determining the oxidation conversion quantitatively for individual particle by dissociating particle into constituent atoms and their ionization. The technique is advanced and able to extract more intrinsic information of nanoparticle oxidation owing to non-contact recording mode, narrow size distribution and *in-situ* chemical composition detection. However, it is restricted by large energy consumption for producing uniform nanoparticle aerosol, complex experimental apparatus and only-isothermal conditions.

2.4 Simultaneous TGA/DSC and its Modelling

Due to its simplicity and reliability, simultaneous TGA/DSC is used as a popular technique to investigate the thermodynamic properties of nanoparticles. Some research works have been done on oxidation of nanoparticles. A brief introduction of the technique and a related work on nanoparticle oxidation adopting TGA/DSC is reviewed.

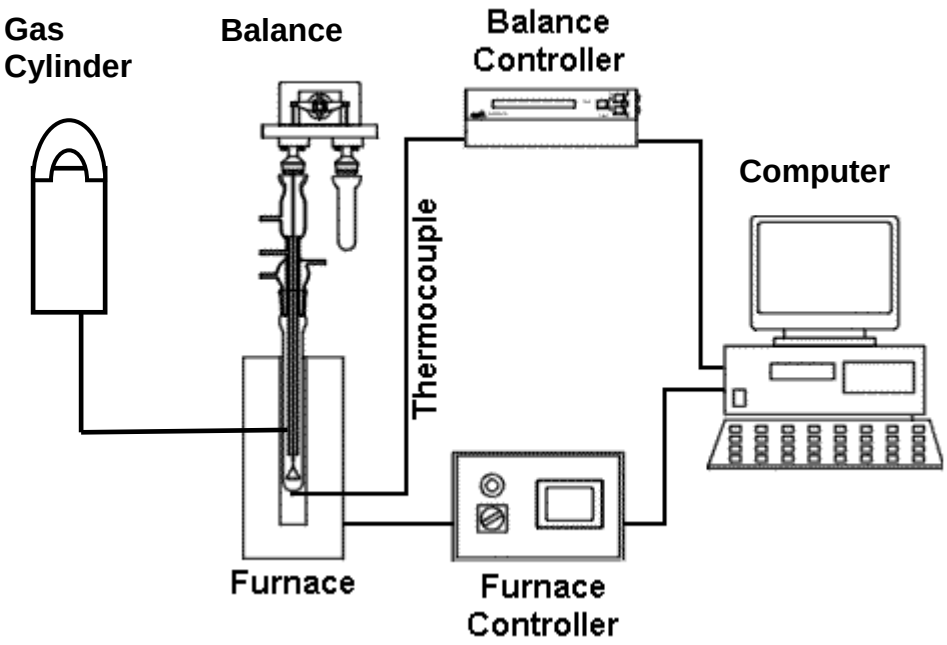

Figure 2.3: Scheme of simultaneous TGA/DSC
(Redrawn from http://www.cielec.com/lab/microbalance/weight_force_recording_-microbalance.html)

TGA is an experimental technique that is performed on samples to determine changes in weight in temperature-related change. The sample is loaded on a high-precision balance with a pan (generally platinum or alumina) in a thermo-insulated furnace in which the temperature is controlled by a computer-controlled electrical heater. The temperature can be adjusted up to 2000 °C. The weight change is recorded by a microbalance to a reference weight gain. Weight, temperature, and their change are measured preciously by computer-controlled microbalance and thermocouple. DSC is a thermoanalytical technique that measures the difference of heat required increasing the temperature of a sample and reference which is adjusted to nearly the same temperature. The samples are usually materials whose heat capacity is well-defined. Notice that the particulate samples are assumed to be homogeneous heat conductive without heat transfer barrier. Since many transitions and reactions are kinetic events which are both time and temperature's functions. This causes

the lagging effect in measurement during TGA/DSC. The lagging effect means that they will shift to a higher temperature when heated at a higher rate because it has less time at any specific temperature. Actually it is fundatmental information of extracting kinetic parameters, but needs correction when measuring melting point. All the thermodynamic transitions measured by DSC in this thesis such as melting is hereafter mentioned as corrected one. DSC and TGA are convenient to be coupled into one set of instrument to monitor a weight and heat change of the same process simultaneously. Derived directly from weight information, the weight derivative to time or temperature (under given heating rate), *dm*/*dt* and *dm*/*dT* can also be obtained, which is referred as Differential thermal analysis (DTA). The atmosphere in furnace is generated by a gas supply to the furnace. The atmosphere may be purged with an inert gas to prevent any reaction or desired gas to allow reaction to take place. A typical simultaneous TGA/DSC is schemed in **Figure 2.3**.

Many models based on TGA have been proposed by different authors based on different emphasises (Karmhag *et al.*, 2000, 2001, 2002; Eisenreich *et al.*, 2004; Trunov *et al.*, 2006; Rai *et al.*, 2006). All these referenced models assume that the particles are spherical and even distributed in size before oxidation occurs, which is a potential source of model failure in nanoscale situations.

Oxidation of a set of aluminium particle samples ranging from micrometer to nanometer are studied by Eisenreich *et al.* (2004, 2005), which is the only analytical model directly based on TGA data in an ambient atmosphere in the references covered by this thesis till it is being written. The oxidation was found to proceed in two sequent steps. The first step of oxidation occured below 627 °C and was thought to be governed by chemical reaction kinetics. First oxidation step typically generated an oxide layer of about 8 nm that is independent of initial particle size. This result was consistent with the oxidation of boron; however, no kinetic parameters were derived for this stage in their study.

In the second oxidation step, the diffusion of oxygen to metal core and the oxidation reaction occured simultaneously and takes control of the oxidation process. Assuming uniform temperature distribution throughout the sample, the profile of diffusing oxygen from the surface to reaction front was given by a steady state one dimensional concentration profile:

$$c_o = c_{o,k} + (c_{o,s} - c_{o,k}) \frac{1 - R_K / r}{1 - R_K / R_s} \tag{2.39}$$

where c is the concentration, r is the radius variables, the R_o, R_s and R_K represent oxygen, surface and reaction front radius respectively.

In the model, the diffusing oxygen was assumed to be consumed completely at the reaction front, in a first order of chemical reaction and oxide form stoichiometrically. Diffusing oxygen at reaction front was consumed by first order reaction

$$\frac{dn_o}{dt} \propto -4\pi R_K^2 K(T) c_{o,k} \qquad K(T) = Z_K \exp(-E_K / RT) \tag{2.40}$$

Diffusing rate at reaction front

$$\frac{dn_o}{dt} \propto -4\pi R_K^2 D(T) \left(\frac{dc_o}{dr}\right)_{r=R_K} \qquad D(T) = Z_D \exp(-E_D / RT) \tag{2.41}$$

where n_0 is oxygen mole number, Z_k and E_k are frequency factor and activation energy of chemical reaction and Z_D and E_D are frequency factor and activation energy of the diffusion.

By applying the reaction formula of oxidation of the aluminium, the relation of consumption rate between oxygen and aluminium is

$$\frac{dn_o}{dt} = \frac{3dn_{Al}}{4dt} \tag{2.42}$$

When combining **Equations 2.40-2.42** the reaction radius R_k is obtained by:

$$\frac{dR_K}{dt} = \frac{4M_{Al}D(T)}{3\rho_{Al}} \cdot \frac{c_{o,s}}{D(T)/k(T) + R_K(1 - R_K/R_S)} \qquad (2.43)$$

Under isothermal conditions, **Equation 2.43** can be integrated resulting in an inverse equation for *t*;

$$t = -\frac{3\rho_{Al}}{4M_{Al}D(T)c_{o,s}} \cdot \left[\frac{D(T)}{K(T)}(R_K - R_S) + \frac{3R_K^2 - R_S^2}{6} - \frac{R_K^3}{3R_S} \right] \qquad (2.44)$$

To process the non-isothermal TGA-curves with a linear heating rate, numerical integration has to be applied.

Despite that the model fairly well predicts an uncompleted oxidation process below 977 °C, the model is oversimplified and should be treated as an ideal model. The drawbacks are: only the diffusion of oxygen had been considered and at their experimental heating rate (5 °C/min) the diffusion of aluminium can not be negligible (Campbell *et al.*, 1999), *i.e.* the activation energy obtained was for interplay of diffusion of oxygen and aluminium, especially at elevated temperatures (627 °C < *T* < 977 °C) where the model did not match remarkably. The weight increment in TGA was treated as function of reaction front calculated. And the function was derived from the least square fit of experimental TGA-curves. In this mathematical treatment, they assumed that the concentration profile given by **Equation 2.39** was always applied. Actually the steady-state concentration profile is not always validated; however, the profile keeps changing. The time-independent treatment, *i.e.* **Equation 2.39**, can be adopted only if when the consumption of species under study at interface is quantitatively balanced by their diffusion from larger distances (Rai *et al.*, 2002, 2006). In addition, Trunov *et al.* (2005b, 2006a) discovered that oxide layer on the surface of aluminium particles at low temperatures undergoes phase transformation as a common route is: Amorphous $Al_2O_3 \rightarrow (\gamma, \delta, \theta)\text{-}Al_2O_3 \rightarrow \alpha\text{-}Al_2O_3$, where γ, δ, θ alumina are the metastable intermediate phases with similar densities. Among these phases $\alpha\text{-}Al_2O_3$ is thermodynamically stable and usually referred as ‘natural phase’ in most applications and normal conditions.

Obviously, Eisenreich model is unable to reflect the possible phase change during oxidation, mainly because of unrealistic assumptions and therefore fails to provide insight of reaction kinetics. Though Trunov *et al.* (2005b, 2006a) detected the polymorphous phase transformation, a clear kinetic process of the oxidation is not quantatively extracted.

It is worth pointing out that the transitions and reactions occurring at nanoscale have much smaller timescale than a usual run of TGA/DSC lasting several hours. The information obtained from TGA/DSC only reflects collective phemomena of a powder sample of nanoparticles. The interpretation of the data from it should be carefully managed as quantitative estimations of powder sample of nanoparticles by assistance of many other experimental techiniques and convincing theories.

2.5 Oxidation of Metallic Particles at Reduced Scale

It is straightforward and reasonable to apply the extended models of oxidation for spherical particles to nanoparticles because the length scale of these models is well within nanometres. An obvious difficulty lies in the multiple particles powder whose size distribution varies among samples. Some successful models dealing with micrometer particles such as **Equation 2.13** of Carter's model use an average radius with the assumption of uniform size distribution. This approach works well for micrometre nickel particles as well as a few hundred nanometres nickel particles (Karmhag *et al.*, 2000, 2001, 2003) Why does the approach of using average radius work well for micrometer sample whose obviously has non-uniform size distribution? The reason is that the measured average size is usually close to that of primary particles in the sample. The finest particles in micrometre sample do not have remarkable effect on properties of interest at this dimensional scale. It is not valid anymore at nanoscale that those primary particles dominate the oxidation while the effect of smallest

particles is neglected. In contrast, the particle size distribution and morphology have great impact on oxidation and hence must be accounted.

In spite of complexity among different nanoparticle samples, a remarkable feature of nanoscale oxidation is that many properties are size-dependent associated with the large surface-to-volume ratio. Only a slight change in the surface of oxide attached to metal substrate can significantly affect physical and chemical properties of nanoparticles due to the large surface to-volume ratio especially for applications such as conductors, catalysts and optical devices etc. (McCallum, 1970; Urban *et al.*, 1997). In term of oxidation process, many distinct features at nano scale were found including the size-dependent reactivity (Trunov *et al.*, 2006), depressed ion diffusion originating from high stress caused by thin oxide surface (Chen *et al.*, 2005) and self-limiting oxidation (Torre *et al.*, 2002).

Neglecting the effect of impurities present, the complexity of nanoscale oxidation is that, at these reduced dimensions, the apparent bulk scenario of oxidation is substantially affected and distorted by the high surface energy and its induced effects. The particle size effect on the oxidation of aluminium, iron and copper particles was investigated by Eisenreich *et al.* (2005). For all three metals investigated, the oxidation reaction depended on the particle size in regard to transient oxide formation and formation temperatures. In terms of oxide phase, nanoscale Al samples formed θ-Al_2O_3 and γ-Al_2O_3 simultaneously at 500 °C, whereas both of these oxides subsequently transformed to α-Al_2O_3 at 975 °C producing nano-scaled oxide particles. However, aluminium particles with sizes from 2 to 25 μm only formed α-Al_2O_3, starting at temperatures close to the melting point (Trunov *et al.*, 2006). Nano-sized iron nanoparticles formed α-Fe_2O_3 from 340 °C and no other oxides, which is different from bulk iron oxidation in which many forms of oxide phases were observed in the similar temperature range. On nano-sized copper particles the formation of Cu_2O started at 140 °C, transforming completely to CuO at 300 °C which also occured at relatively lower temperature. Particles at reduced dimension bear high surface/volume

ratio to enhance the heat releasing and other thermal properties during oxidation. The size morphology and distribution compose a heterogeneous environment and hence act as controlling factors of heat transfer, oxidation, combustion and ignition. The particular particles for modelling are usually taken in account with regularly geometric shapes such as spheres and rectangles. The shapes and size distribution are significantly determined by material type and synthesis methods. In practical applications, the size shape and distribution are essentials and challenges to modelling. It is desirable to use uniform distribution samples beneficial both to modelling and application by neglecting the effects of size distribution. For instance, a particular aluminium nanoparticle, 'Alex' (electro-exploded aluminium) is used by many authors due to its good uniformness (Ilyin, 2002; Kwok *et al.*, 2002; Gromov *et al.*, 2006). The onset and peak temperatures of aluminium oxidation is reported to depend on the size distribution and the peak temperature of narrow size distribution is 50 °C higher than those for broad size distributions samples (Trunov *et al.*, 2006a, 2006b).

For ultra fine particles, a common assumption that the thermal enthalpy H remains constant theoretically and depends only on thermodynamic and chemical properties of global reaction that is not be true anymore for ultra fine particles. A theoretical equation describing the the dependence of the latent heat of melting, H_m, on the bulk value of latent heat, H_b , particle diameter, d and metal atomic bond, l, (Jiang *et al.*, 2002) is expressed as

$$H_m = H_0 \exp\left(-\frac{2H_0}{3RT_0}\frac{1}{\frac{d}{6l}-1}\right)\left[1-\frac{1}{\frac{d}{6l}-1}\right] \tag{2.45}$$

Pantoya *et al.* (2006) did experiment on nano Al +MoO_3 thermite reactions to reveal the dependence of changing of enthalpy on heating rate (Pantoya *et al.*, 2005). The thermites of 76 nm in diameter heated at 2.5 °C/min have an average ΔH of 3596 J/g, which is reduced to an average ΔH of 1962 J/g for

15 °C/min. The mentioned thermite reaction is diffusion limited and the duration of the reaction of different heating rates will significantly influence the reaction progress and shift the enthalpy value. Trunov *et al.* (2005a, 2006a) revealed that the onset of aluminium oxidation is not dependent significantly on heating rate as which 5, 10, 20 and 40 °C/min are applied, but the initial augment of mass due to aluminium oxidation increase by decreasing heating rates that can be attributed to diffusion control step of oxidation. Trunov *et al.* (2005a) suggested that rate of particle self-heating due to aluminium oxidation varies as functions of particles size and when the rate exceeds external heating rate ignition will happen. The heat transfer mechanisms of specific features of different systems also would have a significant effect on the specific ignition temperatures (Granier *et al.*, 2004; Hu *et al.*, 2005; Hunt *et al.*, 2005; Trunov *et al.*, 2005, 2006).

As the oxidation process is closely linked with ion transportation and affected by the stability of the oxide shell, understanding the melting phenomenon is very important. For bulk crystal materials, equilibrium thermodynamic properties such as the melting temperatures are independent upon external conditions; however, the melting temperature and melting enthalpy of nanoparticles are strongly dependent on particles size and morphology. Because of the increased fraction of loosely bounded atoms at reduced dimension, melting can be easily induced by motive atoms that results in lower melting temperatures. This phenomenon has been widely accepted theoretically and experimentally by many researches (Karmhag *et al.*, 2000, 2001, 2003; Pantoya *et al.*, 2005; Trunov *et al.*, 2006a, 2006b). The melting of solid metal could enhance the diffusion transportation of cation and ion, and affect the mechanical stability of the oxide shell which is crucial to the onset of ignition and combustion (Park *et al.*, 2006). In addition the melting of metal core has been confirmed to be able to induce a large pressure gradient in the order of GPa/nm (Chen *et al.*, 2005). At such pressure gradients, the oxide shell will be under tension and metal core be under compression due to the density difference (Rai *et al.*, 2006), which

could, under particular conditions, break the oxide shell and expose core metal to rapidly accelerate the oxidation process. Given this possible interplay, the relationship between oxidation and melting also draw some attention among different researches. For example Rai *et al.* (2006) reported that the oxidation occurs much earlier than the melting occurs while Trunov *et al.* (2006b) argued that the onset of oxidation is closely linked to the beginning of melting.

To accurately measure melting phenomena at nanometer scale, techniques such as hot-stage TEM and small angle X-ray scattering (SAXS) are deployed, which can be used to determine the point at which crystalline structure of nanocrystals starts to be lost. Conventional DSC technique is still commonly used to reveal melting due to its convenient operation and accuracy.

For example Trunov *et al.* (2006) reported that the melting temperature of aluminium was 570 °C at a mean diameter of 44 nm, which was 90 °C less than that of bulk aluminium. Similar melting depression phenomena have been observed for many other nanoparticles (Huh *et al.*, 1999; Ilyin *et al.*, 2002; Rai *et al.*, 2002, 2004, 2006; Kelzenberg *et al.*, 2007). For nanoparticles the melting temperatures are generally fitted as functions of particle diameter, oxide layer, interfacial surface tension and bulk melting points. The models developed recently linking melting point, T_m to oxide thickness of aluminium as

$$T_m = T_0\left[1-\frac{4\sigma_{sl}}{H_0\rho_{Al}(d\ -2h_{ox})}\right] \tag{2.46}$$

where d is the metal core diameter, h_{ox} is the oxide shell thickness, T_0 is the melting temperature of bulk aluminum, H_0 is the enthalpy of fusion of bulk material, and σ_{sl} is the interfacial surface tension between the solid and the liquid. Another model (Eckert *et al.*, 1993) proposed that the melting point

is depending on the length of the metal atomic bond, *l*, similar **Equation 2.45** for latent heat of

$$T_m = T_0 \exp\left(-\frac{2H_0}{3RT_0} \frac{1}{\left(\frac{d}{6l} - 1 \right)} \right) \tag{2.47}$$

A classical general equation of melting at reduced scale for different materials are proposed as (Hanszen, 1960)

$$T_m = T_0 \left\{ 1 - \frac{2}{H_0} \left[\frac{\sigma_{sl}}{\rho_s (d/2 - h_0)} + \frac{\sigma_{lv}}{d/2} \left(\frac{1}{\rho_s} - \frac{1}{\rho_l} \right) \right] \right\} \tag{2.48}$$

where σ_{lv} is the liquid-vapour surface tensions and ρ_s and ρ_l are the density of bulk solid and liquid. The parameter h_0 is critical thickness as an adjustable factor. Despite the fact that nickel is one of the most widely used metals, there is still a great uncertainty on the intrinsic value of its surface tension, even in bulk scale with large inconsistence.

The early melting shift the oxidation mechanism by providing different diffusion pathways of oxidative species, where vacancies and defects dominate at solid state (Cachart *et al.*, 1969; Khoi *et al.*, 1975; Atkinson *et al.*, 1979, 1985; Mitra *et al.*, 1987) or causing interior stress depressing ion diffusion. A detailed review and discussion on nanoparticle melting and pressure can be reached in later chapters.

Oxide layers generated on pure bulk metal usually act as passivated films to protect metals from further corrosion. For fast energetic application the passivated layers formed on the surface may have some negative effects, which could impede the diffusion paths of reactants during the oxidation process. In heterogeneous oxidative enviroment the diffusion limited rate is mainly attributed to the thickness, structure and composition of the oxide layer (Giri *et al.*, 2001; Grainer *et al.*, 2004). The natural oxide layer is

usually caused by storage of particle sample. Many techniques such as XRD, EDS, X-ray photoelectron spectroscopy (XPS) and high-resolution TEM (HRTEM) are available to characterize the surface layer morphologies of the nanoparticles. Auger electron spectroscopy (AES) is applied as a main experimental technique to study diffusion through oxide/metal interface (García-Méndez *et al.*, 1999**)**. Campbell *et al.* (2005) had done a quantitative work on atomic diffusivity in oxide in use of molecular dynamics simulations. They also assumed that the pressure gradient along interface is the dominant driving force of the diffusion. The pressure existing within particles are experimentally studied by many researchers (Chen *et al.*, 2005; Rai *et al.*, 2006; Park *et al.*, 2006). In consideration of the nano dimension the existence of interface pressure is explained and implemented in several kinetic models (Rai *et al.*, 2006; Park *et al.*, 2006). However the diffusion coefficients calculated by different works have large discrepancies. The nanopowder is naturally heterogeneous for oxidation. Additional considerations are necessary to describe the oxidation kinetics when the oxides grow to cause discontinuities in the oxide coverage and particle morphology. The discontinuity may introduce isotropic compression on lattice of oxide resulting ultra high stress at interface of oxide and parent metal. It is known that the ion diffusion coefficient D can be affected by the stress in the relation of $D = D_0\exp(-vP/k_BT)$, where D_0 is at the stress-free state, P is the hydrostatic pressure, v is the activation volume, k_B is the Boltzmann constant, and T is the temperature. In the oxidation of Cu-Cu_2O, the stress can dramatically decrease the diffusion coefficient on the order from range of 10^{-1} to 10^{-4}. Correspondingly, change of about 4 orders in magnitude in the rate constant (Chen *et al.*, 2005)

Another issue of interest is the morphology of oxide layers. If the uniform layer forms on the particle surfaces the data of TGA and DSC is supposed to be more reproductive. Otherwise uncovered areas of non-uniform surface of core metals will react with oxidised atmosphere directly that may induce chemical kinetic controlled stage to shift the oxidation mechanisms. Gromov *et al.* (2006) did measurements on long term effects of different

passivated layers coated on aluminium including some organic substances such as paraffin, stearic acid, oleic acid and found that natural passivated layer (alumina) after six years storage can achieve only 3% attenuation on final conversion ratio compared with the fresh prepared aluminium. But the exothermal enthalpy and activity in air decreased by 90% due to the growth of alumina layer.

The discontinuity also acts as hot-spots which localize the energy produces associated space-time fluctuations in the thermodynamic fields, such as pressure and temperature may lead to fierce reaction therefore is critical for energetic application (Baer, 2003; Kelzenberg *et al.*, 2007). The multiple particles powder inevitably undergoes agglomeration and sintering because the high surface-to-volume ratio makes the sample more sensitive to external thermal environment. Once a powder sample is exposed to an ignition source, the fast heating creates huge internal thermal stresses due to thermal expansion and volumetric strain during metal melting. In individual nanoparticle, the volume change associated with melting could induce large pressures. The oxide will grow from metal particles without forming a coherent crystal structure connecting the metal substrate. The core-shell structure, mismatch of crystal structure and density difference will cause pressure at the order of GPa in nanosized dimension. This hugely build-up pressure could cause rupture of the oxide shell. The unbalanced pressure forces between the exposed molten metal surface and solid core could generate an unloading wave that creates huge tensile pressures resulting in dispersion of ultrafine liquid clusters which vigorously explode at high speed. The clusters may react with oxygen (or nitrogen) in the air or other gaseous oxidizer in scenario of which oxidation is not limited by diffusion (Pantoya *et al.*, 2005).

Given the complex of nanoscale oxidation, there is a need to develop a general methodology of modelling oxidation of metallic nanoparticles in which the material's distinct features are integrated without unrealistic

assumptions. The model should also have capability of unveiling reaction mechanism behind the complicated nanoscale reality. According to the previous discussion, the conventional oxidation models coupled with direct measurement of oxide growth are difficult to apply on nanopowder due to heterogeneous reaction environment and experimental challenge of direct measurement. Some analytical models based on TGA are meaningful trials, however, uniform size distribution and unjustified kinetic assumptions are involved inevitably. In the field of nanoparticles oxidation the experimental results obtained from conventional TGA/DSC have not been put under kinetic study in use of isoconversion method. The study is inspired by the model-free feature of isoconversional method which can avoid unrealistic mechanism assumptions for naturally heterogeneous nanoparticles undergoing complex processes during oxidation.

2.6 Chapter Summary

The oxidation theory of thin metal planar film are reviewed in this chapter and the space charge and its induced electric field affect the oxidation in course of diffusion of reactive species such as ion, electrons and the model is convenient to be extended to spherical geometry. Though they are restrained in isothermal conditions and homogeneous or mono-particle situations, a model developed by Carter (1960) based on core-shell diffusion successfully is applicable to nickel nanoparticles. The kinetic model of metal is built on the thermochemical data of reactants. Related experiment tools and reaction models, particularly, the isoconversion method are reviewed in this chapter.

Chapter 3

Experimental Study of Oxidation of Nickel Nanoparticles

3.1 Introduction of Nickel and its Oxidation

Nickel particles have been conventionally used in many industrial and consumer products including magnets, stainless steel, special alloys, coinage, plating and glasses. Due to the increased specific surface area and reactivity, nanometer sized nickel particles could significantly improve the quality of conventional products and promote new applications, which include catalysis for promoting hydrogenation process (Pina *et al.*, 2003) and for controlled growth of carbon nanotubes (Ducati *et al.*, 2004), application of nickel colloids as printing inks in microelectronic devices to manufacture of conductive multilayer electrical contacts and interconnections (Tseng and Cheng, 2006), development of high-performance solar absorbing coatings for increased solar energy conversion (Karmhag *et al.*, 2000) and being potential ferromagnetic candidate as susceptor materials and Curie temperature based control for processing applications in composite materials (Suwanwatana *et al.*, 2003). Among all these applications, nickel particles are typically exposed to an oxidative environment and their performance is greatly affected by the subsequent oxidation process. The formation of an oxide layer at the nickel surface could degrade the performance such as under catalytic and ferromagnetic conversion conditions. With an increasing use of nickel nanomaterials, this problem and cost of corrosion is expected to increase. Therefore it is essential to understand the oxidation behaviour of nickel nanoparticles.

The growth kinetics of nickel oxide layers at bulk level have been widely investigated for a long time and the results have been summarized in several books and review articles (Fromhold, 1976, 1980, 1988; Karmhag *et al.*, 2001). Only limited studies, however, have been carried on about the oxidation of particles and even fewer of nanometer particles. For large nickel particles, theories based on diffusion (Carter, 1960) and on the coupled current approach (Fromhold, 1988; Niklasson *et al.*, 2003) have been proposed. Within the limited studies at nanometer scale, the oxidation behaviour of nickel nanoparticles has been found to be remarkably different from that of large particles and bulk nickel materials. The activation energy of oxidation above Curie point, θ_c = 358 °C, appears to be in the range 1.6-1.8 eV (Graham, 1972; Atkinson, 1981; Sales, 1985), but at lower temperatures widely different values ranging from 1.3 eV to 2.65 eV (Sales, 1983) have been found. Suwanwatana (2003) reported apparent activation energies 1.55, 1.32 and 1.12 eV, for nickel particles with diameters of 79 nm, 0.7 μm, and 3μm between 250-350 ° C. Karmhag *et al.* (1999) reported nickel particles with an approximate diameter of 5 μm have apparent activation energy of about 1.5 eV in the temperature range 300-700 °C. Later they (Karmhag *et al.*, 2003) reported a non-linear growth for nano nickel particle with diameter of 15 nm, in the range of 135-235 °C, which gives activation energy 1.34 eV, though it is unclear yet whether the depression of activation energy is genuinely a particle size effect or an experiment fluctuation. Above the Curie point, they used 1.6 eV, which is bulk's value. Karmhag (2001) also derived 1.73 eV for nickel nanorod those diameter is 30 nm, and height is 300 nm. The experimental investigation is generally based on the thermogravimetric analysis and operated under isothermal conversion conditions (Karmhag *et al.*, 2000; Tseng *et al.*, 2002; Niklasson and Karmhag, 2003), where the conversion ratio is limited to small values *i.e.* < 20.0% by weight.

It is unknown if the mechanisms at low oxidation ratio could be extended to high oxidation ratios and the influence of heating rate on the oxidation

kinetics is also unclear. Metal nanoparticles are typically covered by oxide layers as passivated surfaces to protect them from further oxidation, the composition and thickness of these layer play significant roles in the oxidation process, however the detailed sample characterization and composition analysis of the oxide layer are apparently neglected in most of reported experiments (Karmhag, 1999; Rai *et al.*, 2002, 2004, 2006), which might be one primary reason for the wide data scattering as reported. On the mechanistic understanding of oxidation at nanometer scale, large data variation has been found on the values of activation energy of oxidation derived from the classical Arrhenius type mechanism (Ortega, 2001), and there are still no convincing theories on the oxidation of nanoparticles.

3.2 Experiment

Simultaneous Thermal Analyser (STA1500) from the Rhenometric Scientific was selected to carry on the oxidation experiments. Both TGA and DSC analyses of STA1500 were carried out at same time, assuring identical conditions. STA1500 utilizes the highly accurate and internationally accepted temperature calibration. The weight of nickel nanoparticles was controlled at small amount, 10±0.5 mg, to minimize the temperature gradient within the sample. The samples were loosely deposited on an alumina cylindrical crucible with diameter of 5.77 mm, and all oxidation experiments in TGA/DSC were performed in air under atmospheric pressure. Each sample was run one time at each heating rate. The gas flow rates were set at 20 ml/min. Precautions were taken for the air floating and convection effect that could induce data fluctuation, since the data collection is sensitive to vibration of platform.

The sample nickel particles were purchased from the Sigma-Aldrich Company, UK. The particles before and after oxidation were characterized under a TEM (JEOL JEM 2010) to determine their size and shape profile. Sample TEM pictures are shown in **Figure 3.1**. The as-received nickel particles are approximately spherical with a wide particle size distribution

between 10 to 100 nm. The averaging particle size estimated from TEM images is as 30 nm, which is similar to the nominal size from the provider. Similar average size value is also obtained from the Brunauer-Emmett-Teller (BET) multipoint method, where the specific surface area of original nickel samples is measured as 4.405 m^2/g equivalent to an average particle size of 28 nm.

In order to quantitatively investigate the oxidation behaviour, the element composition of as-received nickel nanoparticles and particle samples after oxidation experiments were analyzed by an Energy Dispersive X-Ray Spectrometer (EDS) from the Oxford Instruments, equipped with the INCA Energy 300 system. Unlike nickel particles investigated by other researchers, *i.e.* Karmhag *et al.* (1999, 2001), which contained some common metal impurities such as Fe, Co, Cr and Cu, the EDS analysis confirmed the high purity of metal nickel content, 99.9% by weight, which is consistent with the data from the manufacturer assuming no oxidation during storage. The EDS analysis identified the presence of oxygen element in nickel powders, 0.72 to 4.9% by weight at different sampled areas, **Table 3.1**, prior to the experiments, which implied some initial oxidation of nickel particles occurred during the production or storage period. This is likely be caused by the non-uniform distribution of defects of nickel crystal structures. Statistical oxygen weight concentration of these seven areas is 1.64% by weight, which represents a nickel oxide concentration of 7.65% by weight. This represented a mean oxidation layer thickness of 5.0 nm for an average nickel particle size of ~30 nm. Though limited by the accuracy of the equipment, this simple EDS analysis clearly reveals the existence of a non-homogenous profile of the initial oxidation. It should therefore be cautious to model oxidation kinetics without considering this initial oxidization or simply through applying a uniform oxide layer thickness.

Table 3.1: EDS composition analysis of Nickel nanoparticles

Element	Region 1 (Weight)	Region 2 (Weight)	Region 3 (Weight)	Region 4 (Weight)	Region 5 (Weight)	Region 6 (Weight)	Region 7 (Weight)	Average (Weight)
O	1.29%	0.94%	2.23%	1.44%	4.9%	1.64%	0.72%	1.87±1.4%
Ni	98.71%	99.06%	97.77%	98.56%	95.10%	98.36%	99.28%	98.13±1.4%

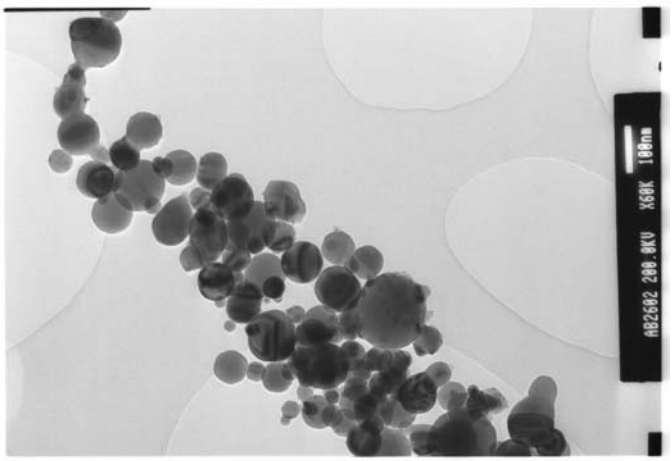

Figure 3.1: TEM image of nickel particle sample

The basic parameters for activation energy calculation, conversion ratios at given temperatures, are determined from TGA data by assuming a stoichimetric oxidation reaction, *i.e.* the weight gain is assumed to be equal to the consumed oxygen. Although some stoichimetric oxide such as Ni_2O_3, Ni_2O_2 and NiO_x were reported during the oxidation of some nano-nickel structures (Allouti *et al.*, 2006; Zhou *et al.*, 2006; Han *et al.*, 2007; Sasi *et al.*, 2007), a homogeneous transition from Ni to NiO is assumed in this study, which has also been confirmed by a separated *ex-situ* XRD experiment for samples before, during and after oxidation the nickel oxidation shown in **Figure 3.2**. As discussed in **Section 2.1**, there are initial oxide layers for all specimens before the experiments. This initial oxidation has to be taken into account in the data processing. Attempts have been made to calculate the activation energy without considering this oxide layer,

which results in reduced values of activation energies. The calculated values could differ in over 30% if counting all the sample weight as pure nickel. This could help explain some data scattering reported in the literatures on the activation energy of nickel particles (Ortega, 2001; Karmhag *et al.*, 1999, 2001). As shown in **Figure 3.2**, a complete oxidation can be assumed at the maximum weight.

The initial oxide weight, W_{iox}, is calculated by solving a mass balance equation

$$W_{iox} + (W_i - W_{iox})(N_{NiO} / N_{Ni}) = W_f \tag{3.1}$$

where W_i and W_f are the initial and final weight of the specimen, N_{NiO} and N_{Ni} are the molecular weight of NiO and Ni respectively.

The initial oxide weight is calculated from following equation:

$$W_{iox} = (W_i N_{NiO} / N_{Ni} - W_f) / (N_{NiO} / N_{Ni} - 1) \tag{3.2}$$

And the initial nickel weight, W_{iNi}, is

$$W_{iNi} = W_i - W_{iox} \tag{3.3}$$

The conversion ratio at a particular temperature T, $\alpha(T)$, is then determined from

$$\alpha(T) = \frac{(W(T) - W_{iox}) - W_{iNi}}{(W_f - W_{iox}) - W_{iNi}} \tag{3.4}$$

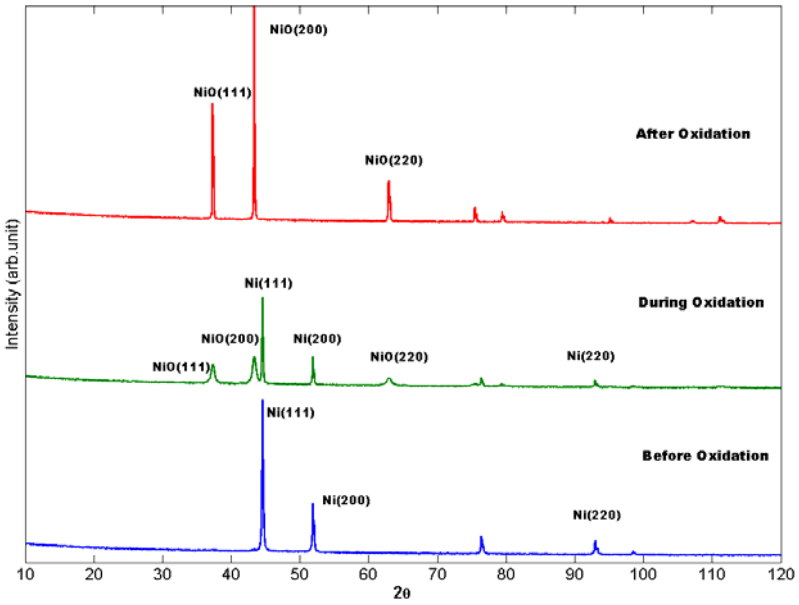

Figure 3.2: XRD of Nickel sample before, during and after oxidation

3.3 Isothermal Heating of Nickel Nanoparticles

For comparison with conventional theory, the isothermal oxidation of nickel is conducted at first place. The processing method of isothermal oxidation is adopted from Kamharg *et al.* (1999a, 1999b, 2000, 2001, 2003) described as below. The oxide ratio, α, has a general dependence on temperature under isothermal condition given by temporal Arrhenius equation in which reaction model term is a function of time

$$\alpha = \exp(-E_a / k_B T) f(t) \tag{3.5}$$

The logarithm of a particular conversion ratio, $\ln(\alpha_i)$ at particular oxidation ratio α_i under two different isothermal temperatures is expressed as

$$\ln \alpha_i = -E_a / k_B T_1 + \ln f(t_1) = -E_a / k_B T_n + \ln f(t_n) \tag{3.6}$$

The logarithm at a specific value of $\alpha = \alpha_i$ will give the two corresponding isotherms of temperatures T_1 and T_n

$$\ln f(t_n) = \ln f(t_1) - \left(\frac{E_a}{k_B T_1} - \frac{E_a}{k_B T_n} \right) \tag{3.7}$$

Thus $\ln f(t_n)$ can be considered as a constant translation from $\ln f(t_1)$ for any given conversion ratio α_i. The isotherms should therefore fall onto a single slope curve in a double logarithm plot ($\ln \alpha$ *vs.* $\ln t$) because the translation is only a function of temperature. The activation energy of the oxidation is hereby obtained from the slope of this 'master plot'. Isothermal TGA heating experiments were performed for 10 hours at 250, 300, 350, 400 and 450 °C using 10 mg nickel samples. The samples are all heated up at 30 °C/min to reach the given temperatures. Only the data from isothermal section was processed and the oxidation conversion *vs.* time with passavition layer being considered is presented in **Figure 3.3** as well as their fitted data presented in **Figure 3.4**. Notice the isotherm at 450 °C had severe fluctuation of data curve due to an accidental collision of instrument. The simple linear fitting was deployed for the raw data to get smoother curves.

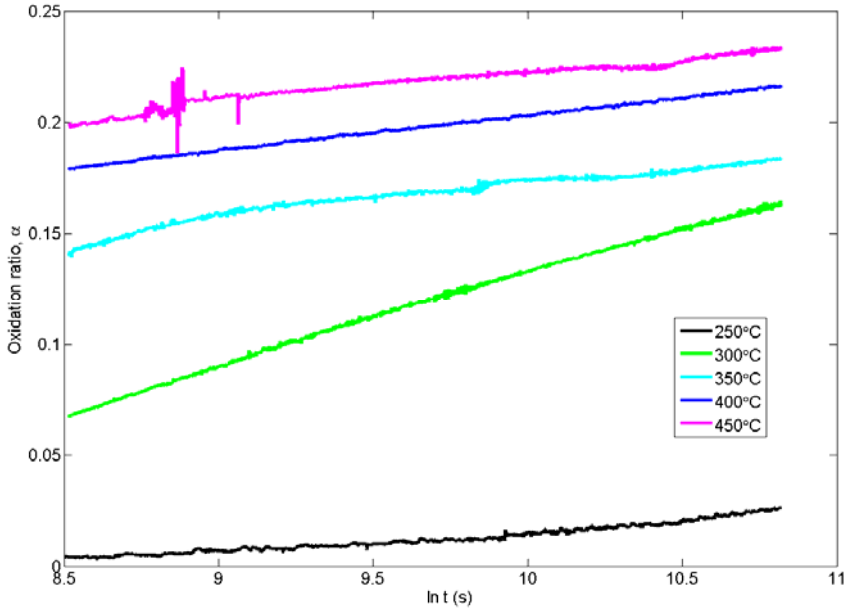

Figure 3.3: Raw data of nickel sample under isothermal heating

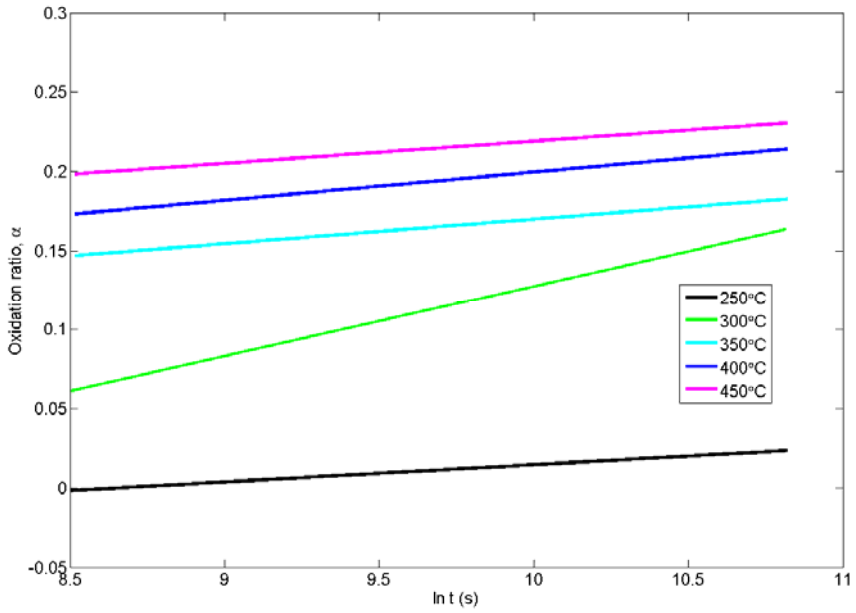

Figure 3.4: Fitted data of nickel sample under isothermal heating

The results from the oxidation measurements were shown in **Figure 3.5** where the conversion was plotted against time in a double logarithmic plot for all runs at each isotherm. It is seen that there are fairly large deviations from a series of single lines. The plots were not as expected to be located on single slope curve.

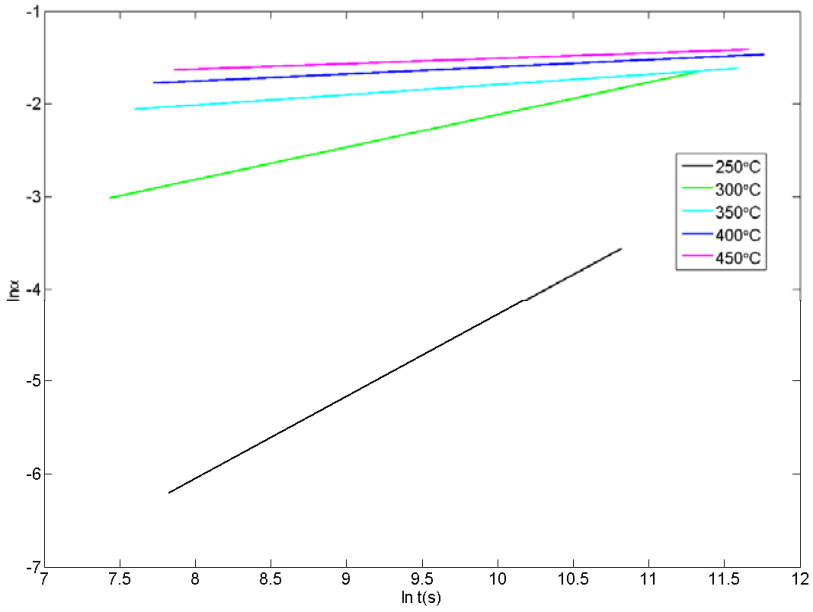

Figure 3.5: Double log plot of conversion ratio under isothermal heating

For temperatures regions under investigation, significant discrepancies appear. The isotherm of 300 °C has distinctly bigger slope than others above 300 °C while largest slope is from isotherm at 250 °C. Notice that the isotherms at 350, 400, and 450 °C displayed similar slopes, which implied that a possible change of oxidation mechanism at $T > 350$ °C. The masterplot is plotted with these three isotherms by translating the 400 and 450 °C to align with 350 °C as shown in **Figure 3.6**. Since the isotherms overlap only in a limited region, the data point at $t = 8000$ s was used as a reference in the translation of all isotherms. From **Equation 2.55**, it is seen that the activation energy of the oxidation process is obtained by plotting the shifts of the logarithms of the different isotherms ($\ln t_n - \ln t_1$) against the inverse temperature, $1/T_n$. The activation energy is calculated from the slope of the fitting curves. In **Figure 3.7** the shifts of the $t = 8000$ s approximated data points are plotted against the inverse temperature and an apparent activation energy of ~1.30 eV is found from the linear fit. Of note that the turning temperature of slope is 350 °C, which is close to Nickel's Curie point, $\theta_c = 358$ °C. Sales and Maple (1977) observed a departure from the fixed activation energy value at temperatures above Curie point ($\theta_c = 358$ °C) for microsized nickel particles, in the size range of 60-125 μm. It is indicated in their study that the activation energy below θ_c is 1.0 eV higher than that at temperature above θ_c, whereas E_a drops from 2.65 eV to 1.60 eV. The low activation energy found in this study from the masterplot, ~1.30 eV, is lower than that of micrometer samples (see **Figure 3.7**). The slope-change phenomenon might be related to the enhanced ion and electron mobility during paramagnetic-ferromagnetic transition (Sales and Maple, 1977).

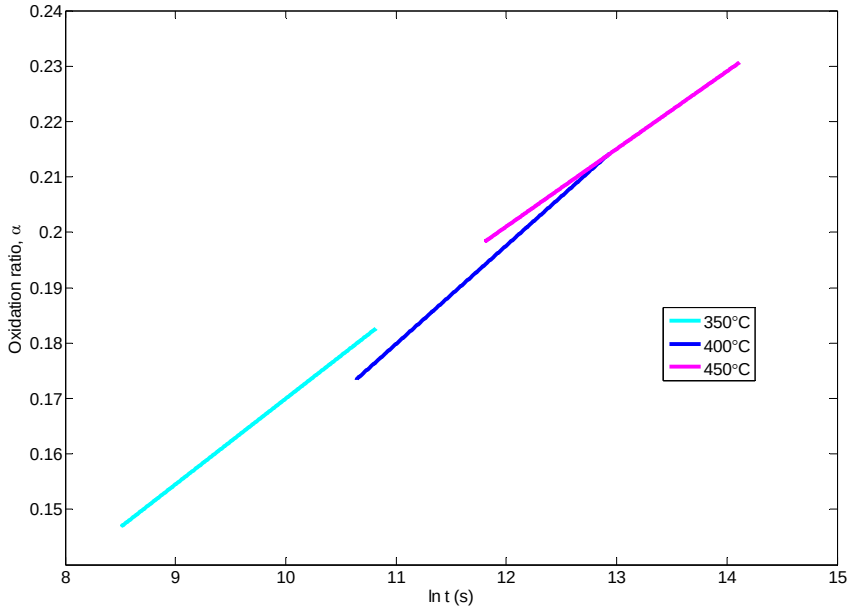

Figure 3.6: Master plot of nickel isothermal data

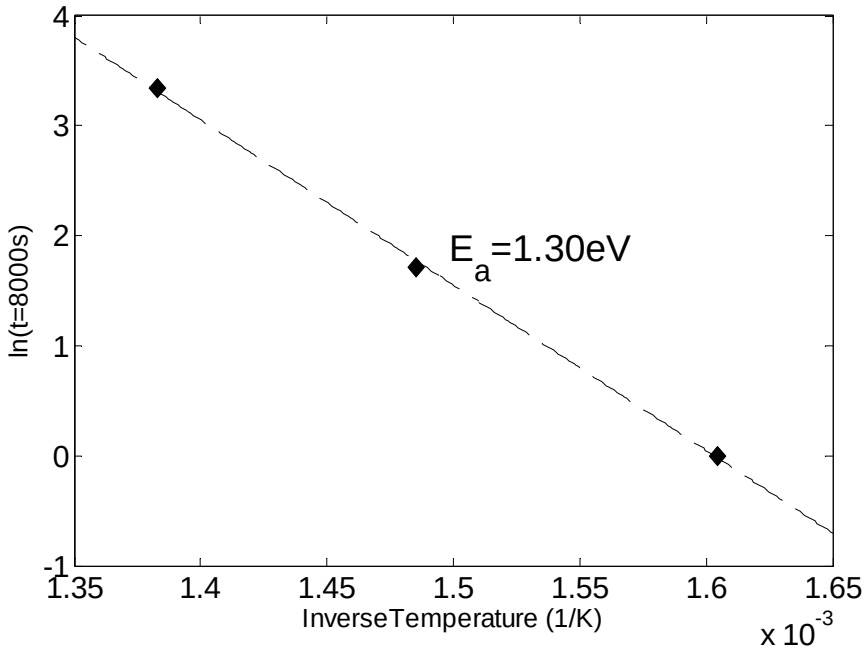

Figure 3.7: Activation energy of oxidation in reference of *t*=8000s

A qualitative comparison was made between this experimental kinetics data and oxidation theory of Carter's, in reference to **Equation 2.13**. The initial particle radius r_0 is the average value we found, ~30 nm. The relative volume expansion is 1.52 when Ni converts to NiO (Karmhag *et al.*, 1999a,

1999b). The rate constants were displayed in a double-log plot shown as **Figure 3.8**.

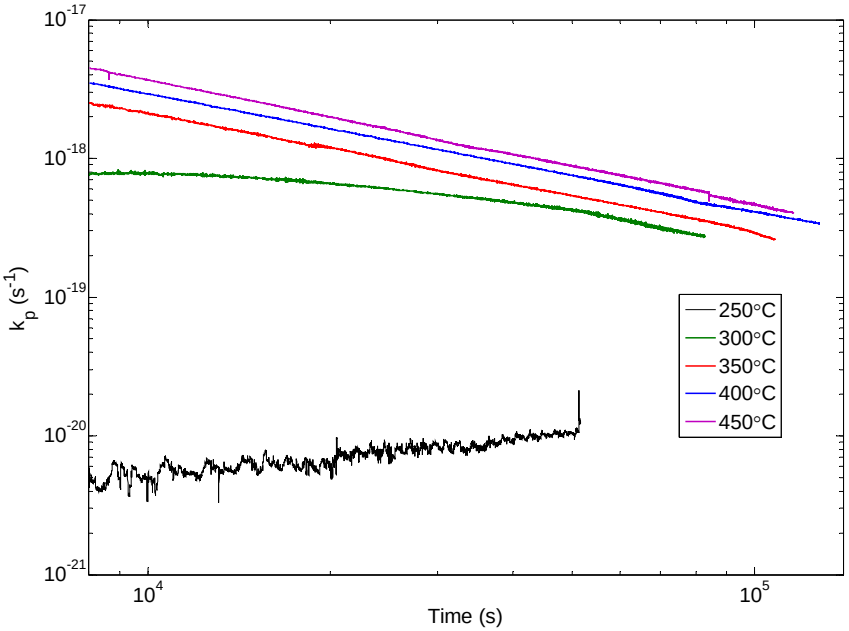

Figure 3.8: Rate constant based on Carter's equation

The difference of slopes appears in plot of rate constants and the distinction of different isotherms holded as well, see **Figure 3.8**. The values of k_p remain in range of $10^{-18.5}$ to $10^{-17.5}$ at each isotherm implying a rough agreement with Carter's model. The average rate constants at 250, 300, 350, 400 and 450 °C are 7.74×10^{-21}, 4.87×10^{-19}, 7.73×10^{-19}, 1.01×10^{-18} and 1.29×10^{-18} m^2/s respectively. In comparison with Karmhag's results for 5µm nickel particle whose rate constants were 5×10^{-21} m^2/s at 300°C, 2.5×10^{-20} m^2/s at 350 °C and 2.5×10^{-20} m^2/s at 400 °C (Kamharg, 1999a, 1999b, 2000), there is two order increase in the magnitude of reactivity for nickel nanoparticles. The Carter's model is derived from the core-shell diffusion-controlled mechanism in which oxide forms initially at the surface of nickel particle, and oxidation proceed subsequently as oxygen penetrates through the nickel oxide shell. The results for nickel imply that the Carter's model is roughly applicable on isothermal oxidation of the used nanoscale samples and the diffusion-control mechanism prevails above the Curie point of

nickel, though whether the appearing data fluctuation is caused by genuine nanoscale effect or experimetal error are difficult to be identified.

3.4 Non-isothermal Heating of Nickel Nanoparticles

Non-isothermal heating can cover much wider range of temperatures than isothermal experiment during a same period of time. The dynamic change of kinetic parameters will be also investigated. The oxidation of same nickel samples were carried out under non-isothermal conditions in the same apparatus. The experiments were started at room temperature and performed under iso-conversion conditions, with heating rates varying at 1, 2, 5, 8, 10, 15 and 20 °C/min with good DSC repeatability by loading another set of 20 mg samples. The TGA data of 20 mg samples displayed less repeatability due to unfinished reaction during the same period. The difference between heat rates was much bigger than sample variation. The experiments were performed for a few hours, depending on the heating rate, until the sample weight did not change with time, *i.e.* a complete oxidation.

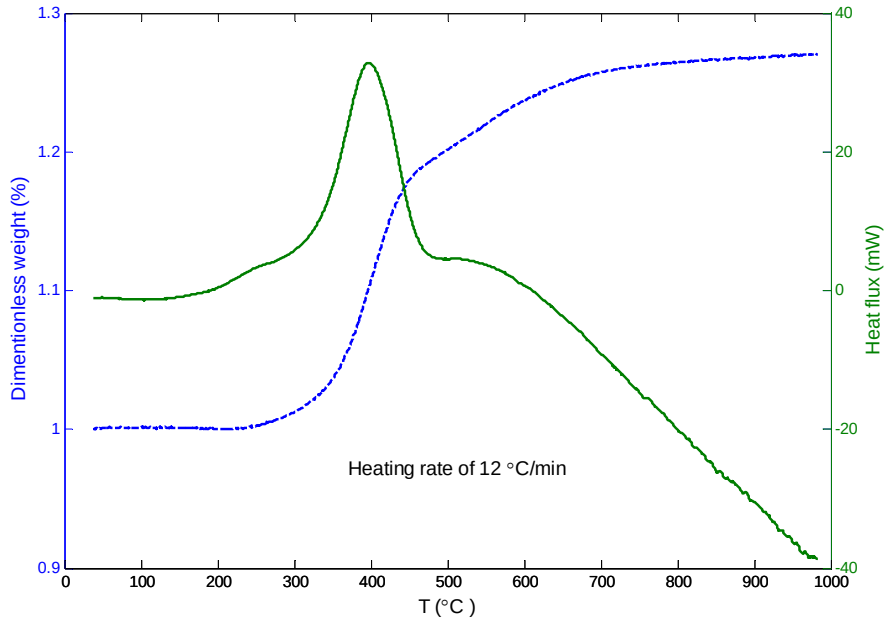

Figure 3.9: Sample TGA/DSC curves of nickel nanoparticle

The typical measured TGA/DSC was showed in the **Figure 3.9**. At early stage of heating, the weight of nickel nanopowders stays constant, or a very slight decrease for some samples, ≤ 0.37% by weight, at temperatures before ~200 °C. This is probably due to the absorbed residues such as water and/or carbon dioxide while samples were exposed to atmosphere (Uchikoshi *et al.*, 1994). The residue weights of all samples were deducted from original weight for the data analysis. The nanoparticles begin to show weight gain at temperature ~250 °C in the thermogravimetric analysis, an implication of oxidation occurs at this temperature, where a slight increase in the DSC curve is observed shown in **Figure 3.10** and **Figure 3.12**.

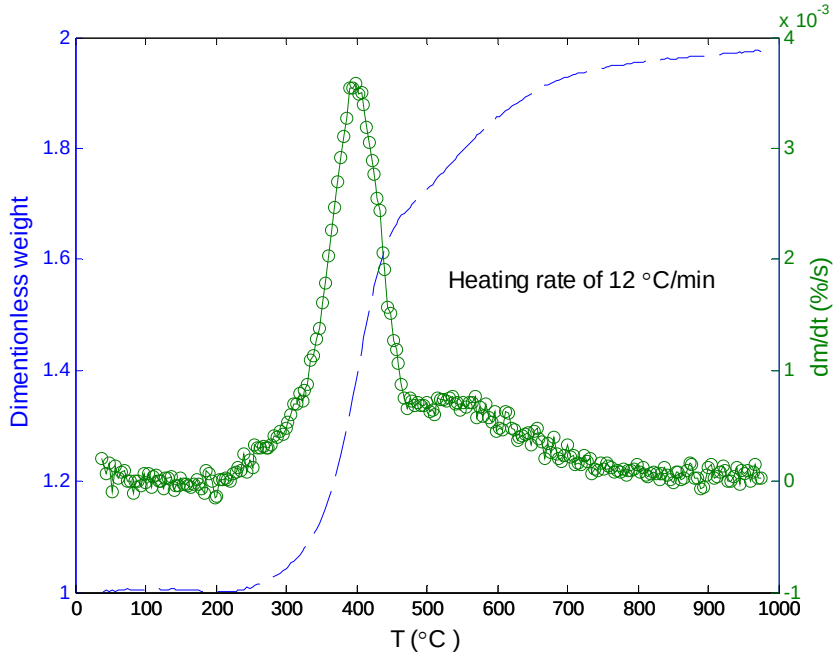

Figure 3.10: Sample TGA/DTA curves of nickel nanoparticle

Comparing to the typical initial oxidation temperature of bulk nickel materials, the oxidation of nanoparticles occurs at a much lower temperature. The fastest reaction occurs at a temperature at ~398 °C where the DSC peak is detected due to the exothermic oxidation reaction. A pronounced change in the oxidation kinetics, as observed from the slope change of the TGA curve, occurs at temperature ~450 °C. The decreased oxidation rate extends towards a higher temperature before approaching to a constant value asymptotically, an indication of the full oxidation of the specimen. Of note

is that negative DSC values are observed at temperatures over ~600 °C. As the DSC curve can only become negative when the endothermic melting rate exceeds the exothermic oxidation reaction, an early partial melting of heated specimen must have been experienced, far below its bulk value, ~1400 °C (Metals Handbook, American Society of Metals, 1979).

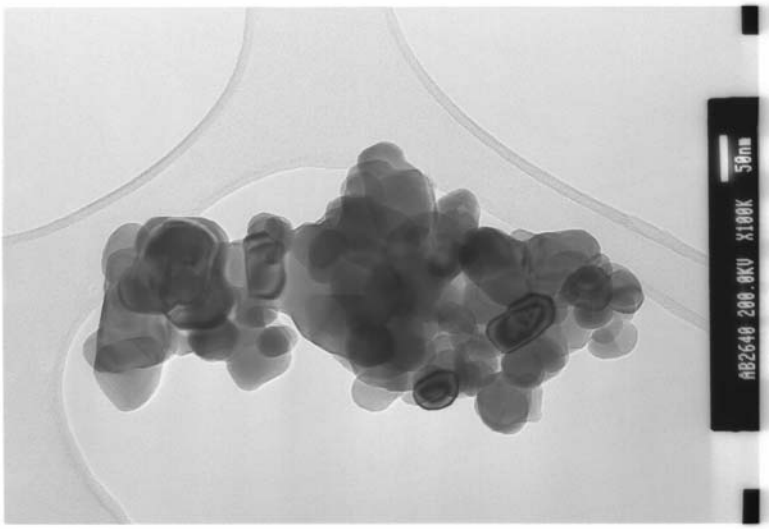

Figure 3.11: TEM image of nickel sample after oxidation

The early melting phenomena were also verified by the TEM picture of oxidized sample where large aggregates with irregular shapes are formed, see **Figure 3.11**. Similar characteristic points were also observed from the DTA curves as shown in **Figure 3.14**. The final weight increase of this sample material is 25.4%, which is slightly lower than the ideal weight increase of 27.3% for a complete pure-nickel oxidation. As observed from the EDS analysis, typical nanopowder samples contain some initial oxides, presumably a thin layer of amorphous oxide, before experiments. By assuming a completed oxidation at the end of the experiment, the initial oxygen content can be re-calculated as 1.5%, which is consistent with the EDS analysis.

3.4.1 Activation energy

Figure 3.12 shows different thermogravimetric curves under different heating rates. All TGA curves shift towards higher temperatures with increasing heating rates. Both initial oxidation temperature and characteristic temperature of oxidation slope change increase with increasing heating rates. There are, however, some variations, from 24.7% to 25.8%, on the final weight increase ratio, which correspondents to initial oxygen concentrations of 1.2% to 2.0%.

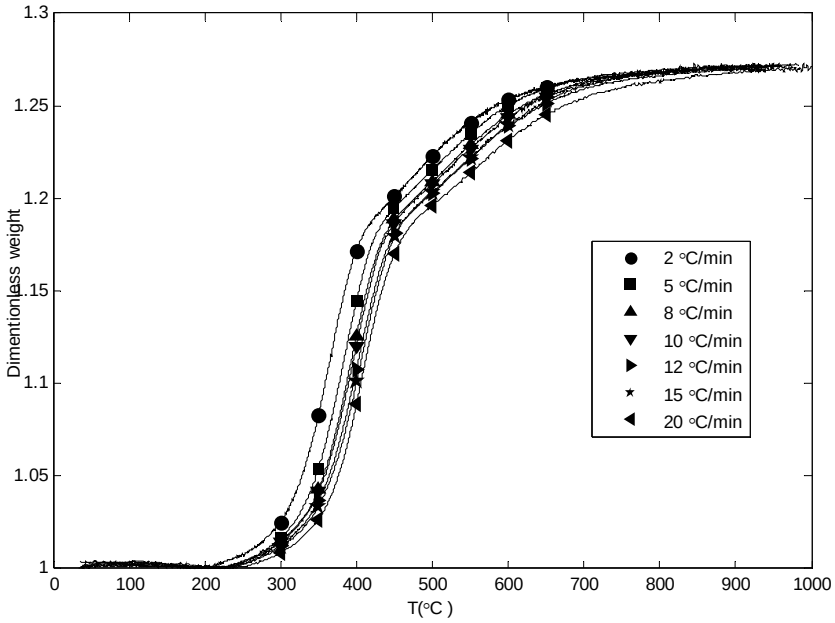

Figure 3.12: TGA curves at different heating rates

Similar DSC patterns are also observed under different heating rates, **Figure 3.13**. The positive sign of the DSC curve implies the strong exothermic reaction due to oxidation. Both peak heat flux and correspondent temperatures increase with increasing heating rates, **Table 3.2**. At high temperatures, most of the baselines of DSC curves overlap within the instrumental uncertainty for different heating rates. Of note that there is a base heat flux 3 mW initially for the highest heating rate 20 °C/min, which will be considered for further data processing. The DTA curves have similar

patterns with DSC curves, which again reflect the oxidation rate, see **Figure 3.14**.

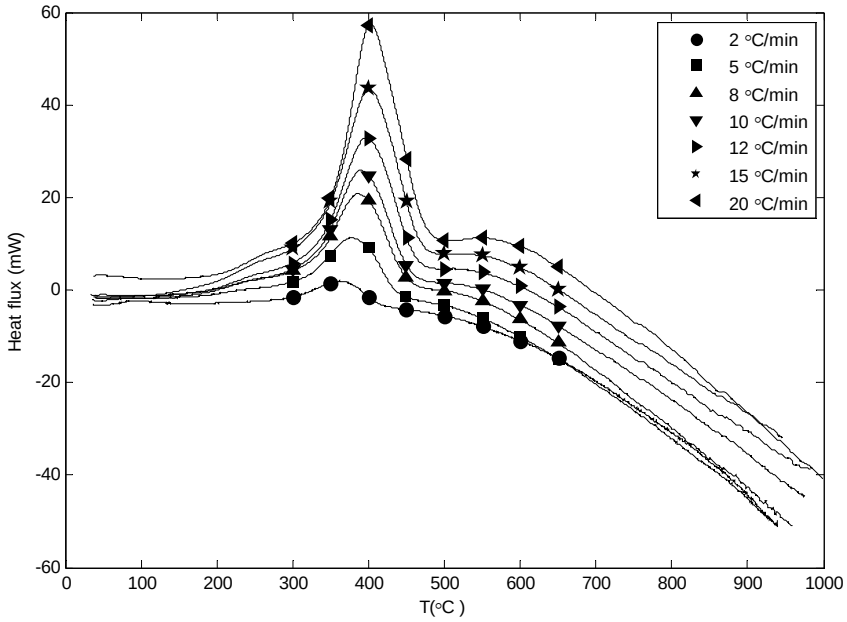

Figure 3.13: DSC curves at different heating rates

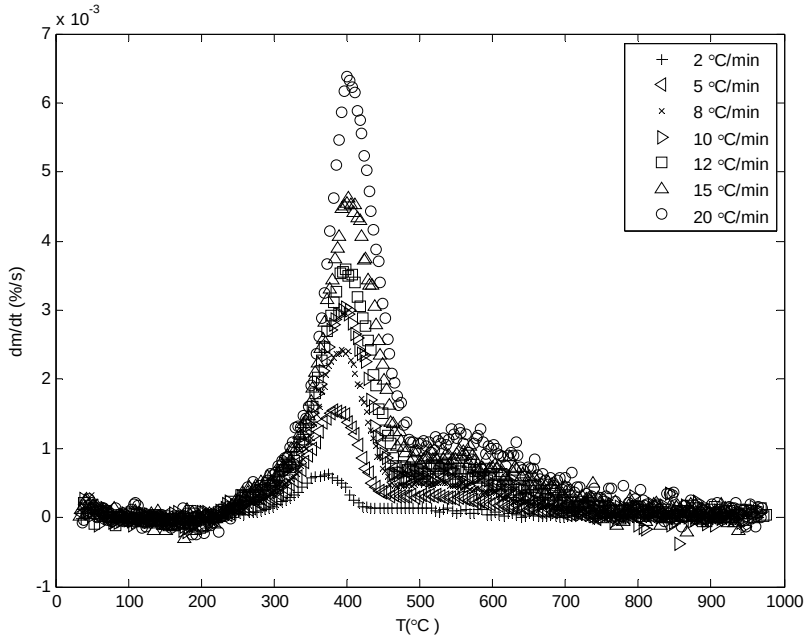

Figure 3.14: DTA curves at different heating rates

Table 3.2: DSC peak heat flux and correspondent temperature

Heating rate (°C/min)	2	5	8	10	12	15	20
Peak heat flux (mW)	1.95	11.23	20.76	25.90	32.86	43.48	57.43
Correspondent peak temperature (°C)	362.18	378.46	387.40	662.99	389.84	401.39	403.59

Both differential and integral methods are used to calculate activation energies at different conversion ratios and the result is shown in **Figure 3.15**. It clearly shows that all these methods have similar activation energy profiles. Unlike its counterpart at bulk level where the activation energy is a fixed value, the activation energy of nickel nanoparticles exhibits a strong function of the conversion ratio. It increases firstly with the increasing of conversion ratios, reaching a maximum value at a conversion ratio of 50% and decreasing afterwards. The calculation from all integral methods is pretty similar: all activation energy data fall within a boundary line of $\pm$ 10% around the mean values. There is an early peaking of activation energy and slightly large scattering of activation energy based on the differential method, which is due to the approximation of differential values $d\alpha / dT$ whose value is difficult to obtain experimentally because its high sensitivity to the baseline stability (Starink, 1996).

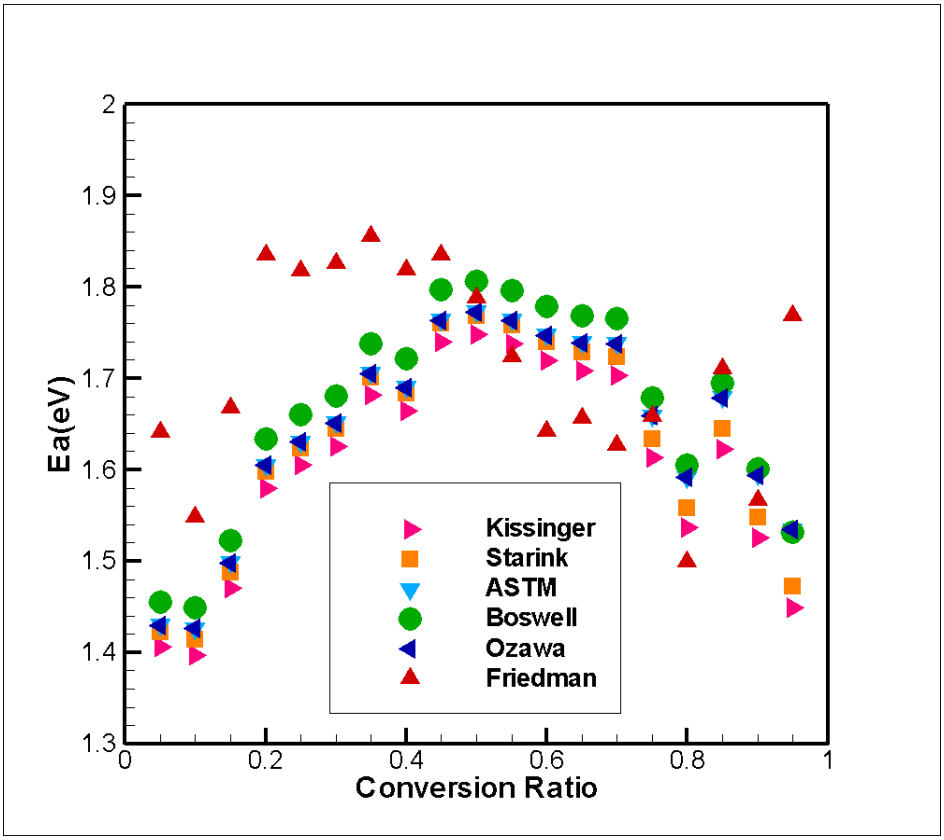

Figure 3.15: Activation energies as a function of conversion ratios

Figure 3.15 also shows that the activation energy of nickel nanoparticles generally falls into between 1.4 and 1.8 eV. The value is smaller than bulk values, which are in the range of 2.0-2.6 eV (Aktinson and Taylor, 1981), and similar to those derived from the isothermal method for nickel particles at micro/nanometer scale, *i.e.* 1.55 eV for 79 nm nickel particles (Suwanwatana *et al.*, 2003), 1.5 eV for 5 μm particles (Kamharg and Niklasson, 1999), 1.34 eV for 14 nm particles (Kamharg *et al.*, 2001). All these isothermal studies, however, derived only a single value of activation energy for nanoparticles. In theory, constant activation energy should be held for some homogeneous reactions where all freely moving reactant molecules are identical and unaffected by the product formation. However for solid state reactions especially oxidation at nanoparticle level, the reacting entities in a solid are not isolated during chemical changes proceeding in the rigid structure but interact with neighbours to which each

is bonded. There is the possibility during the reaction, that the reactant may undergo progressive modification of their reactivity by factors that may include crystal defect formation, particle disintegration, development of intra-crystalline strain etc. Furthermore, the initial reactivity of the individual particles that constitute the original reactant may be appreciably different due to variations of particle sizes, sintering, grain boundaries, crystal faces of different indexes exposed, crystal imperfections and damage etc. Sintering is also a factor taken into account in the contribution of various activation energies given that the severe morphology changing is observed in **Figure 3.11**. The sintering produces agglomerates and is expected to slow the oxidation kinetics (Wakuda *et al.*, 2008). The grain boundaries contained in large number of small crystallites facilitate the diffusion and the grain growth decrease the oxidation since the space charges may build upon oxide as they thicken and interfere with the movement of oxidative reactants. The root cause lies in the theory of parabolic law of bulk nickel growth, in which a linear diffusion in homogeneous field is assumed. The range of qaE_a is used to give an approximate whether the built-in potential at the oxide interface can be neglected while $qaE_a << k_BT$. The actual growth of oxide gives rise to a nonlinear effect as barriers for ion diffusion, which results in a growth equation deviated from its ideal bulk model. The distortion is more likely to occur on the used sample with detectable initial oxide surface. The increasing activation energy as oxidation proceeds may reflect the increasing reaction barrier caused by the various effects. The declining activation energy might be due to the relaxation of ion diffusion and eased environment of oxidation after Curie transition. Thus, the average reactivity of the assemblage of reactant particles may not remain constant as reaction progresses.

It appears plausible that variable activation energies should be used in order to accurately model the oxidation kinetics of nanoparticles. The single activation energy is thought to be interpreted only when an individual

homogenous reaction step is clearly identified (Opfermann, 2000). The various activation energies are also potentially capable of handling the oxidation of nanoparticles undergoing polymorphous phase transformation, *e.g.* aluminium (Vyazovkin and Wight, 1997). With respect to the isoconversional method we adopted, most solid-state reactions are not simple one-step processes with overlap and competition of multiple reactions. The kinetic compexities are not limited to multiple chemical steps, including more physical processes such as nucleation and growth, imperfection distribution, sublimation along with other reactions, surface adsoption, diffusion of a gaseous product through the sample, rate of growth varying along each crystallographic axis of a nucleus, particle size and morphology and localized melting (Khawam and Flanagan, 2005). The isoconversional technique may reflect complexity of the reaction mechanism in the term of a functional dependence of the activation energy on the ratio of conversion. The modelling fitting technique fails to reveal complex kinetics under isothermal conditions, but produce unambiguous values of E_a and k_0. It is suggested that the use of isoconversion method is an effective methodology of predicting kinetics of complex reactions (Vyazovkin and Wight, 1997; Galwey, 2004). Furthermore, by bringing the temperature ranges of isothermal and non-isothermal experiments close to each other, the isoconversion method is possible of producing consistent Arrhenius parameters for isothermal and non-isothermal results (Vyazovkin and Wight, 1997). Even though, in an identical temperature region where each reaction step is identified, the isoconversion and isothermal methods actually give different activation energy surface. Therefore, despite this significant difference between the two methods, the overall single activation energy, 1.30 eV found by isothermal experiment is slightly smaller than the value range corresponding with same conversion extent, *i.e.* $\alpha < 0.23$, which is 1.4-1.6 eV while the corresponding temperature range is above Curie point (358 °C). However, it is impossible to directly compare two results in which non-isothermal experiment go through much bigger conversion and temperature regions.

3.4.2 Reaction kinetics

The conventional master plot method is used to determine the reaction kinetics. By using a reference at a half conversion ratio, $\alpha = 0.5$, **Equation 2.22** is converted into:

$$\alpha(0.5) = \frac{k_0 E_a}{\beta k_B} p(y_{0.5}) \tag{3.8}$$

where $y_{0.5} = E / k_B T_{0.5}$, Dividing **Equation 2.22** by **Equation 3.8**, the following equation is obtained:

$$\frac{g(\alpha)}{g(\alpha_{0.5})} = \frac{p(y)}{p(y_0)} \tag{3.9}$$

Theoretical master plots can be obtained by plotting $g(\alpha)/g(\alpha_{0.5})$ for various $g(\alpha)$ functions as listed in **Table 2.1**. Once the activation energy has been determined, an appropriate kinetic model can be extracted by comparing the experimental master plot with the theoretical master plots for various reaction models. The plotting of experimental curve requires an approximation of $p(y)$ as it is analytically insoluble and various approximation methods have been proposed as described in **Section 2.2.1**. As the variation of these approximations generally is small, Kissinger's approximation is used here, $p(y) \approx \exp(-y)/y^2$.

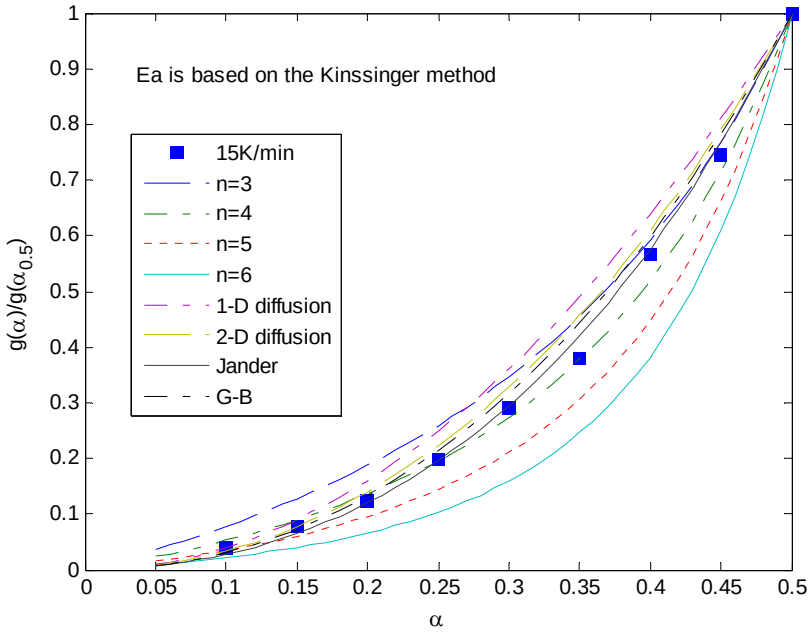

Figure 3.16: Kinetic model fitting at α < 0.5

The comparison of experiments with a number of reaction models is shown in **Figure 3.16**. The variable activation energies obtained from the model-free Kissinger method are used in the calculation. The figures show that at the low conversion ratio, **Figure 3.16**, the difference between different reaction models is small. A number of models including the diffusion based Jander equation, Ginstling-Brounshtein equation (G-B model) and 2-D diffusion model, and a 4th order homogeneous model can model the oxidation mechanism reasonably well, with the Jander equation having the best fit. However as the conversion ratio increases to over 50%, **Figure 3.17**, the diffusion based mechanisms become un-reliable and there is a large difference between the experimental results and predictions. The difference increases with increasing conversion ratios. However the experimental data can be predicted approximately by a pseudo-homogeneous model at an order between 4 and 6. It is generally accepted that the oxidation mechanism of Ni for thicker oxide films is dominated by diffusion of ion vacancies along grain boundaries in NiO (Cachart *et al.*, 1969; Khoi *et al.*, 1975; Atkinson *et al.*, 1979, 1985; Mitra *et al.*, 1987). The diffusion based mechanism with consideration of a built-in electric field has been accounted

for the observed oxidation of nickel with various particle sizes. The conclusion has been reached, mostly based on the iso-thermal and electrochemical methods (Graham *et al.*, 1972; Sales and Maple, 1977; Atkinson, 1985), and the conversion ratio is typically small, *i.e.* less than 20%. Within this low conversion ratio regime, the diffusion mechanism can be obtained. As shown in the TGA/DSC curves in **Figure 3.12** and **Figure 3.13**, there is a salient slope change at the conversion ratio 0.5. This has been also reflected in the activation energy curve, the calculated activation energy based on both differential and integral methods decreases as the conversion ratio over 0.5.

It is therefore expected that there is an oxidation mechanism change, which support the kinetic model fitting. Such a mechanism change at different oxidation stages has also been mentioned in other macroscopic studies, *e.g.* Peraldi *et al.* (2002) observed a crystallographic orientation dependent growth of bulk nickel oxidation and found that at high temperatures (> 1000 °C) the diffusion could not be the only operating mechanism. Similarly to isothermal study where the slope of masterplot changes, the reaction mechanism change at vicinity of Curie point of nickel (θ_c = 358 °C). As some research figured out, the mobility of ion associated with reactive species is increased dramatically at the vicinity of θ_c (Sales and Maple, 1977). The sintering process in which contact areas of particles are reduced may also affect the oxidation mechanism. These possible influences might be linked with the mechanism change from diffusion controlled to homogeneous reactions models. Strange though, the experiment shows that oxidation rate decreases while the activation energy decreases as the conversion ratios exceeds 0.5. This might be caused by the early melting of nickel nanoparticles that hinders the transportation of oxygen species.

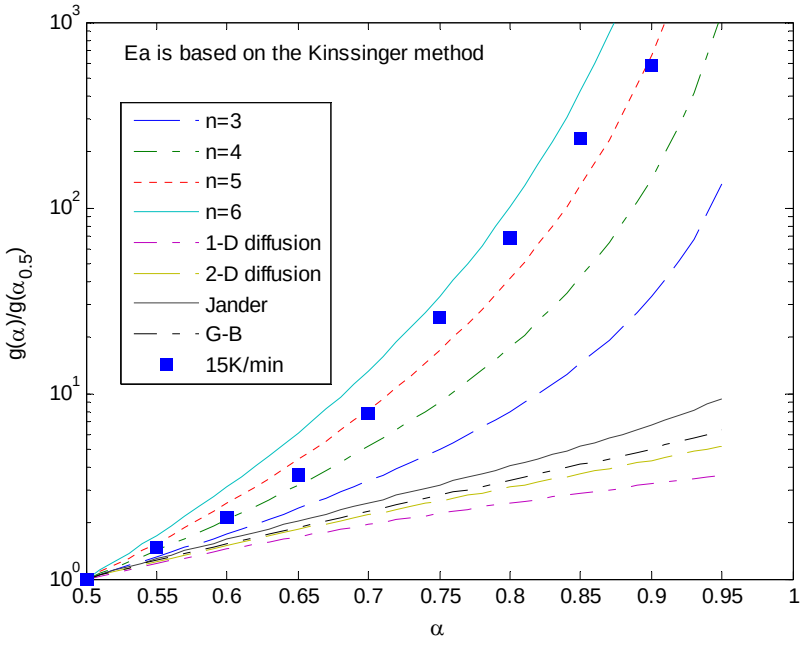

Figure 3.17: Kinetic model fitting at α > 0.5

Although the diffusion based Jander equation has been found to model the oxidation very well at low conversion ratios, due to the large agglomeration after oxidation, see **Figure 3.11**. The Jander equation assumes a constant particle size during the reaction, and it is expected that it is valid only at low conversion ratios even at macroscopic level. As the oxidation progress to higher conversion ratios, there will have large particle size change where the Guintling equation, which modifies the Jander equation by considering the particle thickness increasing process, should be more suitable (Park *et al.*, 2005). However as shown in **Figure 3.17**, this modification could not account for the discrepancies between experiments and predictions. Attempts have been made to observe the local phenomenon such as the particle size increase and volume expansion ratio after the oxidation experiments. The volume expansion ratio of Ni to NiO, 1.53 theoretically and 1.665 experimentally (Aylward, 1976; Powder Diffraction File, 1991), is difficult to observe due to the large agglomeration and early melting, as well as the size change of individual nickel particles in the progress of oxidation experiments. The Jander equation fitting is likely to be associated

with the average effect of agglomeration, in which reaction cross-section change can be neglected.

3.4.3 Kinetic compensation effect

Due to lack of detailed reaction information, it still remains unknown if this well fitting is a reaction character reflecting size effect or the quantitative discrepancies between the theory and experiments. This leads to an estimation of the kinetic compensation effect (KCE). KCE is to describe that a set of varied Arrhenius parameters, *i.e.* pre-exponential factor, k_0, significant changes with magnitudes of apparent activation energy. The relationship between these two parameters is usually expressed as

$$\log k_0 = B + cE_a \tag{3.10}$$

where B and c are empirical constants. It is fundamentally consistent with the assumption that there is an isokinetic regime if the k_0 and E_a obey the equation. The essential interpretation of the existence of the KCE is whether the reactions under study are complex. Examining compensation effect is consequently to suggest the isokinetic regime for a homogeneous or heterogeneous reaction (Galwey and Mortimer, 2006).

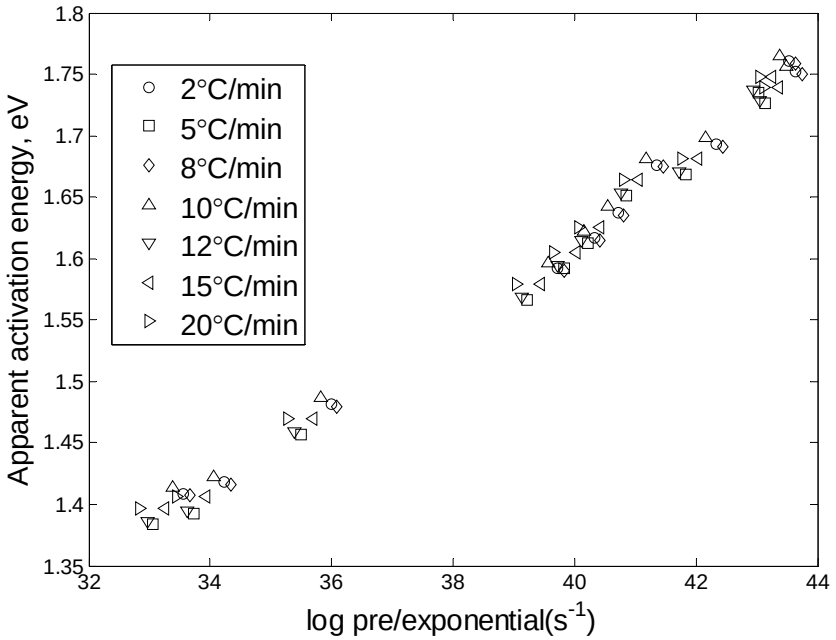

Figure 3.18: Kinetic compensation effect at α < 0.5

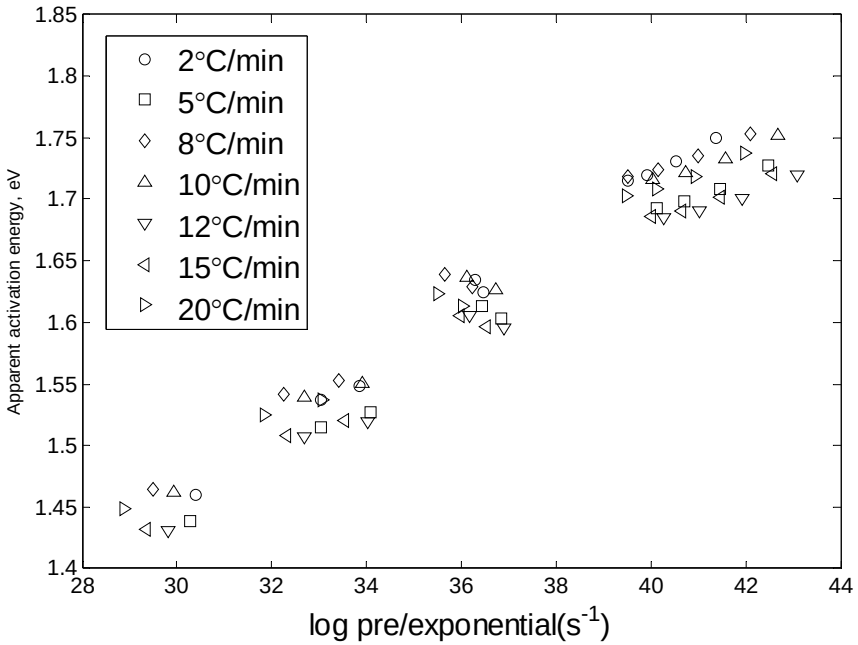

Figure 3.19: Kinetic compensation effect at α > 0.5

Remarkably kinetic compensation behaviour remains a consistent phenomenon of widespread occurrence from oxidation of CO on Pt, Pd, Rh to the heterogeneous catalytic reactions (Galwey and Mortimer, 2006). The results of KCE of nickel oxidation under study are presented in **Figure 3.18**

and **Figure 3.19**, for $\alpha < 0.5$ and $\alpha > 0.5$ respectively. The two-regimes found in previous section are separated investigated. The diffusion control step ($\alpha < 0.5$) gave satisfactory linear Arrhenius plots but in the pseudo-homogeneous step ($\alpha > 0.5$) apparent Arrhenius parameters calculated from these rate data showed marked variations. However, the general linear pattern of Jander equation plots indicates that the reaction is within the isokinetic regime. The pseudo-homogeneous reaction step has larger scattering features implying with potential reaction complexity. The study done for KCE of catalyst showed that the KCE is influenced by the surface sensitivity to reaction conditions including the coverages and reactivities of absorbed participants varying within the temperatures. The KCE observed in this oxidation experiments is believed to be rooted in the activity diminution as reaction proceeds, similar in the magnitude of relatively low apparent magnitudes of E_a. In a more detailed way, it suggests that the used individual samples undergo nonsynchronous surface oxidation during different heating rates, and the particle morphology varies under different heating rates due to the coalescence and agglomeration caused by previous oxidation. Morphology change and other variables must also collectively contribute, to some extent, to the scatter of deviations from linear KCE at second regime of mechanism.

3.4.4 Particle size effect

A sample with larger size range is used to investigate the size effect based on isoconvensional method. The samples are obtained and characterized in the same way as previous study. Larger nickel particles in the size of ~220 nm (0.22 μm), shown in **Figure 3.20** and **Figure 3.21,** are investigated in a temperature range between 20 °C and 700 °C.

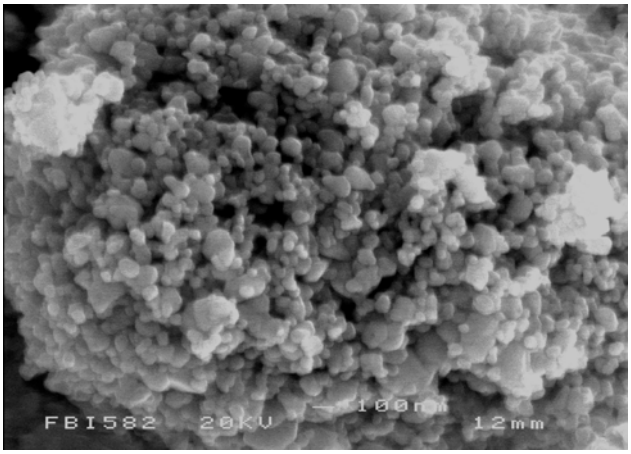

Figure 3.20: SEM image of larger nickel sample

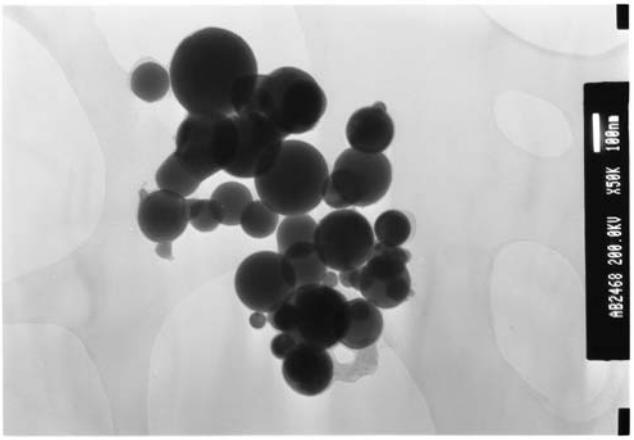

Figure 3.21: TEM image of larger nickel sample

The effect of the oxidation on the size distribution can be seen in **Figure 3.22** where different heating rates are deployed. The large size samples display no weight gain but loss until about 450 °C. Such a phenomenon is not expected since small size samples have larger specific surfaces that are more prone to gas/water contents. A possible explanation of initial weight decrease is that, for large nickel particles, the residuals of water condensed from moisture during the storage period existed in interstitial between particles. These large amounts of residuals are believed to be responsible for the overlapped TGA/DCS curves under different heating rates. The weight gain is observed when the temperature is higher than 450 °C. The reaction of large nickel sample is slower than 30 nm sample where a turning point appears on its TGA curve. The growth of oxidation is quite stable up to the

highest temperature 700 °C. During the oxidation process, the conversion rate is much slower compared with its nanoscale counterpart. The highest value only reaches 10-20% depending on heating rates, while the theoretical maximum, 27.3%, is obtained for nanometre materials. In term of DSC, there is no exothermic peak detected within the experimental range. For the smaller particles, the peaks are attributed to early melting of nickel nanoparticles. While for large particles, the continuous increase in heat flux reflects a solid-state oxidation of particles without significant melting pheonemna. It is expected that the nanoparticles are able to give much higher heat at the most severe oxidation temperature. The contrast results shows the endothermic melting of nanoparticles offset some portion of higher heat released associated with nanoparticles.

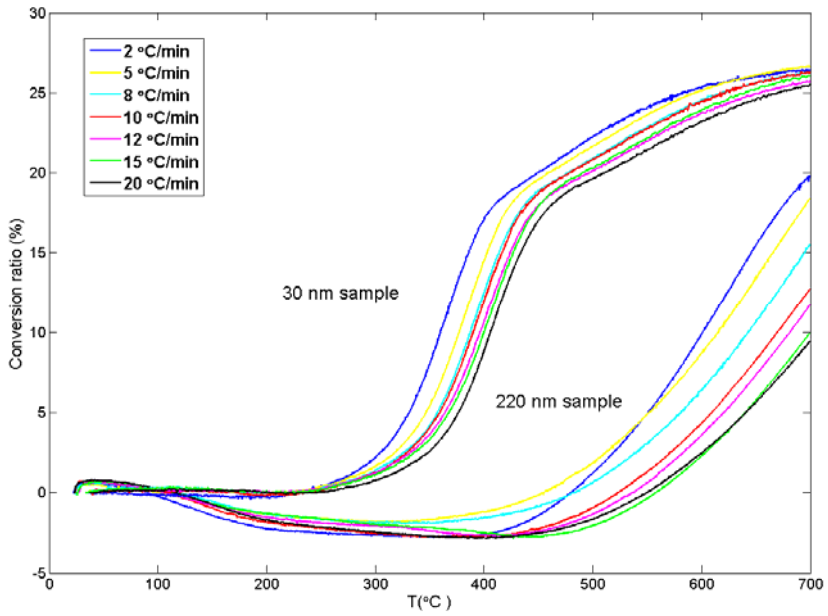

Figure 3.22: Comparison of TGA of nano and micro nickel samples

The general experimental techniques (*e.g.* TGA, DSC, and DTA) provide a global measure of the rate or extent of a process that usually involves several coexisting, competing or overlapping steps with different activation energies. For this reason, experimentally derived kinetic parameters of a solid-state process are interpreted as estimation of the overall process. The ability of isoconversional methods to reveal reaction complexity should

therefore be established on reaction detail obtained from ancillary experimental technique, *i.e.* elementary reactions should be identified and isolated. The model-free feature of this method is a crucial step toward the ability to draw mechanistic conclusions from kinetic data. The isoconvensional method is not yet used to fit the data of oxidation of metallic nanoparticles conducted in conventional techniques like TGA, DSC, and DTA.

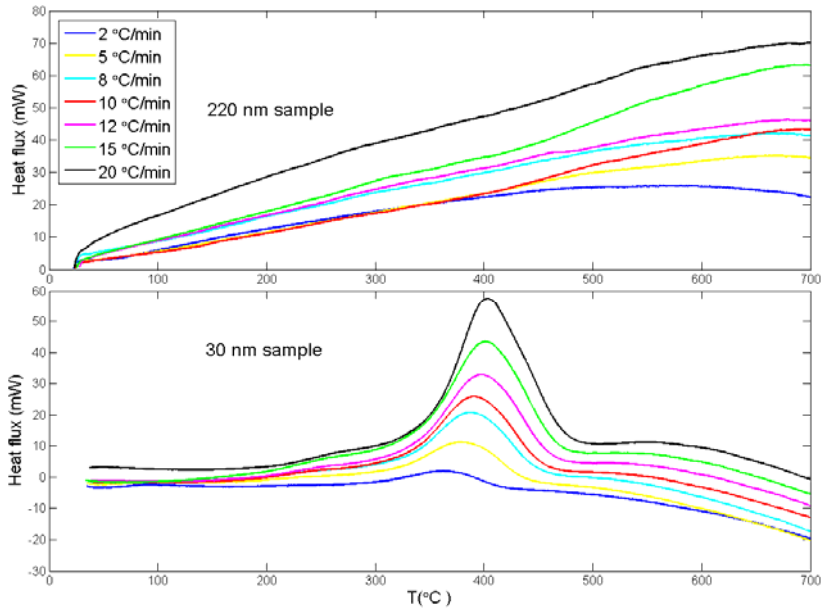

Figure 3.23: Comparison of DSC and DTA of two nickel samples

3.5 Chapter Summary

This chapter presents that an isothermal oxidation in TGA technique of nickel nanoparticles with diameter of ~30 nm can not be modelled at all the isothermal temperatures of interest. There is a discrepancy at 300 °C; the Carter's model fits the isothermal data above 300 °C, revealing a diffusion control reaction. The activation energy, 1.3 eV is obtained. The samples are subject to continuous heating under simultaneous TGA/DSC. Isoconversion methods are applied to process the non-isothermal data for which an one-

step oxidation is identified in assistance of many experimental methods including XRD, SEM, TEM and EDS.

The estimated 1 nm thick oxide layer covering the metal core is taken into account of calculation of activation energy. The initial oxidation and melting temperature of nickel nanoparticles were observed to occur around 300 °C and 500 °C, respectively, which are much smaller than the bulk values. Six different methods were investigated to calculate the activation energy, and similar activation energy values were obtained. The activation energy of nickel nanoparticles was smaller than that of the bulk nickel, implying a decreased energy barrier for oxidation. The activation energy of nickel nanoparticles was dependent on the conversion ratio. It increased with conversion ratios at 0.5, and then decreased afterwards, ranging between 1.4 and 1.8 eV. The oxidation kinetics was found to be diffusion dominated and can be well-modelled by the classical Jander equation at 0.5. At higher conversion ratios, a pseudo-homogeneous model with reaction orders between 4 and 6 could describe the experiment reasonably well. The found changing mechanism of oxidation at conversion ratio, 0.5 and the discrepancy at ~300 °C in previous isothermal investigation are believed to be caused Curie transition in which mobility of oxidative ions are enhanced. The KCE and size effect on non-isothermal oxidation is also assessed revealing a deeper insight on those reactions.

Chapter 4

Experimental Study of Oxidation of Tin Nanoparticles

4.1 Introduction

The iso-conversion method applied on oxidation is only validated when the oxide phases and oxidation route, *i.e.* each individual reaction step, is identified. It must be careful to extend this method to oxidation process with competing or overlapping reactions. Some experiments must be carried out in order to identify elementary reactions to support kinetic models. From aspects of kinetic processing based on thermal analysis, the promising analysis method for complex reactions is to use multivariate non-linear regression (Opfermann, 2000) or other algorithms such as genetic algorithm (Maitra *et al.*, 2007). The form of equations that multivariate non-linear regression deals with is all the same: Arrhenius equations. The two elements of kinetic trilogy, k_0 and E_a, are obtained from non-linear regression process to experimental data by iterative calculation of the minimum sum of least squares. However this method introduces a questionable distinction from iso-conversion method, which is only single value of k_0 and E_a is intentionally calculated for each elementary reaction. As suggested in previous chapter, nickel nanoparticles oxidation undergoing heterogeneous reaction environment, single value of E_a is insufficient of uncovering scientific insight. Kinetic function, $f(\alpha)$ as differential reaction model is obtained from the best fit of experimental data to several established kinetic models, which are unchanged to the isoconversional method. Although the multiple step oxidations face challenges experimentally and analytically, a case study of a two-step oxidation of tin nanoparticles is presented in this

chapter aiming at demonstrating extent of isoconvensional method on modelling nanoscale oxidation.

Bulk tin is the basis for many eutectic alloys and widely used in glass industry as floating batch. Applications of tin nanoparticles extended into transparent anti-static film, as an anti-microbial, anti-biotic and anti-fungal agent when doped with silver and incorporated in medicine bandages and textiles. Another potential is as confined acoustic and optic phonons in use of their electrical, biomedical and bioscience properties (Zhang *et al.*, 2008; Bottani *et al.*, 2007). SnO as a *p*-type semiconductor is used as anode materials, coating substances and catalysis and precursor of production of SnO_2 (Han *et al.*, 2001). Tin dioxide is also used as wide-band gap semiconductors, however, in more widespread usage partially because of its thermodynamic stability, as transparent electrodes in liquid crystal display (LCD) and optoelectronic devices in solar energy conversion or as chemical sensors (Choi *et al.*, 1997). SnO exists as a metastable phase at ambient conditions and decomposes into Sn and SnO_2 above its disproportionation temperature with variety of intermediates. The thermal oxidation and crystal growth of Sn are widely used approaches of synthesising SnO. The disproportionation of SnO is a synthetic routine for SnO_2. Preparation of nanostructures of these interesting oxides such nanowires and nanoparticles does not only improve conventional properties related to its bulk counterparts but also promote attractive novel applications. Relevant development research is underway in nano electronics and photonics materials, such as micro-electro-mechanical systems (MEMS), nano-electro-mechanical systems (NEMS) and biomedical nanomaterials. The knowledge about control of the preparation conditions of those attractive metal and oxides must be preconditioned with understanding of oxidation mechanism for these oxides. In spite of their many-sided properties and broad applications, the oxidation process of tin particles ranging from micrometer to nanometer is essential, however, not clear, especially in effect of the intermediate, which is objective of many studies.

It is generally agreed that SnO, which forms at the initial stage of oxidation of Sn, is metastable and decomposes according to the disproportionation reaction even in the absence of oxygen:

$$2SnO \rightarrow SnO_2 + Sn \qquad \text{(I)}$$

The early extensive study of this reaction was done in 1960s (Tivota, 1964). In this study the process of aqueous synthesised SnO was thought to experience a two-step decomposition process. The activation energies estimated were 385 and 38 kJ/mol, respectively. This reaction has been also described as one-step first order reaction later on (Lawson, 1967). Intermediate oxide was reported to appear in this process, however, in which SnO-SnO_2 transformation mechanisms are still unclear. Stoichiometric form of intermediate was proposed to be Sn_3O_4 (Mareno, 2001) and Sn_2O_3 (Griefers, 2005). Based on these two proposed intermediates forms, two contradict mechanisms were established. Mareno *et al.* (2001) concluded that the SnO-SnO_2 disproportionation was composed of two sequential first-order reactions with reaction rate constants $k_1 = 2.47\times10^{-4}$ s^{-1}, and $k_2 = 1.13\times10^{-5}$ s^{-1} respectively. Avrami-Erofeev reaction with exponent of $m = 2$ and activation energy $E_a = 166$ kJ/mol was found fitting the same process well (Griefers *et al.*, 2005). Furthermore, a multiphase system, *i.e.* several SnO_x suboxides, with x ranging from 1.33 to 1.5 was ascribed as the intermediates by some XRD evidence (Sangaletti, 1998). Even with these disputes, the temperature range of this decomposition was roughly consistent, *i.e.* onset at 360 °C (Griefers, 2005) and SnO fully converted at 550 °C (Mareno, 2001) or higher up to 600 °C (Pan, 2001).

The onset oxidation of of bulk Sn could be at quite low temperatures. Hillmanand and Chumbley (2002) found that the Sn samples exhibited growth of Sn and SnO_2 low to 125 °C in dry environmental conditions. The SnO-SnO_2 transformation and completion were reported being able to proceed at various temperatures greatly depending on annealing duration

(Choi *et al.*, 1997). Therefore there is no general agreement to define a universal transformation temperature for SnO-SnO_2, and it intrinsically depends on external conditions mentioned before.

The isothermal kinetic mechanism of oxidation of tin thin film formed by vapour deposition was studied (Wu *et al.*, 2000).The formed oxide layer was taken as a mixture of SnO, Sn_3O_4 and SnO_2. Activation energy is derived as 0.336 eV based on the Wanger model through isotherms at 250 °C, 300 °C, 350 °C and 400 °C and the thickness of tin layer had good consistency with the parabolic growth law, *i.e.* the square of increased oxide layer thickness is proportional to the elapsed time. The oxidation of tin was controlled by the diffusion of oxygen (Geurts, 1984). In this manner of oxidation for bulk tin, since the concentration of oxygen had gradient along the formed oxide layer where oxygen concentration in the layer close to surface is higher than that of oxygen atom in the unreacted tin lattice, the oxygen diffuses towards the metal layer underneath and the growth of formed oxide layer proceeded towards the interior of the bulk tin. However, neither of these researches was based on a clarified oxidation routine in which the existence of intermediates had great impact on kinetic process. Moreover, it was reported that amorphous oxide in chemical form of SnO_2 was induced by oxidation at 225 °C, close to tin's melting point (231.9 °C), while SnO_2 was crystallized into tetragonal form (Huh *et al.*, 1999). After a long annealing (22 hours), the dense orthorhombic SnO_2 was present due to high pressure posed by existing oxide shell.

Higher above 1300 °C the gas phase of SnO emerges and the decomposition of SnO_2 (Leite, 2001) according to reaction (II) must be taken into account:

$$SnO_2(s) \rightarrow SnO(g) + \frac{1}{2}O_2(g) \qquad \text{(II)}$$

To solve the dispute many studies were conducted on thermodynamic features of various stannic oxides. For example, the stable oxides in the Sn-O binary system are thought to be Sn_3O_4 and SnO_2 from in the phase

diagram (Massalski, 1986), the structures and stabilities of intermediate compounds, such as Sn_2O_3, Sn_3O_4 and Sn_5O_6, are still open to debate. Very recently Seko *et al.* (2008) used first principle calculation to conclude the theoretical feasibility of synthesis of Sn_2O_3 and Sn_3O_4 both of which are not yet artificially produced or experimentally investigated.

Based on the estimation of adjustable parameters from Cahen *et al.* (2003), molar Gibbs free energies of two stannic oxides are:

$$^{0}G_{SnO}^{solid} = -294112 + 96.347T \text{ (J/mol)} \tag{4.1}$$

$$^{0}G_{SnO_2}^{solid} = -581195 + 183.114T \text{ (J/mol)} \tag{4.2}$$

Since the oxidation reaction can proceed spontaneously and the product oxide can exist stably when Gibbs free energies are negative, within the temperature range of TGA/DSC, 30-927 °C, the thermodynamic stabilities of three solid oxide are in order, SnO > SnO_2. For a granular tin material, SnO-SnO_2 disproportionation was found to be complete by about 477 °C (Mallikaa *et al.*, 2001). It was indicates that SnO existed in its stable state from 25 °C up to ~270 °C. Generally the oxidation from SnO to SnO_2 varied dependently on many factors such as deposition method, initial oxygen concentration, annealing temperature and humidity (Han *et al.*, 1997; Hillman *et al.*, 2006; Charvin *et al.*, 2008). Besides those aspects the oxidation at nanoscale induces many more different mechanisms. Some distinct features of nanoscale Sn include melting point depression and kinetic changing (Huh *et al.*, 1999; Kolmakov *et al.*, 2003). In nanoscale dimension a synergy of various factors may cause a diffusion-controlled oxidation by easing the ion diffusion path as well as nucleation oxidation is present since the high ratio of surface is beneficial to nuclei.

In a SnO_2/SnO redox circle with humidity environment the isothermal hydrolysis of SnO nanoparticles within size range of 50-100 nm, was found by Charvin *et al.* (2008) that this reaction proceeded in a zero order with an

apparent activation energy of ~67.4 kJ/mol. Kolmakov *et al.* (2003) investigated the thermal oxidation of Sn nanowires with identification of intermediates suboxides in use of *in-situ* XRD technique, and proposed a procedure of two-step oxidation, *i.e.* an initial ion diffusion controlled step and a dominant kinetic controlled step subsequently, which was consistent with mechanism for RGTO-grown (rheotaxial growth and thermal oxidation) submicrometer tin particles and films (Sberveglieri *et al.*, 1990; Aste *et al.*, 1994). Compared to the bulk tin, the coexistence of SnO and SnO_2 is observed in a little broader temperature range of 200-500 °C. The coexistence of SnO and SnO_2 is visible until all of tin is consumed. However, neither of these mechanism researches has quantitative description of oxidation, *e.g.* activation energies and diffusion coefficients. Meanwhile the nanowire studied by Kolmakov *et al.* (2003) was prepared by use of an ordered arrayed template made of porous alumina, which hindered applicable extent to other common morphologies, such as free-packed nanoparticles. Still with contradiction, the disproportionation of SnO has received much attention. Sn-SnO oxidation at nano-micrometer scale which occurs at relatively low temperature is neither experimentally investigated solely nor kinetically estimated separately.

In this chapter, the nanophase tin powder as synthesized was oxidized in ambient air by simultaneous TGA/DSC method with different heating rates and the powder was then oxidized in a set of isothermal annealings up to 900 °C. The morphology and crystal phases were investigated by means of SEM and XRD.

4.2 Experiment

4.2.1 Sample characterization and experimental results

Dried tin nanoparticles are used in the experiments, which was made from the micro-emulsion technique and purchased from the Sigma-Aldrich

company, UK. The particles before and after oxidation were characterized under a TEM (JEOL JEM 2010) to determine their size and shape profile. The particles are spherical having a large particle size distribution, **Figure 4.1**. The average particle size is 110 nm in diameter, which is consistent with the range, *i.e.* < 150 nm, as specified by the supplier. The average oxide layer based on this value is estimated to be 3.7 nm in thickness as detailed in **Section 3.2**. The thin oxide layer can be seen surrounding the particles, reflected by the image intensity in **Figure 4.1**. However, it was found from this investigation that the oxide layer was highly non-uniform by element concentration analysis on different locations obtained by an Energy Dispersive X-ray Spectroscopy (EDS, Oxford Instruments) equipped with INCA Energy 300 System. EDS measurement on different areas showed a large variation in oxygen concentrations, i.e from 1.4% to 10.6% by weight listed in **Table 4.1**. Simultaneous TGA/DSC experiments were performed using a STA 1500 instrument under both isothermal and constant rate of heating conditions. Atmospheric air was supplied as the oxidizer. A small quantity of 10 mg tin nanoparticles was used in the experiments, which was contained in an alumina crucible, to minimize the heat gradient inside the sample. Five series of experiments were performed at constant heating rates of 2, 5, 8, 15 and 20 °C/min, with the cut-off temperature at 750 °C. Isothermal heating of tin nanoparticles was performed at 200, 300, 400, 500, 600, 700, 800 and 900 °C for 4 hours. High resolution SEM (Inspect F, FEI Company, EU) was used to reveal the morphology of sample after oxidation shown in **Figure 4.2**. The samples were then cooled by inert gases to preserve the structure and phase information of tin nanoparticles for *ex-situ* XRD analysis (Siemens D5000).

Table 4.1: EDS composition analysis of Tin nanoparticles

Element	Region 1 (Weight)	Region 2 (Weight)	Region 3 (Weight)	Region 4 (Weight)	Region 5 (Weight)	Region 6 (Weight)	Region 7 (Weight)	Average (Weight)
O	0.61%	0.79%	0.57%	1.43 %	1.18 %	0.19 %	0.53 %	0.76±0.4%
Sn	99.39%	99.21%	99.43%	98.57 %	98.82%	99.81%	99.47%	99.24±0.4%

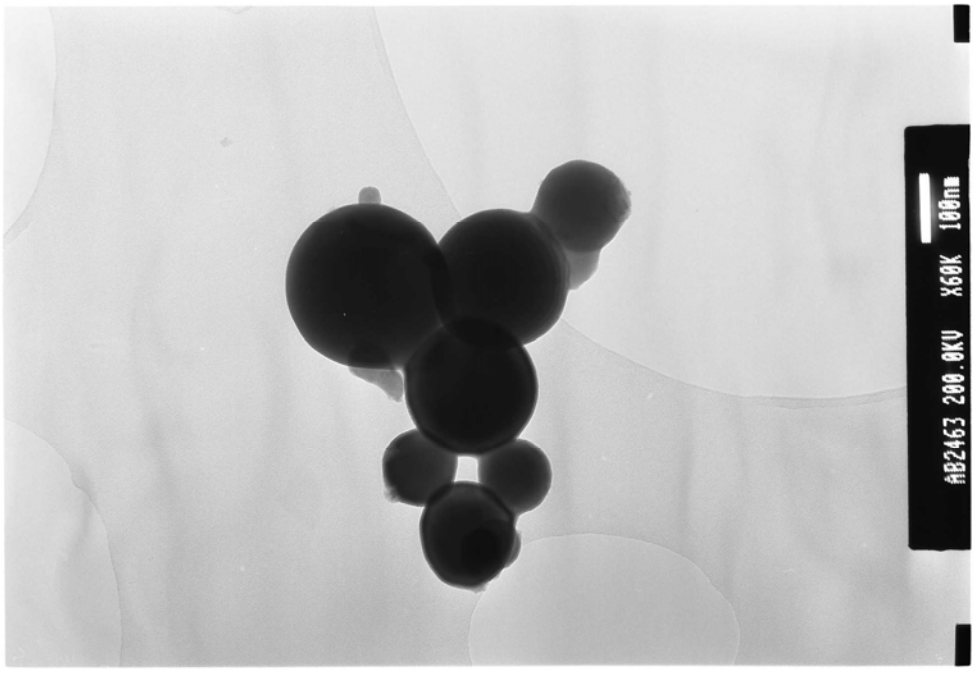

Figure 4.1: TEM image of tin nanoparticle sample

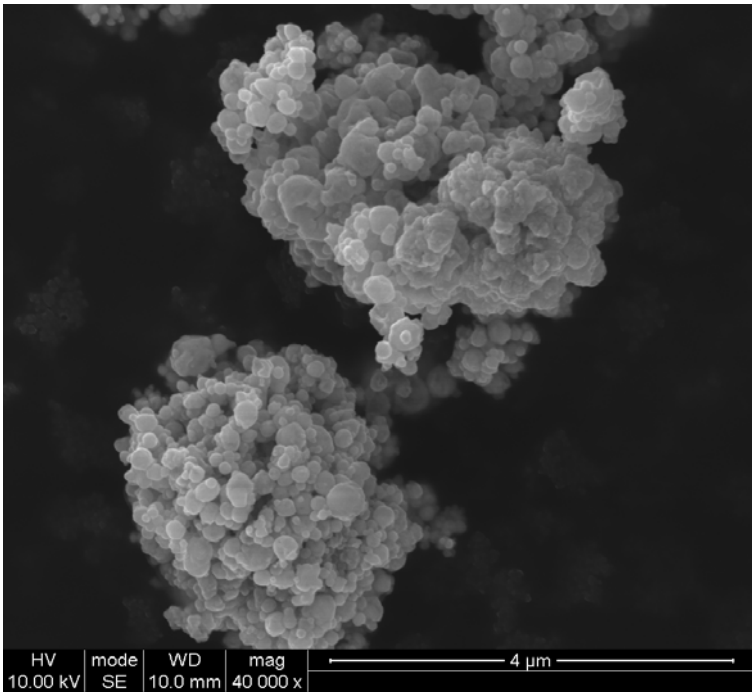

Figure 4.2: SEM image of tin nanoparticle sample

Figure 4.3 shows a typical example of measured TGA/DSC data at a fixed heating rate of 8 °C/min. The weight of tin nanopowders stays constant, or a very slight decrease (≤ 0.5% by weight) for some samples at temperatures below ~180 °C. This is probably caused by the absorbed residues such as water and/or carbon dioxide as samples were exposed to atmosphere. The residue weights of all samples are deducted from the original weight for later data analysis. Nanoparticles begin to show salient weight gain at ~200 °C in the TGA curve where a fast increase in the DSC curve is observed, as an implication of significant oxidation that has already occurred at this temperature. In **Figure 4.3** along DSC curves there appear three exothermal peaks tagged as A, C, D and an endothermal peak indicated as B whose peak values are listed in **Table 4.2**.

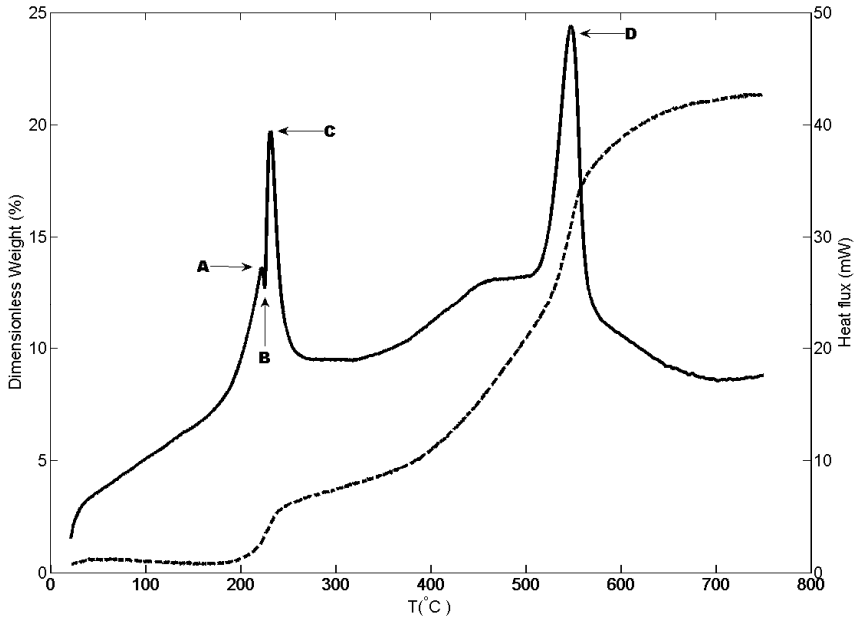

Figure 4.3: Example of TGA/DSC curves at heating rate 8 °C/min

Two distinct stages of oxidation occur afterwards. The first stage oxidation occurs after ~200 °C, and converts ~20% of tin within a small temperature span of about 50 °C. During this stage, the fastest oxidation occurs at a temperature of ~230 °C, which is evidenced by the first DSC peak, and the TGA curve reaches a quasi-plateau at ~270 °C. Notably there is a rapid small decrease in the DSC curve immediately before its rapid rise, with an implication of significant melting of some tin nanoparticles that absorbs some heat from the exothermic oxidation reaction. After a short transition period, the second stage of rapid oxidation occurs at ~400 °C and finishes at ~600 °C. Rather than increasing with the oxidation rate, there is a small plateau exists for the DSC curve in the temperature range of 450-500 °C. There is also a pronounced change in the oxidation kinetics, as observed from the slope increase of the TGA curve, occurring at ~550 °C. Similar characteristic points are also observed from the DTA curve, as shown in **Figure 4.4**. DTA curves exhibit only single peak at low temperatures about 230 °C, which confirms again that the dual-peaks of DSC at about 230 °C are related to the melting-oxidation synergy. The gap between the two peaks

reflects the melting of tin core and the primary peaks are associated with the fastest exothermal oxidation.

4.2.2 Influence of heating rates

The influence of the heating rate on the TGA, DSC and DTA curves are shown in **Figure 4.4** and **Figure 4.5** respectively. Similar phenomena as described above are obtained under all heating rates. The oxidation is nearly completed at about 700 °C under all the heating rates where no weight gain is detected due to the large surface area of nanosized powders.

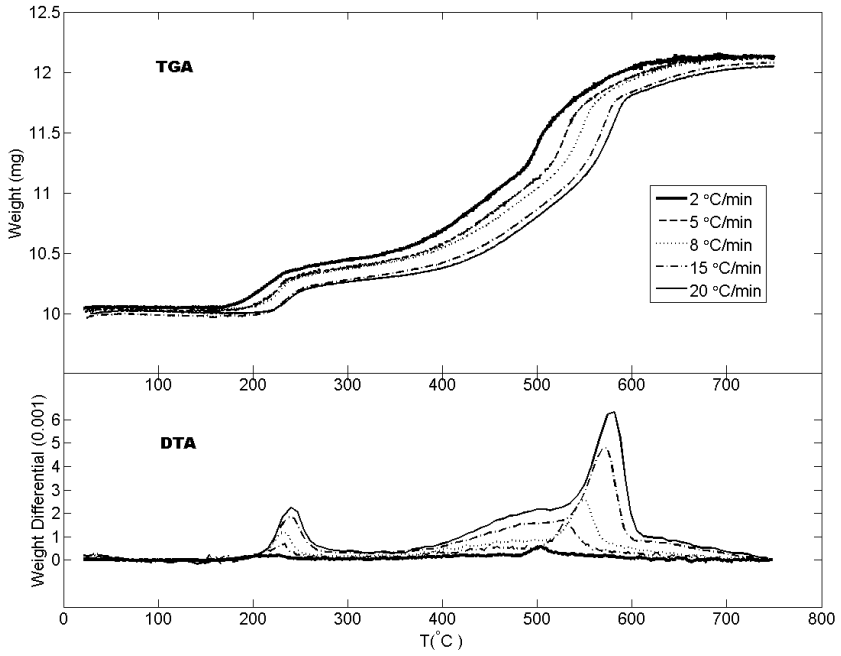

Figure 4.4: TGA/DTA of tin nanoparticles at different heating rates

The TGA curves show that the final weight increase of tin nanoparticles is between 12.1 to 12.3 mg with an average mass gain of 12.11 mg at different heating rates. This corresponds to an average of weight gain of 21.1%, whereas a theoretical value 27.0% increase in weight is expected for a complete oxidation of tin to the stable phase, SnO_2. This implies a possible incomplete oxidation of tin or more likely, some parts of original tin nanoparticles are oxidized prior to the experiments. To clarify the cause, *ex-*

situ XRD study is performed to the samples under constant rates of heating without isothermal annealing, which indicates that no Sn or SnO trace existed for the final product. This suggests the final oxide for experiments performed under constant rate of heating is the stable phase, SnO_2, and the weight gain difference between experimental and theoretical value is due to the existence of initial oxide layers. The existence of initial oxide layers has also been reported by other studies. For instance, It was considered that the SnO_2 as the only oxide of the initial oxidation layer (Kwon *et al.*, 2005). However this XRD study on the original samples identifies that the initial passivation layer is a mixture of SnO and SnO_2, see **Figure 4.6**. Because the initial oxide composition has no effect on the re-calculation of the pure tin content of pre-oxidation samples, the initial oxide layer is ascribed to a tannic oxide mixture. The appearance of oxygen species of initial specimen may be formed during the manufacturing process or as a consequence of possible low temperature oxidation during the storage period. As confirmed by a separated EDS measurement, the average weight percentage of oxygen is ~4.7%, which gives the oxide amount of 2.2 mg that is roughly consistent with the re-calculated average value of 1.82 mg assuming the passavition layer is SnO_2. EDS studies also show that the particle shape with oxide layer is highly non-uniform by which the compostion concentration is listed in **Table 4.1**.

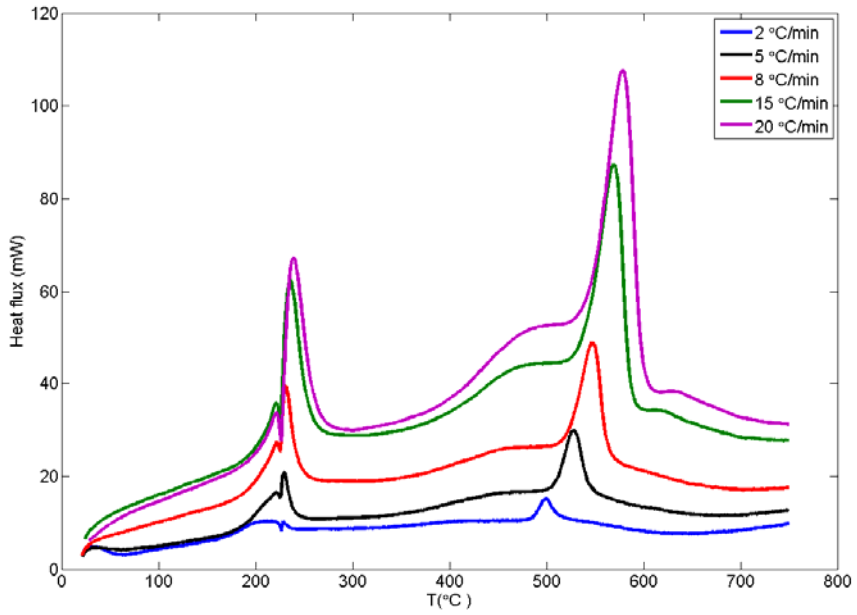

Figure 4.5: DSC curves of tin nanoparticle at different heating rates

Table 4.2: Peak values of DSC curves

Heating rate	Exo-peak **A**/°C	Endo-peak **B**/°C	Exo-peak **C**/°C	Exo-peak **D**/°C
2 °C/min	210.8	226.5	228.3	499.6
5 °C/min	226.8	225.9	229.6	528.1
8 °C/min	227.4	225.1	231.2	547.4
15 °C/min	227.6	226.4	235.7	569.5
20 °C/min	228.2	225.8	239.1	577.9
average	224.16	225.94	232.78	544.50

The peak temperatures of DSC curve are in the range of 220-250 °C and 500-600 °C for the first and second rapid oxidation respectively, which are summarized in **Table 4.2**. These values are highly consistent with the corresponding DTA curves. The amplitude of DSC peaks decreases with decreasing heating rate and consequently the baseline becomes more difficult to establish. The heat capacity associated with the phase transformation is therefore difficult to identify. One phenomenal indication is that at low temperature, DSC curves have dual peaks consecutively. In addition it is difficult to identify accurately the melting point for samples since the exothermal oxidation occurs nearly simultaneously with the

endothermic melting. The sudden DSC drop immediate before the rapid rise of the second DSC peak is an indication of the fast melting. Notably the endothermic peak between the dual exothermic peaks is quite constant under different heating rates, which is attributed to a thermodynamic equilibrium process, *i.e.* endothermic melting versus exothermic oxidation. It is believed that fast melting happens in the neighbourhood regime of the first DSC peaks under all heating rates. If there is any melting depression in reference to the bulk melting point of T_m = 231.9 °C, the melting temperature depression is small, only 6 °C. Lai *et al.* (1996) developed an equation linking tin particle size and its melting point which is expressed as below

$$T_{m,Sn} = 232 - 782\left[\frac{\sigma_s}{15.8(r - t_0)} - \frac{1}{r}\right] \tag{4.3}$$

The interfacial surface tension between the solid and liquid, σ_s, is 48 mN/m, and t_0, the critical thickness of the liquid layer at T_m, is 18 Å. The found value of melting point is slightly smaller than the predictive value of 232 °C calculated from equation for a 110 nm nominal diameter (Lai *et al.*, 1996). In **Equation 4.3** tin particles with diameter larger than 90 nm have no melting depression when compared with its bulk material.

4.3 Phase Transformation

As reported in previous section, particle samples at various isothermal heatings in air for four hours are conducted for *ex-situ* XRD studies. XRD patterns for the samples of tin and its oxides were obtained with an X-ray diffractometer (Siemens D5000) using Cu Kα radiation with 2θ range of 5-120°. Different phases of tin oxides were observed as shown in serial figures from **Figure 4.6** to **Figure 4.14** in which hollow squares, solid squares and solid circles represent SnO, SnO_2 and Sn respectively. The initial passavition layer was identified as a mixture of Sn and a small amount of SnO and SnO_2. At temperatures of 200, 300 and 400 °C, there were only

traces of SnO identified SnO_2 was identified from 500 °C and co-existed with SnO until 700 °C.

Only two thermodymically stable phases, cassiterite form of α-SnO_2 (tetragonal crystal) and romarchite form of α-SnO (orthorhombic crystal) are present. Some other metastable structures of SnO and SnO_2 are existent (Choi *et al.*, 1997; Griefers *et al.*, 2006). As temperature becomes higher than 800 °C, only the cassiterite form of SnO_2 exists. The peaks corresponding to Sn can be indexed to a tetragonal cell of Sn with a = 5.82 Å and c = 3.17 Å. The unit cell parameters of SnO are a = 3.80 Å and c = 4.836 Å as well as SnO_2 with lattice constants of a = 4.740 Å and c = 3.190 Å which agrees well with the reported values from JCPDS card, No. 41-1445 by Joint Committee on Powder Diffraction Standards. If the dual-peaks of TGA are ascribed to be two consecutive oxidation/disproportion progresses, *i.e.* Sn-SnO and SnO-SnO_2, the temperature range is similar to the results of Griefers (2005). It has been reported that the intermediate phase could be converted to SnO_2 after a long annealing time, *i.e.* ~20 hours (Huh *et al.*, 1999). However in this XRD study, the intermediate phase is preserved due to the relatively short period of annealing time (4 h). It is also true for the continuous heating mode which ran only a few hours (< 7 h), the oxide phases are ascribed to be the intermediates. The morphology after oxidation under heating rate of 2 °C in SEM is shown in **Figure 4.2**, which displays agglomeration in the form of micrometer clusters with irregular shapes.

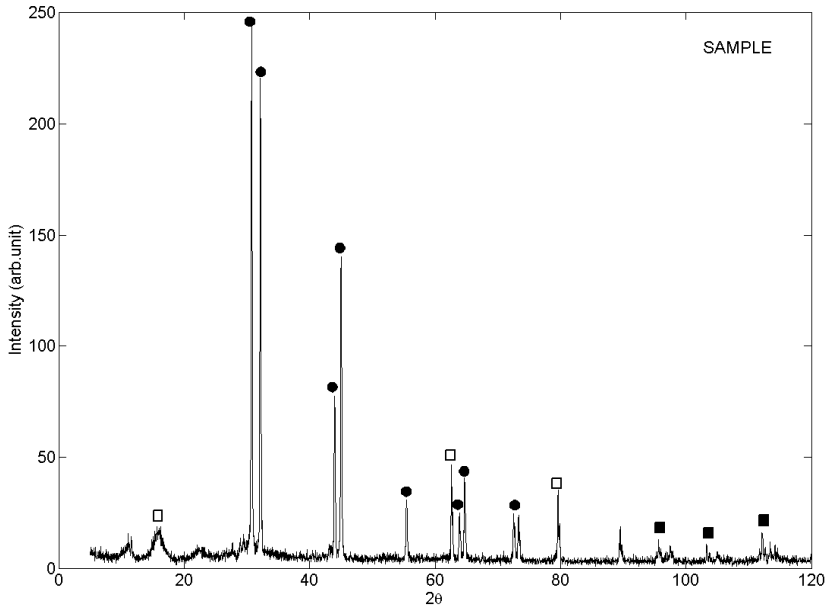

Figure 4.6: XRD of tin nanoparticle sample
(Notation: hollow square, **SnO**; solid square, **SnO_2**; solid circle, **Sn**)

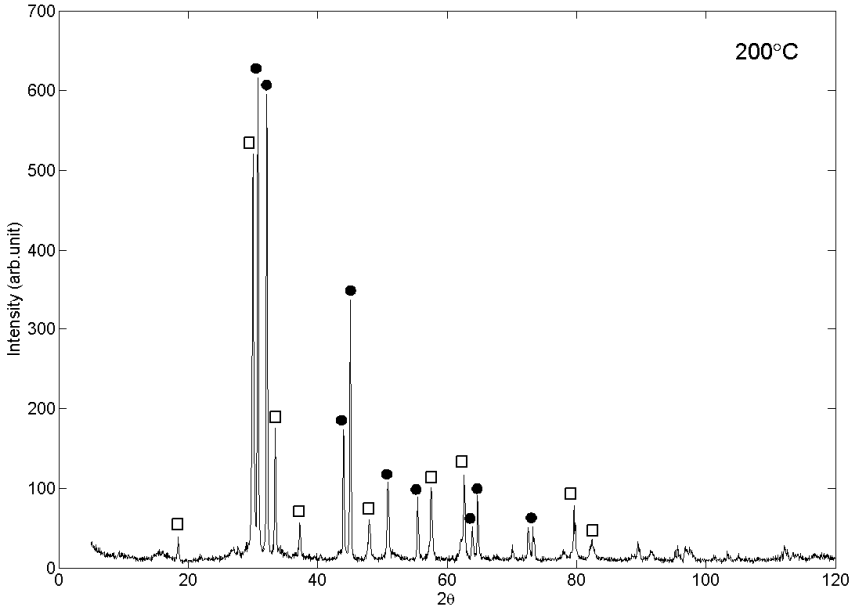

Figure 4.7: XRD of tin nanoparticle sample after oxidation at 200 °C

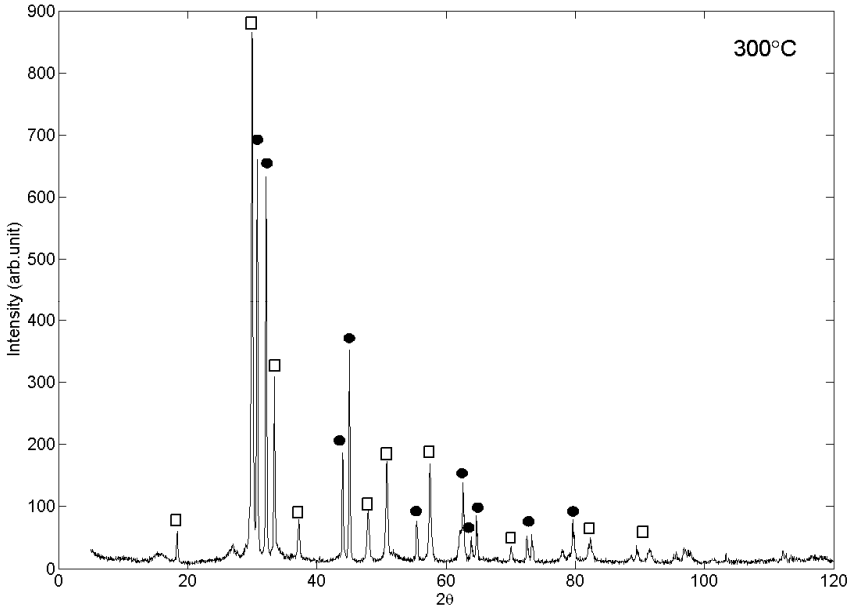

Figure 4.8: XRD of tin nanoparticle sample after oxidation at 300 °C

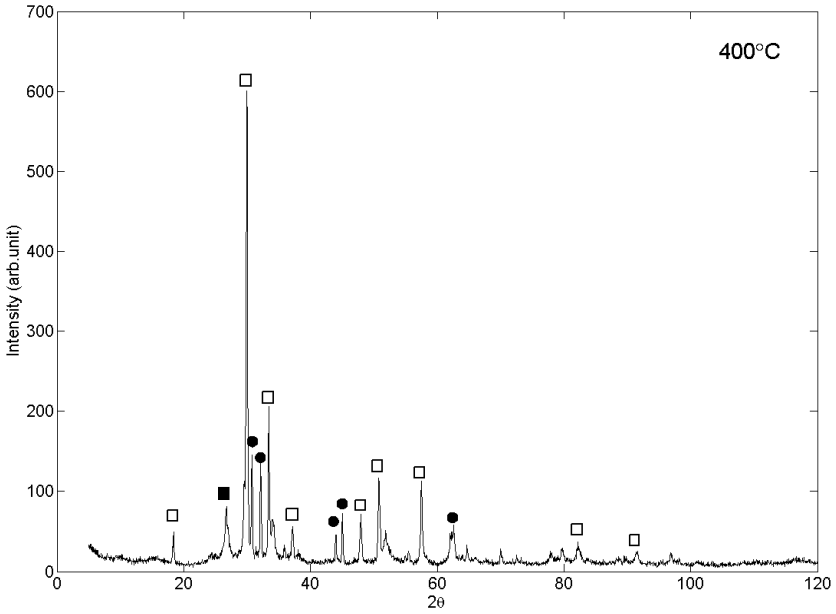

Figure 4.9: XRD of tin nanoparticle sample after oxidation at 400 °C

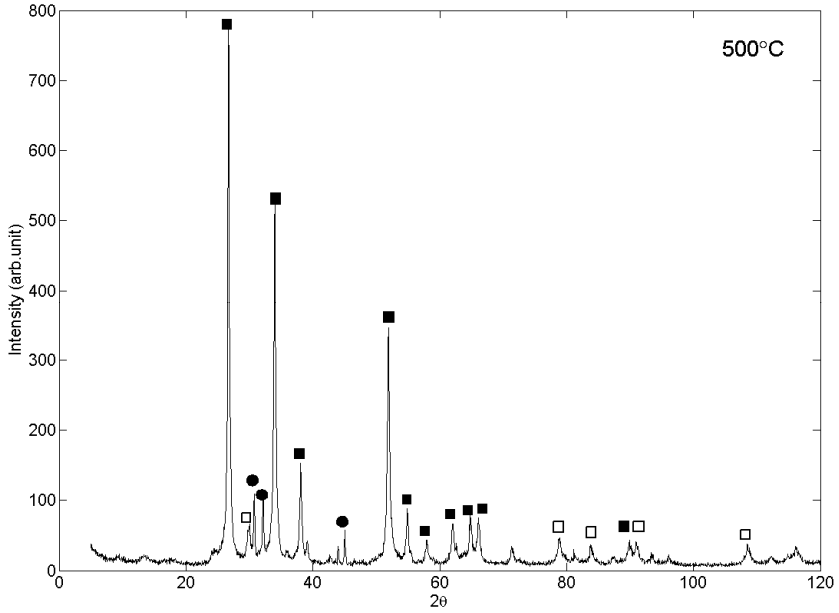

Figure 4.10: XRD of tin nanoparticle sample after oxidation at 500 °C

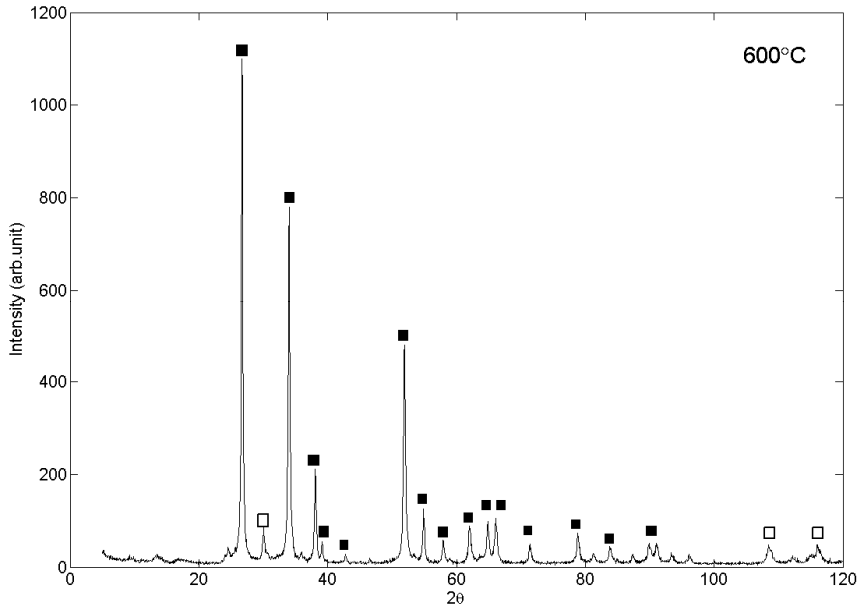

Figure 4.11: XRD of tin nanoparticle sample after oxidation at 600 °C

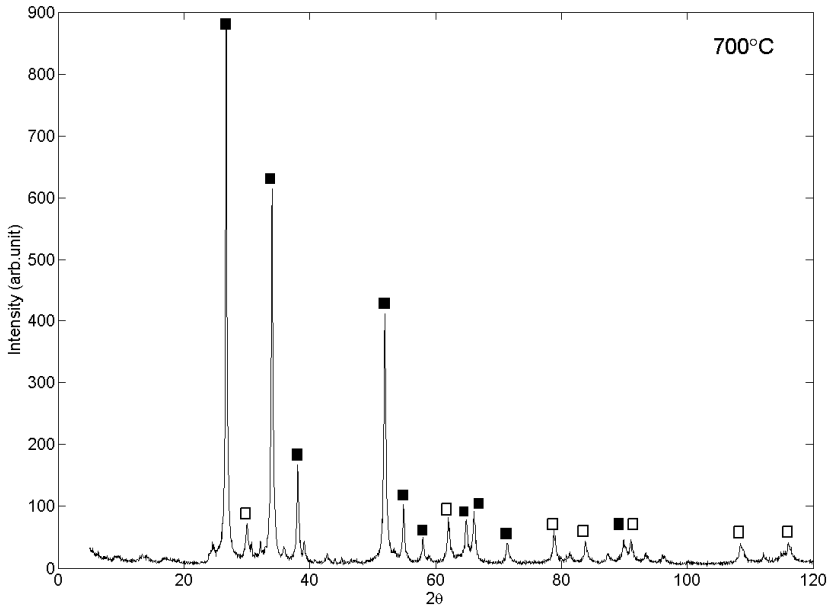

Figure 4.12: XRD of tin nanoparticle sample after oxidation at 700 °C

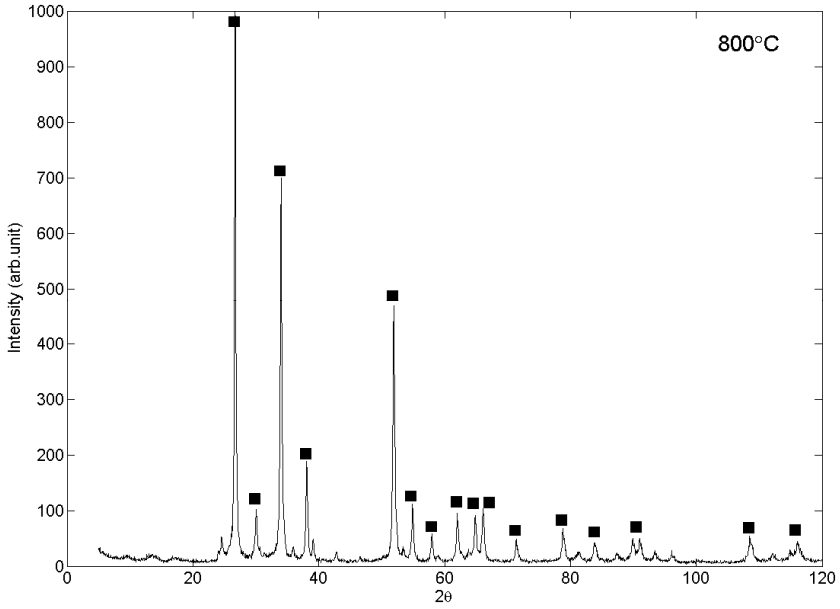

Figure 4.13: XRD of tin nanoparticle sample after oxidation at 800 °C

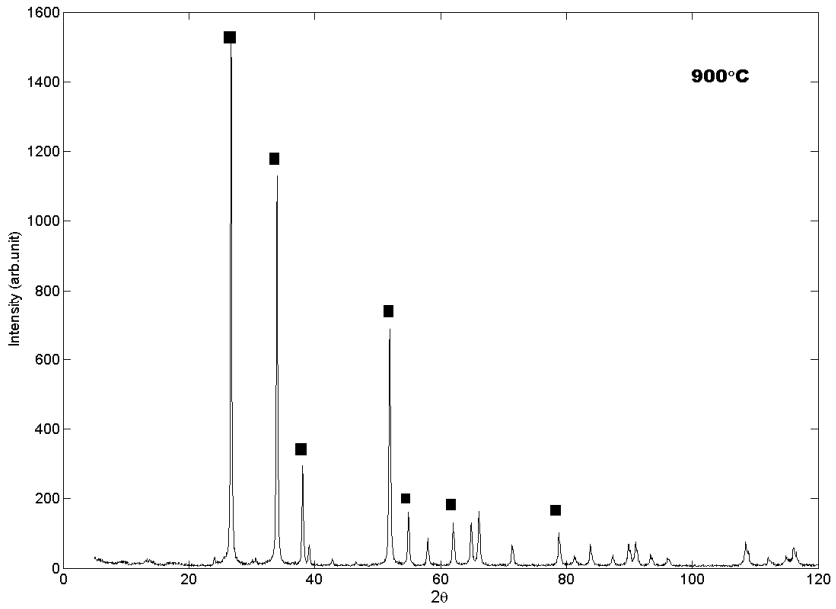

Figure 4.14: XRD of tin nanoparticle sample after oxidation at 900 °C

Based on the literature review and studies aformentioned, kinetic modelling for low temperature oxidation was established on the assumptions of below:

(I). The temperature range for low oxidation is set at below 400 °C and the reaction progress range is cut off at a conversion ratio of 0.4. As shown in **Figure 4.4**, the temperature at the conversion ratio of 0.4 is 324.99, 337.93, 361.27, 382.69 and 412.75 °C respectively for heating rates increases from 2 to 20 °C/min. Among these heating rates, there is only one heating rate, the 20 °C/min, having the conversion temperature of slightly higher than 400 °C, at which it was assumed that no SnO_2 phase is triggered due to the short time of heating caused by such a high heating rate. The two steps of oxidation are more clearly seperated in a condensed figure of all XRD, **Figure 4.15**.

(II). Since the TGA is performed for nine hours and no obvious weight gain is observed when the plateau is reached, the only final phase of oxides after the plateau formed in TGA is assumed to be SnO_2. This assumption allows

us to re-calculate the initial oxide and re-build the reaction process of Sn-SnO in use of the weight gain obtained by TGA.

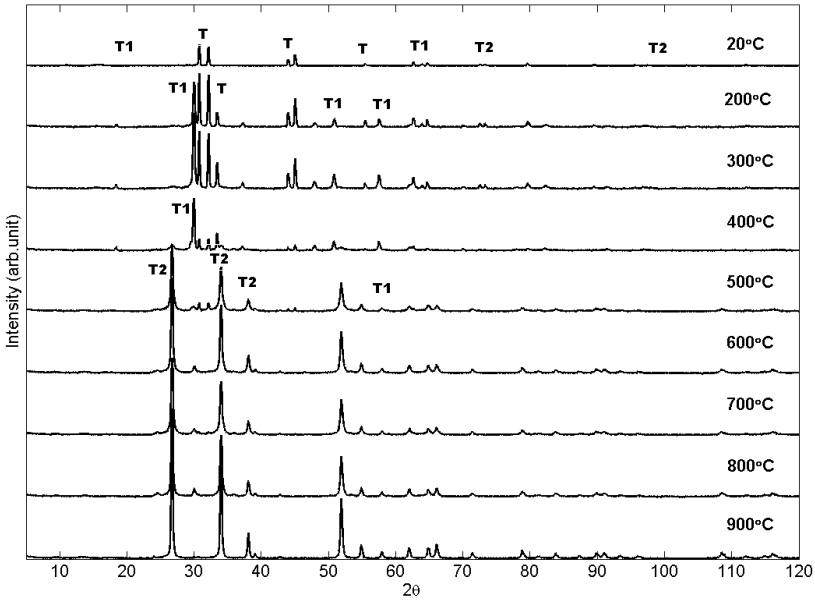

Figure 4.15: XRD study at different isothermal temperatures (Notations : T1: SnO; T2: SnO_2; T: Sn)

4.4 Kinetic Modelling

The Kissinger integral method (**Equation 2.23** and **2.24**) was deployed in this study for tin. The basic parameters for the calculation of activation energies, conversion ratios at given temperatures, are determined from TGA data by assuming a stoichimetric oxidation reaction. A homogeneous transition from Sn to SnO is assumed for low temperature oxidation of tin nanoparticles. The initial oxidation is taken into consideration in the data processing. Different methods previously used for nickel oxidation are still applied here to calculate the activation energy of the first stage oxidation, which include the Kissinger method (Kissinger, 1957), the Boswell method (Boswell, 1980), the Flynn-Wall-Ozawa method (Flynn and Wall, 1966; Ozawa, 1992), the ASTM method (ASTM standard, 1994) and the Starink method (Starink, 1996). All these analysises showed very similar results.

Therefore only the results from the Kissinger method are presented here. The activation energy, E_a, is found to be a strong function of the conversion ratio, α, as shown in **Figure 4.16**. The activation energy has a pronounced sinusoidal-shape and falls into a wide range between 0.4 and 1.4 eV. The activation energy increases to 1.3 eV from about 1.0 eV at the conversion ration of 0.17. It starts to decline to the minimum value of 0.4 eV, corresponding to a conversion ratio of 0.32, and then increases again to 0.7 eV at 40% conversion ratio. Generally the diffusion controlled oxidation process has low activation energies. The minimum activation energy, 0.32 eV is consistent with the value obtained from an isothermal oxidation of tin thin film, 0.336 eV (Wu *et al.*, 2000). The maximum value of E_a, 1.33 eV, is slightly smaller than the value for one of the SnO-SnO_2 disproportion transformation. The profound variation of the apparent activation energy derived from the constant rate of heating method reflects the complicated nature of the oxidation process of nanoparticles, which is different from the bulk material.

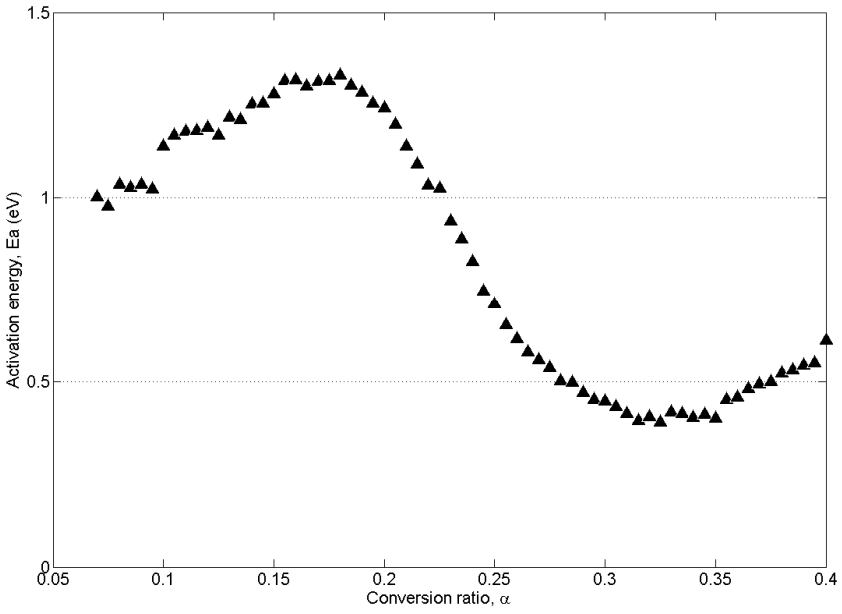

Figure 4.16: Oxidation activation energy of tin nanoparticles

Once the activation energy has been determined, an appropriate kinetic model can be found by comparing the experimental master plot with the

theoretical master plots for various reaction models. Considering the intermediate SnO and the resultant complicated nature of reactions described above, it is difficult to fit a single reaction to what is obviously a multiple step progress with competing reactions, especially when SnO and possible intermediates have long lifetime. Furthermore, as only the oxidation process involves a mass change, TGA curve will ignore the possible amorphous-crystallographic transformation except for any self-heating effects, and the interplay of melting and oxidation will further complicate the modelling process. Here the oxidation kinetic investigation will be focused on the low temperature, where only a single step reaction, *i.e.* from Sn to SnO, is employed.

Using activation energies calculated from the Kissinger method, the integral form, $g(a)$, is reproduced which has the same representation in **Equation 2.22**, under low temperatures as shown in **Figure 4.17** for all heating rates, where the ratio of $g(\alpha)$ to its middle value $g(\alpha_m = 0.2)$ is plotted against the conversion ratio. The best fitting based on the one-step mechanism *i.e.* Sn+O = SnO, involves a kinetic function in the integral form of $g(\alpha) = (-\ln(1-\alpha))^n$ and its differential form of $f(\alpha) = \frac{1}{n}(1-\alpha)(-\ln(1-\alpha))^{-(n-1)}$, which is the classical Avrami-Erofeev random nucleation and growth of nuclei model with an order of n = 0.25 for heating rate of 8 °C (Avrami, 1939, 1940, 1941; Erofeev, 1960). Of note that at low heating rates such as 2 °C/min, sintering is likely to occur and at high heating rates such as 20 °C/min, oxidation is supposed to be insufficient. Even considering the effect of heating rates, the reaction mechanism is proved to be still in the domain of Avrami-Erofeev mechanism only with slight variation of the reaction order, i.e value of n from 0.20 to 0.288 as the heating rate increases from 2 °C/min and 20 °C/min, seeing **Figure 4.17**. The average reaction order over five heating rates under study is n = 0.235. The KCE of different heating rates is shown in sub-plot of **Figure 4.17**, in which the linear relation between activation

energy and logarithm of pre-exponential factor confirms that the first stage oxidation is well within the isokinetic regime.

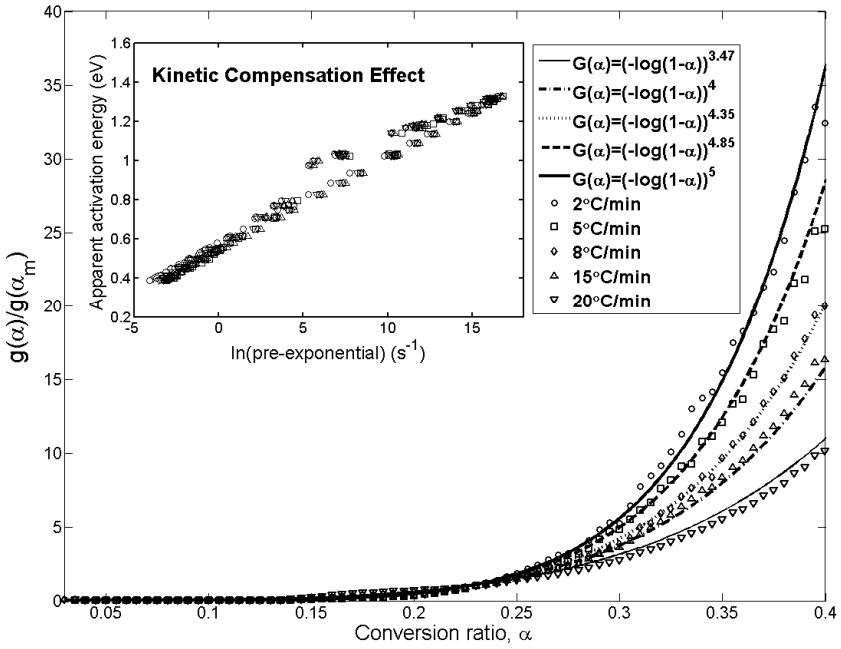

Figure 4.17: Reaction mechanism and KCE of heating rates

The nucleation-controlled mechanism is likely to be associated with the low melting point of tin and the induced large pressure (Huh *et al.*, 1999). Because of the presence of oxide shells, the diffusion of oxygen and ion become more difficult to go through this oxide barrier and no considerable reaction happens before 200 °C. When the temperature increases to the neighbour regime of the melting point of tin, 231.9 °C, the tin core or smallest tin particles starts to melt. As the mixture shell of the SnO and SnO_2 has no epitaxial relationship with the tin core, thermal expansion of liquid content of tin core and oxide growth encapsulated in the shell will induce extremely high pressure gradient due to the size effect. Based on the density difference and some estimations on modulus of Sn, SnO and SnO_2 and by neglecting thermal expansion effect caused by the temperature changing, the compression pressure for the used samples (d = ~110 nm including thickness of oxide shell = ~3.7 nm) is estimated to be as high as ~4.9 GPa. Despite this high value of estimated pressure, it is still not enough to cause phase transition from stable α-SnO to a high pressure phase γ-SnO,

which is a massicot structure present above 12 GPa (Adams *et al.*, 1992; Wang *et al.*, 2004). In the calculation, it was assumed that the mixture shell is far more rigid than the pure metal core since the elastic modulus of SnO_2, 280.6 GPa, is much higher than that of the Sn metal, about 50 GPa (Zheng *et al.*, 2004; Griefer *et al.*, 2006; Deligoz, 2008). Thermal expansion coefficient of Sn is 23×10^{-6} °C^{-1} (Subramanian, 2007), which is 35% higher than that of SnO_2, 17×10^{-6} °C^{-1} (Ono *et al.*, 2000). It was reported that SnO displayed a strong anisotropy in compression with bulk modulus of K_m = 35-38 GPa (Wang *et al.*, 2004; Griefer *et al.*, 2006). Although lacking reliable value of thermal expansion coefficient of SnO, it can be confidently considered that the shell, which is a mixture of SnO and SnO_2, to be much more brittle than the metal core based on the estimation from the effective media theory. Melting and growth of SnO relative to that of the more rigid SnO and SnO_2 mixture shell produces a large pressure on the tin core as the nanoparticles are heated. The incoherent interface between core and shell and the induced high pressure make heterogeneous nucleation favourable. The second stage involving formation of SnO_2 is a process of overlapping oxidations as described in **Chapter 2**. The difficulty of modelling this stage is to obtain the simultaneous content of each oxide as temperature is increasing. *In-situ* XRD will be good candidate for this purpose. The oxidation proceeds with two oxidations and a discompostion, *i.e.* $2Sn + O_2 = 2SnO$, $Sn + O_2 = SnO_2$ and $2SnO = SnO_2 + Sn$. The kinetic equations and initial conditions of describing the process are as

$$\begin{aligned}
&\frac{d\alpha_i}{dT} = f(\alpha_i)\frac{A_i}{\beta}\exp(-E_i / RT) \\
&\frac{d\alpha}{dT} = \sum_{i=1}^{N} g_i \frac{d\alpha_i}{dT} \\
&\sum g_i = 1 \\
&\alpha = \sum g_i \alpha_i
\end{aligned} \tag{4.4}$$

The overall conversion ratio reflected in recorded TGA is α while α_i is the conversion ration of the i-th single reaction and g_i is the partitioned contribution of each equation. Mathematically there is a hope to fit the obtained TGA data into these equations in adoption of multivariate non-linear regression (Opfermann, 2000). However, the assumption that partitioned contribution of each reaction is fixed throughout the overall reaction must be deployed. Another issue induced by this proposed fitting method is that the activation energy derived from multivariate non-linear regression is mono-value for each reaction involved, rather than a function of conversion ratio. Both of the issues are inconsistent and unfeasible with the first stage oxidation and undermine the effort of modelling nanoparticle in isoconversional method as degeneracy. Therefore the hope of uncovering the kinetic process in observed second stage oxidation is in the future development of experimental proofs.

4.5 Chapter Summary

This chapter is all about an experimental study of thermal oxidation of tin nanoparticles (d = ~110 nm) with a passivation shell consisting a mixture of SnO and SnO_2 are conducted using the simultaneous TGA/DSC technique. A two-stage oxidation phenomenon is identified. The first stage occurs at low temperatures demonstrating the formation of SnO, with the fastest oxidation occurring at ~235 °C, which is consistent with results of fine tin powders. The second stage includes the disproportionation of SnO and a continuing oxidation of residual tin, both of which resulting in the generation of the final stable oxide phase, SnO_2. The dividing temperature of two stages is approximately 400 °C as identified by an *ex-situ* XRD analysis. The oxidation kinetics at the first stage (Sn-SnO) is investigated by the Kissinger approximation method, and the activation energy is found to vary from 0.32 to 1.33 eV having a pronounced sinusoidal-shape dependent on the conversion ratio. The kinetic can be well described by a classical nucleation mechanism, the Avrami-Erofeev model which is believed to be associated with the melting and pressure built up of the confined metal core

embedded in a rigid oxide shell of tin nanoparticles. In addition the compensation effect of different heating rates is estimated showing that the first stage oxidation is well within the isokinetic regime. This work suggests that the isoconvensional method has good transferability into tin nanoparticles featuring with two-step oxidation and provide a sound methodology of investing clearly identified reaction in a more complicated multiple step oxidations.

Chapter 5

Numerical Study of Sintering of Nickel Nanoparticles

5.1 Introduction

It is expected that atomistic simulation can play a key role in place of experiment in the field of nanoparticles because the experimental exploration of nanoparticles will inevitably encounter various technical problems even regardless of the cost. In the uprising of computer development, many techniques have been developed able to simulate different kinds of physical and chemical phenomena from electron structure of atom to micrometre-sized particles. One example of the dramatic distinction between bulk material and nanosized material is the melting phenomenon. Melting, a phase transformation from a crystalline solid state that is rigid and topologically long-range ordered into a liquid state that is topologically long-range-disordered, is a common phenomenon in nature. Melting is crucial to nanoparticle/clusters thermodynamic properties and subsequent performance. Under equilibrium conditions, melting of bulk usually occurs in a very narrow temperature and pressure range spontaneously. A small change in temperature or pressure could completely change the phase from one status to another. When the size of material is reduced dramatically, the surface to volume ratio is increased, which makes the melting of nanoparticle different from that of their bulk counterpart. For instance, reduced particles have complicated size dependence and premelting phenomena. There are many empirical equations that describe the size-melting relation based on experiment and/or theory, some already discussed in previous chapters.

Experimentally, a melting transition is determined by measuring the caloric curve of the material, *i.e.* heat change as a function of temperature. The heat capacity is the derivative of the caloric curve. The melting of nanoparticle has been widely investigated by caloric curve (Schmidt and Haberland, 2002; Baletto and Ferrando, 2005; Gallego *et al.*, 2007). When heat capacity curve displays sharp peaks, the phase transition is first-order, which is sensitively related to the volume change of the system. This is an advantage for identifying melting point by computer simulation because the thermal energy of a material system is usually convenient to compute from coordinates and velocities of a set of atoms. Meanwhile, as described in the previous chapter, sometimes it is difficult to identify melting point by conventional experiment methods such as the DSC, from a complex thermodynamic scenario, *e.g.* overlapping of exothermic and endothermic processes.

In the category of phase transition, there are also many solid-solid transitions that include transformations between crystal phases and between glass and crystal phases. Different phase transition may involve evolution of local structure, chemical component change and more complicated change such as ferroelectric, alloy and intermetallic compounds. The theory of phase transition was studied by Gibbs in early 19th century, and a comprehensive and powerful statistical thermodynamic method has been developed since then. Being solidly built upon the principle of statistical thermodynamics, molecular dynamics is able to monitor the phase evolution closely in assistance of visualization and many quantitative analytical techniques. The challenges of phase transition in nanomaterial also include transient time, constraint geometry and different transport mechanisms.

Sintering as a common occurrence in lifetime of nanoparticles spanning from synthesis process to application stage, is still a major concern for simulation and experiment. The sintering of bulk materials is explained by solid state diffusion with continuum models. The diffusive flux, j, which is

defined as the volume of matter passing across unit area perpendicular to the flux direction per unit time, is assumed to be linearly dependent on the gradient of chemical potential μ_s of the diffusing species. The gradient of chemical potential is associated with the gradient of stress acting normal to the grain boundary and that of free surface curvature.

$$j = -\frac{D\delta}{k_B T}\frac{\partial \mu_s}{\partial s} \tag{5.1}$$

where D is diffusivity, δ is the characteristic thickness of diffusion, k_B is Boltzmann constant, T is the absolute temperature and s is the local coordinate along the diffusion path.

The classical thermodynamics successfully identifies six diffusion mechanisms for macroscopic sintering. For instance, the well-known Kelvin equation describing the dependence of sintering on vapour pressure, which is the foundation of classical sintering theory supported by nanoscale experimental evidence (Nanda *et al.*, 2002), as expressed in **Equation 5.2**.

$$\frac{P_S}{P_{S0}} = \exp\left(\frac{4\gamma_n M}{\rho_p RTd}\right) \tag{5.2}$$

where γ_n is the surface tension of nanoparticle, M is the molecular weight, ρ_p is the density of the particle, R is the gas constant, T is the temperature and d is the particle diameter. The assumptions based on continuum model break down at nanoscale. For example, at nanoscale the particles do not melt at same temperature as the melting temperature is greatly size-dependent. The relation between particle size and melting or melting-related property, for example, the vapour pressure, is not linearly coupled and therefore can not be described by continuum equations. The initial stage of sintering is marked by the neck shrinkage and as the sintering proceeds the inter-connected pores form spatial structures among multiple-particles. The direct

observation of the initial sintering at nanoscale is very difficult because it usually lasts a few picoseconds (Ding *et al.*, 2009).

The kinetic properties of nanoparticles are obviously difficult to handle by experiment. Kinetic behaviours such as diffusion and various flows occurring at nanoscale dimension show strong statistical characteristics that makes macroscopic measurable quantities difficult to be related to microscopic reality. Molecular dynamics (MD) as a 'model-free' technique provides a robust method aiming to quantitively reproducing nanoscale phenomena. Though the works in this thesis studied both non-reactive scenarios (sintering and core-shell structure) under purely vacuum conditions, MD is able to investigate environmental effects such as moisture and complex multi-particle effect usually occurring at very short time, which are hard to be detected and measured by experimental techniques. Furthermore, MD allows for going deep into the atomic details of solid state reaction such as oxidation of particles in which bulk reaction kinetic model and conventional experiments fail to capture.

5.2 Molecular Dynamics

Molecular dynamics (MD) is a computer simulation method widely employed for molecular/atomic systems (Allen and Tildesley, 1987; Smit and Frenkel, 2001; Rapaport, 2004). The MD simulations are modelled as ensembles of interacting particles under specific conditions. Given the initial coordinates and velocities of an ensemble of particles that interact in a force field whose total potential denotes as U, based on Newton's second law states,

$$m_i \frac{d^2 r_i}{dt^2} = F_i = -\frac{\partial U}{\partial r_i} \tag{5.3}$$

This method integrates the equation of motion numerically, updates coordinates and velocities at each integration time step. From the obtained particles trajectories one can calculate various global system properties as statistical averages. Similar to Newtonian gravitational field, the term 'force field' (FF) refers to a theoretical construct of all contributing interactions posed on the system, although sometimes the term 'potential' holds the same implication. Along with the development of some reliable FF such as tight binding method (TB), embedded atom method (EAM) and Finnis-Sinclair (FS), MD is proved to be suited for the study of metallic systems (Andersen and Jepsen, 1984; Daw and Baskes, 1984; Finnis and Sinclair, 1984). In 1984, Daw and Baskes (1984) firstly proposed the concept and algorithm of EAM for metallic materials. Meanwhile, a method based on similar theory was developed by Finnis and Sinclair (1984). These theories describe the energy contribution of an atom in an *N*-atom interacting system as a function of local electron density at the atom's site. Since its appearance EAM has been successfully applied to many properties of metal materials both in macro and nanoscale, such as surface, alloy, crack, dislocation, grain boundary, stack dislocation and phase transition. However, assuming the same molecular composition and atomic connectivity through the simulations, many FF catergorized as 'non-reactive MD' including CHARMM, AMBER, GROMACS and many others, are essentially unable to simulate the chemical reaction, the ultimate energy releaser, in which bonds between atoms form and break (Brooks *et al.*, 1983; Cornell *et al.*, 1995; van der Spoel *et al.*, 2005). The straightforward solution is to use *ab initio* or quantum mechanics/molecular mechanics (QM/MM), which need tremendous computational effort and therefore do not suit for materials simulation consisting of millions of atoms lasting some nanosecond of simulation time. Therefore many reactive MD force fileds are developed aiming at simulating chemical reactions at mesoscale. The foundation of all these force fields is based on the theory of bond order and bond length relationship by Pauling (1947). A reactive FF must parameterize the intermolecular interaction and bonding terms together in a function of the

reaction coordinates embedded into classical FF description. Some established bond-order reactive force fields regarding different situations include Reactive Empirical Bond Order (REBO), Tersoff, Brenner and ReaxFF (Tersoff, 1986, 1988; Brenner, 1990; van Duin *et al.*, 2001; Strachan *et al.*, 2005). These FF are proved to be very successful and able to simulate a wide variety of chemical reactions from a few hundred atoms to millions of atoms with relatively low computational cost and satisfactory accuracy in comparison with *ab initio.*

5.2.1 Motion of atoms

The MD used conventional Newton's second law to describe the interaction between atoms. For *N*-body systems the equation of motion based on it is as below:

$$\frac{d^2 r_i}{dt^2} = F_i(r_1, r_2, ...r_N) \tag{5.4}$$

where

$$F_i(r_1, r_2, ...r_N) = -\nabla_{r_i} U_i(r_1, r_2, ...r_N) \tag{5.5}$$

Here r_i is the position vector of the particle i, F_i is the total force acting on particle i and U_i is the total potential energy from which the force is derived.

Considering computational efficiency and accuracy, only several algorithms are suitable for MD simuation such as 'leap frog' and 'predictor-corrector'. The velocity Verlet algorithm is among them and used in this work because it does not alter time reversal symmetry of the integration which is crutial to preserve the accuracy of locations and velocities (Verlet, 1967). The form of the velocity Verlet integration scheme is given in equations below.

$$x_i(t+\Delta t) = x_i(t) + \Delta t v_i(t) + \frac{(\Delta t)^2}{2m_i} F_i(t)$$
$$v_i(t+\Delta t) = v_i(t) + \frac{\Delta t}{2m_i}\left[F_i(t) + F_i(t+\Delta t)\right] \quad (5.6)$$

In **Equation 5.6**, x is the position of atom i, v is the velocity, and F_i is the net force on the given atom i. Positions and velocities are obtained and updated at the next time step, $t + \Delta t$, based on the values at the current time step t. In order to do the very first iteration, initial values of x, v and F are needed, so a simulation is always initiated before a run can start. For example particles may be placed in an array or on a grid for simplicity and velocities can be randomly assigned from an appropriate distribution. The initial configuration of metallic solid is convenient to be its perfect crystal structure. The first set of forces can then be obtained from the initial positions.

5.2.2 Temperature and potential energy

Temperature is a state variable that specifies the thermodynamic state of the system. It is also an important concept in dynamics simulations. This macroscopic quantity is related to the microscopic description of simulations through the kinetic energy, which is calculated from the sum of atomic velocities. Temperature is a thermodynamic quantity, which is meaningful only at equilibrium. It is related to the average kinetic energy of the system via the equipartition principle of the statistic thermodynamics. This principle states that each degree of freedom either in momentum or in coordinates, which appears as a squared term in the Hamiltonian, has an average energy of $k_BT/2$ associated with it. This is true for momenta p_i which appear as $p_i^2/2m$ in the Hamiltonian, where the bracket denotes the ensemble average,

$$\left\langle \sum_i^N \frac{p_i^2}{2m} \right\rangle = \langle K \rangle = \frac{N_f k_B T}{2} \quad (5.7)$$

In an unrestricted system with N atoms, the number of degrees of freedom N_f is $3N$ because each atom has three velocity components (v_x, v_y and v_z). It is convenient to define an instantaneous kinetic temperature function:

$$T_{\text{instant}} = \frac{2K}{N_f k_B} \tag{5.8}$$

The average of the instantaneous temperature $T_{instant}$ is the thermodynamic temperature T in MD simulation. Temperature is calculated from the total kinetic energy and the total number of degrees of freedom. For a non-periodic system:

$$\frac{(3N-6)k_B T}{2} = \sum_{i=1}^{N} \frac{m_i v_i^2}{2} \tag{5.9}$$

Six degrees of freedom are subtracted because both the translation and rotation of the center of mass are ignored. And for a periodic system, **Equation 5.9** becomes

$$\frac{(3N-3)k_B T}{2} = \sum_{i=1}^{N} \frac{m_i v_i^2}{2} \tag{5.10}$$

Here only the three degrees of freedom corresponding to translational motion can be ignored, since the rotation of a central cell imposes a torque on its neighbouring cells. The sum on the right side of **Equation 5.10** is the kinetic potential and the rest from the entire energy is potential energy, which is calculated by the various forms of potentials defined and parametred in the force field. In most cases, the potential energy is the sum of pair, bond, angle, dihedral, improper and *k*-space long-range energy. During dynamics, kinetic and potential energy exchange with each other and the temperature changes as a consequence. To maintain the correct temperature, the computed velocities have to be adjusted appropriately. To keep the simulation at a constant T or P, so called ‘thermostat’ or ‘barostat’ are used as common control methods. Several different algorithms are

developed such as the Andersen (1980) and the Parrinello-Rahman barostats (Parrinello and Rahman, 1980), and the Nosé-Hoover (Nosé, 1984; Hoover, 1985) and the Berendsen thermostats (Brendsen, 1986). Nosé-Hoover thermostat is used through this study whenever it's referred. In addition to maintaining the desired temperature and pressure, the 'thermostat' and 'barostat' must produce the correct statistical ensemble, which demands that the probability of occurrence of a certain configuration obeys the laws of statistical mechanics.

5.2.3 Ensembles

In addition to maintaining the desired temperature, the temperature-control mechanism must produce the correct statistical ensemble. This means that the probability of occurrence of a certain configuration obeys the laws of statistical mechanics. Restricted by computer speed, simulation system can only contain some limited numbers of particles from which there may have big difference compared with real materials. Ensemble is a concept in statistical thermodynamics. For an equilibrium system macroscopic properties can be calculated from the average of the every possible microscopic state. The equilibrium ensembles usually include microcanonical ensemble (N, V, E), canonical ensemble (N, V, T), isothermal-isobaric ensemble (N, P, T), isobaric-isoenthalpic ensemble (N, P, H), grand canonical ensemble (μ, V, T), Gibbs ensemble and semi-grand ensemble. When the number of particles within consideration is up to quite large value, these various equilibrium ensembles are equivalent to each other for treating real materials. When the number of particles in MD is far more less than the one considered in statistical physics, the statistical average will be different for various ensembles. Generally speaking NVE ensemble is not practical when comparing with experimental or theoretical results. So, usually other ensembles are preferred depending on what thermodynamic quantity is kept constant including the number of particles, volume, pressure, temperature or chemical potential: either canonical

ensemble, *i.e.* constant-NVT, isothermal-isobaric ensemble, *i.e.* constant-NPT or grand canonical ensemble *i.e.* constant-μVT.

5.2.4 Energy minimization

According to initial temperature the initial velocities are generated so as to produce a Maxwell-Boltzmann distribution at the desired temperature, the distribution does not remain constant as the simulation continues. This is especially true when the system does not start at a minimum-energy configuration of the structure. This situation often occurs since structures are commonly minimized only enough to eliminate any hot spots. The minimization of configuration is another tricky topic of MD. A long-term stable configuration usually corresponds to that at global energy-minima. Unfortunately there is no rigorous method to find general global minima. This makes searching global minima all over phase-space to be the holy grail of multidimensional optimization. Despite the theoretical and practical difficulties, there are two mathematical techniques guiding the minima searching, *i.e.* steepest descents (SD) and conjugate gradient (CG), widely used to find local minima which might be the global minimum by some chance. SD is difficult to be convergenced as its drawback. However, due to its robustness, SD can be always performed no matter how far the current position deviates from the minimum energy location. Furthermore global optimization is done by more advanced methods such as simulated annealing and genetic algorithm that usually take longer time. A general strategy of minimization is that SD is conducted at very first steps, and followed by other optimization algorithms, usually CG. Even though all of these methods do not guarantee the capture of global minima in any finite time, it is still necessary to perform minimization/optimization upon the system before MD simulation to avoid the *N*-body system falling into a metastable stage associated with a local minimum. The metastable situation basically means that the thermodynamic states are not genuinely equilibrium

stable, but have much longer lifetime during which their values appear unchaged.

5.2.5 Force field

Force field (FF) in molecular dynamics is the explicit function form of comprehensive interaction potentials acting on atoms in a system, which is usually an analytical function of total energy to atom coordinates. The selection of FF is crucial to the valididation of MD simulation. The well-known Lennard-Jones potential (L-J potential) was proposed as early as in 1924, which is a pioneering molecular potential expressed as below:

$$U_{LJ}(r_{ij}) = 4\varepsilon\left[\left(\frac{\sigma}{r_{ij}}\right)^{12} - \left(\frac{\sigma}{r_{ij}}\right)^{6}\right] \tag{5.11}$$

where ε is the depth of the potential well, σ is the finite distance at which the interatomic potential is zero, and r_{ij} is the distance between the particles i and j. This is a typical pairwise potential and consists of a strong repulsive term ($1/r_{ij}^{12}$) describing the Pauli repulsion at short ranges and a weak attraction term ($1/r_{ij}^{6}$) describing the long range van der Waals force. Although very few materials except argon dimmer can be accurately modelled by L-J potential, it and its derived forms have been implemented into today's many force fields as a pairwise fractional potential.

Metal system is widely investigated under the framework of Embedded-Atom-Method potential (EAM) in MD. It is based on effective medium theory and derived from energy functional theory, where all atoms are viewed as embedded in the host system consisting of all other atoms (Daw and Baskes, 1984). The embedding energy is electron-density dependent. EAM force filed is expressed as:

$$U_{EAM} = \frac{1}{2}\sum_{ij}\Phi(r_{ij}) + \sum_{i}\Theta(\bar{\rho}_i) \tag{5.12}$$

The potential function consists of pair-interaction term $\Phi(r_{ij})$ and density-dependent potential $\Theta(\bar{\rho}_i)$. In the approximation of EAM, $\Phi(r_{ij})$ is the pair interaction between atoms whose separation is given by r_{ij}. The pair interaction potential can drop smoothly by introducing the cubic spline function where the sums are over the atoms *i* and *j*. The embedding function Θ is the energy required to embed an atom into the background electron density $\bar{\rho}_i$ at site *i* where $\bar{\rho}_i$ is given by a linear supposition of spherically averaged atomic electron densities, while in the Modified Embedded Atom Method (MEAM), embedding function is augmented by angularly dependent terms. EAM is easily extended to alloys in which the pair-interaction term $\Phi(r_{ij})$ is designed to be arithmetic or geometric average of each atom's individual pairwise potential, which has been proved as a feasible approach (Angelo *et al.*, 1995).

5.2.6 Potential truncation and neighbour list

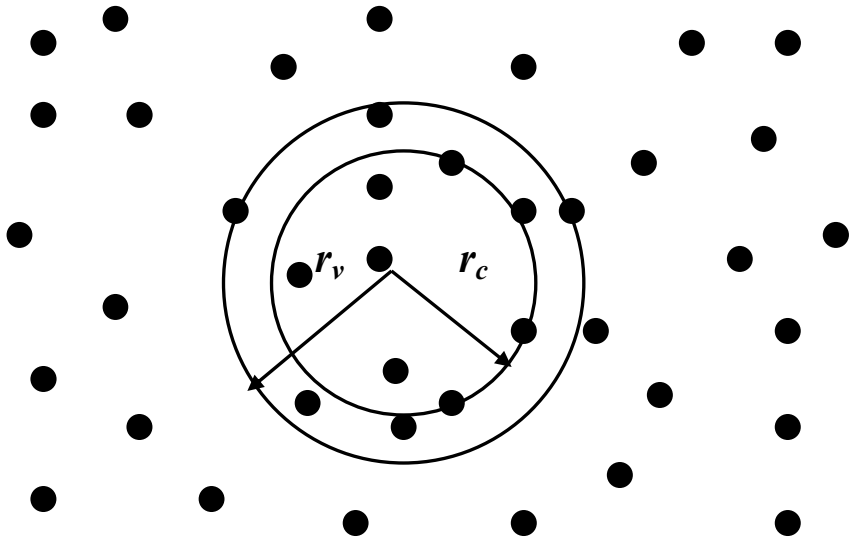

Figure 5.1: Scheme of neighbour list

For a *N*-body system, if the interactions are not not truncated, $N(N\text{-}1)/2$ pair interactions must be counted in and consequently the $N \times N$ scale computations are needed for evaluation of energy (Rapaport, 2004). The computational cost of a large system will be tremendous if all these pairwise interactions are calculated. To reduce the computation cost while preserving sufficient accuracy, the potential is truncated from a given distance beyond of which the interactions between atoms are relatively weak. It is to avoid singular point in potential function by inserting a function to have a smooth decrease to zero at cut-off distance. The idea of potential truncation is to exclude the interaction beyond a cut-off distance, r_c. Only interaction of particles located within cut-off distance in each cell box are evaluated. The potential can be truncated at cut-off radius in two ways: the first is to 'simple cut' shown in **Equation 5.13** and the second one is to impose a smooth truncation at cut-off radius in **Equation 5.14**. The two methods make negligible difference without drift of results for MD simulation if numerical algorithm is carefully designed.

$$U^S(r_{ij}) = \begin{cases} U(r_{ij}) - U_c & (r_{ij} < r_c) \\ 0 & (r_{ij} > r_c) \end{cases} \tag{5.13}$$

$$U^S(r_{ij}) = \begin{cases} U(r_{ij}) - U_c - \left(\dfrac{dU(r_{ij})}{dr_{ij}}\right)_{r_{ij}=r_c} & (r_{ij} < r_c) \\ 0 & (r_{ij} > r_c) \end{cases} \tag{5.14}$$

The other method able to save CPU time is to conditionally renew the particles within cut-off distance. Each such an update is expensive since it involves $N \times N$ operations for an *N*-particle system. A common technique is called a neighbour list, in which the particle environment is book-kept. Verlet list is a commonly used method, illustrated in **Figure 5.1**. A second cut-off distance r_v is introduced within which a list of particles are made. Only if the particle's displacement is bigger than 'the shell', $(r_v - r_c)$, the neighbour list is renewed. Otherwise only the particles in the current list are

considered. This design in order to save computational time avoids checking every particle in the system every time once a force calculation is made. In low-temperature solids where the particles do not move very fast, it is possible to do an entire simulation without or with only a few updatings, whereas in simulation of liquids, updating every 5 or 10 steps is quite common.

5.2.7 Computational programs and system

Large-scale Atomic/Molecular Massively Parallel Simulator (LAMMPS) is used throughout this study (http://lammps.sandia.gov/). It is a molecular dynamics program developed by Sandia National Laboratories, USA. The visualization for MD trajectory is through Visual Molecular Dynamics (VMD), which is developed by University of Illinois at Urbana-Champaign, USA (http://www.ks.uiuc.edu/-Research/vmd/). Another MD simulation package, MD++, (http://micro.stanford.edu/~caiwei/Forum/2004-12-12-MD++/) developed by Stanford University, USA is used to generate an starting configuration of silicon cluster. An optimization tool, Packmol, developed by State University of Campinas, Brazil, is used to optimize the starting configuration of silicon and oxygen system in **Chapter 7.** LAMMPS, VMD, MD++ and Packmol are all open source codes distributed under the terms of the GNU General Public License. A FORTRAN-version of ReaxFF with which several trial simulations were performed is provided by Dr. Adri van Duin of Pennsylvania State University, USA. A C++ version of function file processing ReaxFF bonding list which was not available in LAMMPS when I was doing this work, was provide by Dr. Aidan Thompson of Sandia National Laboratory, USA. This function code inspired me in my coding work of processing bonding information of simulation.

A set of personal in-house codes have been developed for pre-processing input data and post-processing the output data of MD. The in-house codes

appended in **Appendix 2** were all programmed in MATLAB® of the MathWorks Limited, USA.

The simulations were conducted on a Dell® Precision T7400 Workstation with operation system of Red Hat® Enterprise Linux 5, equipped with 4 Quad Core Intel® Xeon processors and 4 GB memory.

5.3 Background on Sintering

So far the motivation of study is concerned about modelling oxidation of metallic nanoparticles. In case of oxidation, particle size and morphology such as particle shape and surface layer are critical to their oxidation behevious. Actually the morphology-related challenges of nanoparticle widely exist in synthesis, production, storage and many functional applications. The quality of nanoparticles synthesized from the gas phase route is controlled by the coagulation process, where the size of the spherical particles and the growth of agglomeration are determined by the rate of collision and subsequent coalescence. During the condensation process, formed nanoparticles collide with each other and sintering occurs, forming larger particles of agglomerates. Different particle size and morphology can be formed depending on the relative speed of the collision and sintering. Inception, coagulation, condensation, and sintering are the important steps to form different nanoparticles. The relative timescale of the sintering and the coagulation processes determines the shape and the size of the nanoparticles. Understanding the controlling sintering process could result in improved function of produced nanoparticles and prevention of potential hazard. For instance, ultrafine particles can be formed from the condensation of un-burned hydrocarbon fuels, which provide large areas for heterogeneous condensation of toxins such as aromatic hydrocarbons, arsenic and other heavy metals (Neeft *et al.*, 1996). The potential health effect of these air pollutant particles and the regulations imposed upon the ambient concentration of small particles require a fundamental

understanding of the kinetics of sintering and coalescence process. Given such an important industrial and environmental relevance, it is important to understand the sintering kinetics of nanoparticles. Extensive experimental and theoretical studies have been conducted on the sintering process of large particles, and many mechanisms have been established.

For large particles there are found six different contributing mechanisms including surface diffusion, lattice diffusion from surface, vapor transport, grain boundary diffusion, lattice diffusion from grain boundary, and lattice diffusion through dislocations. Several studies reveal that the sintering process increases and have distinct features as particle size decreases (Koch and Friedlander, 1990; Chiang *et al.*, 1996).

In order to characterize the sintering process quantitatively, Koch and Friedlander (1990) have developed the K-F model explaining particle growth in a process of coagulation and sintering. Described by the K-F model, the sintering rate depends mainly on the excess surface of the particle over a spherical particle with the same mass. A particle tends to reduce its free surface to minimize the free energy. This causes the rounding of the particle, finally the formation of a sphere. The asymptotic equation as **Equation 5.15** describes the sintering process (Koch and Friedlander, 1990)

$$\frac{da}{dt} = -\frac{1}{t_s}(a - a_{final}) \tag{5.15}$$

where a is the surface area, a_{final} spherical surface and t_s is the sintering time. From macroscopic continuum theories of sintering via surface diffusion, the sintering time t_s is predicted to vary with the fourth power of the particle size

$$t_s = \frac{k_B T_S}{25 D \gamma d_A^4} R^4 \tag{5.16}$$

where R, D, γ, T_S and d_A are the radius of the primary particles within the agglomerates, the diffusion constant, the surface free energy, sintering temperature and the atomic diameter, respectively. The K-F model is also a foundation of the surface volume model (Patterson and Kraft, 2007) and the primary particle list model (West *et al.*, 2007). The volume and the surface area of each particle as independent variables are tracked in the surface-volume models which are difficult to be determined accuarately at nanoscale.

Due to the small length scale and the fast sintering process, MD provides a model-free technique for the sintering studies of nanomaterials. The kinetic information of atoms during sintering are readily collected during simulation and the relations between different factors of interest are then easier to investigate in a more fundamental manner without any assumptions. Microscopically, the sintering process is a result of both surface motion and grain boundary motion to minimize the total sum of surface energy and grain boundary energy. However due to the presence of high surface curvature and large atomic forces, the sintering process of nanoparticles are expected to be radically different to their counterparts at the micrometre or millimetre size range. Many experimental and theoretical studies have been conducted on the coalescence and sintering of different types of metal and metal oxide nanoparticles including gold, copper, nickel, silicon, iridium and titanium oxide (Zhu and Averback, 1996; Raut *et al.*, 1998; Zeng *et al.*, 1998; Hendy *et al.*, 2003; Arcidiacono *et al.*, 2004; Hawa and Zachariah, 2004, 2007; Panigrahi, 2007; Koparade and Cummings, 2005, 2007; Pawluk and Wang, 2007). The general trend resulting from these studies reveals that the sintering process increase as particle size decreases, and it has been generally reported that surface and grain boundary diffusion are the two contributing transport processes for the sintering of copper and gold nanoparticle (Zeng *et al.*, 1998; Arcidiacono *et al.*, 2004; Wakai, 2006). There are however still many inconsistence even contradictions. Some conventional solid state sintering models, such as the Koch and Friedlander (1990) model, have been reported to be able to predict the sintering process

of nanoparticles (Arcidiacono *et al.*, 2004; Hawa and Zachariah, 2006), which contrasted significantly to the results from other results such as Lewis *et al.* (1997) and Mazzone (2000) who claimed that the MD results could not be predicted by these conventional theories at all. While a significant orientation effect was reported for TiO_2 nanoparticles (Koparde and Cummings, 2005) and gold nanoparticles (Arcidiacono *et al.*, 2004), it was claimed that the relative orientation of the particles had very little effect on the shrinkage of aluminium nanoparticles (Raut *et al.*, 1998). Little studies have been conducted on the kinetics of sintering while large data scattering was reported for the bulk activation energies, and the kinetics of different regimes of sintering particles such as the surface, the necking and the core were not distinguished clearly. Among the sintering studies in use of MD, the kinetics of different geometric regions of sintering particles such as the surface, the neck, and the core has not been clearly distinguished.

Most of these sintering studies employed two equal-sized spherical particles although in reality, the engineering process involves coalescence and sintering a number of particles with un-even size distributions. Actually the macroscopic theory is mainly developed based on two-particle model (Kuczynski, 1980; Chiang *et al.*, 1996). The study of initial stage of sintering is basically established on the two-particle model. It is because the distinction of this stage is the neck shrinkage, considering more particle does not make theoretical difference. As the sintering proceeds the inter-connected pores form spatial structure between multiple-particles. The quantitative description of sintering is very difficult and the pores instead of particle become the object of sintering study. For example, Coble model describes the kinetic mechanism of shrinking pores (Coble, 1961).

A few limited studies for unequal sized particles revealed that different phenomena were expected (Zeng *et al.*, 1998; Zhan *et al.*, 2002; Hawa and Zachariah, 2006). For instance, Hawa and Zachariah (2006) revealed that the deformation of the smaller particles and convection processes dominated the coalescence of small liquid particles, but diffusion process dominated

the coalescence process of solid-like particles. One more complicated phenomenon related to nanomaterials is their size-dependent properties. An example is that early melting can occur at elevated temperatures that interplay with the sintering process. Proper sintering study needs to consider these size-dependent properties.

5.4 Simulation Setting

The classical EAM potential developed by Foiles (1985) was used in this MD study of two nickel particles. The three quantities needed of the EAM total energy in form of **Equation 5.12** are the pair potentials $\Phi(r)$, the embedding functions $\Theta(\rho)$, and the electron densities ρ_i of atom i which is a sum of local atomic electron densities, ρ^a

$$\rho_i = \sum_{j(\neq i)} \rho_j^a(r_{ij}) \tag{5.17}$$

The atomic electron densities ρ^a obtained from the Hartree-Fock calculations and the form of atomic density is then written as

$$\rho^a(r) = (N - N_s)\rho_d^a(r) + N_s\rho_s^a(r) \tag{5.18}$$

where N is the total number of outer electrons, N_s is a measure of the s electron content of atomic density, ρ_s^a is the density of the outer s orbitals, and ρ_d^a is the density of the outer d orbitals. The pairwise potential is expressed in form of simple polynomial of an effective charge $z(r)$,

$$\Phi(r) = Z^2(r)/r$$
$$Z^2(r) = a_1(r_0 - r)^3 + a_2(r_0 - r)^4 \tag{5.19}$$

The values for Nickel are, N_s = 0.86, a_1 = 0.070937, a_2 = 0.146031, r_0 = 3.0045. The electron densities are in units of $Å^{-3}$ and the energies are in electron volts (eV). The embedding energies are expressed in term of natural splines. The knots used for the spline and corresponding value of $\Theta(\rho)$ are listed in **Table 5.1**.

Table 5.1: Fitting parameters of EAM potential

ρ	$\Theta(\rho)$
0.0	0.0
0.01446	-3.5847
0.02891	-5.1449
0.05783	-3.4041
0.06650	0.0

The MD simulations were carried out in the NVT canonical ensemble and the constant temperature was maintained by the Nosé-Hoover thermostat. Free-forming nickel nanoparticles were investigated in a vacuum without imposing periodic boundary conditions to simulate isolated nanostructures. The possible oscillation induced by Nosé-Hoover thermosat in the simulation was avoided by placing a dragging force periodically by equilibrating the system at the imposed constant temperature for 10,000 steps with the time step fixed at 1.0 fs (femtosecond). The potential cut-off distance was defined as 4.5 Å. The Verlet neighbor list was employed in all simulations.

Two un-even sized nickel particles were simulated in this study. The large nickel cluster consists 2,112 atoms, measuring 3.52 nanometer in diameter, which are arranged spatially in a face centered cubic (FCC) lattice in a spherical shape. Similarly, a small nickel cluster consisting of 276 atoms, or 1.76 nm in diameter, is placed in the close vicinity of the large particle. The two crystallographic axes of the two nickel particles are consistent with the

coordinate's axis to have same space orientation without tilting. This makes the possible grain boundary naturally coherent and do not cause reorientation of particles. Initially the atom clusters were constructed. In order to investigate the kinetic of sintering of particles in different regimes, the nickel crystals were partitioned into different layers with equal distance of dR = 1.25 Å each, the half of unit cell constant, the inter-atomic distance in pure nickel, which results in 10 and 5 radial layers of nickel atoms for the large and small nickel particles. The outmost layer of nickel atoms was defined as 'surface layer', the first three layers from the surface, including the surface layer, was defined as 'outer layer' and further inwards layers were defined as 'core'. Tracing atoms are arranged to study the dynamics of each regime during the sintering process.

Both isothermal heating and constant rate of heating methods were investigated by MD simulations. For the isothermal study, simulations were performed at constant temperatures between 800 and 1500 K at temperature interval of 100 K. Before each run, the two clusters were equilibrated separately for 5×10^4 steps. After removing the angular momentum, they were positioned in a single simulation box and the small cluster only has the translational displacement along the abscissa of the large cluster. The distance between the two surface layers was set as 4 Å, just within the EAM cut off distance, to enable the surface atomic interactions. The sintering simulation was then initiated for 200 ps (picosecond). The same temperature span was used for the constant rate of heating method for 40 ps, which brings the nominal heating rate of 17.5 K/ps.

5.5 Melting of Nickel Nanoparticles

Because of the great surface/volume ratio, the nanoparticles are more eligible to early melting. Such an early melting phenomenon can significantly affect the sintering process. In the framework of classic thermodynamics, melting of a solid is known as a first-order discontinuous

phase transformation occurring at a critical temperature at which Gibbs free energies of the solid and the liquid states are equal, *i.e.* T_0 of the solid. The melting process of a solid involves an abrupt change in latent heat and volume at T_0, which is a convenient indicator in term of numerical simulation. Melting kinetics of low-dimensional materials, in which surfaces and/or interfaces play a dominant role, is much deviated from that for the conventional bulk solids. For example, the melting point of free-standing nanometre-sized particles is remarkably depressed relative to T_0 (Jin and Lu, 1998). It is also observed that when the nanoparticles are properly coated by (or embedded in) a high-melting-point matrix, the melting point of the particles can be elevated above T_0 (Jin and Lu, 1998), which is also found in the next chapter, which rarely happens in bulk solids (Mei and Lu, 2007). Single particle MD simulations were conducted first for individual particles to benchmark the methodology and establish a base for the sintering study.

For MD simulations, a useful method of evaluating the melting temperature of a nano-cluster is to evaluate the point of discontinuity in the potential energy. This is based on the fact that the potential energy is a function of volume of system (Jin and Lu, 1998). For particles of a few nanometres, the first order transition from the solid phase to the liquid phase is of a fast transient nature and typically occurring in the order of 10^{-14} s (Anderson, 1997; Jin and Lu, 1998), which can be well reproduced by MD studies. There have been many studies in which melting of nanostructured materials is evaluated by this approach (Jin and Lu, 1998; Mei and Lu, 2007). Both constant rates of heating (CRH) and isothermal methods were investigated on the melting of individual nickel particles as shown in **Figure 5.2** and **Figure 5.3**. Both methods reveal similar phenomenon with slight different values probably caused by different relaxation time. At low temperatures, the average potential energy per atom increase linearly with increasing temperatures. The melting phenomenon is identified by the distinct rise in the average potential energy due to the release of latent heat, which occurs

at ~1100 K and ~1500 K for the small and large cluster respectively as revealed by both methods.

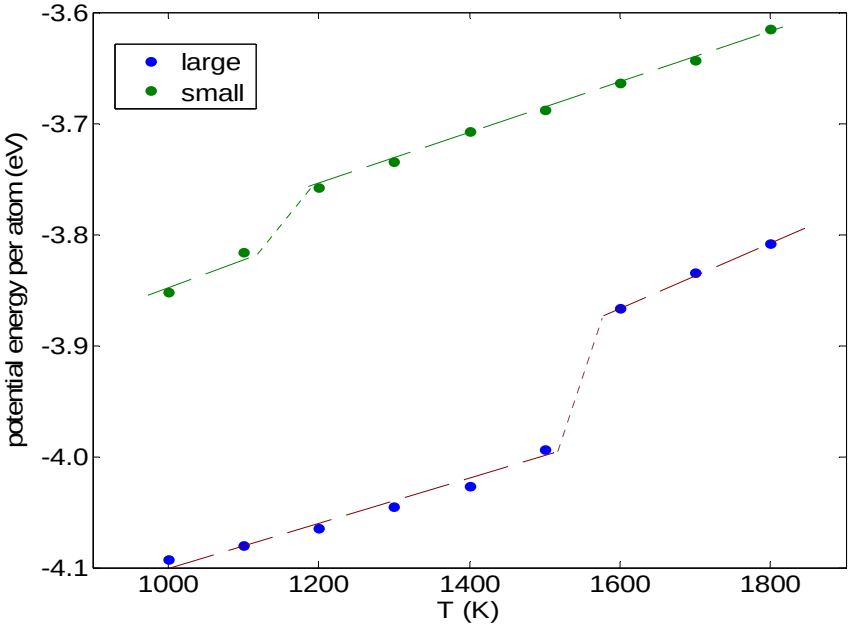

Figure 5.2: Potential energy per atom under isothermal heating

Figure 5.3 also reveals that the discontinuity in the average potential energy has a wide temperature range in the melting point due to the large fraction of the surface atoms. It has been demonstrated both experimentally and theoretically that the melting process of a crystalline substance starts from the surface layer and propagate into the interior that results in a surface melting temperature significantly slower than the bulk melting points. One would expect similar phenomenon occurs for nanoscale nickel clusters. To reveal such a phenomenon, the particles were partitioned into different layers, of which index number is up-ordered when the atoms are outwards from the cluster center. The average potential energy per atom of each layer was calculated as shown in **Figure 5.4** under CRH conditions. It shows that the energy per atom of different regimes increases linearly with temperature at low temperatures and begin to jump at a characteristic temperature. However the value of the characteristic temperature is different, increasing from the surface to the core, which implying a stepwise melting from the surface to the inner cluster. Such a result is plausible as the core atoms of

the cluster have higher coordination numbers than the surface atoms. As the cluster heats up, disorder first appears at the surface due to the broken bonds associated with surface atoms, resulting in the surface melting, which then propagates inwards. As the surface melting occurs, the cores remain nearly rigid and solid-like. The surface melting temperature is ~1200 K while the overall melting occurs ~1500 K for the large cluster. Similarly a surface temperature of ~900 K is identified for the small cluster.

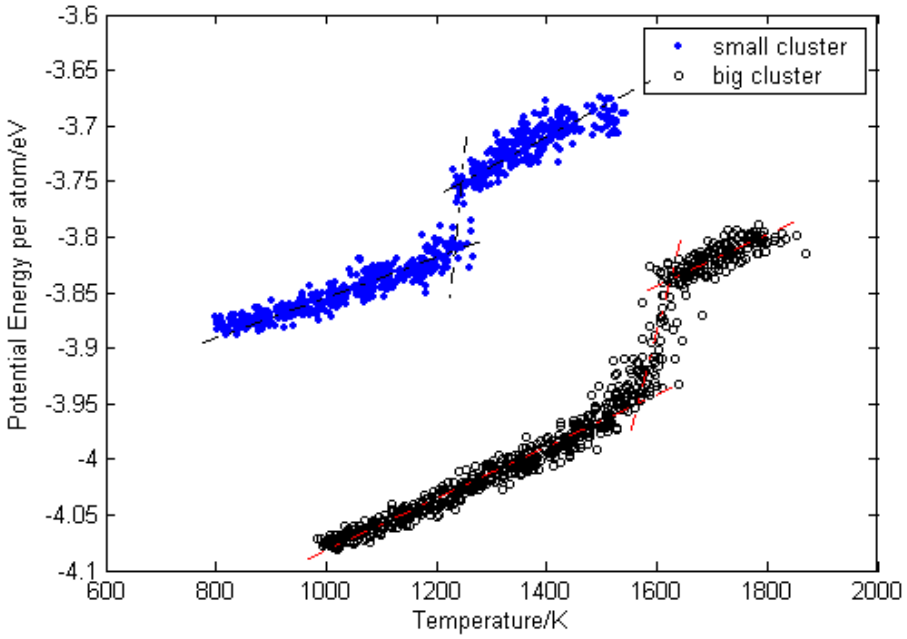

Figure 5.3: Potential energy per atom under constant rates of heating

The surface melting and the formation of the liquid-like surface layer will affect significantly the subsequent sintering process. This has been revealed by thermodynamic analysis and experiments that the coalescence process begins with nanoparticle contact, followed by the alignment of the coalescing planes at the interface between the nanoparticles, where the liquid-like mobility of the nanoparticle surface layers is essential to achieve this. When a small particle coalesces with a larger one, the smaller one rotates to orient its places to those of the larger one (Jose-Yacaman *et al.*, 2005).

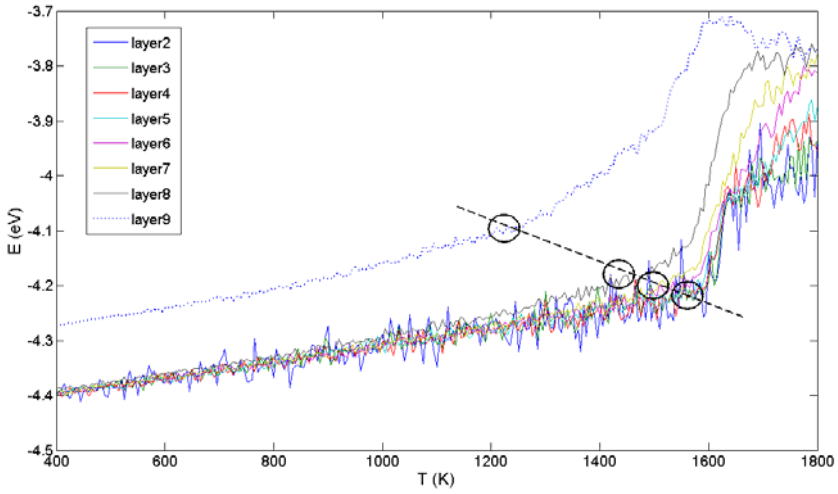

Figure 5.4: Layered potential energy per atom of large cluster

The calculated melting temperatures of different sized particles are compared with a few empirical correlations. The results follow the same trend as the predictions from correlations but at slightly higher values. For instance, the predicted melting temperature depression, defined as the melting temperature of particles over that of the bulk value, are 0.7 and 0.5 for 3.52 and 1.76 nm nickel particles from Cao *et al.* (2006), while the MD simulated results are 0.75 and 0.55 based on the surface melting temperature. Such a difference is believed to be associated with the accuracy of the interaction potential.

5.6 Sintering of Nickel Nanoparticles

A typical sintering scenario is shown in **Figure 5.5** at a constant temperature of 1300 K. Two clusters were positioned within the cut off distance of the interaction potential and sintering was initiated at t = 0 ps after the initial equilibrium of the two clusters (see **Figure 5.5**). The sintering process occurs rapidly in the first a few picoseconds. A neck forms at t = 0.01 ps (**Figure 5.5b**), and reaches a diameter close to the size of the small cluster at t = 0.5 ps (**Figure 5.5c-d**). This was then followed by a slow process (**Figure 5.5e-f**), reaching a full sintering at 200 ps where the small cluster becomes in-distinguishable.

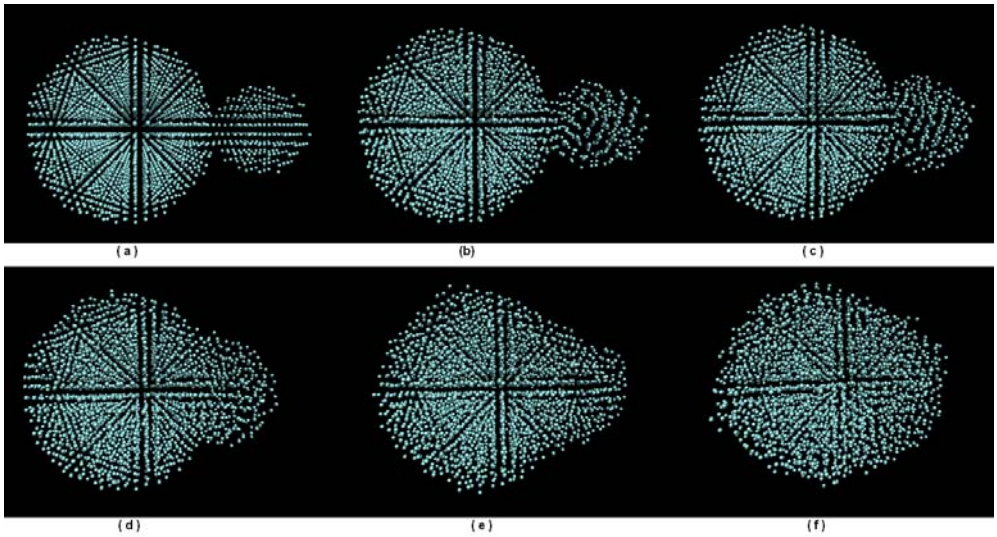

Figure 5.5: Nickel melting temperature comparisons at 1300 K
(Simulation time point: **0, 0.01, 0.05, 0.5, 2, 200 ps** for snapshots from ***a*** to ***f***)

5.6.1 Shrinkage ratio

The sintering process can be quantified by measuring the shrinkage, $\zeta = \Delta L / L_o$, which is defined as the change in the center-to-center distance of the particles ΔL ($\Delta L = L_o - L$) over the initial distance, L_0. For all sintering under different temperatures, the shrinkage curve can be characterized by three stages illustrated in **Figure 5.6**. The stage *I* is the neck formation is marked by a sharp decrease in the center-to-center distance between the particles. The shrinkage appears to be independent of temperature in this initial stage, as evidenced by the similar shrinkage gradients $d\Delta L / dt$ among different sintering temperatures. Such an observation is similar to that of Zeng *et al.* (1998) and Arcidiacono *et al.* (2004), which is presumably because the dominant mechanism for early stage nanoscale sintering does not require thermal activation. The simulation also shows that in the stage *I*, the shrinkage ratio and duration increases with increasing temperature, implying an easier sintering process at elevated temperatures. The stage *II* comes after the rapid neck formation and is marked by a temperature dependent characteristic with lower sintering rates, which is seen by the slope change after 5 ps. In this stage,

the shrinkage is sensitive to thermal activation as the surface diffusion and grain boundary diffusion becomes dominant in this stage, such behaviour becomes important after some degree of shrinkage is formed and the neck curvature is significantly reduced. Of note that for sintering at low temperatures, *i.e.* $T < 900$ K, there is a small recovering process in the second stage, the center-to-center distance increases slightly after the initial rapid neck formation. This is presumably due to the solid status of both particles, resembling behaviours of soft collision. The stage *III* marks the end of the sintering as evidenced by the nearly constant shrinkage values, varied between 0.1 and 0.4 depending on the sintering temperature from partial to full sintering. The increasing shrinkage ratio with temperature is associated with the increased diffusion process at higher temperatures.

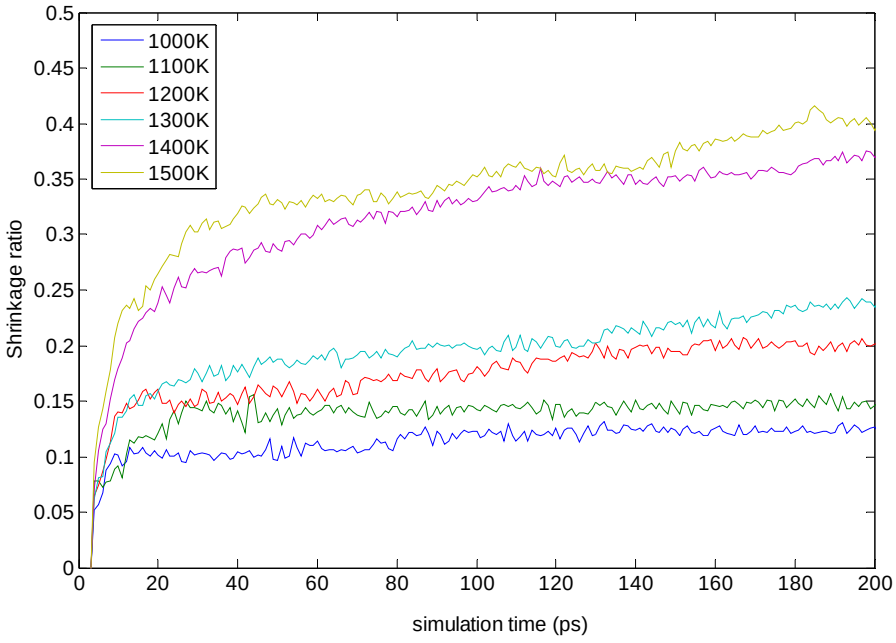

Figure 5.6: Shrinkage under different temperatures

5.6.2 Gyration radius

Similarly, the sintering process can be characterized by the gyration radius, R_g as defined below

$$R_g^2 = \frac{1}{M}\sum_i m_i (r_i - r_c)^2 \tag{5.20}$$

where M is the total mass of the group and r_c is the centre-of-mass position of the group. The time evolution of the gyration radii during the particle sintering is illustrated in **Figure 5.7**. Similar to the shrinkage analysis, the three-stage sintering scenario is easily recognized. The sintering starts with a rapid initial stage, t < 10 ps, independent of the particle size and initial temperature, followed by a slow transition process that approaches asymptotically to the final stage, where constant values are reached. However different to the shrinkage analysis, the final gyration radius is quite similar for heating temperatures above 1200 K as the surface melting of the large cluster occurs, and the small cluster is fully molten, **Figure 5.8**. However the two clusters does not form a single spherical cluster within the 200 ps simulation range, as the final snapshot of MD shown in **Figure 5.5f**. While for large particles, the sintering occurs in the solid state in this temperature range, it is apparent that a transient liquid phase sintering or viscous flow sintering occurs for nanoparticles of a few nanometers diameter. The viscous flow mechanism is important to model the sintering process. In the late stage of the sintering, it could be driven by the self diffusion driven by surface tension gradients resulting from a non-perfect sphericity at the solid-liquid interface.

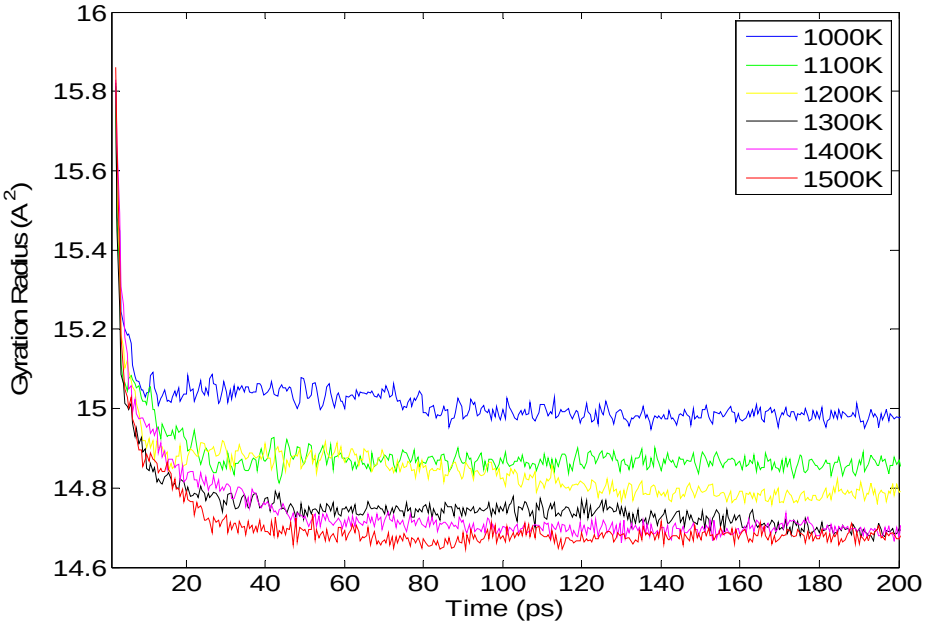

Figure 5.7: Gyration radius of the two sintering clusters

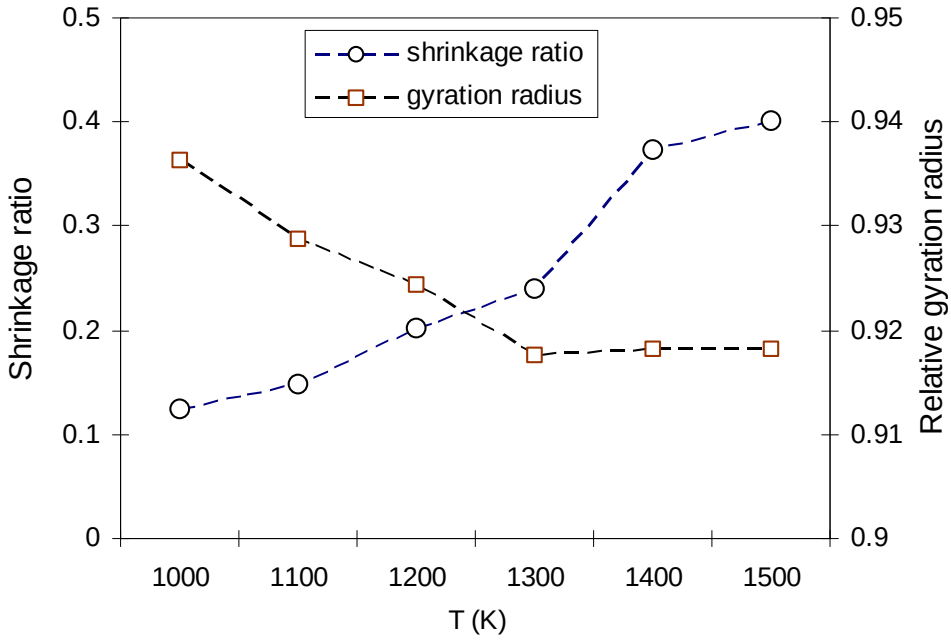

Figure 5.8: Shrinkage ratio and the gyration radius after sintering

5.6.3 Mean square displacement

In the nanoscale regime, the diffusion pathways are mixed and overlapped. The melting of particles makes the situation even hard to adopt constiuun

model. Instead of idnetifying classical six diffusions, the diffusivity of different geometric regions was investigated. The mean square displacement (MSD) is a measure of the average distance a given particle in a system travels and can provide a good approximation of diffusion. The MSD is defined as:

$$MSD = \left\langle r^2(t) \right\rangle = \left\langle \frac{1}{N} \sum_{i=0}^{N} \left(r_i(t) - r_i(0) \right)^2 \right\rangle \tag{5.21}$$

Here, N is the number of particles, t corresponds to time, and $r_i(t) - r_i(0)$ is the vector distance travelled by a given particle over the time interval. MSD simply tells how far a group of atom travel in a given time interval.

Examples of the average MSD of the large and small cluster during the sintering process are shown in **Figure 5.9**. The magnitudes of MSD increase with time, being higher at higher temperatures. Both clusters have initial rapid increase in MSD, being more pronounced for the small cluster, which resembles the initial fast sintering as revealed by the shrinkage and gyration radius study.

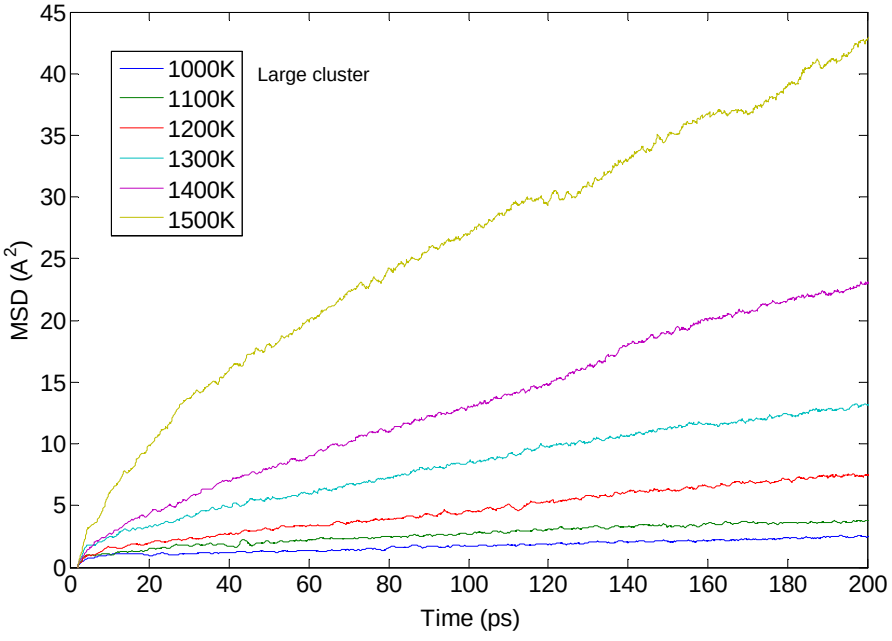

(a)

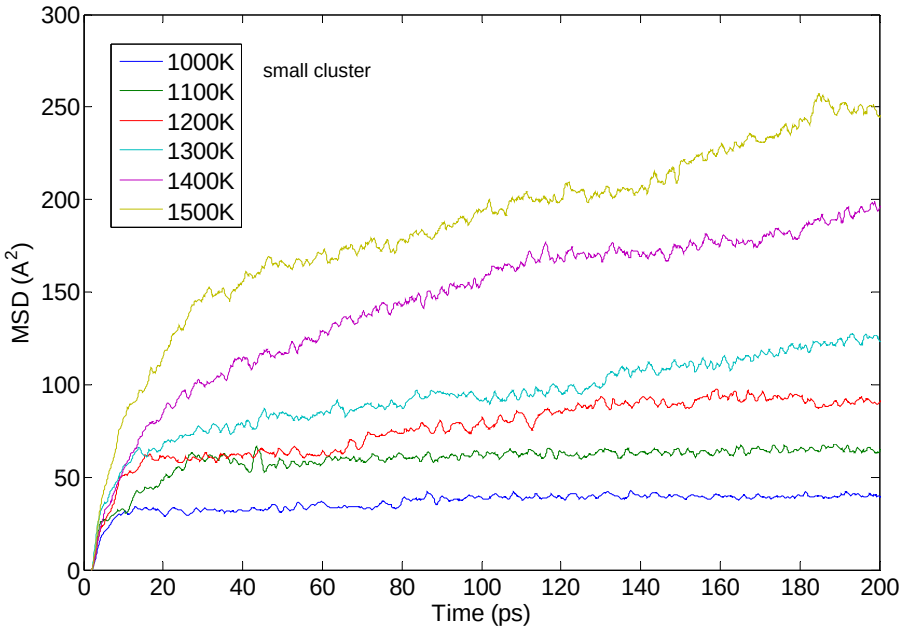

(b)

Figure 5.9: MSD of two clusters at different temperatures (a) large cluster and (b) small cluster

In order to reveal the sintering mechanism, the MSD of different regimes during the sintering process at two typical temperatures are plotted in **Figure 5.10**. It is evident that the largest magnitude of MSD is observed on the surface layer, and the magnitude decreases towards the cluster center. The result also illustrates that the MSD behaves quite differently between the large and small clusters. For the large cluster at the low temperature, *i.e.*, ~1000 K (see **Figure 5.10a**), the MSD of all regions increase slowly with time with small MSD values, 10 $Å^2$ in 200 ps for the surface layer. The MSD difference between the core and surface regime is small, 6 $Å^2$, which implies that there is no remarkable diffusion from this region at this temperature, and atoms tend to oscillate around the balanced lattice position. When the isothermal temperature was elevated to 1200 K or higher (**Figure 5.10b**), large temporal evolution of MSD was observed in all selected regions of the large cluster. The MSD of the surface layer increase nearly

linearly, reaching ~80 Å^2 in 200 ps and difference between the surface layer and the core becomes large, due to the surface melting of the large cluster.

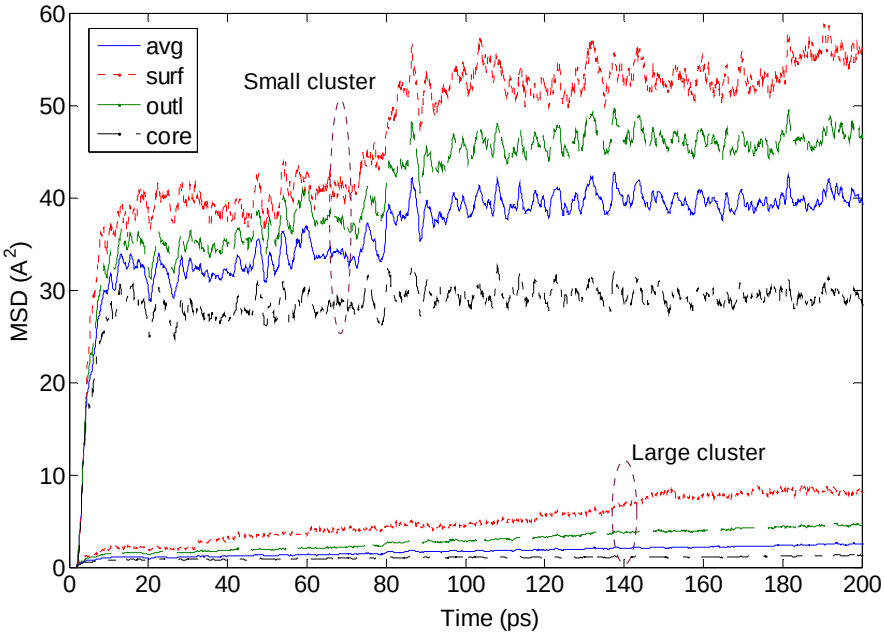

(a) T=1000 K

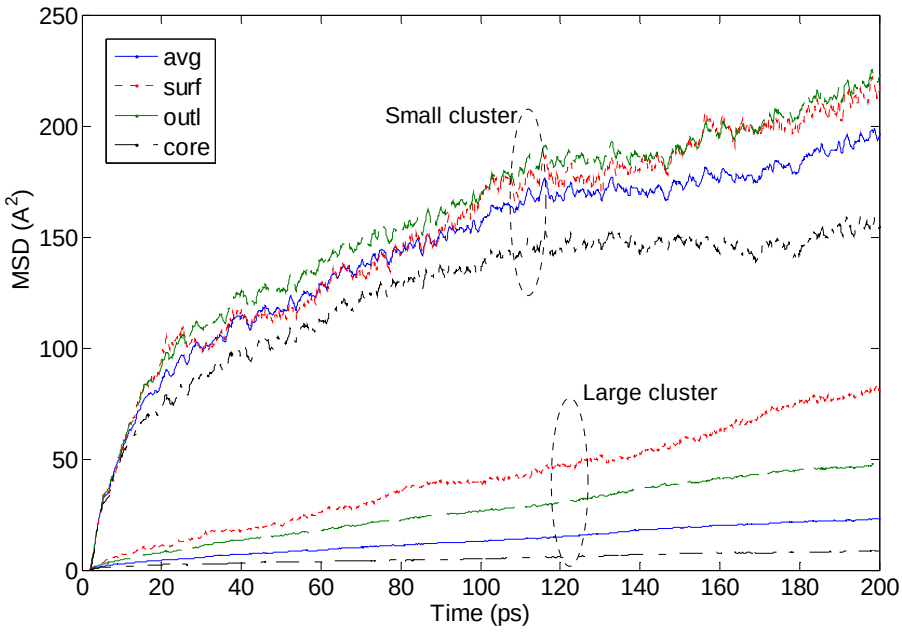

(b) T=1500 K

Figure 5.10: Comparison of MSD of two clusters of different layers

One phenomenon of interest is that the small cluster had large initial MSD increase, from 0 to 20-30 Å^2 at T = 1000 K and 50 Å^2 at T = 1500 K, at the

beginning stage independent of temperature. This is due to the displacement in the first stage of the sintering, caused by the 'attraction' from the large cluster *i.e.* the surface and outer layer atoms, as the MSDs of these temperature-independent behaviours are larger than the separation distance. New equilibrium position is re-established for the small cluster as the repulsion and attraction upon the small cluster is roughly balanced. It should be noted that as there is no long-range interaction like the 'gravity' for EAM potential with cutting off distance, it is impossible for the small cluster to move entirely like a rigid particle. There is possibly some plastic deformation during this stage as reported by Zeng *et al.* (1998). Some results presented by Hawa and Zachariahl (2006) are thought to be associated with this phenomenon. The ratio of the MSD at the surface to that of the core reflects the surface melting phenomenon (Shi, 1994). There is a smoothly decrease of MSD values from the surface layer towards inside at low temperature ~1000 K, as the surface melting occurs for the small cluster while the core is still solid-like. Such a trend disappears at temperature over ~1200 K where the MSD value of the surface layer and the outlayer are similar, which is believed to be associated with the global melting of the small cluster as discussed in the **Section 5.5**.

5.6.3 Root mean square displacement

The average root-mean-square thermal displacement is a good parameter to analyse the atomic motions near the melting point, which is defined as in **Equation 5.22**

$$RMSD(dt) = \frac{\sum \sqrt{\left\langle \sum_{t=0}^{T-dt} \left(r_i(t+dt) - r_i(t) \right)^2 \right\rangle}}{N} \tag{5.22}$$

where N is the atom number in the selected regions. **Figure 5.11** shows the RMSD results obtained by averaging the trajectories of 200 ps of different regimes at an interval of dt = 10 ps. It clearly shows that surface and outer

layer atoms have higher RMSD than those in the core regime. An empirical criterion to assess the melting temperature is proposed by Qi *et al.* (2001), who defined the critical RMSD to be molten as 0.6 Å (~24% of the bulk inter-atomic distance of Ni). For the large clusters shown in **Figure 5.11a**, the RMSD of surface and outer layer exceeded 0.6 Å at temperatures over 1400 K, and for the small cluster the criterion of melting is reached at a temperature of smaller than 1000 K. These values are roughly consistent with the previous analysis in surface melting through the potential energy per atom. The value, RMSD = 0.6, provides a simple criterion to identify the surface melting phenomenon, however it should be cautious for direct applications as different potentials are used. The Sutton-Chen potential was used in Qi's study (Qi *et al.*, 2001); further studies are required to justify if the criterion can be applied directly in this study. It is worth to point out that the RMSD mentioned here is an empirical parameter used to compare with some references. It is not the root mean square deviation widely used as a measure of the differences between values predicted by a model or an estimator and the values actually observed from the thing being modeled or estimated

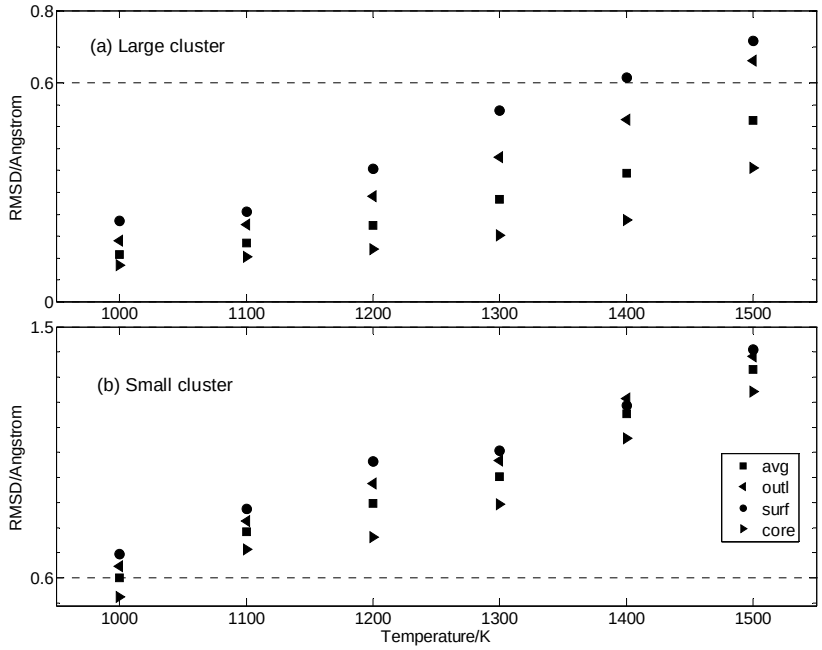

Figure 5.11: RMSD of two clusters

5.6.4 Diffusivity and activation energy

The big advantage of MD is that the properties of interest are derived from well-established statistical method without mechanical assumption, typically referring to continuum model. The significance of MSD is that it contains information on the atomic diffusivity in relation to diffusion coefficient. The slope of MSD is related to the diffusion coefficient $D(T)$, which can be calculated using the Einstein equation,

$$D(T) = \lim_{t\to\infty} \frac{\langle r^2 \rangle}{2dt} \tag{5.23}$$

where $<r^2>$ is the mean square displacement of the atoms in the time t and d is the dimensionality of the system, which equals to 3 in this work. As shown in **Figure 5.4**, it is clear that surface properties play an important role in the coalescence event. Different regimes have different diffusivities, being larger for atoms closer to the surface. The result of diffusivity of different regimes calculated from MSD is shown in **Figure 5.12**. It clearly shows that the diffusivity is a regime-dependent and size-dependent behaviour, *i.e.* being larger in the surface regime and being smaller for the large particle. Nearly all these regimes displaced a linear relationship between ln (D) and $1/T$, typical Arrhenius type, which can be expressed as:

$$D(T) = D_0 \exp[-Q_v / k_B T] \tag{5.24}$$

where D_0 is the pre-exponential factor that is independent of temperature, Q_v is the activation energy, T is the absolute temperature and k_B is the Boltzmann constant. The average activation energies of the two particles are calculated as 0.497 and 0.581 eV respectively for the large and small clusters; such values are much smaller than the bulk values, which are in the range of 2.0-2.9 eV, but in the similar values compared with other nanoscale nickel sintering experiments. For instance, the average activation energy for

sintering of nickel particles with d = 6.2 nm was determined as 0.62 eV from both direct *in-situ* Differential Mobility Analyzer (DMA) and *ex-situ* TEM analysis (Tsyganov *et al.*, 2007). Panigrahi (2007) also obtained experimentally the activation energy of sintering as 0.68 eV for 30 nm ball milled nickel particles.

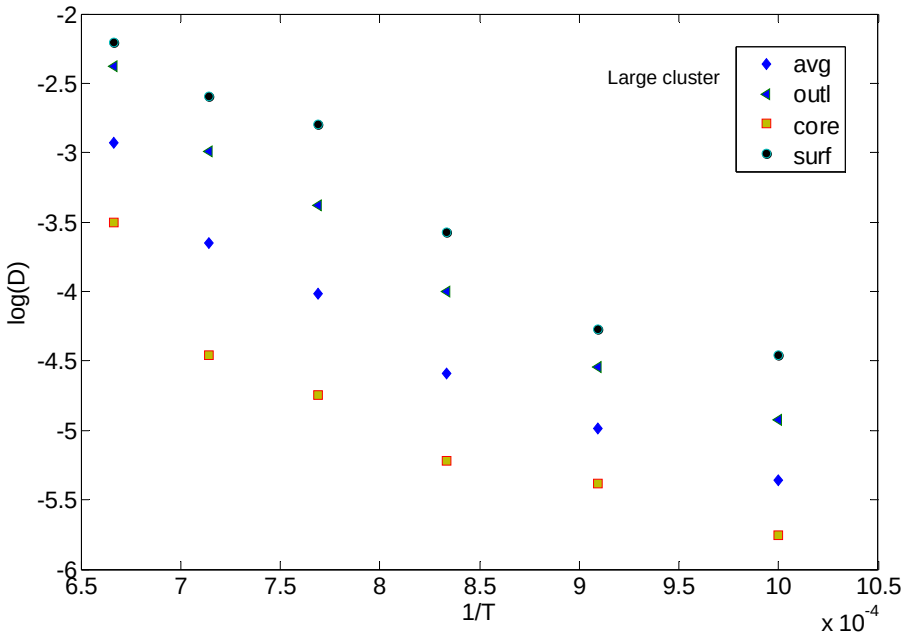

(a)

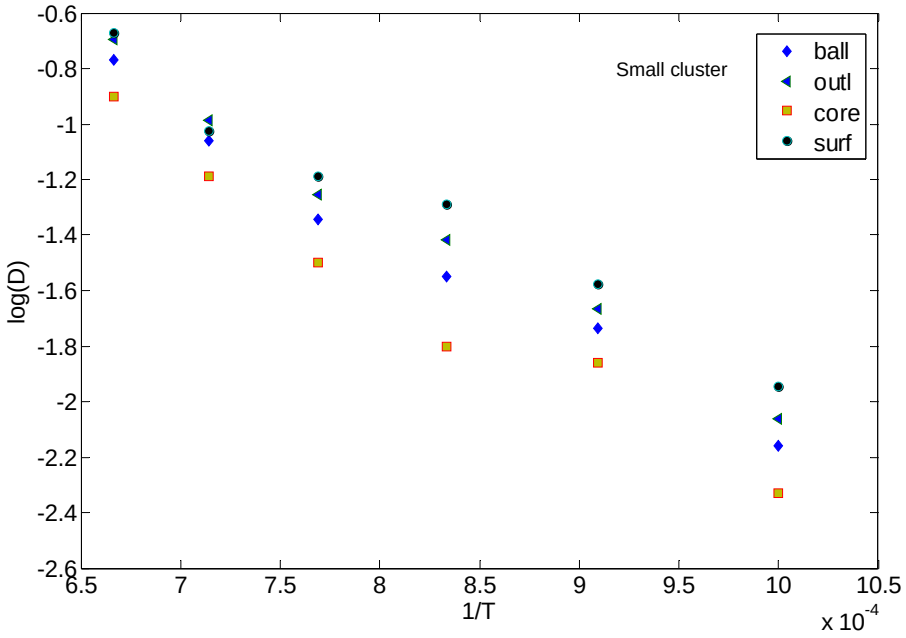

(b)

Figure 5.12: Diffusivity calculation

For large particles, it has been widely accepted that the activation energy of surface diffusion is proportional to the melting temperature of crystalline solids, $E_{sp} / E_{sb} = T_{mp} / T_{mb}$, where E_{sp} and E_{sb} refer to the surface diffusion activation energy at particle and bulk level, and T_{mp} and T_{mb} refer to the melting temperature at the particle and bulk level. If such proportionality is extendable to nanoparticles, the activation energy ratio should be around 0.5-0.7 as revealed from the melting study. However the MD study reveals a different phenomenon, the activation energy reduction ratio, which is in the range of 0.2-0.3, is much smaller than the melting temperature depression ratio. Other studies were also conducted including the modelling of the necking growth and coalescence time, t_s, based on **Equation 5.16** in K-F model (Koch and Friedlander, 1990; Xing and Rosner, 1999). The results show that surface diffusion is not the sole mechanism for sintering. It is apparent that beside the surface diffusion, there are other mechanisms that contribute to the sintering process that may include the grain boundary diffusion, viscous flow, plastic deformation and surface tension gradient resulting from a non-perfect sphericity in solid-liquid interface. Similar conclusions have also been reached by a very recent study by Pan *et al.* (2008) for sintering of two gold nanoparticles with equal diameters. It was found that the surface diffusion and grain boundary diffusion are the controlling mechanisms for sintering nanoparticles over 10 nm in size.

5.7 Chapter Summary

The sintering and melting of two different sized nickel nanoparticles (3.52 and 1.76 nm in diameter) were simulated by a MD method in this chapter. In order to study the dynamics of the sintering process, both particles were partitioned into different regimes where tracing atoms are arranged. Some specific conclusions are reached that include: The tracking of different regimes of nanoparticles reveals the feature of surface melting, which occurs at the surface firstly, propagates inwards as heating temperature

increases and influences the subsequent sintering significantly. The sintering of two different sized nanoparticles occurs in a three-stage scenario as revealed by the shrinkage, the gyration radius, MSD and RMSD studies. The first stage sintering is independent of temperature, and the late ones are driven by surface diffusion and grain boundary diffusion. The sintering diffusivity is identified to be regime-dependent and particle size dependent, being higher at the surface layer and larger for smaller particles. The activation energy during the sintering is found to be much smaller than the bulk value but is consistent with other nanoparticle studies. The sintering of different sized nanoparticles is a complicated phenomenon. It has been suggested that beside the surface diffusion, grain boundary diffusion, viscous flow, plastic deformation and surface tension gradient resulting from a non-perfect sphericity in solid liquid inter-face may also contribute to the sintering process (Zhu and Averback, 1996; Raut *et al.*, 1998; Zeng *et al.*, 1998; Nanda *et al.*, 2002; Hendy *et al.*, 2003; Arcidiacono *et al.*, 2004; Hawa and Zachariah, 2004, 2007; Panigrahi, 2007; Koparade and Cummings, 2005, 2007; Pawluk and Wang, 2007; Ding *et al.*, 2009).

Chapter 6

Numerical Study of Thermal Behaviours of Core-shell Structured Al-Ni Nanoparticle

6.1 Introduction

Bimetallic systems have received intensive interest recently due to their practical significance in materials processing. Example applications include shape memory alloys and super-alloys with improved mechanical properties such as high strength with relatively light weight and good corrosion resistance. Suitable engineered composite particles, which are able to utilize the distinct properties of both materials, are important for advanced materials and engineering applications. For instance, nickel-coated aluminium particles have been found to be able to improve the combustion characteristics of Al. It was demonstrated that such composite particles can reduce agglomeration, eliminate combustion instabilities, promote flame propagation velocity and avoid formation of passavition layers (Lebrat and Varma, 1994; Yagodnikov and Voronetskii, 1997; Price *et al.*, 2000; Babuk *et al.*, 2001; Varma *et al.*, 2002). In the energetic applications, Ni-coated Al particles and synthesized nickel aluminides, which are lightweight materials with high melting points and high energy density, good mechanical properties at elevated temperatures, and good corrosion resistance when exposed in highly oxidative atmosphere, are considered as attractive potential candidates for energy carriers.

Such composite particles can be synthesized by various methods such as cyclic electroplating, electroless plating, continuous combustion and chemical vapour deposition at relatively low cost (Breiter *et al.*, 1997; Andrzejak *et al.*, 2007). The particles' thermo-response under non-oxidation

scenarios and the interactions between Ni and Al and its consequent structural properties are essential for the oxidation behaviour and its subsequent functional performance. For conventional bulk materials, Ni-Al phase diagram shows that nickel-rich solid solution formed at high temperatures (T >= 1000 K), and several phases in the state of intermetallic compounds including Ni_5Al_3, Ni_3Al, NiAl, Al_3Ni and Ni_2Al are found at lower temperatures, which are dependent on the temperature and atom concentrations (Schryvers *et al.*, 1993; Debiaggi *et al.*, 1999; Chushak *et al.*, 2003; Kazanc, 2008). Beside these complexes, Ni-Al intermetallic phase transition at nanometer scale is expected to have some unique features related to the high ratio of surface atoms and different reaction mechanisms of nanomaterials. A shift of those transition temperatures at nanoscale has been observed both experimentally and theoretically (Pabi *et al.*, 1996; Debiaggi *et al.*, 1999). The thermal and mechanical properties of nanoparticles can display some unique behaviour associated with the size-dependent properties such as melting depression and other low-dimension effects.

Only limited studies have been conducted on nickel-coated aluminium at the nanometer scale. Some prior research on combustion synthesis of nickel aluminades showed that some intermediate nickel aluminides formed prior to the final product in the form of NiAl or $NiAl_3$ (Andrzejak *et al.*, 2007). The aluminium core became molten and spreading over solid Ni shell, and the fracture induced by thermal expansion of liquid Al core was observed experimentally (Thiers *et al.*, 2002). A similar fracture phenomenon is also obtained through a molecular dynamics simulation for an Al-core/Ni-shell nanoparticle (Delogu, 2007a and 2007b). The phase stability of Ni-Al nanoparticles was studied numerically at low temperatures (Debiaggi *et al.*, 1999). Several phases were distinguished for a 2.8 nm Ni-Al composite nanoparticle, *i.e.* B2, Ll_2 and FCC solid solution and a phase similar to Ll_0 martensite (all the crystal lattice structures in this chapter are hereby represented by Strukturbericht Designations). Delugo (2007a, 2007b)

investigated the demixing phenomena of stoichiometric NiAl nanoparticles and found that Ni_3Al phase could nucleate from the parent NiAl matrix. Such a demixing resulted in a solid Ni-rich interior and an Al-rich surface layer. The thermal and mechanical response of Ni coated Al nanoparticles with total radius of 4 nm were studied by Delugo (2007a, 2007b). The fracture of the shell was observed by a computer simulation, which clearly revealed a variety of different dynamical processes at the nanometre scale as compared with that at bulk scale. These dynamical behaviours of core/shell system are sensitive to geometry configuration, particularly the shell thickness. A study of such behaviour at the individual particle level is essential for the fundamental understanding.

The present study will investigate the heating and cooling behaviour of a shell-core structured Ni-Al composite nanoparticle through a MD simulation. The detailed thermodynamic properties and structure evolution during a continuous heating and under two different solidification rates will be investigated through the characterisation of the gyration radius, radial distribution function, atom number distribution, radial distribution function (RDF), MSD, RMSD and layered potential energy distribution.

6.2 Simulation Methods

Simulations were performed with LAMMPS by classical molecular dynamics in use of an Embedded-Atom-Method (EAM) force field developed by Angelo *et al.* (1995). Different to the short range potential, the EAM potential includes both pairwise repulsions and many-body density dependent cohesions as expressed by **Equation 6.1** and **6.2**.

$$U_{alloy-EAM} = \frac{1}{2}\sum_{ij}\Phi_{t_i t_j}(r_{ij}) + \sum_{i}\Theta_{t_i}(\bar{\rho}_i) \tag{6.1}$$

$$\bar{\rho}_i = \sum_{j(\neq i)}^{n}\rho_{t_j}(r_{ij}) \tag{6.2}$$

where r_{ij} is the distance between two atoms, $\Phi(r_{ij})$ is the standard two body potential, the subscripts t_i and t_j denote the elemental types of atom i and j, and $\Theta(\rho_i)$ is the energy associated with the density ρ_i at atom i, respectively.

Different from the single element EAM potential (**Equation 5.18-5.19**) for nickel in previous chapter, the pairwise interaction potential $\Phi(r_{ij})$ is the same as the Morse potential (Morse, 1929)

$$\Phi(r) = D_M \left\{1 - \exp[-\alpha_M (r - R_M)]\right\}^2 - D_M \tag{6.3}$$

where D_m, R_m and α_m are the depth, distance to the minimum, and a measure of the curvature at the minimum of Morse potential, being listed in **Table 6.1**.

The density function ρ_i of atom i is defined as

$$\rho(r) = r^6[e^{-\beta r} + 512e^{-2\beta r}] \tag{6.4}$$

where β is an adjustable parameter as 3.6408 and 3.3232 Å^{-1} for Ni and Al respectively.

Table 6.1: Fitting parameters of alloy EAM potential

	Ni-Ni	**Al-Al**	**Ni-Al**
D_M (eV)	1.5335	3.7760	3.0322
R_M (Å)	2.2053	2.1176	2.0896
α_M (Å^{-1})	1.7728	1.4859	1.6277

The composite nanoparticle is constructed from their perfect crystal measuring 4 nm in diameter with a shell thickness of 0.5 nm. It includes an inner core of aluminium containing 2,016 atoms and a shell of nickel with 3,620 atoms, separated by a gap of 3.0 Å between the core and shell atoms,

shown in **Figure 6.1**. An energy minimization process is performed upon the whole system before simulation started. The simulation is carried out within Nosé-Hoover thermostat scheme of the NVT canonical ensemble and performed by the EAM force field. The simulation time step is set as 1.0 femtosecond. Non-periodic boundary condition is imposed to simulate an isolated unsupported bimetallic particle. The temperature range in this study is from 300 K to 1600 K. For the heating simulation, the system is kept at 300 K for 40 ps within the NVT ensemble to achieve an equilibrium state. For the solidification simulation, an additional relaxation time of 40 ps at 1600 K is conducted before implementing the cooling process. To analyse the geometry-dependent properties, aluminium atoms are classified into five groups with equal distance of Δr = 0.66 nm each in the radius direction. Two quenching rates for solidification are simulated: 6.5 K/ps and 0.13 K/ps, corresponding to runtimes of 2.0×10^5 and 1.0×10^7 fs. Hereafter those two quenching rates are termed as the fast and slow quenching rates respectively.

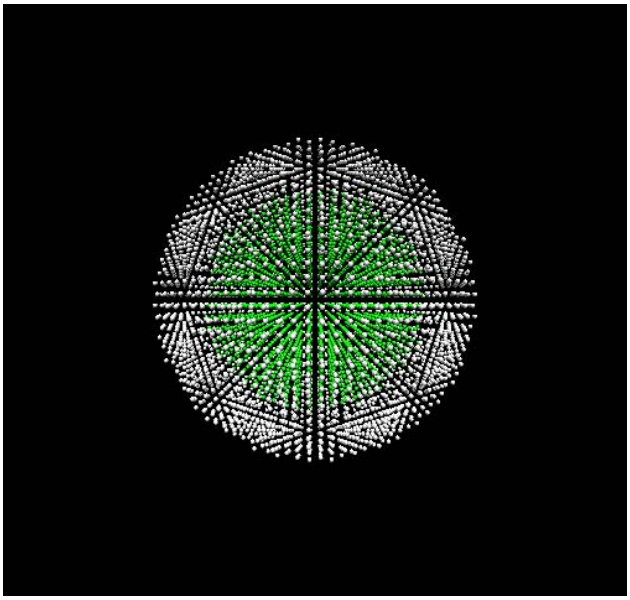

Figure 6.1: Initial Configuration of core-shell Al-Ni
(Al atoms are coloured in green while Ni atoms in grey)

6.3 MD Simulation

6.3.1 Heating simulation

A constant rate of heating (0.65 K/ps) is employed in the simulation, *i.e.* the particle is heated gradually for 2×10^6 time-steps, which is equivalent to 2000 ps, from 300 K to 1600 K. The potential energy, enthalpy and other parameters of different regimes are calculated every 20,000 steps. The thermodynamic and structure properties of the bimetallic particle are investigated in detail as described below.

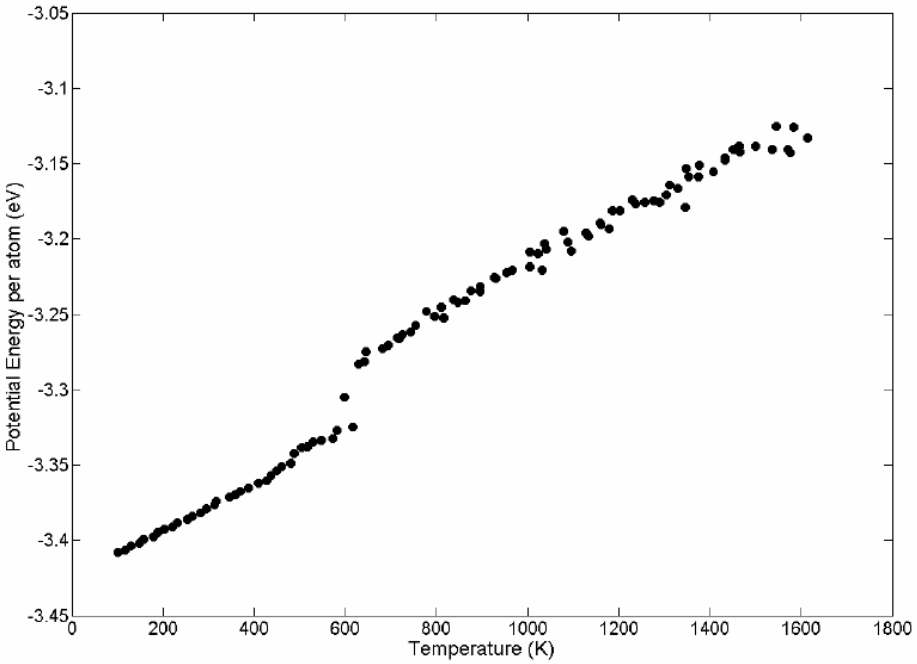

Figure 6.2: Potential energy of pure aluminium particle (*d* = 4 nm)

Single particle MD simulations are conducted first for a pure aluminium particle to benchmark the methodology and establish a comparative basis for below heating and cooling study of the composite particle. Melting is a first-order phase processes that have been well-established. It can be easily revealed by an abrupt changing of potential energy (Mei and Lu, 2007). **Figure 6.2** shows an example of the variation of potential energy with temperature for a 4-nm in diameter aluminium particle. At low temperatures,

the average potential energy per atom increases linearly with increasing temperatures. The melting phenomenon is identified by the distinct rise in the average potential energy due to the release of latent heat, which occurs at about 620 K. In this case, the melting temperature is determined as ~620 K, which is significantly lower than its bulk value, 933 K. In general, the values of melting temperature for aluminium using this EAM potential are higher than experimental value, while the values for nickel are much lower than expected based on experiment (Weingarten *et al.*, 2009). Different-sized pure aluminium nanoparticles were simulated, and the result shows a strong size-dependent melting temperature, which is due to the increased fraction of loosely bounded surface atoms at reduced dimension. The size-dependent MD simulated melting temperatures are compared with a few other experimental and simulation results (Alavi and Thompson, 2006). One example is shown in **Figure 6.3**, where consistent results are obtained, with a maximum difference of 25%, which shows the robustness of the current MD simulation. Different sized pure aluminium nanoparticles were simulated, which exhibits a strong size-dependent melting temperature depression due to the increased fraction of loosely bounded surface atoms at reduced dimension. The size-dependent MD simulated melting temperatures are compared with a few other experimental and simulation results (Alavi and Thompson, 2006; Zhurkin *et al.*, 2006), **Figure 6.3**, which shows a good agreement. After the benchmark study, detailed heating and cooling study for nickel-coated aluminium particles are then conducted, as described below.

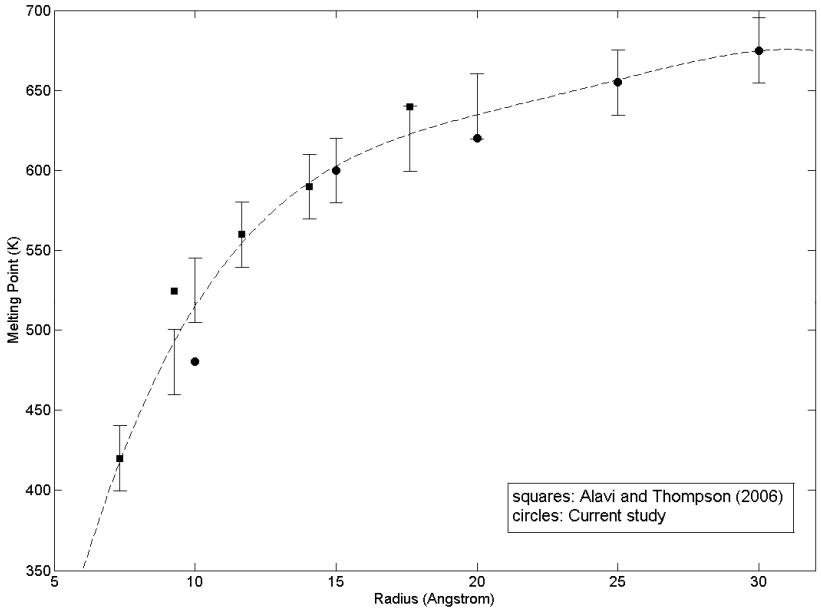

Figure 6.3: Comparison of the melting point of Al particle

A typical particle evolution scenario is shown in **Figure 6.4** for a constant rate of heating of 0.65 K/ps. In the simulation, the whole system is re-centred every five steps and **Figure 6.4** displays the 2-dimensional cross-sectional view cut through the centre of mass. Since the volume of the whole system is constant, these snapshots are taken as radial representations of the whole system. With the increase of temperature, the diffusion is clearly visible with aluminium core atoms diffusing outward and shell nickel atoms diffusing inwards. The composite particle becomes slighted deformed. Aluminium atoms reach the outmost surface of the composite particle at ~750 K, and continue spreading over the surface with the increase of temperature. The process speeds up as the aluminium core becomes molten. At ~1050 K, the surface of the composite particle forms an aluminium-rich layer. More molten aluminium atoms migrate to the outer surface as the temperature increases further. The inward diffusion accelerates as the nickel shell becomes melted. A well mixed liquid aluminium-nickel functional droplet forms at the end of the heating. The outmost region of the liquid particle is Al-rich which is evidenced by the atom distribution (number of atom divided by the region volume) of final

configuration of the heating mode shown in **Figure 6.5**, where the functional particle is uniformly represented by ten layers. However, as the low-energy component, aluminium is not sufficient to seal the surface, which is beneficial for liquid cluster to nucleate during the cooling process.

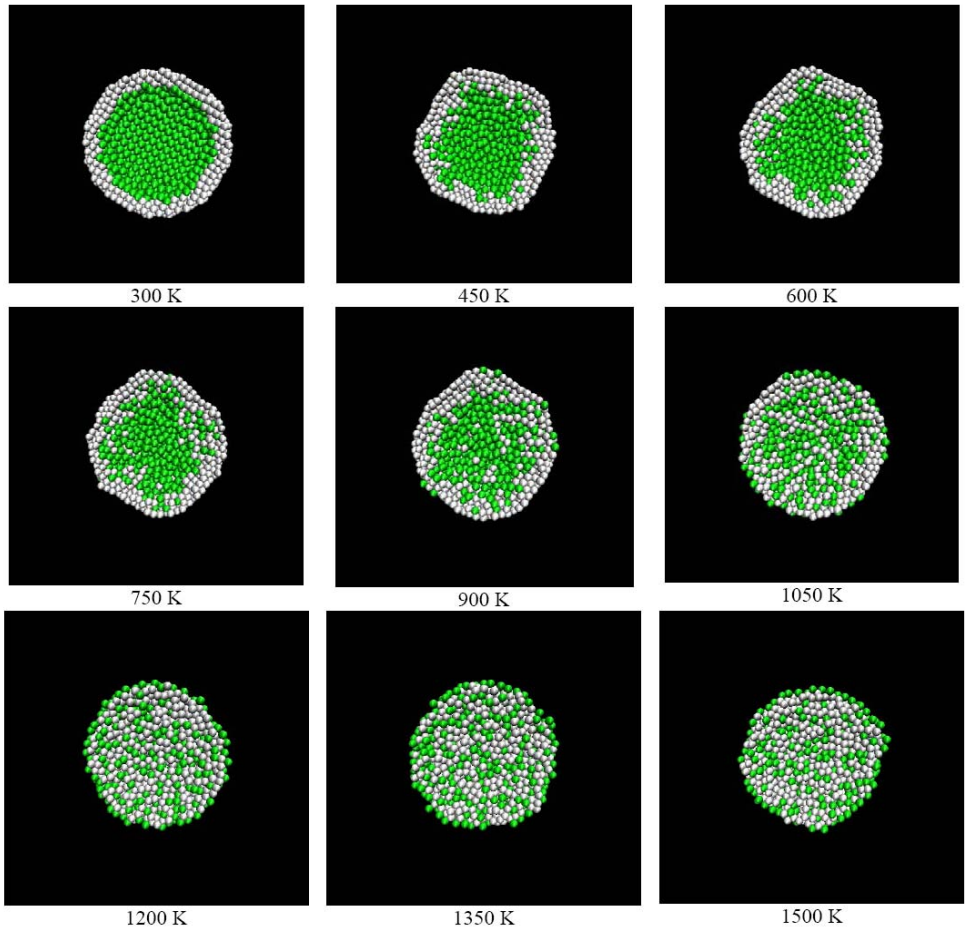

Figure 6.4: Snapshots of the system cross-section under heating

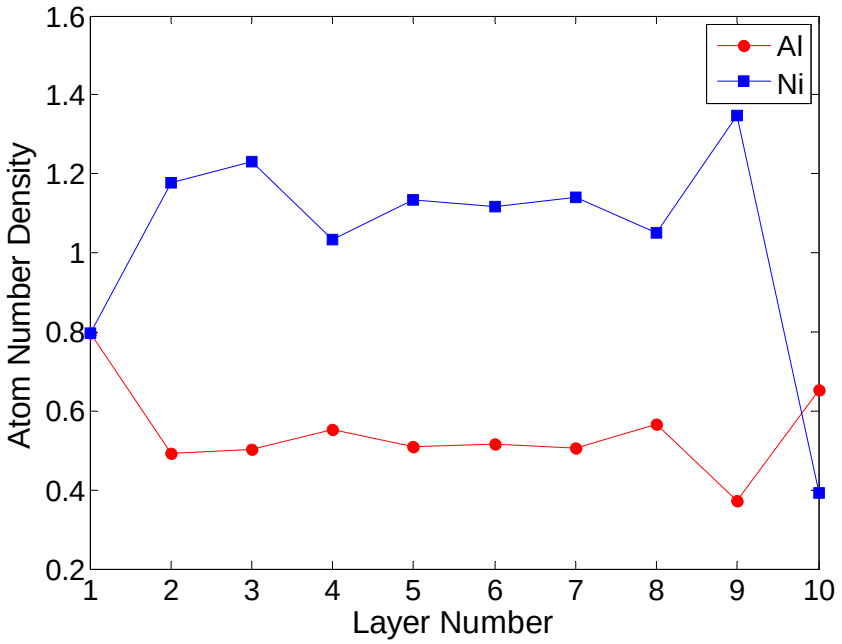

Figure 6.5: Atom distribution in the molten state (*T* = 1600 K)

The profile of potential energy per atom for the composite particle under a constant rate of heating 0.65 K/ps, from 300 K to 1600 K, is reported in **Figure 6.6**. Different to a linear increase followed by an abrupt jump for a pure aluminium particle as shown in **Figure 6.2**, the average potential energy of the composite nanoparticle exhibits a distinct V-shape with the increase of temperature, *i.e.* the composite particle experiences a nearly linear decline of potential energy at low temperatures, reaching to a minimum value at ~1000 K, before a linear increase. Similar behaviour is observed for both nickel and aluminium atoms of the composite particle as shown in **Figure 6.7** and **Figure 6.8**. The minimums for aluminium and nickel atoms are 820 K and 1050 K respectively. The phenomena is believed to be associated with the 'hiccup' profile of temperature and pressure for Ni/Al nanolaminate found by Zhao *et al.* (2006, 2007a, 2007b). It is due to a synergy between the mixing effort of Ni and Al and a disordering effect under continuous heating. Under NVT scheme, the system is undergoing a thermostat and its temperature of whole system increases under heating conditions. At relatively low temperatures, the atomic mobility is increased by the external heat source. Consequently due

to mutual diffusion of two elements and the constraint of a constant whole volume, a two-way movement is caused, *i.e.* nickel atoms move towards the core while aluminium atoms towards the surface. Such a two-way movement introduces the mixing of Ni and Al, which have an exothermic alloying nature. Meanwhile the external heat source keeps solid structural disordering. The released energy will either go towards melting that makes atoms disorder or increasing atomic mobility that elevates the temperature. The V-shape of potential energy, **Figure 6.6**, implies the dominance of melting latent heat. The enthalpy value is calculated directly from its thermodynamic definition of $\Delta H = U + PV$, where U is the total energy, P is pressure and V is volume. The initial potential energy decrease is mainly due to the substitution of Ni-Ni and Al-Al interaction by Ni-Al interaction, which is confined in the fixed volume. Such a scenario is different from the increase in potential energy for pure element where local order of atoms dominates atomic interaction. As the intermixing between Ni and Al is spontaneous driven by a negative ΔH, the enthalpy of this process is a convex function of relative concentration of Ni-Al, which is consistent with other studies (Witusiewicz *et al.*, 2000; Ma, 2005). Clearly the minima in the potential energy are related to the melting phenomena. If taking the temperature at the minimum potential energy as a result of global melting phenomenon, the global melting of the nickel-coated aluminium particle is 1020 K, and the aluminium core is ~820 K and nickel shell is 1050 K. As described previously, the pure bare auminium with the same diameter of the aluminium core, 4 nm, has a melting temperature of 620 K. The core/shell structure hence enhances the thermal stability of the aluminium core.

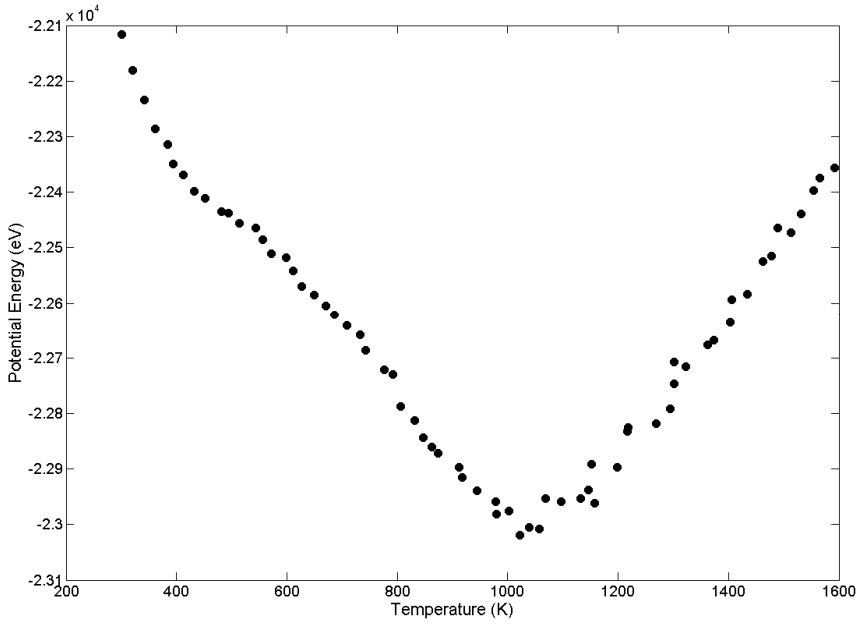

Figure 6.6: Potential energy profile of all atoms under heating

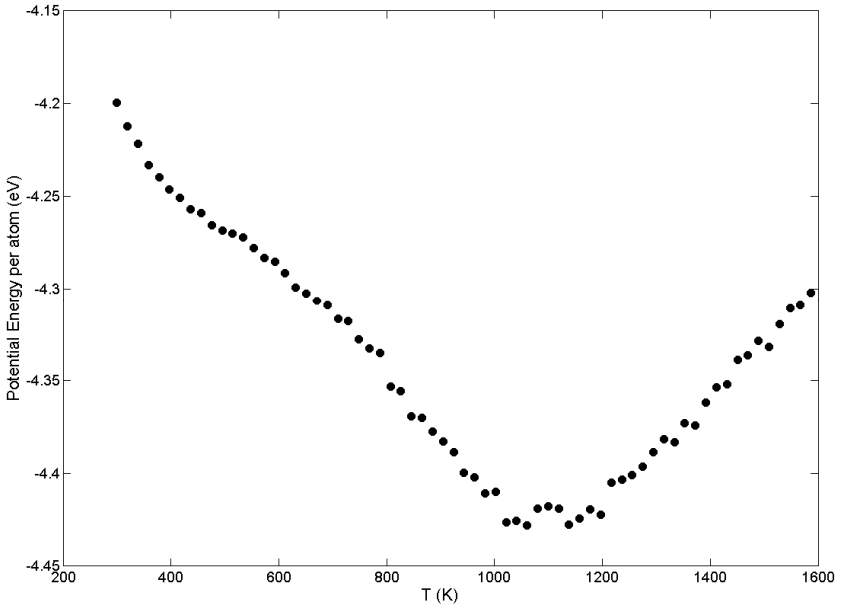

Figure 6.7: Potential energy profile of Ni atoms under heating

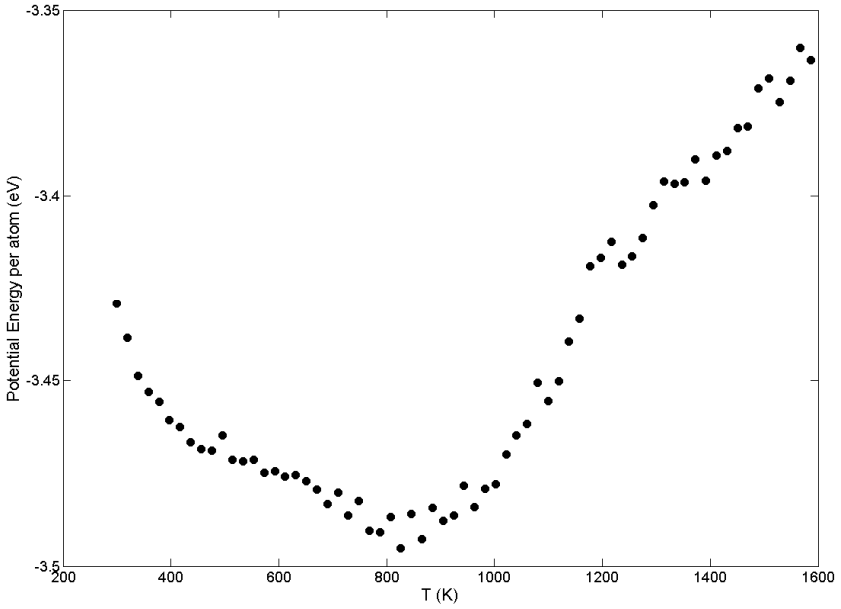

Figure 6.8: Potential energy profile of Al atoms under heating

The minimums for aluminium and nickel atoms are ~800 K and ~1050 K respectively. The decline of the potential energy and other related thermal properties at low temperature is different from that of single-element particles, which is believed to be associated with the volume reduction due to different diffusion capability of nickel and aluminium atoms. Apart from being temperature sensitive, the potential energy is also a strong function of volume. The initial decline of the average potential energy is believed to be correspondent to the contraction of the whole particle, as illustrated by the gyration radius, R_g computed by **Equation 5.20** of the composite particle as shown in **Figure 6.9**. Due to relatively small number of atoms (N = 5636) used in current simulation the volume of system would have some statistical fluctuations. The different atom weight of two elements makes it difficult to accurately estimate volume from the gyration radius. However as estimation, the nominal volume of particle can be calculated from a nominal radius, R_n, which can be related to gyration radius through an empirical equation as

$$R_n = R_g \left(\frac{5}{3}\right)^{0.5} + R_c \tag{6.5}$$

where R_c is the nearest-neighbour atomic distance taken as 2.59 Å for Ni-Al system (Kazanc, 2008).

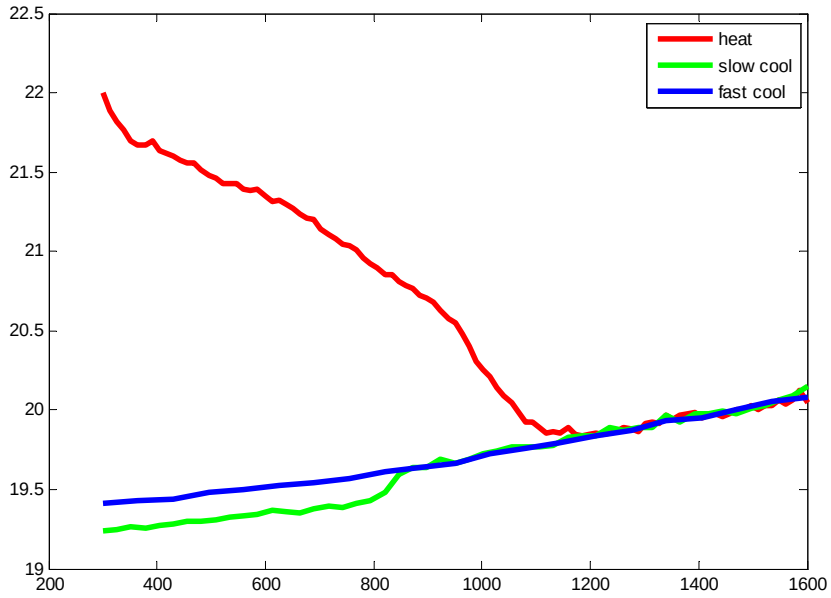

Figure 6.9: Gyration radius of the heating and two cooling processes

Figure 6.9 clearly shows that the gyration radius of the composite particle experiences a first decrease and then increase process with the increase of temperature. The shrinking of the whole particle is believed to be caused by different diffusion capability of nickel and aluminium atoms, as shown by the root mean-square-displacement (RMSD) by tracing atoms at different radial layers, **Figure 6.10**.

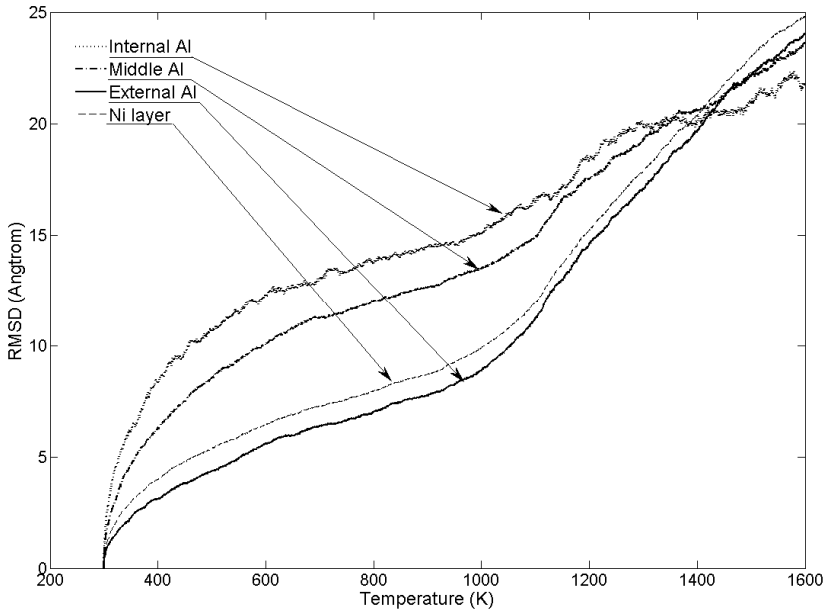

Figure 6.10: RMSD of different layers during the heating process

It clearly shows that the atom mobility varies with elements and layers. The RMSD is based on atom random walk and statistically an opposite diffusion trend is assumed for Ni and Al. The minima of the gyration radius give a good indication when global melting occurs. From **Figure 6.11**, the global melting temperature of the functional particle is identified ~1070 K, which is very similar to that from potential energy analysis. Of note that the external aluminium layer, which is located at Ni-Al interface, has similar magnitude of RMSD with nickel layer atoms in its vicinity. This is likely to be ascribed to the effect of atoms in the regime of Ni-Al interface.

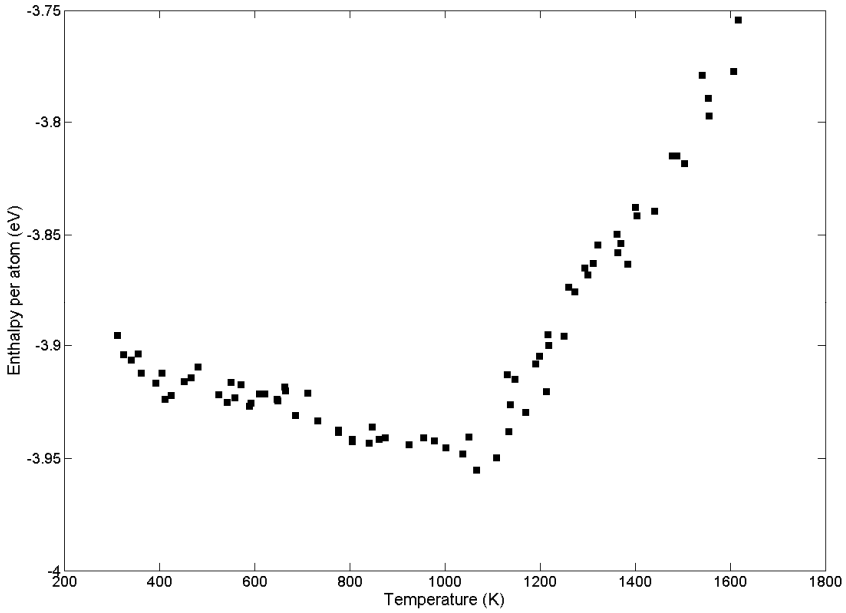

Figure 6.11: Enthalpy profile of Ni-Al system during the heating process

During the heating process, the internal pressure is building up with the increase of temperature and the maximum is obtained around the global melting temperature, **Figure 6.12**. The local stresses are calculated by averaging the per-atom stress tensor in a group over a 2.0 ps interval, which shows a large variation over the temperature i.e from 0.38 GPa to 0.02 GPa. The per-atom stress tensor for each atom has a general form shown as the equation below (Plimpton *et al.*, 2010)

$$S_{ab} = -[mv_a v_b + \frac{1}{2}\sum_{n=1}^{N_p}(r_{1a}F_{1b} + r_{2a}F_{2b}) + \frac{1}{2}\sum_{n=1}^{N_b}(r_{1a}F_{1b} + r_{2a}F_{2b}) + \frac{1}{3}\sum_{n=1}^{N_a}(r_{1a}F_{1b} + r_{2a}F_{2b} + r_{3a}F_{3b}) + \frac{1}{4}\sum_{n=1}^{N_d}(r_{1a}F_{1b} + r_{2a}F_{2b} + r_{3a}F_{3b} + r_{4a}F_{4b}) + \frac{1}{4}\sum_{n=1}^{N_t}(r_{1a}F_{1b} + r_{2a}F_{2b} + r_{3a}F_{3b} + r_{4a}F_{4b}) + \sum_{n=1}^{N_f} r_{i_a}F_{i_b}] \quad (6.6)$$

where *a*, *b* take on values *x*, *y*, *z* to go through the 6 components of symmetric tensor: *xx*, *yy*, *zz*, *xy*, *xz* and *yz*. The first term is a kinetic energy contribution for atom *i*. The second term is a pairwise energy contribution

where n loops over the N_p neighbours of atom i, r_1 and r_2 are the positions of the two atoms in the pairwise interaction, and F_1 and F_2 are the forces on the two atoms resulting from the pairwise interaction. The third term is a bond contribution of similar form for the N_b bonds which atom i is part of. There are similar terms for the N_a angle, N_d dihedral, and N_i improper interactions atom i is part of. Finally, there is a term for the N_f fixes that apply internal constraint forces to atom i. For the case of metal system, only the first three terms are included.

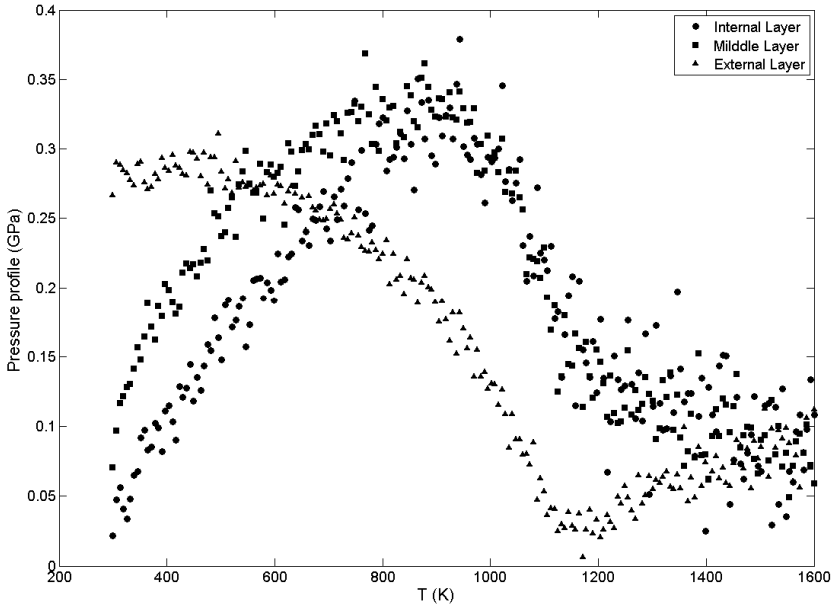

Figure 6.12: Pressure profile for different regimes of Al core

The pressure peak of the inner aluminium occurs at 950 K, just before the defined 'global melting point' of 1000 K. Consecutively the pressure declined to reach a plateau of 0.1 GPa. Compared to other studies, *i.e.* 1.0 GPa pressure for a 10 nm-radius aluminium core wrapped in alumina (Campell, 2005), and a Ll_2 2315-atom Ni_3Al cluster displayed a pressure up to 5 GPa (Zhurkin, 2006), the MD calculated values are quite small. As shown in **Figures 6.6-6.8**, the migration of molten Al atoms into the solid nickel shell is initiated before global melting of core, and meanwhile the melting of Ni of 0.5 nm in thickness occurs near 1000 K, close to the whole melting point. At temperatures higher than the global melting temperature,

both the core and shell are in molten status, which would not produce a high pressure. The competition between alloying reaction and melting, as discussed previously, will ease the pressure increase associated with the phase change. So it is believed that the pressure peak is due to the maximum thermal expansion of solid atoms where the functional particle has shrinking tendency to its minimum volume, just before the global melting, and the decreasing pressure is associated with global melting process.

6.3.2 Solidification simulation

The solidification simulation continues after heating the composite particle to 1600 K. Since a long time heating (400 ps) has been performed, a sufficient mixing of aluminium and nickel atoms is obtained. An additional relaxation time of 40 ps at 1600 K is conducted before implementing the cooling process. Cooling rates from 6.5 K/ps and 0.13 K/ps were studied.

The average potential energy per atom for two cooling rates is shown in **Figure 6.13**. With the decrease of temperature, the fast cooling rate results a smooth decrease of the potential energy, which results in a glassy phase formation. The slow cooling simulation produced an abrupt decrease in the potential energy, beginning at 900 K and finishing at 800 K, a clear indication of the formation of crystal structure. Together with the heating case, the variation of the gyration radius is shown in **Figure 6.9**, which correlates well with the melting studies as in the heating case.

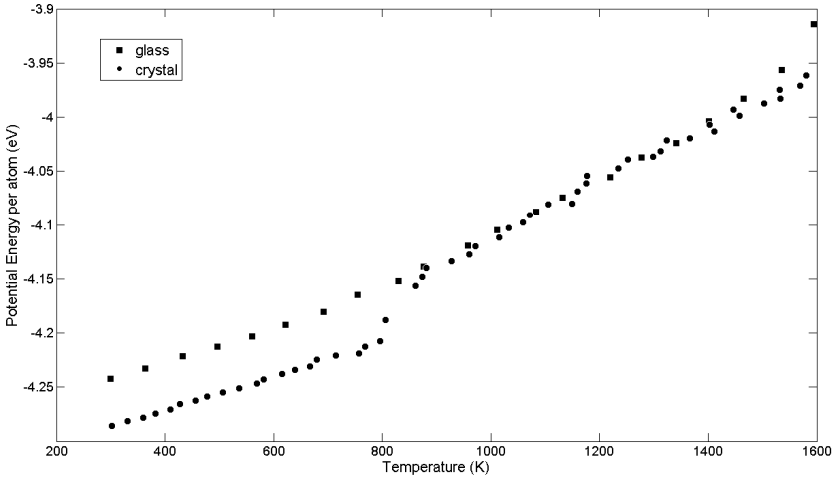

Figure 6.13: Potential energy profile under two cooling rates

Radial Distribution Functions (RDF) are employed to monitor particle structure evolutions during the simulation, Radial distribution function describes the structural correlation of how the atomic density varies as a function of the distance from one particular atom, which provide an statistical estimation on material local structure. Its general form in spatially homogeneous systems is (Rapaport, 2004),

$$g(r) = \frac{2V}{N_m^2}\left\langle \sum_{i<j} \delta(\vec{r} - \vec{r}_{ij}) \right\rangle \tag{6.7}$$

where N_m is the numbers of total atom of interest, V is the volume of the atom assembly. The RDF is shown in **Figure 6.14 (a)** and **(b)** for two cooling cases.

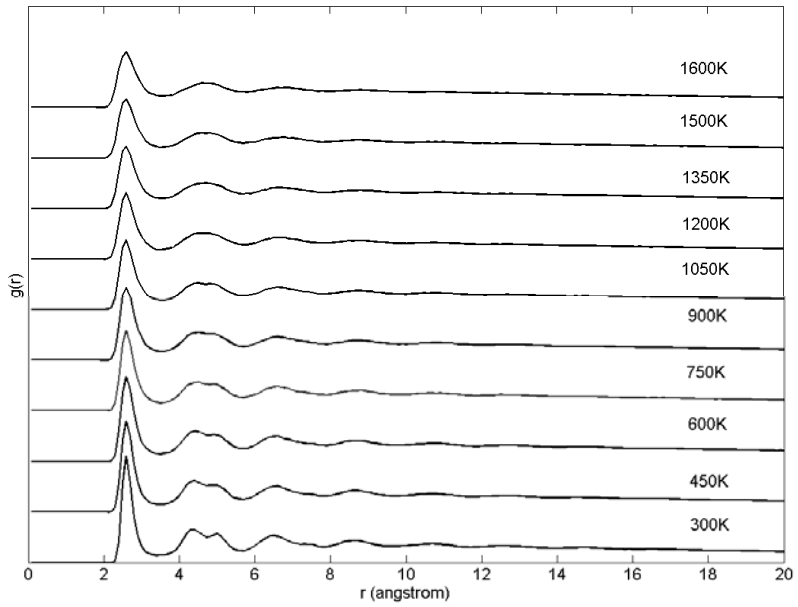

(a) cooling rate of 6.5 K/ps

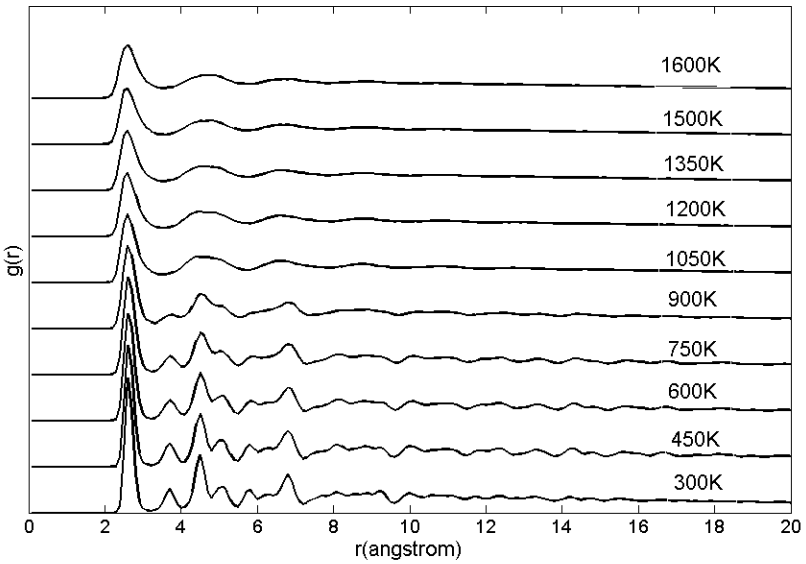

(b) cooling rate of 0.13 K/ps

Figure 6.14: RDF of the functional particle under two cooling rates

For the quenching simulation, the RDF peaks, whose height and positions reflect the local order of structure, increase as the temperature decreases. For the cooling rate of 6.5 K/ps, the second peaks are not remarkable at high temperatures above ~900 K. Below ~900 K, more peaks besides the primary

peak start to emerge and grow. A split of the second peak into two sub-peaks occurs at ~600 K, which is an indication of the glass phase formation (Tsumuraya *et al.*, 1988). The sub-peaks develop subsequently with the decrease of temperature. The glass formation during fast quenching is also reflected by its thermodynamics properties, i.e the decrease of the average potential energy and gyration radius linearly without an abrupt change as shown in **Figure 6.13**.

A typical glass state is also visible in the final snapshot of the quenching shown as **Figure 6.15**. Wendt and Abraham (1978) proposed an empirical criterion for the onset of amorphous glass by defining the parameter, $R_{WA} = g_{min}/g_{max}$, where g_{min} and g_{max} denote the magnitudes of the first minima and the first maxima of RDF. $R_{WA} = 0.14$ is the threshold value of onset of glass phase. Based on such a criterion, the glass formation temperature is derived as $T_g = 579$ K.

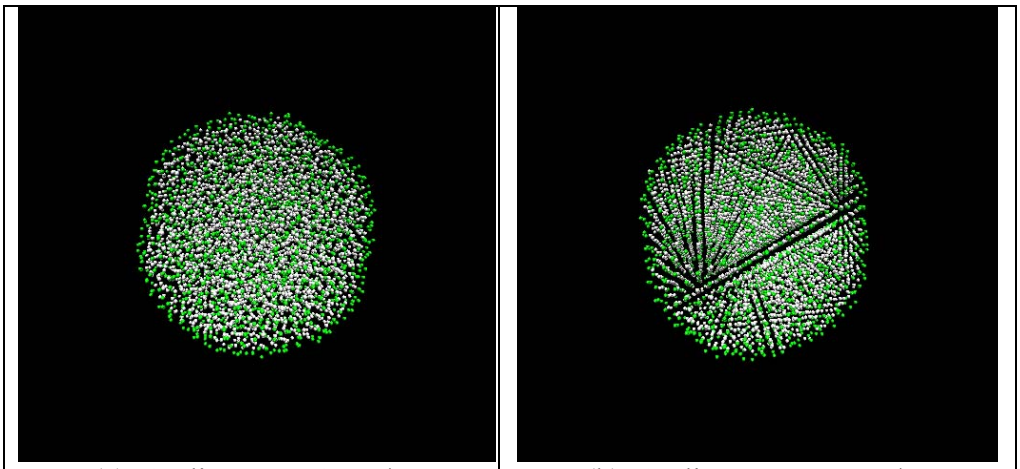

(a) Cooling rate, 6.5 K/ps (b) Cooling rate, 0.13 K/ps

Figure 6.15: Snapshots of the products at two different cooling rates

To reveal the elemental atom distribution during solidification, radial atom number density is plotted in **Figure 6.16** and **Figure 6.17**. At the outmost layer, *i.e.* 10th layer, the atomic number density of aluminium is higher than that of nickel, resulting in an Al-rich surface while at all the other layers the number density is one time bigger. Surprisingly, the molten atom

distribution shown in **Figure 6.16** is not kept in the glass phase caused by fast cooling. The glass phase is sometimes referring a 'frozen amorphous phase' in which the liquid-like atom structure is retained with solid-like atomic mobility. The result displays that during fast cooling process, the atoms can move far enough to have a structure rearrangement. Further study also proved that the glass transition is an extremely fast process, almost instant at glass transition point.

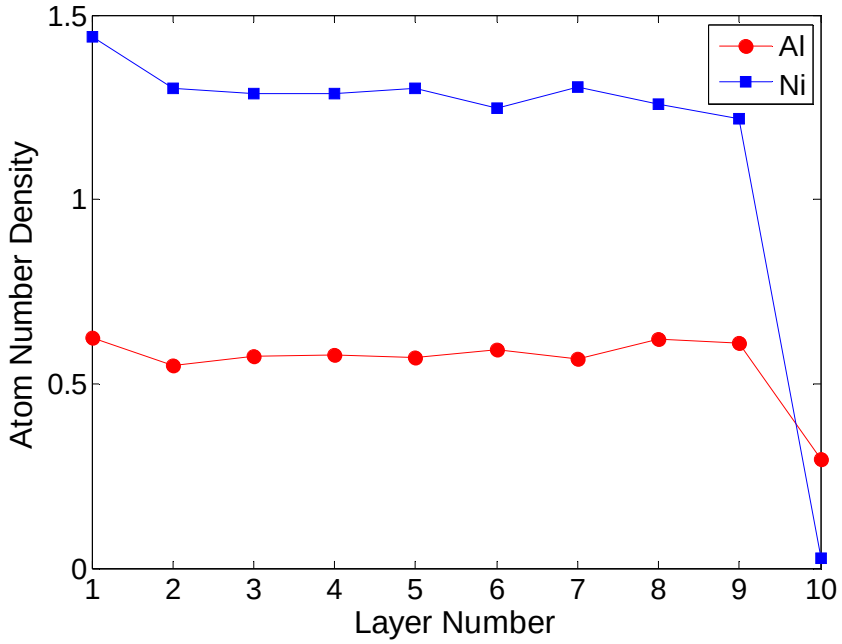

Figure 6.16: Atom distribution in glassy cluster (*T* = 300 K)

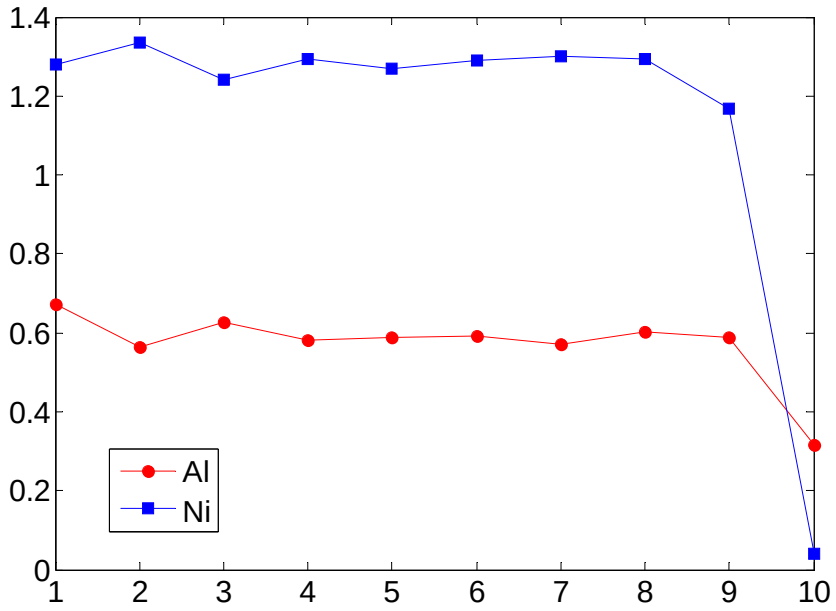

Figure 6.17: Atom distribution in crystallized cluster (*T* = 300 K)

For the slow solidification of 0.13 K/ps, RDF displays features of transition from amorphous liquid to ordered crystal. The solidification point is clearly identified at 900 K by the abrupt decrease of potential energy and gyration radius, **Figure 6.9**. RDF profile shown in **Figure 6.14** illustrates detailed phase evolution during the quench process. The first RDF peak location on the curve corresponds to the nearest interatomic distances which is estimated as 2.59 Å at 700 K in this study. The location of the second peak, which corresponds to the alloy lattice parameter, is found to be 2.9 Å, which agrees very well with the experimental result of 2.88 Å (Miracle, 1993). This proves that the final structure is Ll_2 martensite, NiAl, a FCC crystal. The RDF profile is also in good agreement with the others for Ni-Al alloy under periodic boundary conditions (Kazanc, 2008). Based on the phase diagram of Ni-Al, the phase of $Ni_{3620}Al_{2016}$ at 700 K appears to be mainly in the form of Ni_5Al_3. However different to Kazanc's result (2008), there is no autensite phase found during the quench process, which might be caused by insufficient time of nucleation in the relatively short cooling. From the RDF profile, it shows that the martensite nucleated directly from the molten liquid. It was believed that the difference is caused by different atom distribution at nanoscale. A detailed structure analysis is conducted below.

To reveal the structural information of local order degree, Honeycutt-Andersen (HA) pair analysis is adopted here (Honeycutt and Andersen, 1987).

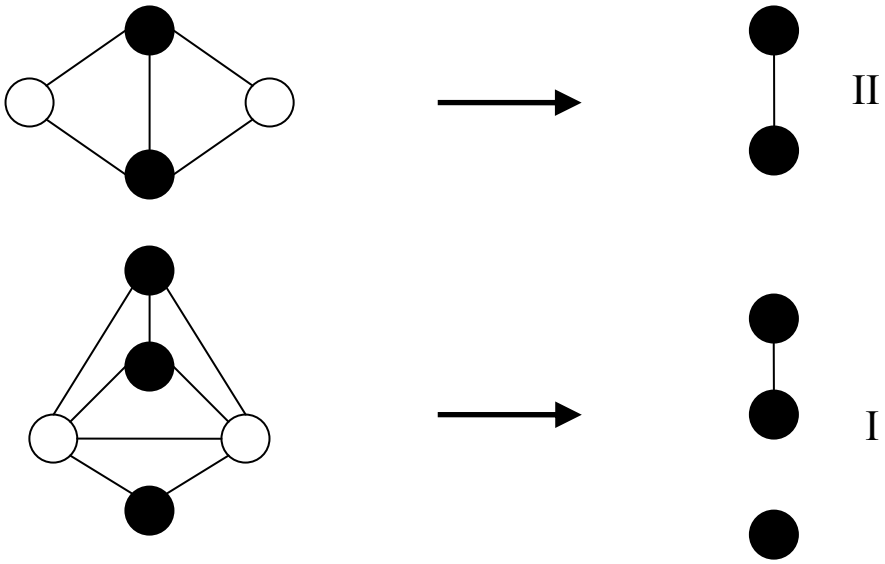

Figure 6.18: Diagrammatic nomenclature for HA pair analysis
(Redrawn from Honeycutt and Andersen, 1987)

In this technique pairs of atoms are classified (i) whether they are near-neighbours, (ii) the number of near-neighbours they share and (iii) the relationship among the shared neighbours. With the classification the atomic pairs can be represented by four integrals. **Figure 6.18** and **Figure 6.19** representing the graphical diagram are shown here.

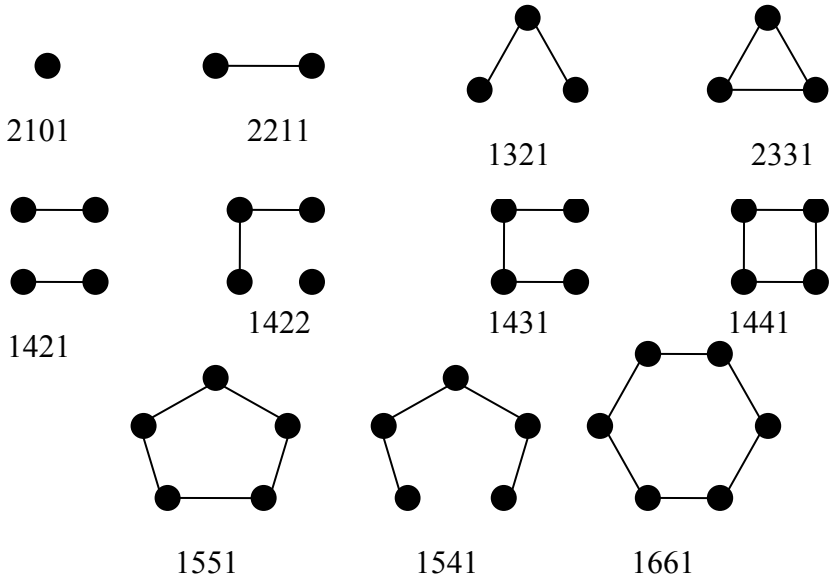

Figure 6.19: Common diagrams in dense atomic systems
(Redrawn from the paper of Honeycutt and Andersen, 1987)

In **Figure 6.18**, white circles represent the atoms under study, *i.e.* root pair, while black circles are the near-neighbours that root pair has in common. Once the distance between atoms are below the determined cut-off, the atoms are taken as 'bonded' and connected by lines. For the brevity, the white circles are eliminated in **Figure 6.19**, with understood presence. The pairs were put into two categories: if the pair root atoms are connected by a 'bond', they are labelled as type *I*, or type *II* if they are not. The first three integers of HA index are characterized as 'type number', 'numbers of near-neighbours shared by the root pair', 'numbers of bonds among the shared neighbour atoms'. The three integers are not sufficient to categorize the bonds uniquely, a fourth integer, whose value is arbitrary as long as it is used consistently, is added to assign the bond diagram a unique index.

When local structures are described by the HA bond-type index, 1551, 1541, and 1431 bond-types are characteristics of typical liquid and amorphous configurations; 1661 and 1441 bond-types are characteristics of BCC crystals; and 1421 bond-type is the characteristics of one of the FCC crystals, while for a hexagonal close-packed (HCP) crystal, the

characteristic bond-types are the 1421 and 1422 ones. In the calculation, the bond distances are obtained from the first minima of the corresponding RDF as 3.5 Å (Tsumuraya, 1988). In this study, no trace of 1422 bond is found, and so all 1421 bonds are counted as FCC. For the convenience of discussion in this paper, the two bond-types of 1441, and 1661 are referred to as body-centred cubic (BCC) and other three bond-types of 1551, 1541, and 1431 are categorized as 'amorphous'. The percentages of HA bonds to bonded atom pairs during solidifications of two cooling rates are shown in **Figure 6.20** and **Figure 6.21**.

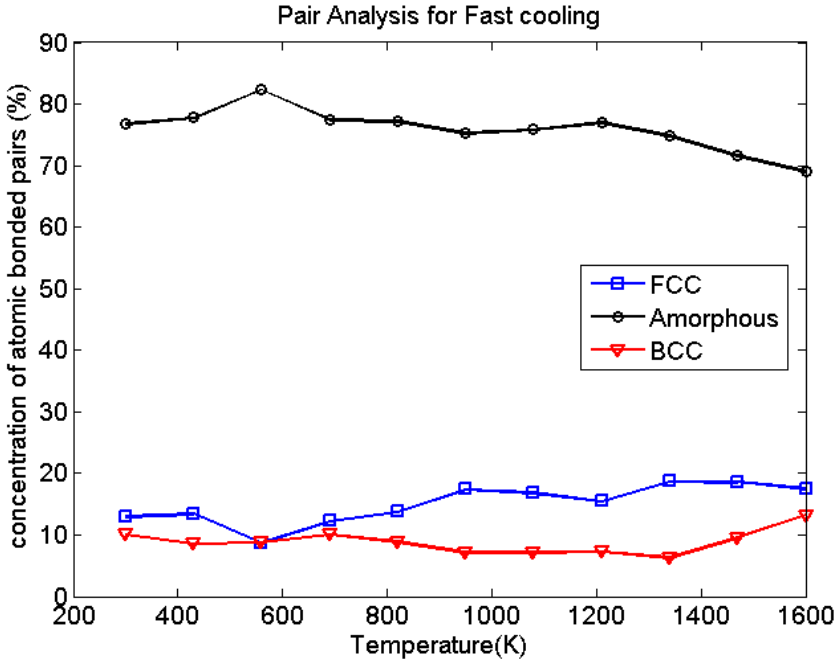

Figure 6.20: Pair analysis for the fast cooling

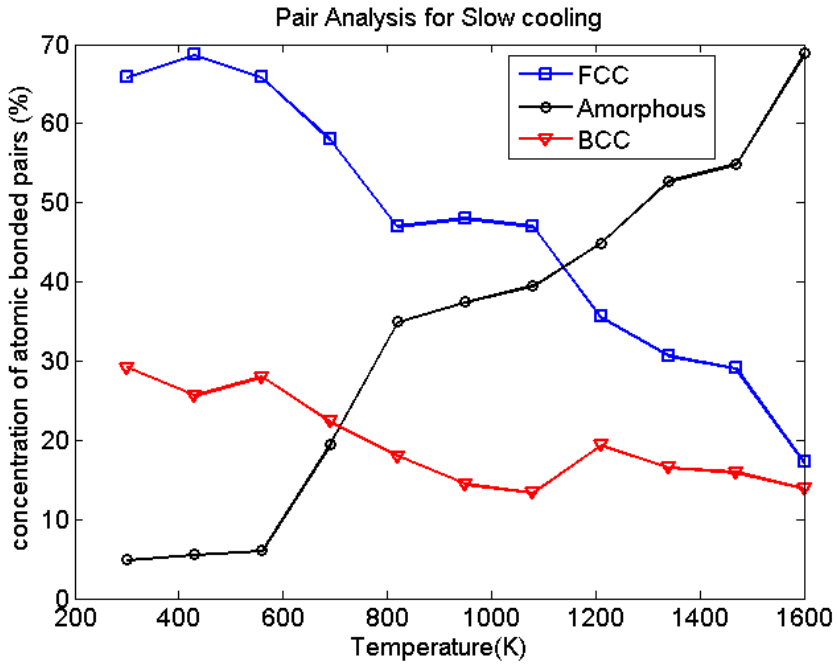

Figure 6.21: Pair analysis for the slow cooling

For the fast cooling rate, the bonds of all three types appear in the liquid state, in which the amorphous bonds prevail accounted to 70% of bonded atoms. It is noticeable that some ordered FCC and BCC already exist in liquid phase at 1600 K. The relative concentrations of all three bonds remain little changed during the solidification process. The amorphous bonds grow slightly from 70% to 75%, and there are slight concentration decreases for both FCC and BCC crystals. However different features are observed for the slow cooling rate. The initial concentration of all three bonds of slow cooling rate is similar to that of the fast one. Amorphous bonds decrease continually as the temperature decreases. An abrupt dropping occurs at 800K, which is in agreement with the the solidification point, reflecting the liquid-solid transition. Notably stable FCC bonds exist in liquid before the nucleation of solidification begins, which are thought to be transformed from the metastable BCC (ten Wolde, 1992). As the solidification is finished, the amorphous bonds disappear and a mixed crystal structure of FCC and BCC are generated.

According to the bulk Ni-Al phase diagram (Muto, 1993), for alloys with ratio of Al to Ni between 0.35 and 0.37, the face-centered tetragonal structure, $L1_0$ martensitic phase, prevails. However in this simulation, no $L1_0$ stable phase is observed at low temperature. This is consistent with the previous results at 1000 K in use of EAM force filed (Foiles, 1987). Although RDF only shows mono-structural for the composite particle, the structural homogeneities are not achieved. BCC bonded atoms were also found to be distributed quite uniformly among the particle, no particular preference site to form, which suggests a homogenous nucleation occurs. If the BCC bonded atoms are considered to be nuclei of austenite, the final structure would be a mixture of Ll_2 and a minor concentration of austenite nuclei finely distributed in the particle. The composition distribution and intermetallic structure cause distinct features in oxidation. In the bulk Ni_3Al alloy, Ni-oxides such as NiO and $NiAl_2O_4$ dominate the oxidation products, while $NiAl_2O_4$ will gradually decompose to NiO and Al_2O_3 at 1073 K (Lee, 2002). In Ni-rich Ni-Al alloys, the selective oxidation of Al causes formation of α-Al_2O_3 and NiO (Kim *et al.*, 2003). Meanwhile NiAl has excellent oxidation resistance, considered as potential candidate for coating material of Ni_3Al due to their chemical compatibility (Kim *et al.*, 2005). An atomic MD simulation also revealed that the oxidation rates for Ni-Al alloys decrease with the increase of Ni composition (Sankaranarayanan and Ramanathan, 2008). Though the comparison of oxidation resistence of different phases was not done in this work by MD, the found Ni_3Al at surface is a preference phase over NiAl which should be avoided for oxidative application in the core-shell structure and fewer nickel contents are favourable for oxidation by making the Ni coating relatively thinner compared with Al core.

6.4 Chapter Summary

The heating and cooling of a shell-core structured Ni-Al composite nanoparticle is conducted in this work based on a molecular dynamics simulation. Some unique behaviour is observed. Two way diffusions for

both aluminium and nickel atoms are observed during the heating simulation, which results in an initial contraction of the composite particle at low temperature. With further increase in temperature, the aluminium core becomes molten. The outward diffusion of aluminium atoms forms an alloy particle with a rich layer of aluminium on the surface. The potential energy and enthalpy of the composite particle exhibits a unique V-shape during the heating process, which is associated with the two-way diffusion of the nickel and aluminium atoms and the subsequent volume change. The global melting point of the nickel-coated aluminium composite particle is identified at 1000 K. The melting point of aluminium core can be enhanced by the shell of nickel from 620 K up to 800 K. The cooling rate significantly affects the final phase formation. A glass phase is formed for a fast cooling rate of 6.5 K/ps, with a glass transition temperature of 600 K. For a slow cooling rate of 0.13 K/ps, a crystal structure of Ll_2 Ni_3Al is formed beginning at 800 K. The detailed pair analysis shows that the slow solidification process produces a mixture of FCC and BCC crystals with only traces amorphous pairs. No austenite-martensite transition was observed. The final structure is non-uniform Ll_2 Ni_3Al wrapped by an Al-rich shell, which is dependent upon the initial Al-Ni composition and constraint geometry at nanoscale.

Chapter 7

Numerical Study of Oxidation of Silicon Nanoparticle

7.1 Introduction

The previous chapters were concerned on two sets of studies: thermal analysis on oxidation and non-reactive MD simulation. Using silicon as an example, this chapter will bring both together in effort to illustrate an oxidation picture with atomic details. As the foundation of information technology, modern silicon microelectronics comes into nanoscale regime where the conventional standard engineering tools reached their failure limit. The increasing demand of integrated circuits, data storage device and fuel cell requires the studies of oxidation of silicon materials and relevant thermal management at nanoscale. Silicon nanoparticles are also potential candidate of energy carriers due to their redundancy, high energy density and stable thermal and chemical properties, which raise the interest of oxidation investigation of silicon at nanoscale dimension. First principle computational methods including *ab initio*, density functional theory (DFT), quantum mechanics/molecular mechanics (QM/MM) have successfully revealed insightful physical and chemical details of silicon material (Torre *et al.*, 2002; Tu and Tersoff, 2002; Bongiorno and Pasquarello, 2004, 2006). However, these studies mainly focused on quantum-related properties, which are electron-dependent at a level of dozens of atoms. There is a need of simulation aiming at energetic properties under various chemical environments at nanoscale. Chemical reactivity involving formation and dissociation of bonds are numerically described by first principle methods in which the geometries, thermal energies, and vibrational energies can be predicted very accurately for small molecules or atom clusters. The complex multi-body interaction of electrons is the root cause of high computation

cost of such methods. For a typical nanoscale reaction consisting of millions atoms and their associated electrons the enormous demand on the first principle computation will push today's most powerful computer to the edge, making it impractical for simulation of nanoscale materials. Moreover, the integration and coupling of obtained information from first principle into measured macroscopic properties face several theoretical chanllenges (Lyubartsev *et al.*, 2009). Experimentally, the cost of managing strongly exothermic reaction is also high in term of instrument and preparation. Additionally many practical thermal effects during experiment may disturb the accurate estimation of properties of interest in oxidation, combustion and ignition. By contrast, multi-million to billion atomic systems refelecting nanoscale reality have been successfully conducted by non-reactive MD on supercomputers (Vashishta *et al.*, 2003; Kadau *et al.*, 2006). These difficulties and notable advantages of MD urge the alternative approach of MD-like empirical force fields (FF) that can implement bond-order-dependent reactions with sufficient accuracy. Some bond order force fields such as DREIDING, UFF, Brenner FF, REBO, AIREBO and Tersoff FF are developed aiming at this object (Tersoff, 1986; Brenner, 1990; Mayo *et al.*, 1990; Rappe and Goddard III, 1991; Cornell *et al.*, 1995). However, neither tailored FF for particular material and chemical reaction, though some of which are remarkably successful on some particular chemical processes, which can adequately address the full chemistry of the breaking and forming of bonds of different elements into a consensus general form.

Reactive Force Field (ReaxFF), developed in California Institute of Technology by van Duin *et al.* (van Duin *et al.*, 2001; van Duin, 2009) provides a atomic level, full-chemistry, and full-physics description of energetic processes of materials without any assumptions or simplifications other than those intrinsic to the FF description of the interactions, in a similar way to that of classical non-reactive FF. Such molecular level character is essential for the development of predictive, physics-based materials models. ReaxFF has covered broad elements in periodic table

including Al, B, Ba, Bi, C, Cl, Co, Cu, F, Fe, H, Li, Mg, Mo, N, Na, Ni, O, Pt, Ru, S, Sb, Se, Si, Ti, W, Y, Zn and Zr. It aims to include more elements in future development. ReaxFF in recent years development has enabled, for example, the simulations with QC-comparable accuracy of the thermal- or shock-induced decomposition of energetic materials under realistic loading conditions, oxygen ion transport in fuel cell, grain boundary proton diffusion, oxidative dehydrogenation, melting and crystallization of aluminium, catalysis of nickel, dynamic transition in the shock structure of an energetic crystal, catalytic selective oxidation processes, self-assembly of silica nanocages, and dynamical crack propagation in silicon (Strachan *et al.*, 2005; Goddard III *et al.*, 2006; Buehler *et al.*, 2006b; Nomora *et al.*, 2007; Su *et al.*, 2007; Chenoweth *et al.*, 2008; Ning *et al.*, 2008; Ojwang *et al.*, 2008; van Duin *et al.*, 2008a, 2008b). The ReaxFF also displays its profound capability of simulating mesoscale phenomena (Buehler *et al.*, 2006a; Nakano *et al.*, 2008).

The total energy of ReaxFF is divided by different potential contributions (van Duin *et al.*, 2003).

$$U_{system} = E_{bond} + E_{vdWaals} + E_{Coulomb} + E_{val} + E_{tors} + E_{over} + E_{under} \tag{7.1}$$

Allowing bonds to break and form during simulations, ReaxFF does not assign chemical bonds or predefine connectivity to atoms before dynamic moves deployed. All the partial potential function is designed to be atomic coordinates dependent. The key parameter is bond order between atom *i* and *j*, BO_{ij}', that is directly calculated from the sum of σ ('single bond'), π ('double bond') and $\pi\pi$ ('triple bond') bond orders from the equation below

$$\begin{aligned} BO'_{ij} &= BO'^{\sigma}_{ij} + BO'^{\pi}_{ij} + BO'^{\pi\pi}_{ij} \\ &= \exp\left[p_{bo,1} \left(\frac{r_{ij}}{r_0^{\pi}} \right)^{p_{bo,2}} \right] + \exp\left[p_{bo,3} \left(\frac{r_{ij}}{r_0^{\pi}} \right)^{p_{bo,4}} \right] + \exp\left[p_{bo,5} \left(\frac{r_{ij}}{r_0^{\pi\pi}} \right)^{p_{bo,6}} \right] \end{aligned} \tag{7.2}$$

where r_{ij}, is the atomic distance, r_0 is the equilibrium bond length, p with subscript is the adjusting unitless parameters whose value changes with atomic distance.

Because it is directly associated with bond break and formation, bond energy potential is detailed presented as

$$E_{bond} = -D_e^{\sigma} BO_{ij}^{\sigma} \exp\left[p_{be,1}(1-(BO_{ij}^{\sigma})^{p_{be,2}} \right] - D_e^{\pi} BO_{ij}^{\pi} - D_e^{\pi\pi} BO_{ij}^{\pi\pi} \qquad (7.3)$$

All parameters in **Equation 7.2** and **7.3** are listed in **Table 7.1-7.3**, in which of note that there is no existence of $\pi\pi$ ('triple bond') in Si-O system.

Table 7.1: Bond radius parameters

atoms	r_0^{σ} (Å)	r_0^{π} (Å)
Si-Si	2.013	1.563
Si-O	1.610	1.294
O-O	1.169	1.020

Table 7.2: Bond order parameters

bond	$p_{bo,1}$	$p_{bo,2}$	$p_{bo,3}$	$p_{bo,4}$	$p_{bo,5}$	$p_{bo,6}$
Si-Si	-0.069	7.94	-0.20	7.54	n/a	n/a
Si-O	-0.519	4.45	-0.37	4.26	n/a	n/a
O-O	-0.161	5.66	-0.25	6.52	-0.16	10.51

Table 7.3: Bond energy parameters

bond	D_e^{σ} (kcal/mol)	D_e^{π} (kcal/mol)	$p_{be,1}$	$p_{be,2}$	$p_{be,3}$
Si-Si	113.8	54.0	0.25	0.26	0.07
Si-O	193.1	41.1	-0.21	0.92	0.77
O-O	118.9	42.8	0.91	0.86	0.86

All of the covalent interactions including E_{val} and E_{tors} dealing with bond angles and torsion angles are expressed in similar analytical forms of bond orders. The bond orders are corrected by E_{over} and E_{under} once the bonds are overcoordinated or undercoordinated. Totally there are 148 parameters in ReaxFF for Si-O system describing total energy potential and the entire related equations and full paramters were described in detail among references (van Duin *et al.*, 2001, 2003, 2008a, 2008b; van Duin, 2009).

In this chapter, the oxidation process is studied for silicon cluster in terms of bonding configuration based on atomic coordinates and bonding list. The study is used to justify the feasibility of ReaxFF force field as a benchmark for further oxidation investigation at scaled-up dimension. This study does not tend to go deeper into chemical details than quantum chemistry (QC), but to present the FF's ability of reproducing thermal and chemical behaviours in interest of engineering aspects.

7.2 Simulation Methods

The simulation was performed in a three dimensional cell box. Each dimension was measured as 54.31 Å in length. The silicon cluster was placed in the centre of the box containing 184 atoms. The same amount of oxygen molecules, 184 O_2, was located in the rest space of the simulation box. Initially the silicon cluster was trimmed from the silicon crystal's face-centered diamond cubic structure with a lattice spacing of 5.43071 Å. The oxygen molecules were arranged in a simply spatial order in which a minimum displacement between molecules is deployed shown in **Figure 7.1**. An optimization was deployed for oxygen molecules to assure that no atom overlapping was caused. Periodical boundary conditions were constructed in all three dimensions. The time step was set as 0.25 fs. Minimization processes were employed on the silicon cluster and oxygen molecules separately and an additional annealing process was conducted for the silicon cluster to produce a more stable configuration shown in **Figure 7.2**. During

the annealing process, the potential energy of the silicon cluster in the cell box without O_2 was minimized and then equilibrated at 300 K in NVT for 50,000 iterations. After equilibration, the temperature was lifted to 1750 K and kept at that temperature for 5000 iterations with subsequent gradual cooling for 100,000 iterations. The silicon configuration after annealing had been changed derivatively from spherical geometry shown as **Figure 7.2**. The O_2-gas was added into the simulation box with the Si-O bonding interaction switched off. The whole system was then minimized to remove any bad residual contacts, during which a root mean square force threshold, 2.0 kJ/mol·Å, was set during minimization. Then the full system was ready for equilibration. After being equilibrated for 5000 iterations in NVT, the entire system of O and Si was ready for subsequent simulation. The simulation was initiated by assigning Boltzmann distribution of velocities at 300 K. The simulation was set into heating temperature regime of 300-3000 K, and lasted 2,000,000 iterations leading to a nominal heating rates, 1.08×10^{13} K/s.

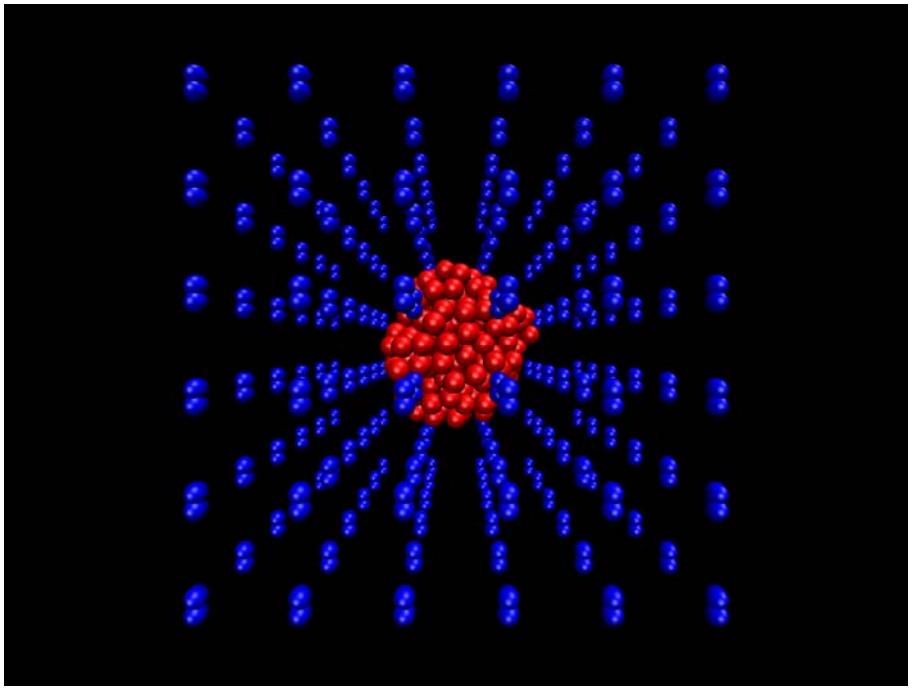

Figure 7.1: Initial configuration of Si-O system
(Si atoms in red and O atoms in blue)

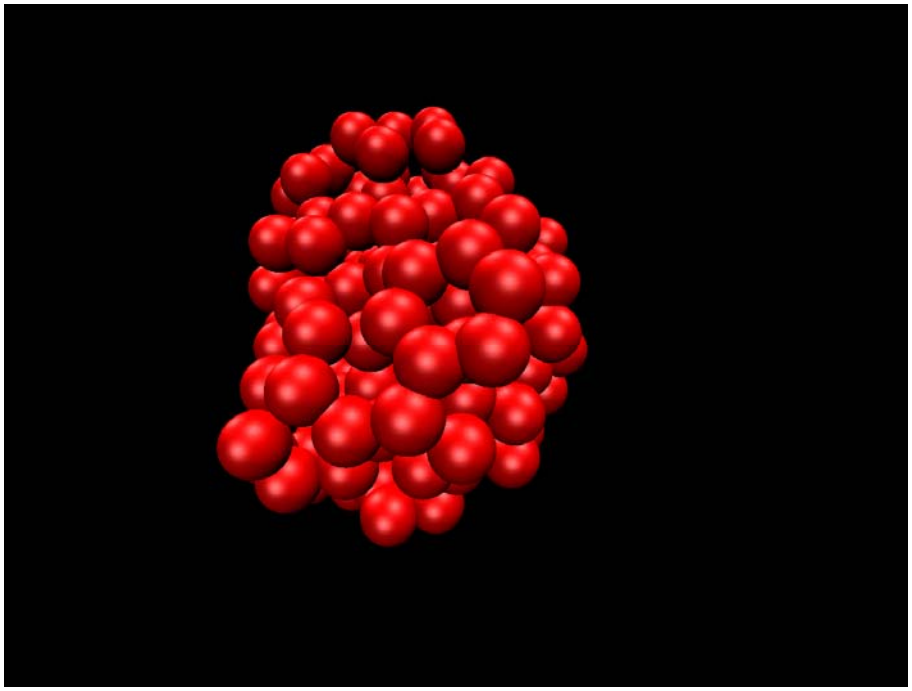

Figure 7.2: Stable configuration of silicon cluster after annealing

7.3 Released Energy

An exothermic process is indicated by the declining of potential energy of the whole system during a heating process illustrated in **Figure 7.3a**. Correspondingly the oxygen molecules are bonded into silicon cluster shown in simulation snapshots of **Figure 7.4**. Usually the heating process will increase the potential energy since the volume of heated system is increased along the increasing kinetic energy. In a NVT ensemble, the system is connected to a 'heat bath' and the kinetic energy is always adjusted to increase to the target temperature. Therefore the decreased potential has nowhere to go but transfers to other energies (bonding energy etc.) and heat released. To calculate the released heat, a separated simulation having the same time span and same heating process was perfomed where the only difference is that bonding reaction between Si and O were switched off, shown as **Figure 7.3b**. The non-reactive heating is an obvious heat-absorbing process where the total energy is increased. Therefore the total heat released for Si-O oxidation should be calculated from the combination

of the heat released at reaction mode and the heat absorbed at non-reactive mode, *i.e.*, [max($E_{reactive}$)- min($E_{reactive}$)]+[max($E_{non\text{-}reactive}$)-min($E_{non\text{-}reactive}$)], where E represents the total energy. The value is equivalent to 5.95×10^4 kJ/mol, or 21.1 MJ/kg, counted as about two third of that of aluminium nanoparticle oxidation of 30.0 MJ/kg (Utgikar *et al.*, 2006).

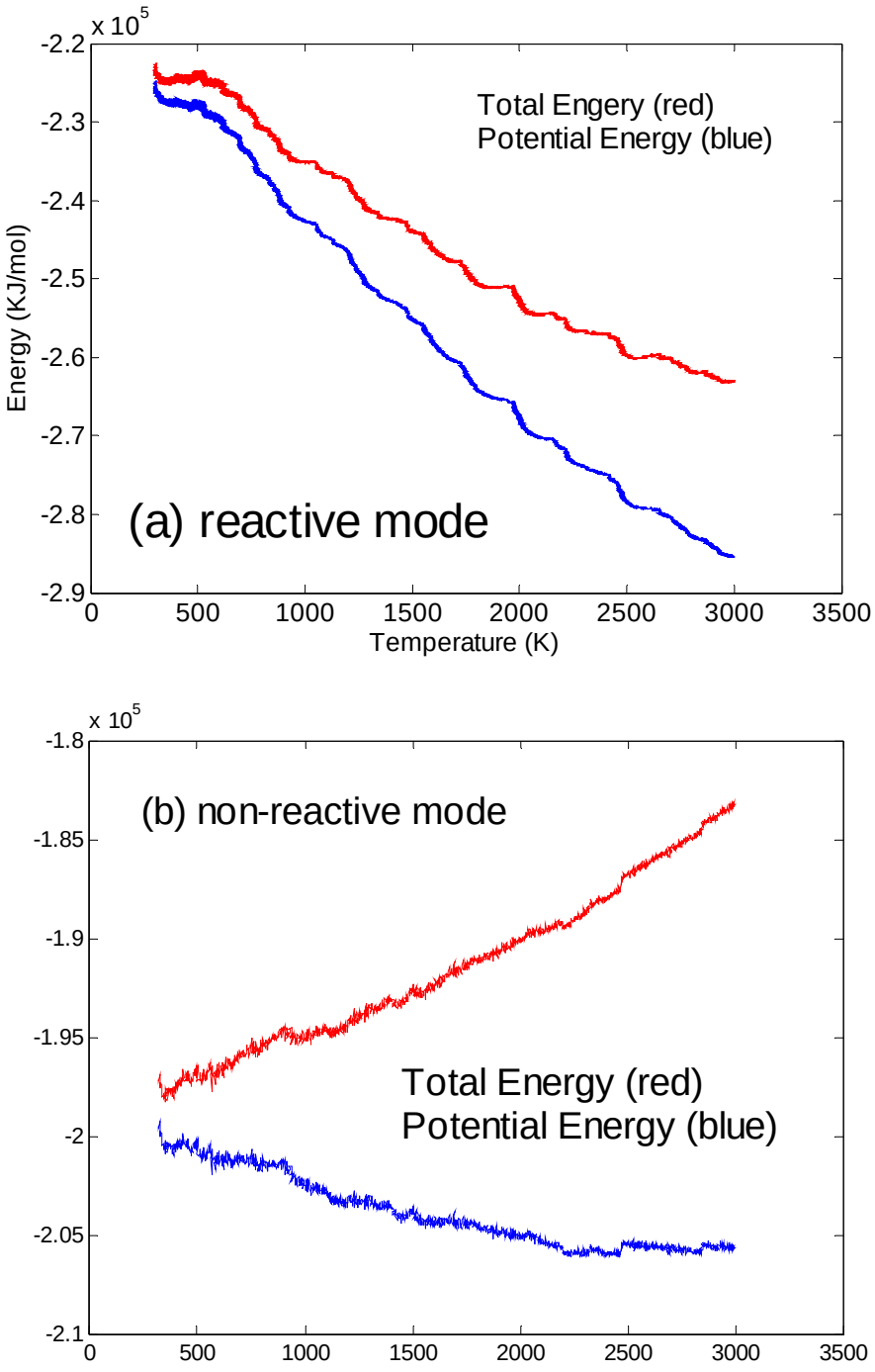

Figure 7.3: Energy at reactive (a) and non-reactive mode (b)

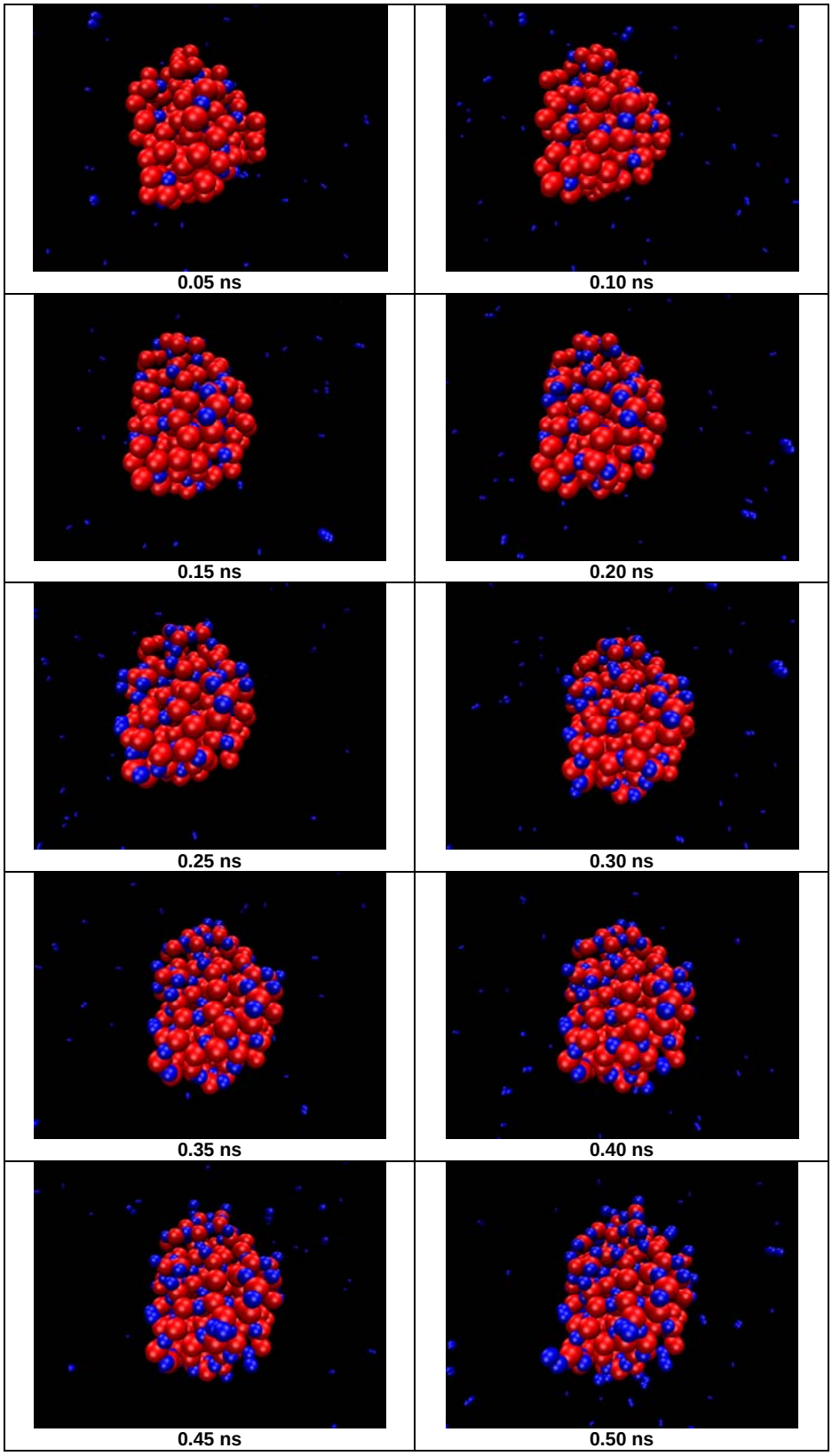

Figure 7.4: Snapshots of silicon oxidation

7.4 Bond Evolution

The bond orders (BO) of chemical element are vital indicators of reliability of a reactive MD simulation. In ReaxFF, BO is directly calculated from the instantaneous interatomic distance to simulate the bonding dynamic, *i.e.* formation and dissociation of bonds. The average BO of oxygen and silicon at each chosen time point are shown in figure respectively. The BO of a particular atom is the sum of partial bond orders to its bonded neighbour atoms. The average value is calculated directly from the sum of each atom over the number of atoms at that time. The calculated bond orders are in good agreement with the bond valence of oxygen and silicon, 2 and 4, as shown in **Figure 7.5** and **Figure 7.6**. Bond length between Si and O is analysed once a Si-O is formed, shown in **Figure 7.7**. The average of bond length is 1.58 Å that is in good agreement with many theoretically calculated values (Demkov *et al.*, 1999; van Duin *et al.*, 2003). Si-O-Si angle analysis shows that most of the Si-O-Si bonds are in the range of 90° to 110° and 125° to 145° displayed in **Figure 7.8** that is in consistency of others (van Duin *et al.*, 2003). The respective mean values of bulk SiO_2 are 1.61 Å (Si-O bond length) and 141° (Si-O-Si) respectively (Schubert *et al.*, 1993). Since the Si-O bonds are localized and it's not appropriate to take this reference value of bulk SiO_2 to the MD case where intermediates are likely to be involed. The bond analysis suggests that the ReaxFF creates a credible oxidation scenario.

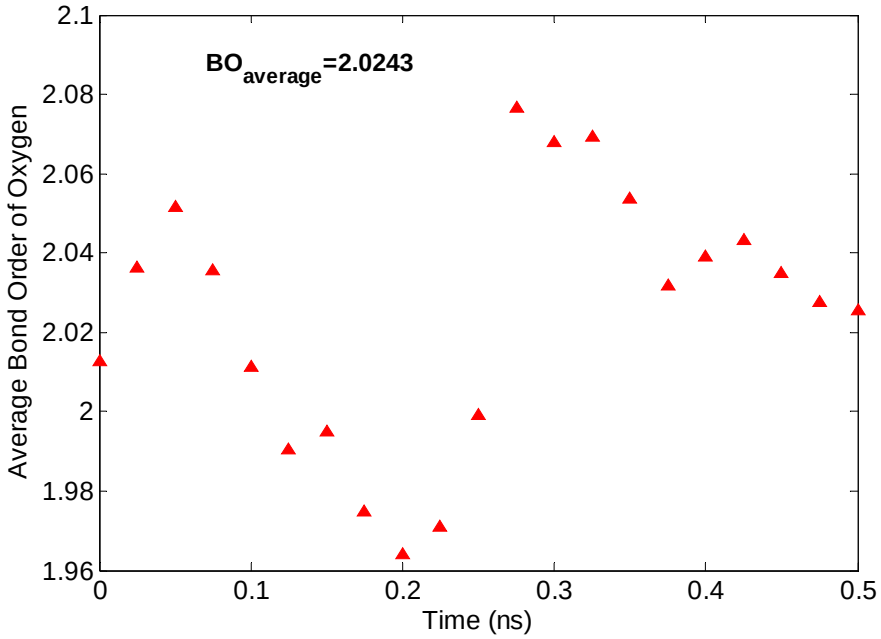

Figure 7.5: Bond order of oxygen

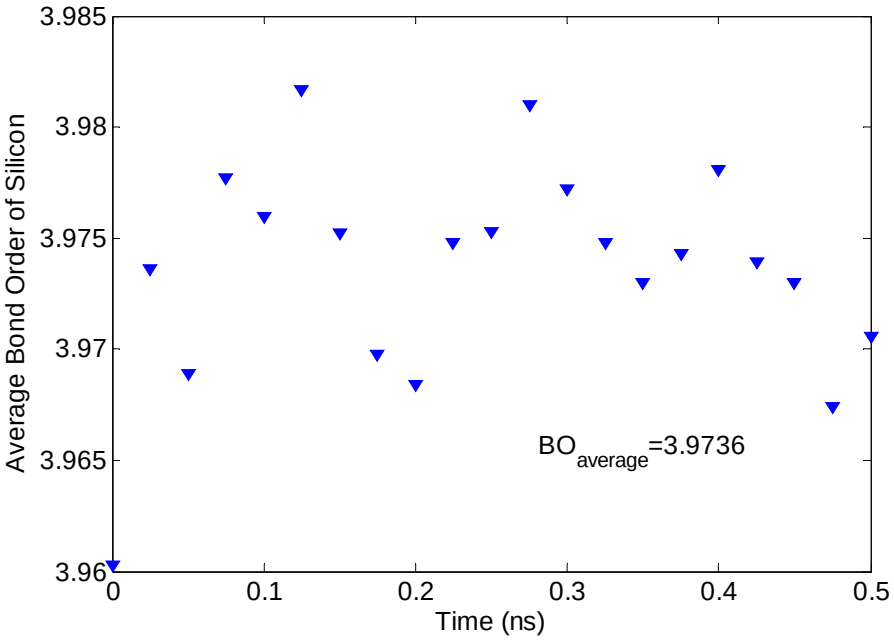

Figure 7.6: Bond order of silicon

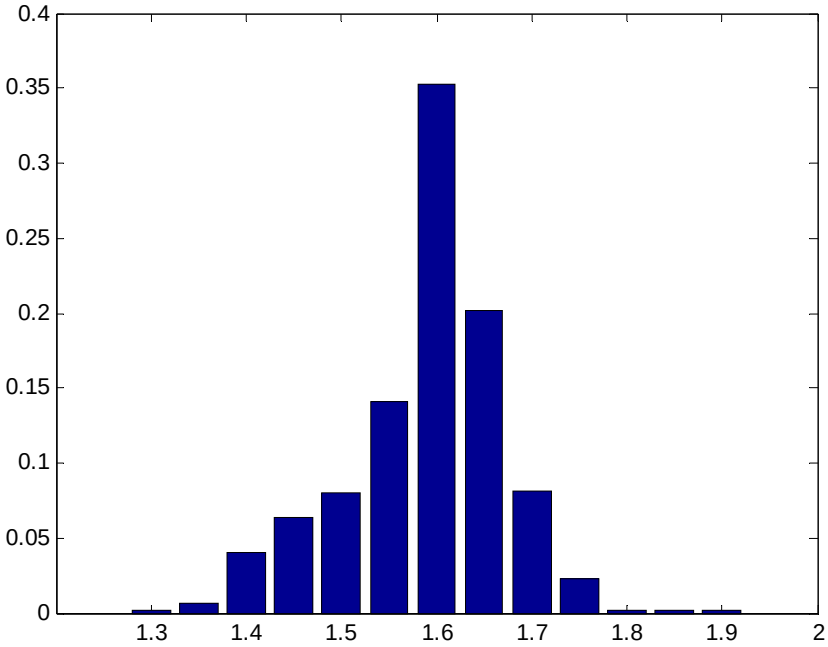

Figure 7.7: Distribution of Si-O Bond length

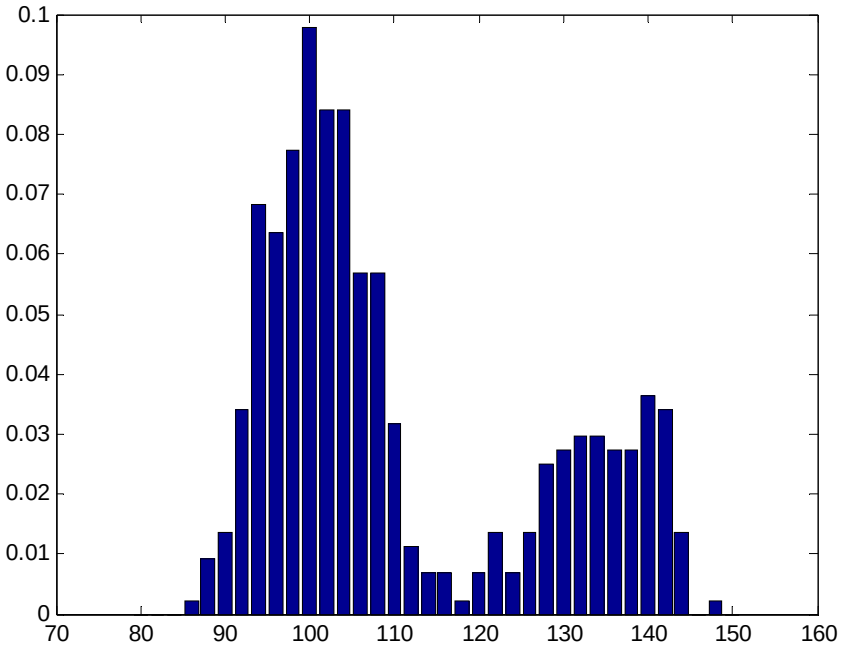

Figure 7.8: Distribution of O-Si-O angle

The oxygen molecules are considered to be consumed once any individual oxygen atom is bonded to silicon during the heating process. The oxygen and silicon contents are shown in **Figure 7.9** and **Figure 7.10**. The oxygen

content decreases as the reaction proceeds. At the end of the simulation, 35% oxygen molecules are bonded to the silicon cluster. Correspondingly the content of silicon atoms is counted shown in **Figure 7.10**, indicating that 90% silicon atoms are bonded at the end of simulation. In consideration of initial atom contents, 65 O_2 molecules and 165 Si atoms are bonded together. Obviously the ratio is not consistent with the ideal crystal of SiO_2. This leads to a more detailed pair analysis as follows.

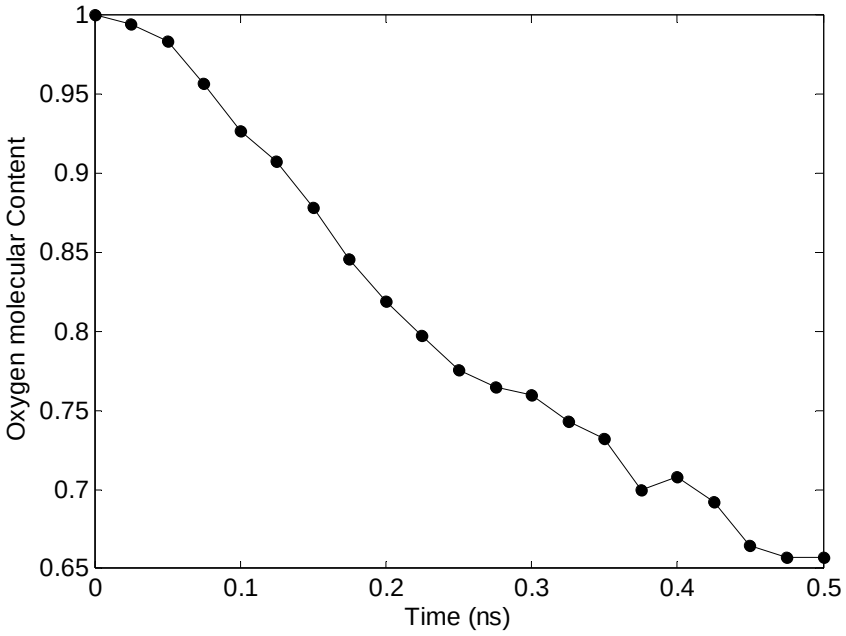

Figure 7.9: Temporal content of oxygen molecules

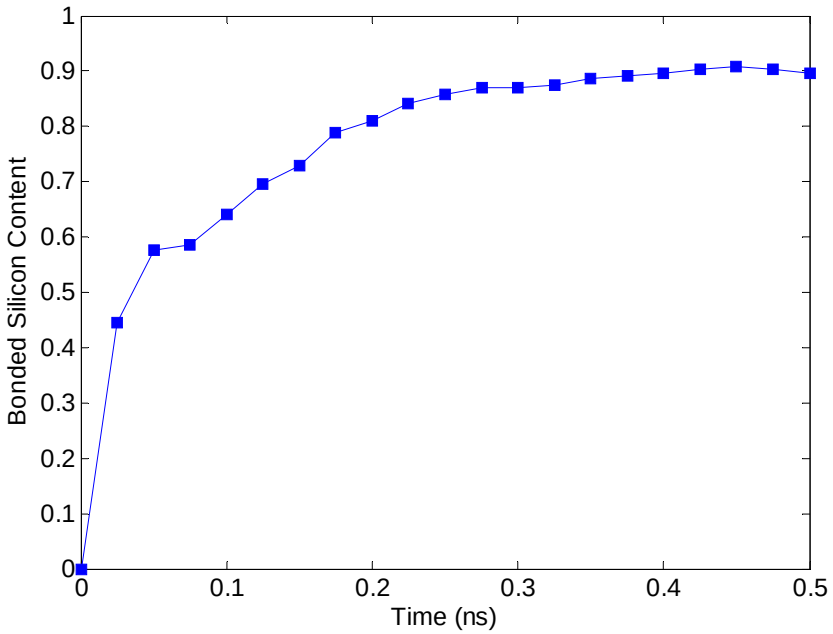

Figure 7.10: Temporal content of bonded silicon atoms

The bonding process of oxygen into silicon is concluded to involve three mixing mechanisms determined by the simulation of DFT and kinetic Monte Carlo (KMC) (Hemeryck *et al.*, 2009). Three types of mechanisms are as followed:

(1) Two oxygen atoms from a dissociative oxygen molecule are bonded directly on silicon, *i.e.* Si-O type of bonding.

(2) The incorporation of the oxygen atom in event 1 into silicon to form Si-O-Si bonds.

(3) The atomic oxygen migration from any previous bonded configurations.

In this study, when one oxygen atom is only bonded with two silicon atoms, it is classified as Si-O-Si. If one oxygen atom from an O_2 molecule is bonded to a silicon atom, *i.e.* an instantaneous oxygen radical, it is denoted as Si-O-O. The existence of oxygen radical is consistent with the little oversaturated valences of oxygen, 2.0243. The most bonding scenarios of oxygen are observed to be oxygen radical and single oxygen atom shared by

two silicon atoms. Even though the total bond order of oxygen is 2, the existence of three-silicon-neighbour oxygen shows that these oxygen atoms are two-coordinated. The configuration is denoted as O-3Si. This bond configuration is believed to be consistent with the nearly 90° Si-O-Si angle found in this study and others (van Duin *et al.*, 2003). The other configuration of two-coordinate oxygen is defined as a structure where one silicon atom bonds two oxygen and two other silicon atoms, which is labelled as 3Si-2O. Here 3Si-2O is used rather than Si-2O because it is found that all root silicon atoms in this configuration is bonded to other two peer silicon atoms. The two oxygen atoms can only occupy the rest bonding sites. The trace of two-coordinated oxygen is consistent with van Duin's result obtained by Si-O-Si angle analysis (van Duin *et al.*, 2003). The two-coordinated oxygen in the form of Si-O is a SiO interstitial and can introduce stoichiometric defects (Pantelides and Ramamoorthy, 1999; Kageshima *et al.*, 2006). The bonding number evolving with temperature is shown in **Figure 7.11**. All configurations observed in snapshots of simulation are shown in **Figure 7.12**. Demkov *et al.* (1999) described the decomposition and incorporation of the O_2 molecule at the silicon surface in DFT simulation. One oxygen atom positions itself into bridging in middle of dimer bond of Si. This structure forms two Si-O bonds length of which is 1.58 Å and the angle of Si-O-Si is 134°. And they also observed that silicon atom three-coordinated by surrounding oxygen corresponding to the O-3Si bond configuration found in this study and two-coordinated structure. Some oxygen bonded to surface silicon stay unchanged and terminated, similar to the Si-O structure. A distinct structure of which a silicon atom inserted into three oxygen atoms on the silicon surface, Si-3O is found in their simulation but is not observed in this study.

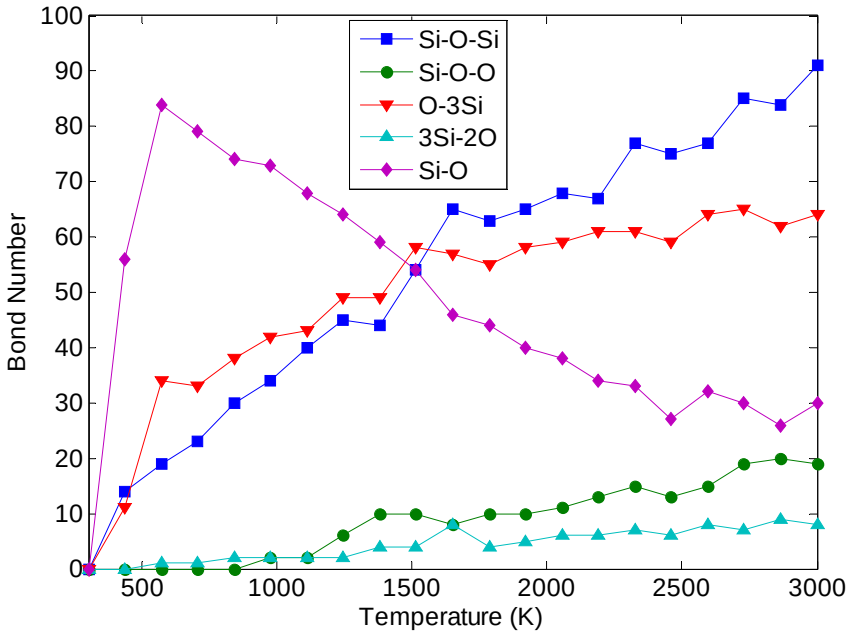

Figure 7.11: Bond configuration evolution

At the early stage of oxidation, the dissociative oxygen atoms absorbed in silicon are predominant in the oxidation. The largest number of Si-O is remarkable at the temperature of 570 K. Then, it can be seen that, this type of bonding starts to decline to about 30% of its maximum value at the end of the simulation. Meanwhile two other configurations, *i.e.* Si-O-Si and O-3Si grow steadily and eventually prevail in the oxidised structure. The explanation of this contrast is that the surface double-bonded oxygen migrates into the silicon matrix and move into the interstitial space of silicon atoms, *i.e.* the transition from Si-O to Si-O-Si and O-3Si during a diffusive process. The MSD obtained for O in Si-O is consistent with the described process, as shown in **Figure 7.13**. Oxygen moves to a relatively long distance averagely (~2 Å) and rests by bonding in between silicon atoms. The slowed motion of oxygen afterwards is due to the local vibration after bonding with silicon. It is worth to point out that the formation of Si-O does not need to overcome any activation energy, which obeys the Maxwell-Boltzmann statistics in gas phase. The probability of this event is governed by the equation, $C_1 PS/\sqrt{MT}$, where C_1 is a prefactor, P is the pressure, S is the surface area, M is the molar mass of oxygen and T is the

temperature. The migration and re-bonding events are determined by an Arrhenius mechanism expressed as $C_2 \exp(-\Delta E_a / k_B T)$ where C_2 is a constant, E_a is the activation energy barrier, k_B is the Boltzmann constant (Hemeryck *et al.*, 2009). It is also noticeable that the two configurations of 3Si-2O and Si-O-O slowly grow and only appear when the temperature is elevated. It is simply because that they are not thermodynamically favourable at the low temperature compared with the Si-O configuration. The occurrence of these two configurations is only possible when the temperature increases as well as more surface silicon sites exposed due to previous bonded oxygen migration.

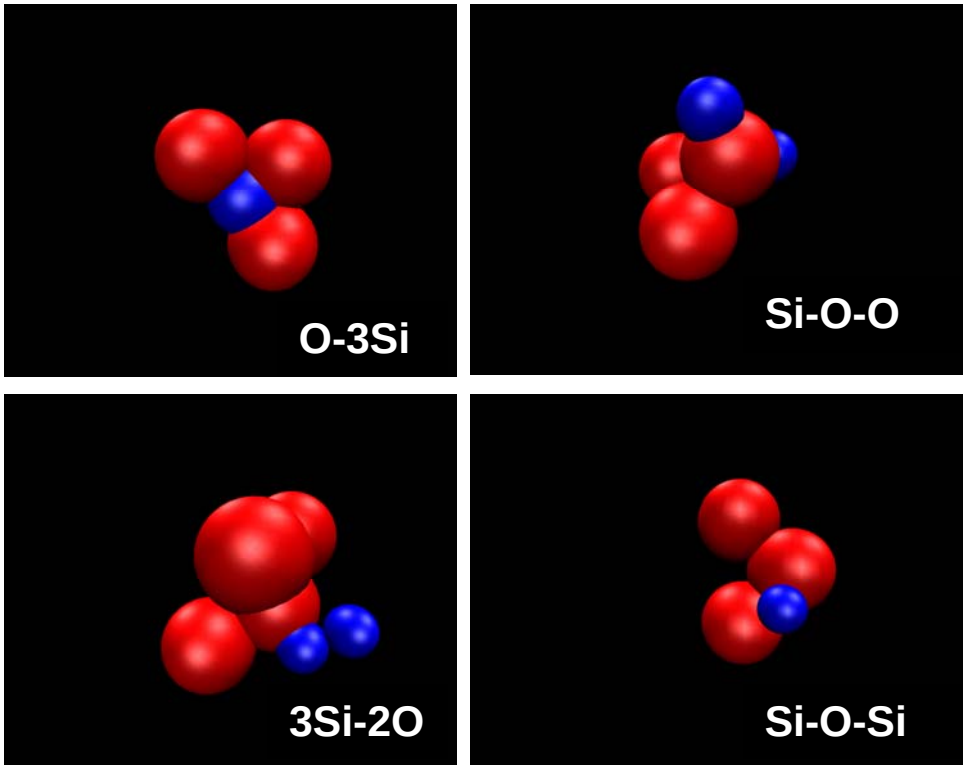

Figure 7.12: Scheme of bond configurations

7.5 Oxygen Exchange Process

A model introduced by Deal and Grove (1965) proposed that the formation of the formation of a thermal oxide film on silicon proceeds via three sequential steps: (i) oxygen insertion into previously formed oxide layer, (ii) diffusion of oxidant through the amorphous Si-O network and (iii) oxidation at interface of silicon and its oxide. The oxidation kinetics is governed by the oxygen diffusion process. The model works very well on silicon oxidation kinetics in agreement with many experimental data particularly of thick silicon film. However, the Deal-Grove model fails in modelling the oxidation kinetics of thin-film oxides (Deal and Grove, 1965; Bongiorno and Pasquarello, 2004). More recently, oxygen exchange processes have also been found to occur at the Si-SiO_2 interface (Bongiorno and Pasquarello, 2005). There are more experimental findings suggesting that, for very thin films, oxygen exchange processes occur throughout the film, in contrast with the Deal-Grove model (Åkermark *et al.*, 1999a, 1999b). Density functional theory (DFT) has been demonstrated to be particularly suitable for providing insight into the atomic processes occurring during silicon oxidation (Pantelides and Ramamoorthy, 1999; Torre *et al.*, 2002; Bongiorno and Pasquarello, 2005). However, oxygen exchange process is not yet investigated by reactive MD in regard to atomic scale information.

Notice that undissociated oxygen were found by direct experimental observation in assistance with tools such as nuclear reaction resonance, secondary ion mass spectrometry, and medium energy ion scattering technique. In this study there is no trace of oxygen molecule diffusing into silicon cluster. The oxygen molecules are all dissociated and then grafted onto silicon surface. The motion of oxygen element is achieved by bonding transition instead of molecule diffusion. The distinction is attributed to high reactivity of surface atoms. The oxygen exchange process is found to occur at Si-SiO_2 interface similar as previously discussed by Demkov *et al.* (1999),

where the oxygen exchange process proceeds by oxygen bonded into surface dimmer silicon moving into backbone structure underneath surface.

The oxygen exchange reactions can be intermediate reactions (Åkermark *et al.*, 1999a; Åkermark *et al.*, 1999b). It is revealed that there are at least two different oxygen exchange processes during dry thermal oxidation of silicon: oxygen exchange between oxygen molecules ($O_2 \leftrightarrow O_2$), catalyzed by the SiO_2, and oxygen exchange between oxygen from the gas phase and the oxygen in SiO_2 as ($O_2 \leftrightarrow SiO_2$). The ($O_2 \leftrightarrow SiO_2$) exchange takes place at the gas/solid surface and at the SiO_2/Si interface. Actually the ($O_2 \leftrightarrow SiO_2$) exchange does occur in this simulation, however, proceeds in a more general form which is between the oxygen molecules and any bonded oxygen atom to silicon. SiO interstitial has a Si-Si bond site. Fundamentally the Si-Si bond site is thought to enhance the bond changing because Si-Si bond is known to be much softer and weaker than Si-O bond (Kageshima *et al.*, 2006).

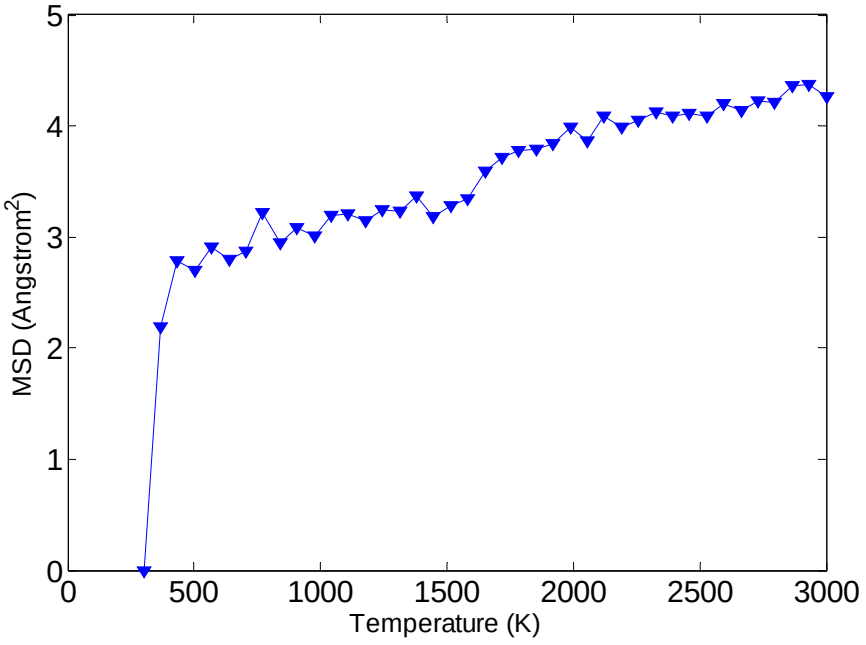

Figure 7.13: MSD of oxygen atom in Si-O configuration

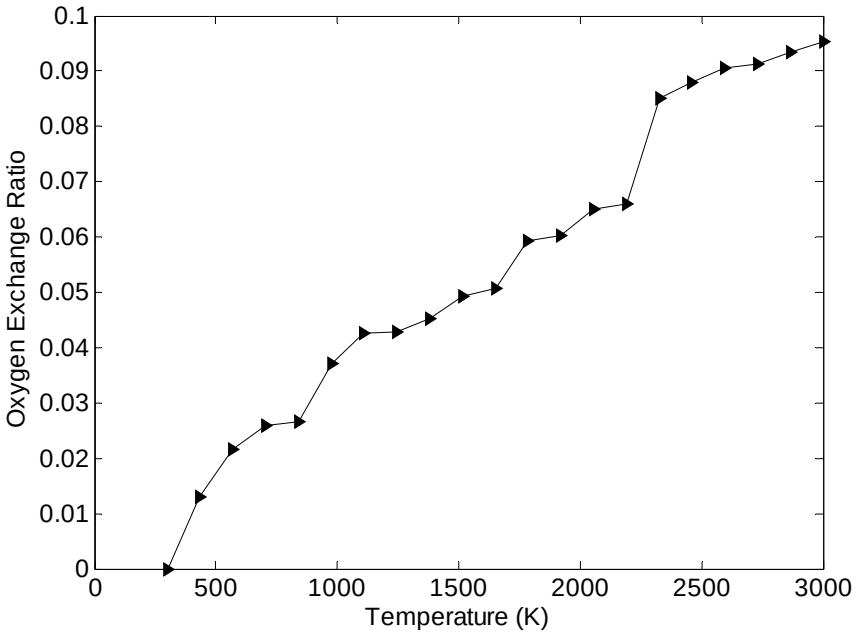

Figure 7.14: Oxygen exchange ratio during heating

7.6 Estimation of Activation Energy

Since activation energy, ΔE_a is occurrence frequency dependent; it is usually determined by the Monte Carlo simulation in which a random series of events occurs. MD is not ideal for this purpose since the technique involves determinative dynamic process. The activation energy is obtained in MD from a reaction pathway along energy surface of configurational space associated with reaction coordinates. The reaction coordinates are defined and the energy of atoms under investigation is book-kept. If any energy barrier is observed the activation energy is subsequently deduced by the energy difference. This task is never easy if the system has many degrees of freedom since the direct mapping from computational simulations of activated processes is profoundly complicated and prohibitively expensive for most molecular systems. The reason is that the identification of reaction path involves separation of various activated process at different time scales, such as intramolecular vibrations and intermolecular diffusion. The main difficulty particularly for MD is to

achieve a sufficient sampling of the relevant range of reaction coordinate values. The umbrella sampling method (Teraishi *et al.*, 1999) and constrained molecular dynamics (Torre *et al.*, 2002) have been used to achieve efficient sampling of surfaces of configuration space that are otherwise inaccessible in the typical time scale of MD simulations. Any metastable configuration needs to be avoided carefully by looking into local minima asscociated with it. However, based on the simplicity that will be discussed below, by skipping all those difficulties, a rough estimation of activation energy can be made for a particular transition. The simplicity used here is that MD is thought to reproduce a genuine physical event of Si oxidation *i.e.* taking the MD simulation as an 'experiment' and all the bonding information obtained as genuine observations. The limitation in theory is obvious: not each configuration of configurational space is covered. The experimental study of bond transformation is operated in a variable-temperature scanning tunneling microscope (STM) by imaging individual molecule and resolving oxygen dissociation and absorption at the atomic scale (Hwang *et al.*, 1998). The oxygen mechanism is proposed to be site hopping of intermediate structure of Si and O bonding. The experimentally found structural hopping frequency is about 10^{15}-10^{16} Hz, which is well within the time span of this simulation. Inspired by their analysis approach in consideration that hopping conduction is one basic oxidation mechanism (Atkinson, 1985) in use of the appearing bonding number at each time point, the activation energy of [(Si-O) → (Si-O-Si)] and [(Si-O) → (O-3Si)] is estimated. Based on **Figure 7.11**, the maximum lifetime of each bond transformation is taken as 1.25×10^{-11} s. The corresponding average transition rate is R_e. From successive bonding numbers taken at various temperatures, the average transition rate at each temperature, which is equal to the ratio of the total number of bonding to the total elapsed time span in assumption that any bond configuration is only converted from that at previous time step. That is to say, there is no bond transformation longer than one timestep, 1.25×10^{-11} s. Similar to the equation of Arrhenius theory, the transition rate is expressed as

$$R_e = R_0 \exp(-\Delta E_a / k_B T) \tag{7.4}$$

The activation energies are deduced from the Arrhenius plots shown as **Figure 7.15** and **Figure 7.16**. The transition from Si-O to Si-O-Si is found to be 0.564 eV and that from strand configuration Si-O to three neighbour configurations O-3Si is 0.970 eV. Therefore the Si-O-Si bonding is more favourable and cost less energy to achieve thermodynamically. Again it is worthwhile to point out that the calculation done here above does not produce the genuine activation energy of the process but a quantitative estimation based on obtained bonding number which has similar form with activation energy.

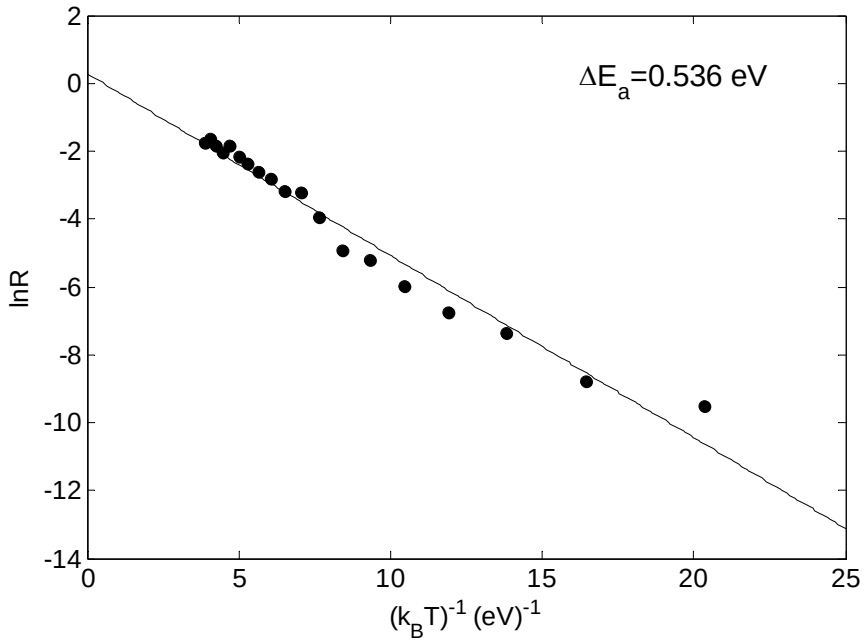

Figure 7.15: Activation energy from Si-O to Si-O-Si

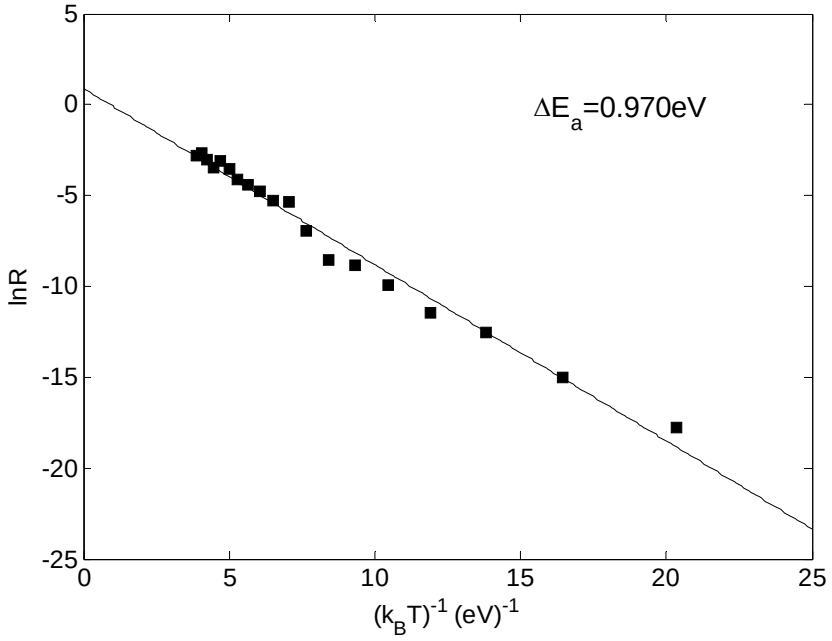

Figure 7.16: Activation energy from Si-O to O-3Si

7.7 Chapter Summary

This chapter presents an atomistic picture for an exothermic reaction of nanoparticle: the oxidation of silicon nanoparticle in use of a reactive MD force field, ReaxFF. The ReaxFF creates a creditable process of oxidation of silicon by reproducing the exothermal reaction and consistent bond order and bond length. The calculated released energy is ~14.14 MJ/kg. An atomic picture of Si-O bond configuration evolution is observed in simulation. Based on the bond evolution, oxygen exchange process is identified and the oxidation sequence is explained by bond transformation of Si-O to more stoichiometric and saturated bonding configurations in term of oxygen exchange process and activation energies of bond transformation based on accounting bonding numbers are approximately estimated by an Arrhenius equation. This study indicates the capability of ReaxFF describing oxidation in an atomic MD level manner with potentials of simulating mesoscale scenarios for larger nanoparticles.

Chapter 8

Conclusions and Future Work

This dissertation conducted a fundamental study of metallic nanoparticles associated thermal phenomena that includes a kinetic study of oxidation of metallic nanoparticles (Ni and Sn) based on thermal analysis and solid-state reactions, and three numerical simulations in use of non-reactive and reactive Molecular Dynamics for sintering, oxidation and several thermodynamic behaviours of various structured nanoparticles (Ni, Ni-Al, and Si). These works advanced the understanding of several aspects of using nanoparticles in potential energy applications. The kinetic studies of oxidation of Ni and Sn nanoparticles help understanding the process of energetic reactions when the nanoparticles are under nanofuel applications and also the catalysis reactions in energy-convertion applications when the nanoparticles are exposed in oxidative environment. Molecular Dynamics investigations provide some intrinsic properties when material is reduced to nanoscale dimension. The sintering study is important for transportation and storage of energetic nanoparticles. The thermal stablility and phase information under heating and cooling of a highly energetic material, Ni-Al composite nanoparticle is investigated for future design of nanofuel. The silicon nanoparticle as a promising nanofuel is studied focusing on its released energy during oxidation. In nanoscience and nanotechnology, the two different methods, *i.e.* simulation and experiment, can benefit each other in many ways. The bridging study between comparible size-time simulation and experiment *e.g.* multiscale simulation associated with nanoscale experiment will greatly advance our understanding on nanoscale phonomena and further expand our vision on nanoscale application.

The experimental study of the oxidation of metallic nanoparticles shows that:

(1) The oxidation at nanoscale was deviated from a homogeneous environment usually associated with bulk situations to a heterogeneous process that was affected by particle size and size-dependent thermodynamic properties such as melting point of particles. The nanoscale kinetic results need to be carefully interpreted and incorporated to reflect pertubations of many complexities such as initial passivation oxide shell, multiple reaction steps, nucleation and growth, localized melting and morphology change due to sintering, and high stress condition.

(2) Unlike its bulk counterpart where the activation energy is invariant, the apparent activation energy of oxidation of nickel nanoparticles, in stoichimetric reaction Ni→NiO depended on the conversion ratio, ranging from 1.4 to 1.8 eV. The oxidation activation energy of fisrt stage of oxidation of tin nanoparticle in stoichimetric form of Sn→SnO, was found to have similar dependent features on the conversion ratio whose value is in the range of 0.32-1.33 eV.

(3) The oxidation kinetics of nickel nanoparticles changed from the diffusion controlled mechanism to a pseudo-homogeneous one as conversion ratios were over 50%. In assistance of isothermal XRD study, a two-stage oxidation scenario was established for tin nanoparticles. The only oxide product was SnO at temperatures below 400 °C, and SnO and SnO_2 coexisted at the temperature range between 400 and 900 °C. On the basis of the identified oxide constituent, the first-stage oxidation of tin nanoparticles was investigated by the isoconvensional method and the oxidation kinetics was identified to be the classical nucleation mechanism that can be modeled by the Avrami-Erofeev equation.

(4) The mechanism change of nickel nanoparticles was believed to be associated with the Curie transition, which was also observed in isothermal oxidation. The melting of tin nanoparticles and large pressure built-up in a rigid oxide shell was believed to be responsible for the heterogeneous nucleation mechanism. The isoconversional method was validated by

undercovering oxidation kinetic for nanoparticles without pre-assigned mechanism assumption.

The numerical study of individual nanoparticle behaviour by MD shows that:

(5) A three-stage sintering scenario of nickel nanoparticles was established by MD without continuum assumption for bulk material. The layered structure of two unequal sized nickel nanoparticles revealed a regime dependent behaviour of diffusivity during the sintering process. Besides the surface diffusion, sintering of different sized nanoparticles was found to be affected by a few other mechanisms such as viscous flow and plastic deformation, and surface tension gradient.

(6) The thermodynamic properties and structural evolution of a Ni-core Al-shell composite nanoparticle during a continuous heating and cooling cycle were investigated through the characterisation of the gyration radius, radial distribution function, atom number distribution, MSD and layered potential energy distribution. Some unique behaviour related to nanometre scale composite particle were identified that included two-way diffusion of aluminium and nickel atoms, enhanced melting of aluminium core through the shell structure, glass phase formation for the fast cooling rate and Ni_3Al phase formation under a low cooling rate.

(7) A reactive force field of molecular dynamics, ReaxFF, was used to simulate the oxidation of silicon nanocluster. The exothermal process and Si-O bond evolution were investigated and a distinct oxygen exchange process during oxidation was reproduced and a simple estimation of activation energy of bonding transition was proposed. MD simulation is proved to be computationally efficient and robust, therefore suitable for future large-scale simulation of reactive processes.

The work presented in this dissertation advanced our understanding of metallic/non-metallic nanoparticles from both reactive and non-reactive

aspects including oxidation, sintering, thermomechanical and structural evolution of functional particlces for sake of potential energetic applications. There are many aspects, however, deserve further work, in particular:

(i) The isoconversional method should not be restrained at one-step oxidation, but be extended to multiple-steps complicated reactions. The potential advance may exist in using different experimental tools, among which, the most promising is single particle mass spectroscopy (SPMS) and employing new mathematical approaches of extracting reaction mechanism from kinetic data such as multivariable non-linear regression analysis, genetic algorithm and artificial neural network.

(ii) Despite of the model-free feature, isoconversional method can not provide a general reaction model for different particle samples with different size distributions, rather for a particular particle sample. The size effect of nanoparticle on oxidation kinetic should be further experimentally and theoretically studied in order to achieve a more general quantitive mechanism description.

(iii) For advanced applications of energetic nanomaterisls, the ignition, combustion and many other energy related properties of utilized nanoparticles require further study. In respect to this work, reproducing DSC curves at fasting heating rates will be a feasible starting point. Multidisciplinary and multiscale modelling technique particularly in consideration of mass transportation, heat transfer and energy balance of an exothermic oxidation reaction should be adopted for a more profound study.

(iv) All the thermal and kinetic analyses and their methodology should be related with bulk material applications and scaled-up phenomena and reactions such as occurrences in Chemical-Looping Combustion (CLC) and Fluidized Bed Reactor (FBR).

(v) Larger scale simulations of particle systems need be performed in use of molecular dynamics, at both reactive and non-reactive situations, in order to bridge the atomic picture and mesoscale reality. New techniques of simulations such as coarse-grain method, for example, dissipative particle dynamics (DPD) might be adopted to describe some mesoscale phenomena. Toward this aim some feasibility work has been conducted by constructing a million-atom simulation on the supercomputer HECToR located in Edinburgh. If so, the isoconversional experimental results can be potentially coupled with the detailed molecular dynamic simulations at such a scale to gain more insightful understanding of various physicochemical properties of nanoparticles.

Appendix 1

LAMMPS scripts

Sintering

```
# melting for Ni system

clear

units           metal
boundary        s s s

atom_style      atomic
read_data       data.apart


pair_style      eam
pair_coeff      * * Ni_smf7.eam


neighbor        0.45 bin
neigh_modify    delay 10

group           all type 1

group           b_ball id <=  2112
group           s_ball id >   2112

#define neck atom group for big and small metal balls

group       b_neck1 id 38    39    58    59    61    81    82
        84    85    104   105   107   124   152   153   155
        176   177   179   180   181   182   183   206   207
        209   210   211   212   213   237   238   240   241
        242   243   244   245   268   269   271   272   273
        274   275   298   299   301   302   303   322   345
        346   367   368   370   371   372   373   374   399
        400   402   403   404   405   406   407   433   434
        436   437   438   439   440   441   442   443   469
        470   472   473   474   475   476   477   478   479
        505   506   508   509   510   511   512   513   514
        515   539   540   542   543   544   545   546   547
        548   571   572   574   575   576   593   618   619
```

621 644 645 647 648 649 650 651 677
678 680 681 682 683 684 685 686 687
715 716 718 719 720 721 722 723 724
725 726 754 755 757 758 759 760 761
762 763 764 765 766 793 794 796 797
798 799 800 801 802 803 804 805 831
832 834 835 836 837 838 839 840 841
864 865 867 868 869 870 871 890 891
893 924 925 927 928 952 953 955 956
957 958 959 960 986 987 989 990 991
992 993 994 995 996 1024 1025 1027 1028
1029 1030 1031

group b_neck2 id 1032 1033 1034 1035 1036 1064 1065
1067 1068 1069 1070 1071 1072 1073 1074 1075
1076 1104 1105 1107 1108 1109 1110 1111 1112
1113 1114 1115 1116 1142 1143 1145 1146 1147
1148 1149 1150 1151 1152 1176 1177 1179 1180
1181 1182 1183 1184 1204 1205 1207 1208 1238
1239 1241 1264 1265 1267 1268 1269 1270 1271
1297 1298 1300 1301 1302 1303 1304 1305 1306
1307 1334 1335 1337 1338 1339 1340 1341 1342
1343 1344 1345 1346 1374 1375 1377 1378 1379
1380 1381 1382 1383 1384 1385 1386 1414 1415
1417 1418 1419 1420 1421 1422 1423 1424 1425
1451 1452 1454 1455 1456 1457 1458 1459 1460
1461 1484 1485 1487 1488 1489 1490 1491 1510
1511 1513 1535 1559 1560 1562 1563 1564 1588
1589 1591 1592 1593 1594 1595 1596 1597 1623
1624 1626 1627 1628 1629 1630 1631 1632 1633
1659 1660 1662 1663 1664 1665 1666 1667 1668
1669 1695 1696 1698 1699 1700 1701 1702 1703
1704 1705 1730 1731 1733 1734 1735 1736 1737
1738 1759 1760 1762 1763 1764 1765 1766 1782
1784 1808 1832 1833 1835 1836 1837 1860 1861
1863 1864 1865 1866 1867 1891 1892 1894 1895
1896 1897 1898 1899 1922 1923 1925 1926 1927
1928 1929 1950 1951 1953 1954 1955 1956 1957
1974 1975 1977 2004 2024 2025 2027 2047 2048
2050 2051 2070 2071 2073 2089 2091

group b_neck union b_neck1 b_neck2

group s_neck id 2114 2122 2123 2134 2143 2151 2152
2153 2154 2157 2168 2169 2170 2171 2174 2186
2187 2188 2191 2204 2211 2212 2223 2224 2225
2226 2229 2241 2242 2243 2244 2245 2248 2261

2262 2263 2264 2267 2279 2282 2291 2299 2300
2301 2304 2316 2317 2318 2319 2322 2334 2335
2336 2337 2340 2353 2361 2368 2371 2382

group the three outmost layers for big and small balls

group b_out1 id 1 2 3 4 5 6 7 8
9 10 11 12 13 14 15 16 17
18 19 20 21 22 23 24 25 26
27 28 29 30 31 32 33 34 35
36 37 38 39 40 41 42 43 44
45 46 47 48 49 50 51 52 53
54 55 56 57 58 59 60 61 62
63 64 65 66 67 68 69 70 71
72 73 74 75 76 77 78 79 80
81 82 83 84 85 86 87 88 89
90 91 92 93 94 95 96 97 98
99 100 101 102 103 104 105 106 107
108 109 110 111 112 113 114 115 116
117 118 119 120 121 122 123 124 125
126 127 128 129 130 131 132 133 134
135 183 184 213 214 215 244 245 246
275 276 324 325 326 327 328 329 330
331 332 333 334 335 336 337 338 339
340 341 342 343 344 345 346 374 375
376 377 406 407 408 409 410 411 440
441 442 443 444 445 446 447 476 477
478 479 480 481 482 483 512 513 514
515 516 517 546 547 548 549 577 578
579 580 581 582 583 584 585 586 587
588 589 590 591 592 593 594 595 596
597 598 599 600 601 602 603 604 605
606 607 608 609 610 611 612 613 614
615 616 617 618 619 620 621 622 651
652 653 654 655 684 685 686 687 688
689 690 691 692 693 722 723 724 725
726 727 728 729 730 731 732 761 762
763 764 765 766 767 768 769 770 771
800 801 802 803 804 805 806 807 808
809 838 839 840 841 842 871 872 873
874 875 876 877 878 879 880 881 882
883 884 885 886 887 888 889 890 891
892 893 894 895 896 897 898

group b_out2 id 899 900 901 902 903 904 905
906 907 908 909 910 911 912 913 914
915 916 917 918 919 920 921 922 923

924 925 926 927 928 929 930 959 960
961 962 963 964 993 994 995 996 997
998 999 1000 1001 1002 1031 1032 1033 1034
1035 1036 1037 1038 1039 1040 1041 1042 1071
1072 1073 1074 1075 1076 1077 1078 1079 1080
1081 1082 1111 1112 1113 1114 1115 1116 1117
1118 1119 1120 1149 1150 1151 1152 1153 1154
1183 1184 1185 1186 1187 1188 1189 1190 1191
1192 1193 1194 1195 1196 1197 1198 1199 1200
1201 1202 1203 1204 1205 1206 1207 1208 1209
1210 1211 1212 1213 1214 1215 1216 1217 1218
1219 1220 1221 1222 1223 1224 1225 1226 1227
1228 1229 1230 1231 1232 1233 1234 1235 1236
1237 1238 1239 1240 1241 1242 1271 1272 1273
1274 1275 1304 1305 1306 1307 1308 1309 1310
1311 1312 1341 1342 1343 1344 1345 1346 1347
1348 1349 1350 1351 1352 1381 1382 1383 1384
1385 1386 1387 1388 1389 1390 1391 1392 1421
1422 1423 1424 1425 1426 1427 1428 1429 1458
1459 1460 1461 1462 1491 1492 1493 1494 1495
1496 1497 1498 1499 1500 1501 1502 1503 1504
1505 1506 1507 1508 1509 1510 1511 1512 1513
1514 1515 1516 1517 1518 1519 1520 1521 1522
1523 1524 1525 1526 1527 1528 1529 1530 1531
1532 1533 1534 1535 1536 1537 1565 1566 1595
1596 1597 1598 1599 1600 1601 1630 1631 1632
1633 1634 1635 1636 1637

group b_out3 id 1666 1667 1668 1669 1670 1671 1672
1673 1702 1703 1704 1705 1706 1707 1708 1737
1738 1766 1767 1768 1769 1770 1771 1772 1773
1774 1775 1776 1777 1778 1779 1780 1781 1782
1783 1784 1785 1786 1787 1788 1789 1810 1838
1867 1868 1869 1898 1899 1900 1929 1957 1978
1979 1980 1981 1982 1983 1984 1985 1986 1987
1988 1989 1990 1991 1992 1993 1994 1995 1996
1997 1998 1999 2000 2001 2002 2003 2004 2005
2006 2007 2008 2009 2010 2011 2012 2013 2014
2015 2016 2017 2018 2019 2020 2021 2022 2023
2024 2025 2026 2027 2028 2029 2030 2031 2032
2033 2034 2035 2036 2037 2038 2039 2040 2041
2042 2043 2044 2045 2046 2047 2048 2049 2050
2051 2052 2053 2054 2055 2056 2057 2058 2059
2060 2061 2062 2063 2064 2065 2066 2067 2068
2069 2070 2071 2072 2073 2074 2075 2076 2077
2078 2079 2080 2081 2082 2083 2084 2085 2086
2087 2088 2089 2090 2091 2092 2093 2094 2095

2096 2097 2098 2099 2100 2101 2102 2103 2104
2105 2106 2107 2108 2109 2110 2111 2112

group b_outl union b_out1 b_out2 b_out3

group s_outl id 2113 2114 2115 2116 2117 2118 2119
2120 2121 2122 2123 2124 2125 2126 2127 2128
2129 2130 2131 2132 2133 2134 2135 2136 2137
2138 2139 2140 2141 2142 2143 2144 2145 2146
2147 2148 2149 2150 2151 2152 2153 2166 2167
2168 2169 2170 2183 2184 2185 2186 2187 2200
2201 2202 2203 2204 2205 2206 2207 2208 2209
2210 2211 2212 2213 2214 2215 2216 2217 2218
2219 2220 2221 2222 2223 2224 2225 2238 2239
2240 2241 2242 2243 2244 2257 2258 2259 2260
2261 2262 2263 2276 2277 2278 2279 2280 2281
2282 2283 2284 2285 2286 2287 2288 2289 2290
2291 2292 2293 2294 2295 2296 2297 2298 2299
2300 2313 2314 2315 2316 2317 2318 2331 2332
2333 2334 2335 2336 2349 2350 2351 2352 2353
2354 2355 2356 2357 2358 2359 2360 2361 2362
2363 2364 2365 2366 2367 2368 2369 2370 2371
2372 2373 2374 2375 2376 2377 2378 2379 2380
2381 2382 2383 2384 2385 2386 2387 2388

group the core atoms by moving outer layers

group b_core subtract b_ball b_outl

group s_core subtract s_ball s_outl

#group the single surface layer atoms

group b_surf id 1 2 3 4 5 6 7 8
9 10 11 12 13 14 15 16 595
596 597 598 599 688 689 726 727 728
765 766 767 804 805 894 895 896 897
898 899 900 901 902 903 904 997 998
1035 1036 1037 1038 1075 1076 1077 1078 1115
1116 1209 1210 1211 1212 1213 1214 1215 1216
1217 1218 1219 1308 1345 1346 1347 1348 1385
1386 1387 1388 1425 1514 1515 1516 1517 1518
2097 2098 2099 2100 2101 2102 2103 2104 2105
2106 2107 2108 2109 2110 2111 2112

```
group        s_surf id 2116    2119    2125    2128    2129    2132    2138
         2141    2144    2147    2151    2168    2184    2201    2205    2208
         2213    2216    2218    2221    2223    2239    2241    2244    2258
         2259    2263    2277    2281    2283    2285    2287    2295    2298
         2314    2318    2332    2336    2352    2355    2362    2365    2369
         2372    2373    2376    2380    2383


velocity       all create 1000.0 3451 mom yes rot yes dist uniform


fix              1   all nvt 1000.0 1000.0 0.10 drag 0.2
fix          2   all momentum 10 linear 1 1 1 angular


fix          stay_b b_ball recenter INIT INIT INIT units box
fix          stay_s s_ball recenter INIT INIT INIT units box

thermo           50
thermo_style    custom step temp pe etotal vol enthalpy

run          2000

unfix         stay_b
unfix         stay_s

#unfix         1
#fix          product all nvt 1000.0 3000.0 200.0 drag 0.2

fix          stay all recenter INIT INIT INIT units box

fix          3   all    rdf 10000 rdf_all_1000K     100  1 1
fix          4   b_ball rdf 10000 rdf_b_ball_1000K  100   1 1
fix          5   s_ball rdf 10000 rdf_s_ball_1000K  100  1 1


fix          6   b_ball ave/atom 10 10 500 x y z
fix          7   s_ball ave/atom 10 10 500 x y z

fix          8   b_neck ave/atom 10 10 500 vx vy vz
fix          9   s_neck ave/atom 10 10 500 vx vy vz


fix          10  b_ball msd  100 msd_b_ball_1000K.out
fix          11  s_ball msd  100 msd_s_ball_1000K.out
fix          12  b_neck msd  100 msd_b_neck_1000K.out
fix          13  s_neck msd  100 msd_s_neck_1000K.out
fix          14  b_surf msd  100 msd_b_surf_1000K.out
```

```
fix          15  s_surf msd  100 msd_s_surf_1000K.out
fix          16  b_outl msd  100 msd_b_outl_1000K.out
fix          17  s_outl msd  100 msd_s_outl_1000K.out

fix          18  b_core msd  100 msd_b_core_1000K.out
fix          19  s_core msd  100 msd_s_core_1000K.out

fix          20  b_core rdf 10000 rdf_b_core_1000K  100   1 1
fix          21  s_core rdf 10000 rdf_s_core_1000K  100   1 1

fix          22  b_outl rdf 10000 rdf_b_outl_1000K  100 1 1
fix          23  s_outl rdf 10000 rdf_s_outl_1000K  100 1 1

compute       1   b_ball ke/atom
compute       2   s_ball ke/atom
compute       3   b_neck ke/atom
compute       4   s_neck ke/atom

compute       5   b_ball pe/atom
compute       6   s_ball pe/atom
compute       7   b_neck pe/atom
compute       8   s_neck pe/atom

compute       9   b_surf ke/atom
compute       10  s_surf ke/atom

compute       11  b_surf pe/atom
compute       12  s_surf pe/atom

compute       13  b_core pe/atom
compute       14  s_core pe/atom

compute       15  b_outl pe/atom
compute       16  s_outl pe/atom

dump          b_ball_ke    b_ball custom 2000 b_ball_ke_1000K.dump c_1
dump          s_ball_ke    s_ball custom 2000 s_ball_ke_1000K.dump c_2

dump          b_neck_ke    b_neck custom 2000 b_neck_ke_1000K.dump
c_3
dump          s_neck_ke    s_neck custom 2000 s_neck_ke_1000K.dump c_4

dump          b_ball_pe    b_ball custom 2000 b_ball_pe_1000K.dump c_5
dump          s_ball_pe    s_ball custom 2000 s_ball_pe_1000K.dump c_6

dump          b_neck_pe    b_neck custom 2000 b_neck_pe_1000K.dump
c_7
dump          s_neck_pe    s_neck custom 2000 s_neck_pe_1000K.dump c_8
```

```
dump          b_surf_ke    b_surf custom 2000 b_surf_ke_1000K.dump c_9
dump          s_surf_ke    s_surf custom 2000 s_surf_ke_1000K.dump c_10

dump          b_surf_pe    b_surf custom 2000 b_surf_pe_1000K.dump c_11
dump          s_surf_pe    s_surf custom 2000 s_surf_pe_1000K.dump c_12

dump          b_core_pe    b_core custom 2000 b_core_pe_1000K.dump
c_13
dump          s_core_pe    s_core custom 2000 s_core_pe_1000K.dump c_14

dump          b_outl_pe    b_outl custom 2000 b_outl_pe_1000K.dump c_15
dump          s_outl_pe    s_outl custom 2000 s_outl_pe_1000K.dump c_16

dump          b_ball_ct    b_ball custom 1000 b_ball_ct_1000K.dump f_6[1]
f_6[2] f_6[3]
dump          s_ball_ct    s_ball custom 1000 s_ball_ct_1000K.dump f_7[1]
f_7[2] f_7[3]

dump          b_neck_v     b_neck custom 2000 b_neck_v_1000K.dump
f_8[1] f_8[2] f_8[3]
dump          s_neck_v     s_neck custom 2000 s_neck_v_1000K.dump f_9[1]
f_9[2] f_9[3]


timestep        0.001

log          log_sinter_1000K

dump          xyz_b_ball   b_ball atom 10000 b_ball_xyz
dump          xyz_s_ball   s_ball atom 10000 s_ball_xyz
dump          xyz_b_outl   b_outl atom 10000 b_outl_xyz
dump          xyz_s_outl   s_outl atom 10000 s_outl_xyz
dump          xyz_b_surf   b_surf atom 10000 b_surf_xyz
dump          xyz_s_surf   s_surf atom 10000 s_surf_xyz

dump            xyz all atom 50 Ni.sinter


run          20000

#jump          in.sinter5
```

Ni-Al system minimization

```
# minimization of the initial system
```

```
clear
echo            both
units           metal
boundary        s s s

atom_style      atomic
read_data       single.NiAl

pair_style      eam/alloy
pair_coeff      * * NiAlH_jea.eam.alloy Al Ni


#group setting

group           all type 1 2

group           al  type 1
group           ni  type 2
include         Al.group
include         Ni.group

neighbor        3.0 bin
neigh_modify    delay 10

restart         10 re.alloy

min_style       sd
minimize        0.5e-6 0.5e-8 200 394

jump            in.alloy
```

Ni-Al Heating

```
# HEATING
clear
echo            both
units           metal
boundary        s s s

atom_style      atomic
#read_data       single.NiAl
read_restart    re.alloy.181

pair_style      eam/alloy
pair_coeff      * * NiAlH_jea.eam.alloy Al Ni


#group setting
```

```
group           all type 1 2

group           al  type 1
group           ni  type 2
include         Al.group
include         Ni.group

neighbor        3.0 bin
neigh_modify      delay 10

#min_style        sd
#minimize         0.5e-6 0.5e-8 200 500


velocity        all create 200.0 838929 mom yes rot yes dist uniform

#Main FIXes and equilibrium

fix             1 all nvt 200.0 200.0 0.05 drag 0.2
fix             2 all momentum 10 linear 1 1 1 angular
fix             3 all recenter INIT INIT INIT units box

timestep        0.001

thermo          2000
thermo_style      custom step temp pe etotal enthalpy press vol


log             eq.200K

run             21819

unfix           1

fix             4 all nvt 200.0 300.0 0.05 drag 0.2

run             40000

log             log.heat1

unfix           4

fix             5 all nvt 300.0 1600.0 0.05 drag 0.2


#velocity vector
```

```
fix             vn ni   ave/atom  10 10 500 x y z
fix             va al   ave/atom  10 10 500 x y z

#MSD

fix             m1n  lay1_Ni    msd 100 msd_Nilay1_heat.out
fix             m2n  lay2_Ni    msd 100 msd_Nilay2_heat.out
fix             m3n  lay3_Ni    msd 100 msd_Nilay3_heat.out
fix             m4n  lay4_Ni    msd 100 msd_Nilay4_heat.out
fix             m5n  lay5_Ni    msd 100 msd_Nilay5_heat.out


fix             m1a  lay1_Al    msd 100 msd_Allay1_heat.out
fix             m2a  lay2_Al    msd 100 msd_Allay2_heat.out
fix             m3a  lay3_Al    msd 100 msd_Allay3_heat.out
fix             m4a  lay4_Al    msd 100 msd_Allay4_heat.out


#RDF

fix             r1n  lay1_Ni    rdf 10000 rdf_Nilay1_heat.out 100 2 2
fix             r2n  lay2_Ni    rdf 10000 rdf_Nilay2_heat.out 100 2 2
fix             r3n  lay3_Ni    rdf 10000 rdf_Nilay3_heat.out 100 2 2
fix             r4n  lay4_Ni    rdf 10000 rdf_Nilay4_heat.out 100 2 2
fix             r5n  lay5_Ni    rdf 10000 rdf_Nilay5_heat.out 100 2 2

fix             r1a  lay1_Al    rdf 10000 rdf_Allay1_heat.out 100 1 1
fix             r2a  lay2_Al    rdf 10000 rdf_Allay2_heat.out 100 1 1
fix             r3a  lay3_Al    rdf 10000 rdf_Allay3_heat.out 100 1 1
fix             r4a  lay4_Al    rdf 10000 rdf_Allay4_heat.out 100 1 1

#GYRATION RADIUS

fix             g1n  lay1_Ni    gyration 10000 gyp_Nilay1_heat.out
fix             g2n  lay2_Ni    gyration 10000 gyp_Nilay2_heat.out
fix             g3n  lay3_Ni    gyration 10000 gyp_Nilay3_heat.out
fix             g4n  lay4_Ni    gyration 10000 gyp_Nilay4_heat.out
fix             g5n  lay5_Ni    gyration 10000 gyp_Nilay5_heat.out
fix             gni  ni         gyration 10000 gyp_Ni_heat.out

fix             g1a  lay1_Al    gyration 10000 gyp_Allay1_heat.out
fix             g2a  lay2_Al    gyration 10000 gyp_Allay2_heat.out
fix             g3a  lay3_Al    gyration 10000 gyp_Allay3_heat.out
fix             g4a  lay4_Al    gyration 10000 gyp_Allay4_heat.out
fix             gal  al         gyration 10000 gyp_Al_heat.out

fix             gall  all       gyration 10000 gyp_all_heat.out
```

```
#POTENTIAL ENERGY-----------------------------------------------------


compute         e1n    lay1_Ni  pe/atom
compute         e2n    lay2_Ni  pe/atom
compute         e3n    lay3_Ni  pe/atom
compute         e4n    lay4_Ni  pe/atom
compute         e5n    lay5_Ni  pe/atom

compute         e6n    ni       pe/atom

compute         e1a    lay1_Al  pe/atom
compute         e2a    lay2_Al  pe/atom
compute         e3a    lay3_Al  pe/atom
compute         e4a    lay4_Al  pe/atom

compute         e5a    al       pe/atom

#STRESS--------------------------------------------------------------

compute         s1n    lay1_Ni  stress/atom
compute         s2n    lay2_Ni  stress/atom
compute         s3n    lay3_Ni  stress/atom
compute         s4n    lay4_Ni  stress/atom
compute         s5n    lay5_Ni  stress/atom

compute         s1a    lay1_Al  stress/atom
compute         s2a    lay2_Al  stress/atom
compute         s3a    lay3_Al  stress/atom
compute         s4a    lay4_Al  stress/atom

#coordination number-------------------------------------------------

compute         c1n    lay1_Ni  coord/atom 2.5
compute         c2n    lay2_Ni  coord/atom 2.5
compute         c3n    lay3_Ni  coord/atom 2.5
compute         c4n    lay4_Ni  coord/atom 2.5
compute         c5n    lay5_Ni  coord/atom 2.5

compute         c1a    lay1_Al  coord/atom 2.5
compute         c2a    lay2_Al  coord/atom 2.5
compute         c3a    lay3_Al  coord/atom 2.5
compute         c4a    lay4_Al  coord/atom 2.5
```

```
#DUMP SETTING------------------------------------------------------

dump        dp1n   lay1_Ni  custom 2000 Nilay1_pe.dump c_e1n
dump        dp2n   lay2_Ni  custom 2000 Nilay2_pe.dump c_e2n
dump        dp3n   lay3_Ni  custom 2000 Nilay3_pe.dump c_e3n
dump        dp4n   lay4_Ni  custom 2000 Nilay4_pe.dump c_e4n
dump        dp5n   lay5_Ni  custom 2000 Nilay5_pe.dump c_e5n

dump        dp6n   ni  custom 2000 shell_pe1100K.dump c_e6n

dump        dp1a   lay1_Al  custom 2000 Allay1_pe.dump c_e1a
dump        dp2a   lay2_Al  custom 2000 Allay2_pe.dump c_e2a
dump        dp3a   lay3_Al  custom 2000 Allay3_pe.dump c_e3a
dump        dp4a   lay4_Al  custom 2000 Allay4_pe.dump c_e4a

dump        dp5a   al  custom 2000 core_pe.dump c_e5a

#-------------------------------------------------------------------

dump        ds1n   lay1_Ni  custom 2000 Nilay1_st.dump c_s1n[1] c_s1n[2]
c_s1n[3] c_s1n[4]  c_s1n[5] c_s1n[6]

dump        ds2n   lay2_Ni  custom 2000 Nilay2_st.dump c_s2n[1] c_s2n[2]
c_s2n[3] c_s2n[4]  c_s2n[5] c_s2n[6]

dump        ds3n   lay3_Ni  custom 2000 Nilay3_st.dump c_s3n[1] c_s3n[2]
c_s3n[3] c_s3n[4]  c_s3n[5] c_s3n[6]

dump        ds4n   lay4_Ni  custom 2000 Nilay4_st.dump c_s4n[1] c_s4n[2]
c_s4n[3] c_s4n[4]  c_s4n[5] c_s4n[6]

dump        ds5n   lay5_Ni  custom 2000 Nilay5_st.dump c_s5n[1] c_s5n[2]
c_s5n[3] c_s5n[4]  c_s5n[5] c_s5n[6]



dump        ds1a   lay1_Al  custom 2000 Allay1_st.dump c_s1a[1] c_s1a[2]
c_s1a[3] c_s1a[4] c_s1a[4] c_s1a[6]

dump        ds2a   lay2_Al  custom 2000 Allay2_st.dump c_s2a[1] c_s2a[2]
c_s2a[3] c_s2a[4] c_s2a[4] c_s2a[6]

dump        ds3a   lay3_Al  custom 2000 Allay3_st.dump c_s3a[1] c_s3a[2]
c_s3a[3] c_s3a[4] c_s3a[4] c_s3a[6]

dump        ds4a   lay4_Al  custom 2000 Allay4_st.dump c_s4a[1] c_s4a[2]
c_s4a[3] c_s4a[4] c_s4a[4] c_s4a[6]
```

```
#-----------------------------------------------------------------

dump        dc1n   lay1_Ni  custom 2000 Nilay1_cn.dump c_c1n
dump        dc2n   lay2_Ni  custom 2000 Nilay2_cn.dump c_c2n
dump        dc3n   lay3_Ni  custom 2000 Nilay3_cn.dump c_c3n
dump        dc4n   lay4_Ni  custom 2000 Nilay4_cn.dump c_c4n
dump        dc5n   lay5_Ni  custom 2000 Nilay5_cn.dump c_c5n

dump        dc1a   lay1_Al  custom 2000 Allay1_cn.dump c_c1a
dump        dc2a   lay2_Al  custom 2000 Allay2_cn.dump c_c2a
dump        dc3a   lay3_Al  custom 2000 Allay3_cn.dump c_c3a
dump        dc4a   lay4_Al  custom 2000 Allay4_cn.dump c_c4a


dump        dvn   ni  custom 2000 Ni_v_1100K.dump f_vn[1] f_vn[2]
f_vn[3]
dump        dva   al  custom 2000 Al_v_1100K.dump f_va[1] f_va[2]
f_va[3]


dump        xyz_n1    lay1_Ni atom 10000 lay1_Ni_xyz
dump        xyz_n2    lay2_Ni atom 10000 lay2_Ni_xyz
dump        xyz_n3    lay3_Ni atom 10000 lay3_Ni_xyz
dump        xyz_n4    lay4_Ni atom 10000 lay4_Ni_xyz
dump        xyz_n5    lay5_Ni atom 10000 lay5_Ni_xyz

dump        xyz_a1    lay1_Al atom 10000 lay1_Al_xyz
dump        xyz_a2    lay2_Al atom 10000 lay2_Al_xyz
dump        xyz_a3    lay3_Al atom 10000 lay3_Al_xyz
dump        xyz_a4    lay4_Al atom 10000 lay4_Al_xyz

log          log.NVT
dump           1 all atom 1000 all_NVT.trj
dump           2 al  atom 1000 core_NVT.trj
dump           3 ni  atom 1000 shell_NVT.trj

run          2000000
```

Ni-Al Solidification

```
# FAST COOLING

clear
echo          both
units         metal
boundary        s s s

atom_style      atomic
```

```
#read_data          single.NiAl
read_restart       re.alloy.181

pair_style         eam/alloy
pair_coeff         * * NiAlH_jea.eam.alloy Al Ni

#group setting



group              all type 1 2

group              al  type 1
group              ni  type 2
include            Al.group
include            Ni.group

neighbor           3.0 bin
neigh_modify       delay 10

#min_style         sd
#minimize          0.5e-6 0.5e-8 200 500


velocity           all create 200.0 984545 mom yes rot yes dist uniform

#Main FIXes and equilibrium

fix                1 all nvt 200.0 200.0 0.05 drag 0.2
fix                2 all momentum 10 linear 1 1 1 angular
fix                3 all recenter INIT INIT INIT units box

timestep           0.001

thermo             10000
thermo_style       custom step temp pe etotal enthalpy press vol

restart            1000 re.alloyfast

log                eq.200K

run                29819

unfix              1

fix                4 all nvt 200.0 1600.0 0.01 drag 0.2

run                70000
```

```
log             log.heat1

unfix           4

fix             5 all nvt 1600.0 1600.0 0.01 drag 0.2

run             100000

unfix           5

fix             6  all nvt 1600.0 300.0 0.01 drag 0.2
#velocity vector

fix             vn ni   ave/atom  10 10 100 x y z
fix             va al   ave/atom  10 10 100 x y z

#MSD

fix             m1n  lay1_Ni    msd 10000 msd_Nilay1_f.out
fix             m2n  lay2_Ni    msd 10000 msd_Nilay2_f.out
fix             m3n  lay3_Ni    msd 10000 msd_Nilay3_f.out
fix             m4n  lay4_Ni    msd 10000 msd_Nilay4_f.out
fix             m5n  lay5_Ni    msd 10000 msd_Nilay5_f.out


fix             m1a  lay1_Al    msd 10000 msd_Allay1_f.out
fix             m2a  lay2_Al    msd 10000 msd_Allay2_f.out
fix             m3a  lay3_Al    msd 10000 msd_Allay3_f.out
fix             m4a  lay4_Al    msd 10000 msd_Allay4_f.out


#RDF

fix             r1n  lay1_Ni    rdf 10000 rdf_Nilay1_f.out 100 2 2
fix             r2n  lay2_Ni    rdf 10000 rdf_Nilay2_f.out 100 2 2
fix             r3n  lay3_Ni    rdf 10000 rdf_Nilay3_f.out 100 2 2
fix             r4n  lay4_Ni    rdf 10000 rdf_Nilay4_f.out 100 2 2
fix             r5n  lay5_Ni    rdf 10000 rdf_Nilay5_f.out 100 2 2

fix             r1a  lay1_Al    rdf 10000 rdf_Allay1_f.out 100 1 1
fix             r2a  lay2_Al    rdf 10000 rdf_Allay2_f.out 100 1 1
fix             r3a  lay3_Al    rdf 10000 rdf_Allay3_f.out 100 1 1
fix             r4a  lay4_Al    rdf 10000 rdf_Allay4_f.out 100 1 1

#GYRATION RADIUS

fix             g1n  lay1_Ni    gyration 10000 gyp_Nilay1_f.out
```

```
fix             g2n  lay2_Ni    gyration 10000 gyp_Nilay2_f.out
fix             g3n  lay3_Ni    gyration 10000 gyp_Nilay3_f.out
fix             g4n  lay4_Ni    gyration 10000 gyp_Nilay4_f.out
fix             g5n  lay5_Ni    gyration 10000 gyp_Nilay5_f.out
fix             g6n  ni         gyration 10000 gyp_ni_f.out

fix             g1a  lay1_Al    gyration 10000 gyp_Allay1_f.out
fix             g2a  lay2_Al    gyration 10000 gyp_Allay2_f.out
fix             g3a  lay3_Al    gyration 10000 gyp_Allay3_f.out
fix             g4a  lay4_Al    gyration 10000 gyp_Allay4_f.out
fix             g5a  al         gyration 10000 gyp_al_f.out

fix             gall  all       gyration 10000 gyp_all_f.out

#POTENTIAL ENERGY-----------------------------------------------


compute         e1n    lay1_Ni  pe/atom
compute         e2n    lay2_Ni  pe/atom
compute         e3n    lay3_Ni  pe/atom
compute         e4n    lay4_Ni  pe/atom
compute         e5n    lay5_Ni  pe/atom

compute         e6n    ni       pe/atom

compute         e1a    lay1_Al  pe/atom
compute         e2a    lay2_Al  pe/atom
compute         e3a    lay3_Al  pe/atom
compute         e4a    lay4_Al  pe/atom

compute         e5a    al       pe/atom

#STRESS-------------------------------------------------------

compute         s1n    lay1_Ni  stress/atom
compute         s2n    lay2_Ni  stress/atom
compute         s3n    lay3_Ni  stress/atom
compute         s4n    lay4_Ni  stress/atom
compute         s5n    lay5_Ni  stress/atom

compute         s1a    lay1_Al  stress/atom
compute         s2a    lay2_Al  stress/atom
compute         s3a    lay3_Al  stress/atom
compute         s4a    lay4_Al  stress/atom

#coordination number-----------------------------------------

compute         c1n    lay1_Ni  coord/atom 2.5
```

```
compute       c2n   lay2_Ni  coord/atom 2.5
compute       c3n   lay3_Ni  coord/atom 2.5
compute       c4n   lay4_Ni  coord/atom 2.5
compute       c5n   lay5_Ni  coord/atom 2.5

compute       c1a   lay1_Al  coord/atom 2.5
compute       c2a   lay2_Al  coord/atom 2.5
compute       c3a   lay3_Al  coord/atom 2.5
compute       c4a   lay4_Al  coord/atom 2.5


#DUMP SETTING-------------------------------------------------------
dump          dp1n   lay1_Ni  custom 10000 Nilay1_pef.dump c_e1n
dump          dp2n   lay2_Ni  custom 10000 Nilay2_pef.dump c_e2n
dump          dp3n   lay3_Ni  custom 10000 Nilay3_pef.dump c_e3n
dump          dp4n   lay4_Ni  custom 10000 Nilay4_pef.dump c_e4n
dump          dp5n   lay5_Ni  custom 10000 Nilay5_pef.dump c_e5n

dump          dp6n   ni  custom 10000 shell_pef.dump c_e6n

dump          dp1a   lay1_Al  custom 10000 Allay1_pef.dump c_e1a
dump          dp2a   lay2_Al  custom 10000 Allay2_pef.dump c_e2a
dump          dp3a   lay3_Al  custom 10000 Allay3_pef.dump c_e3a
dump          dp4a   lay4_Al  custom 10000 Allay4_pef.dump c_e4a

dump          dp5a   al  custom 10000 core_pef.dump c_e5a

dump          ds1n   lay1_Ni  custom 10000 Nilay1_stf.dump c_s1n[1]
c_s1n[2] c_s1n[3] c_s1n[4]  c_s1n[5] c_s1n[6]

dump          ds2n   lay2_Ni  custom 10000 Nilay2_stf.dump c_s2n[1]
c_s2n[2] c_s2n[3] c_s2n[4]  c_s2n[5] c_s2n[6]

dump          ds3n   lay3_Ni  custom 10000 Nilay3_stf.dump c_s3n[1]
c_s3n[2] c_s3n[3] c_s3n[4]  c_s3n[5] c_s3n[6]

dump          ds4n   lay4_Ni  custom 10000 Nilay4_stf.dump c_s4n[1]
c_s4n[2] c_s4n[3] c_s4n[4]  c_s4n[5] c_s4n[6]

dump          ds5n   lay5_Ni  custom 10000 Nilay5_stf.dump c_s5n[1]
c_s5n[2] c_s5n[3] c_s5n[4]  c_s5n[5] c_s5n[6]


dump          ds1a   lay1_Al  custom 10000 Allay1_stf.dump c_s1a[1]
c_s1a[2] c_s1a[3] c_s1a[4] c_s1a[4] c_s1a[6]

dump          ds2a   lay2_Al  custom 10000 Allay2_stf.dump c_s2a[1]
c_s2a[2] c_s2a[3] c_s2a[4] c_s2a[4] c_s2a[6]
```

```
dump          ds3a   lay3_Al  custom 10000 Allay3_stf.dump c_s3a[1]
c_s3a[2] c_s3a[3] c_s3a[4] c_s3a[4] c_s3a[6]

dump          ds4a   lay4_Al  custom 10000 Allay4_stf.dump c_s4a[1]
c_s4a[2] c_s4a[3] c_s4a[4] c_s4a[4] c_s4a[6]


dump          dc1n   lay1_Ni  custom 10000 Nilay1_cnf.dump c_c1n
dump          dc2n   lay2_Ni  custom 10000 Nilay2_cnf.dump c_c2n
dump          dc3n   lay3_Ni  custom 10000 Nilay3_cnf.dump c_c3n
dump          dc4n   lay4_Ni  custom 10000 Nilay4_cnf.dump c_c4n
dump          dc5n   lay5_Ni  custom 10000 Nilay5_cnf.dump c_c5n

dump          dc1a   lay1_Al  custom 10000 Allay1_cnf.dump c_c1a
dump          dc2a   lay2_Al  custom 10000 Allay2_cnf.dump c_c2a
dump          dc3a   lay3_Al  custom 10000 Allay3_cnf.dump c_c3a
dump          dc4a   lay4_Al  custom 10000 Allay4_cnf.dump c_c4a

dump          dvn   ni  custom 10000 Ni_v_f.dump f_vn[1] f_vn[2] f_vn[3]
dump          dva   al  custom 10000 Al_v_f.dump f_va[1] f_va[2] f_va[3]

dump          xyz_n1    lay1_Ni atom 10000 lay1_Ni_xyz_f
dump          xyz_n2    lay2_Ni atom 10000 lay2_Ni_xyz_f
dump          xyz_n3    lay3_Ni atom 10000 lay3_Ni_xyz_f
dump          xyz_n4    lay4_Ni atom 10000 lay4_Ni_xyz_f
dump          xyz_n5    lay5_Ni atom 10000 lay5_Ni_xyz_f

dump          xyz_a1    lay1_Al atom 10000 lay1_Al_xyz_f
dump          xyz_a2    lay2_Al atom 10000 lay2_Al_xyz_f
dump          xyz_a3    lay3_Al atom 10000 lay3_Al_xyz_f
dump          xyz_a4    lay4_Al atom 10000 lay4_Al_xyz_f

log             log.fastalloy
dump              1 all atom 10000 all_f*
dump              2 al  atom 10000 core_f*
dump              3 ni  atom 10000 shell_f*

run             200000

# for slow cooling, only the run step are adjusted
```

Silicon Oxidation

```
# Minimization for silicon cluster

units           metal

boundary        p p p
```

```
atom_style      full
read_data       si.cluster

pair_style      reax 10.0 1.0e-6
pair_coeff      * * ffield.reax 6

#bond_style     harmonic
#bond_coeff     1  150.0000 1.21

run_style       respa 4 2 2 2 bond 1 pair 3 kspace 4

dump            1 all custom 1 sixyz.dump* id mol type q x y z

min_style       sd
minimize        0.5e-5 0.5e-7 500 1000

# Equilibration of oxidation
units           real

boundary        p p p

atom_style      full
read_restart    push.siox.5000

pair_style      reax 10.0 1.0e-6
pair_coeff      * * ffield.reax 6 3

bond_style      harmonic
bond_coeff      1  777.0000 1.21

run_style       respa 4 2 2 2 bond 1 pair 3 kspace 4

#min_style      sd
#minimize       0.5e-6 0.5e-8 200 400

neighbor        2.0 bin
neigh_modify    every 10 delay 0 check no

group           all type 1 2

group           si  id > 320
group           ox  id <= 320


#velocity       si create 1000.0 838929 mom yes rot yes dist gaussian
#velocity       ox create 1000.0 64543 mom yes rot yes dist gaussian
fix             3 all momentum 10 linear 1 1 1 angular
```

```
fix             4 si recenter INIT INIT INIT units box
#fix             5 ox  shake  0.0001 100 0 b 1 a 1

fix                 1 all nvt 1000.0 1000.0 5.0 drag 0.2

thermo          10
thermo_modify           format float %15.14g

timestep        2.5

dump            1 all atom 10 siox.lammpstrj

dump            2 ox custom 10 oxforce.dump id mol fx fy fz

restart         10 eq.siox

run             100000

#ANNEALING
clear

units           real

boundary        p p p

atom_style      full
read_data       extd.cell

pair_style      reax 10.0 1.0e-6
pair_coeff      * * ffield.reax 6

#bond_style      harmonic
#bond_coeff      1  150.0000 1.21

#run_style       respa 4 2 2 2 bond 1 pair 3 kspace 4

#min_style          sd
#minimize           0.5e-5 0.5e-7 500 1000

neighbor        0.3 bin
neigh_modify  every 10 delay 0 check no

group           all type 1

#velocity        si create 600.0 83895 mom yes rot yes dist gaussian
#velocity        ox create 600.0 64543 mom yes rot yes dist gaussian

velocity        all create 500.0 7583 mom yes rot yes dist gaussian
```

```
fix             1 all nvt 500.0 500.0 5.0 drag 0.2

fix             3 all momentum 10 linear 1 1 1 angular

#fix            4 si recenter INIT INIT INIT units box
#fix            5 ox  shake  0.0001 100 0 b 1 a 1

thermo          10
thermo_modify           format float %15.14g

timestep        1

run             5000

unfix           1

fix             heat all nvt 500.0 1750.0 5.0 drag 0.2

run             40000

unfix           heat

fix             cool all nvt 1750.0 500.0 5.0 drag 0.2

dump            1 all atom 100 si.lammpstrj

dump            2 all custom 10000 sixyz.data* id mol type q x y z

run             100000

# OXIDATION
echo            both
units           real
boundary        p p p

atom_style      charge
#read_data      sioxON.data
read_restart    eq.sioxEXTD.100000

pair_style      reax 12.0 1.0e-6
pair_coeff      * * ffield.reax 6 3

run_style       respa 4 2 2 2 bond 1 pair 3 kspace 4

neighbor        2.0 bin
neigh_modify    every 10 delay 0 check no
```

```
group          all type 1 2

group          si  id <= 184
group          ox  id > 184

fix            allsim all nvt 300 2000 1.0 drag 0.5

fix            b1 si reax/bonds  100000 sibond
fix            b2 ox reax/bonds  100000 oxibond
fix            b3 all reax/bonds  100000 allbond

fix            stay1 all momentum 10 linear 1 1 1 angular
fix            stay2 si momentum 10 linear 1 1 1 angular
fix            stay3 si recenter INIT INIT INIT units box


fix            m1n  si    msd 50000 msd_sifix.out
fix            m2n  ox    msd 50000 msd_oxfix.out

fix            g1   si    gyration 50000 gyp_sifix.out

thermo           10
thermo_style    custom step temp pe etotal epair emol elong enthalpy press
vol

timestep         0.25

compute         1    si  pe/atom
compute         2    si  stress/atom
dump           si1  si  custom 20000 si_pesfix.dump c_1
dump           si2  si  custom 20000 si_stsfix.dump c_2[1] c_2[2] c_2[3]
c_2[4]  c_2[5] c_2[6]

log            logSimrest.reax

dump             1 all custom 100 sioxfix.lammpstrj id type xs ys zs

dump           2 all custom 10000 trjallfix* id type q x y z

dump             3 all xyz 100 sioxnvtfix.xyz

dump           4 si custom  50000 trjsi* id q x y z vx vy vz fx fy fz

dump           5 ox custom  50000 trjox* id q x y z vx vy vz fx fy fz

restart        100000 nvt.fix*

run              1000000
```

Appendix 2

MATLAB codes

TGA kinetic analysis

```
% Nickel oxidation experiments by Pengxiang Song July 2007

% colloum 1             2         3           4
%    Time (minute)    T (degree C)      q(mW)      weight (mg)

% upload data


%initial oxide mass and percentage

int_mass=[9.969 9.958 10.083 10.060 9.980 10.031 10.000];% in
unit of mg
int_oxide=[0.647 0.606 0.849 0.851 0.625 0.826 0.975];%in
unit of mg

R=8.314472;%gas constant
eV=1.60217653e-19;%in unit of joule
Na=6.02214179e23;%avgardro constant
E=1.6*eV*Na/1000;%in unit of kJ/mol

load nickel_2cmin.txt;     % heating rate 2C/min
Data1=nickel_2cmin;

load nickel_5cmin.txt;     % heating rate 5C/min
Data2=nickel_5cmin;

load nickel_8cmin.txt;     % heating rate 8C/min
Data3=nickel_8cmin;

load nickel_10cmin.txt;    % heating rate 10C/min
Data4=nickel_10cmin;

load nickel_12cmin.txt;    % heating rate 12C/min
Data5=nickel_12cmin;

load nickel_15cmin.txt;    % heating rate 15C/min
Data6=nickel_15cmin;

load nickel_20cmin.txt;     % heating rate 20C/min
Data7=nickel_20cmin;


% assign data to variables time, tem, heat and mass, Data1
N1start=1;
```

```
N1end=27225;                 %effective data range
time1=Data1((N1start:N1end),1);
Tem1=Data1((N1start:N1end),2);
Heat1=Data1((N1start:N1end),3);  % DSC data
mass1=Data1((N1start:N1end),4);  % TG data
len1=length(time1); % total data points

%total experimental time in second;
t1=(time1(end)-time1(1))*60;
%time interval
dt1=t1/(length(time1)-1);
% repeat the section through all data Data1~Data7

%modify data by initial oxide
mass1=mass1-int_oxide(1);
mass2=mass2-int_oxide(2);
mass3=mass3-int_oxide(3);
mass4=mass4-int_oxide(4);
mass5=mass5-int_oxide(5);
mass6=mass6-int_oxide(6);
mass7=mass7-int_oxide(7);
%percentage of mass increase
massp1=mass1./(mass1(1));
massp2=mass2./(mass2(1));
massp3=mass3./(mass3(1));
massp4=mass4./(mass4(1));
massp5=mass5./(mass5(1));
massp6=mass6./(mass6(1));
massp7=mass7./(mass7(1));

NN=10;     % averaging the first and last effective NN data
mass_inc1=mean(mass1(end-NN+1:end))/mean(mass1(1:NN));
mass_inc2=mean(mass2(end-NN+1:end))/mean(mass2(1:NN));
mass_inc3=mean(mass3(end-NN+1:end))/mean(mass3(1:NN));
mass_inc4=mean(mass4(end-NN+1:end))/mean(mass4(1:NN));
mass_inc5=mean(mass5(end-NN+1:end))/mean(mass5(1:NN));
mass_inc6=mean(mass6(end-NN+1:end))/mean(mass6(1:NN));
mass_inc7=mean(mass7(end-NN+1:end))/mean(mass7(1:NN));
mass_inc=[mass_inc1 mass_inc2  mass_inc3 mass_inc4 mass_inc5
mass_inc6 mass_inc7];

%the maximum increase can be find from massp maxtrix
mass_max=[max(massp1) max(massp2) max(massp3) max(massp4)
max(massp5) max(massp6) max(massp7)];

dN=0.0125
Qmax1=0;
Tmax1=0;
j=1;
for i=N1start:N1end
    if Qmax1<Heat1(i)                  % find DSC peak and
corresponding temperautre
        Qmax1=Heat1(i);
        Tmax1=Tem1(i);
    end
```

```
    if massp1(i)>massp1(1)+j*dN           %  find the
temperature at each specified conversion rate, dN, 2dN,
3dN...................
        T1(j)=Tem1(i-1)+(Tem1(i)-Tem1(i-1))*(massp1(1)+j*dN-
massp1(i-1))/(massp1(i)-massp1(i-1));
        N1cov(j)=i; %record the conversion index
        j=j+1;
    end
end
Qmax_DSC=[Qmax1 Qmax2 Qmax3 Qmax4 Qmax5 Qmax6 Qmax7];% DSC
peak value

Tmax_DSC=[Tmax1 Tmax2 Tmax3 Tmax4 Tmax5 Tmax6 Tmax7];
%-Temperature at DSC peak value
% Qmax_DSC=[1.9466   11.2292   20.7584   25.9005   32.8574
43.4801   57.4344]
% Tmax_DSC=[ 362.0800  378.3600  387.3000  389.7400  398.0600
401.2900  403.4900]

% organizing the temperature data at different conversion
rate, the length of T is different, so not to use the last
conversion rate data
N1=1;  % the point that the temperature begin steadily
increase through data inspection in Excel
NN1=60;  % one minute interval for differentiation, can be
changed to different value
windowSize=6;  % window size for filtering.

Ndt1=NN1*dt1; %Selected time interval
t1=(time1(N1:NN1:len1)-time1(N1))*60;  % unit in second,
starting from t=0;
T1=Tem1(N1:NN1:len1);
Q1=Heat1(N1:NN1:len1);
M1=mass1(N1:NN1:len1);
M1p=M1./M1(1);
M1p=(M1p-1)/0.277;

%find out the index of different conversion ratios
j=1;
for i=1:length(M1p)
    if M1p(i)>=j*0.05
        NN1cov(j)=i;
        j=j+1;
    end
end

%variable gradient
for i=1:length(t1)-1
    %mass gradient
    dmdt1(i)=(M1(i+1)-M1(i))/Ndt1;
    %temperature gradient
    dTdt1(i)=(T1(i+1)-T1(i))/Ndt1;
    %conversion ratio garadient
    dCdt1(i)=(M1p(i+1)-M1p(i))/Ndt1;
    %heat flux gradient
    dQdt1(i)=(Q1(i+1)-Q1(i))/Ndt1;
end
```

```
%filtering data using moving window method, if windowSize =1,
the result yy1 == dmdt1
yy1=filter(ones(1,windowSize)/windowSize,1,dmdt1);
tt1=filter(ones(1,windowSize)/windowSize,1,dTdt1);
qq1=filter(ones(1,windowSize)/windowSize,1,dQdt1);

%selected data for analysis DATA 2
%Regarding Ukrine paper,Koshelev
%half-conversion derived rate
(T/T(0.5))^2*[(d(alpha)/dt)/(d(alpha)/dt)at conversion ration
0.5]

dr1=((T1(1:length(T1)-
1)'/T1(NN1cov(10))).^2).*(dCdt1/dCdt1(NN1cov(10)));
dr2=((T2(1:length(T2)-
1)'/T2(NN2cov(10))).^2).*(dCdt2/dCdt2(NN2cov(10)));
dr3=((T3(1:length(T3)-
1)'/T3(NN3cov(10))).^2).*(dCdt3/dCdt3(NN3cov(10)));
dr4=((T4(1:length(T4)-
1)'/T4(NN4cov(10))).^2).*(dCdt4/dCdt4(NN4cov(10)));
dr5=((T5(1:length(T5)-
1)'/T5(NN5cov(10))).^2).*(dCdt5/dCdt5(NN5cov(10)));
dr6=((T6(1:length(T6)-
1)'/T6(NN6cov(10))).^2).*(dCdt6/dCdt6(NN6cov(10)));
dr7=((T7(1:length(T7)-
1)'/T7(NN7cov(10))).^2).*(dCdt7/dCdt7(NN7cov(10)));

%different model plots
%Comprehansive models fitting
a=(0.05:0.005:0.95);
%Reaction-order models
G1=-log(1-a);%1st order
G2=(1-a).^(-1)-1;%2nd order
G3=0.5*((1-a).^(-2)-1);%3rd order
% phase boundary reaction
G4=a;%one-dimensional symmetry,also zero order reaction
G5=(1-a).^(-1);
G6=(1-a).^(-2);
G7=1-(1-a).^(1/2);%cylindrical symmetry
G8=1-(1-a).^(1/3);%spherical symmetry
%Diffusional Models
G9=a.^2;%one dimension
G10=(1-a).*(log(1-a))+a;%two dimension
G11=(1-(1-a).^(1/3)).^2;%three dimension symmetry, 'Jander
equation'
G12=(1-2*a/3)-(1-a).^(2/3);%three dimension dimension,
'Guintling-Brounshtein equation
%Nucleation Models
%Powder law
G13=a.^(1/2);
G14=a.^(1/3);
G15=a.^(1/4);
%Avrami-Erofeev
G16=(-log(1-a)).^(2/3);%Avrami-Erofeev(n=1.5)
G17=(-log(1-a)).^(1/2);%Avrami-Erofeev(n=2)
G18=(-log(1-a)).^(1/3);%Avrami-Erofeev(n=3)
G19=(-log(1-a)).^(1/4);%Avrami-Erofeev(n=4)
G20=(-log(1-a)).^(1/5);%Avrami-Erofeev(n=5), NOT REALISTIC!
```

```
G21=(-log(1-a)).^(1/6);%Avrami-Erofeev(n=6), NOT REALISTIC!
G22=(-log(1-a)).^(1/7);%Avrami-Erofeev(n=7), NOT REALISTIC!
G23=(-log(1-a)).^(1/8);%Avrami-Erofeev(n=8), NOT REALISTIC!
G24=(1-(1-a).^(1/3)).^2;
G25=((1+a).^(1/3)-1).^2;
G26=((1-a).^(-1/3)-1).^2;
G27=log(a./(1-a));%Prout¨CTompkins
G28=a.^(2/3);
G29=-log(1-a.^2);
%Geometrical Contraction models
G30=1-(1-a).^(1/2);%Contracting area
G31=1-(1-a).^(1/3);%Contracting volume
G32=1-(1-a).^(2/3);
G33=(1-a).^(-1/2);
G34=(-log(1-a)).^2;
G35=(-log(1-a)).^3;
G36=(-log(1-a)).^4;
G37=(-log(1-a)).^5;
G38=(1-a).^(-2)-1;
G39=(1-(1-a)).^(1/4);
G40=((1-(1-a).^(1/3)).^(1/2)).*(1-a);
G41=((1-(1-a).^(1/3)).^(1/2)).*((1-a).^2);
G42=(1-(1-a).^(1/3)).^(1/2).*((1-a).^3);
G43=(1-(1-a).^(1/2)).^(1/2);
G44=1-(1-a).^2;
G45=1-(1-a).^3;
G46=1-(1-a).^4;


T1k=T1+273.15;
T2k=T2+273.15;
T3k=T3+273.15;
T4k=T4+273.15;
T5k=T5+273.15;
T6k=T6+273.15;
T7k=T7+273.15;

y1=E*((R*T1k).^(-1));
p1y=exp(-0.377739-1.894661*log(y1)-1.001450*y1);
y2=E*((R*T2k).^(-1));
p2y=exp(-0.377739-1.894661*log(y2)-1.001450*y2);
y3=E*((R*T3k).^(-1));
p3y=exp(-0.377739-1.894661*log(y3)-1.001450*y3);
y4=E*((R*T4k).^(-1));
p4y=exp(-0.377739-1.894661*log(y4)-1.001450*y4);
y5=E*((R*T5k).^(-1));
p5y=exp(-0.377739-1.894661*log(y5)-1.001450*y5);
y6=E*((R*T6k).^(-1));
p6y=exp(-0.377739-1.894661*log(y6)-1.001450*y6);
y7=E*((R*T7k).^(-1));
p7y=exp(-0.377739-1.894661*log(y7)-1.001450*y7);


% The calculation method has been tested by example data and
kinetic informatino from Zhang et al. 2007 Acta Phys. 23(7)
1095-1098

clear;
```

```
% gas constant, kJ/molk
R=8.314;
% eV and J/mol conversion unit, 1ev=96485.38 J/mol
XX=96485.38;

% data from Getdata curve, kinetic_data_2.m
data=273.15+[273.1183  290.3226  296.7742  296.7742  303.2258
305.3763  318.2796
  301.0753  320.4301  326.8817  329.0323  335.4839  339.7849
350.5376
  318.2796  337.6344  348.3871  348.3871  354.8387  356.9892
367.7419
  331.1828  348.3871  359.1398  361.2903  365.5914  369.8925
378.4946
  339.7849  359.1398  367.7419  369.8925  376.3441  380.6452
387.0968
  348.3871  365.5914  376.3441  378.4946  384.9462  389.2473
395.6989
  354.8387  374.1935  382.7957  387.0968  391.3978  395.6989
402.1505
  361.2903  380.6452  391.3978  393.5484  400.0000  404.3011
408.6022
  369.8925  387.0968  397.8495  400.0000  406.4516  410.7527
417.2043
  376.3441  393.5484  404.3011  406.4516  415.0538  417.2043
423.6559
  382.7957  402.1505  410.7527  415.0538  421.5054  425.8065
432.2581
  391.3978  410.7527  421.5054  423.6559  432.2581  434.4086
443.0108
  404.3011  421.5054  432.2581  436.5591  445.1613  447.3118
458.0645
  425.8065  438.7097  451.6129  455.9140  466.6667  466.6667
481.7204
  460.2151  473.1183  488.1720  490.3226  505.3763  503.2258
524.7312
  486.0215  505.3763  522.5806  526.8817  539.7849  539.7849
561.2903
  520.4301  539.7849  556.9892  561.2903  576.3441  574.1935
597.8495
  565.5914  580.6452  600.0000  608.6022  625.8065  621.5054
653.7634
  638.7097  647.3118  666.6667  677.4194  698.9247  686.0215
739.7849];

data_daphadt=0.0001*[ 0.2993    0.9476    1.5065    1.8339
2.2194    2.8477    3.7795
    0.7081    1.7570    2.4477    3.3701    4.3594    5.3545
7.6918
    1.0561    2.7926    4.3648    5.1620    6.8656    8.6678
12.4920
    1.3791    3.7919    6.1611    7.3114    9.4228   11.8020
17.7760
    1.7960    4.6580    7.7076    9.3674   11.4574   14.2505
21.8380
    2.0711    5.3220    8.8095   10.8635   12.8551   16.1691
24.7139
```

```
    2.2941    5.7667    9.3105   11.4936   13.9965   18.0112
25.5730
    2.3101    5.9762    9.5659   11.8125   13.9906   18.2145
24.9060
    2.3827    5.9597    9.3875   11.6259   13.7395   17.9826
23.2153
    2.2933    5.7536    8.9614   10.9661   12.4763   16.7906
20.8762
    2.1104    5.3185    7.8833    9.6823   11.2270   14.5635
17.8583
    1.9248    4.6886    6.7130    9.0746    9.6770   12.9241
14.5151
    1.2069    3.1942    4.9407    5.8695    6.1267    8.9997
9.5927
    0.5871    1.5747    2.5079    3.1577    2.8453    4.3619
4.7415
    0.4714    1.2502    1.8675    2.3973    2.4904    3.2534
4.5735
    0.5593    1.2828    1.9497    2.6442    2.7364    3.4271
4.4159
    0.4325    1.1438    1.9726    1.9624    2.4332    3.2208
4.2245
    0.3234    0.9204    1.5159    1.7620    1.7230    2.9411
2.9146
    0.1079    0.4370    0.7219    1.0072    1.1887    1.7198
1.4495];

% conversion rate
alpha=[0.05:0.05:0.95];
x=alpha;
%heating rate
dTdt=[2 5 8 10 12 15 20];


% Try the Friedman method

for j=1:length(data(:,1))
DSC_Tp=data(j,:);
% reverse of temperature,   1/T,
DSC_Tp_r=1./DSC_Tp;

for i=1:length(dTdt)
%Kissinger method
    lgdTdt_k(j,i)=-log(dTdt(i)/DSC_Tp(i)^2);
% Starink method
    lgdTdt_s(j,i)=-log(dTdt(i)/DSC_Tp(i)^1.8);
% ASTM E698 method based on Flynn-Wall-Ozawa method , only
this one uses tdhe log10 function
    lgdTdt_a(j,i)=-log10(dTdt(i));
% Boswell method
    lgdTdt_b(j,i)=-log(dTdt(i)/DSC_Tp(i));
% Ozawa method
    lgdTdt_o(j,i)=-log(dTdt(i));
 % Friedman method
   lgdalphadt_f(j,i)=-log(data_daphadt(j,i));
end

%linear fitting to above curve
```

```
fit_k = polyfit(DSC_Tp_r,lgdTdt_k(j,:),1);
fit_s = polyfit(DSC_Tp_r,lgdTdt_s(j,:),1);
fit_a = polyfit(DSC_Tp_r,lgdTdt_a(j,:),1);
fit_b = polyfit(DSC_Tp_r,lgdTdt_b(j,:),1);
fit_o = polyfit(DSC_Tp_r,lgdTdt_o(j,:),1);
fit_f = polyfit(DSC_Tp_r,lgdalphadt_f(j,:),1);


%Activation energy calculation
% Kissinger method
Ea_k(j)=fit_k(1)*R/XX;
% Starink method
Ea_s(j)=(fit_s(1)*R*1.0049)/XX;        % need to integrate a
few steps to get the constant B,1.0049 is estimation based on
Ea from other methods
% ASTM method
Ea_a(j)=(fit_a(1)*R*2.19)/XX;           % need to be further
refined based on the ASTM procedure
%Boswell method
Ea_b(j)=(fit_b(1)*R)/XX;
% Ozawa method
Ea_o(j)=(fit_o(1)*R/1.0518)/XX;
%Friedman method
Ea_f(j)=(fit_f(1)*R)/XX;

end

Ea=[Ea_k' Ea_s' Ea_a' Ea_b' Ea_o' Ea_f'];
```

Sintering Analysis

```
%FCC lattice initial corrdinates, atom weight is unit
%distance = Angstroms
%time = picoseconds
%mass = grams/mole
%energy = eV
%velocity = Angstroms/picosecond
%force = eV/Angstrom
%temperature = degrees K
%avogadro=6.022142e23;
%atomWeight=9.74627e-23;Ni
clear;
initUcell=[10 10 10];
nMol=4*initUcell(1)*initUcell(2)*initUcell(3);
%atom weight of nickel is 58.6934g/mol, density is 8.908gcm-3,
the density in metal unit is (density(gcm-3)/atomweight(gmol-
1))*Aogadro/10e24
density=0.0914;
mol(1:nMol)=struct('r',struct('x',0,'y',0,'z',0),'v',struct('
vx',0,'vy',0,'vz',0));
region=initUcell/((density/4)^(1/3));%cubic 3d region
gap=region./initUcell;
R=region(1)/2;%gap(1)*initUcell(1)/2;
R2=0.5*R;
n=1;
for nz=0:1:initUcell(3)
    for ny=0:1:initUcell(2)
```

```
        for nx=0:1:initUcell(1)
            c=[nx+0.25 ny+0.25 nz+0.25];
            c=c.*gap;
            c=c-0.5*region;
            for j=0:3
                mol(n).r.x=c(1);
                 mol(n).r.y=c(2);
                  mol(n).r.z=c(3);
                if j~=3
                    if j~=0
                        mol(n).r.x=mol(n).r.x+0.5*gap(1);
                    end
                     if j~=1
                         mol(n).r.y=mol(n).r.y+0.5*gap(2);
                     end
                       if j~=2
                           mol(n).r.z=mol(n).r.z+0.5*gap(3);
                       end
                end
                       n=n+1;
                     end
                    end
                end
end

for i=1:length(mol)
X(i)=mol(i).r.x;
Y(i)=mol(i).r.y;
Z(i)=mol(i).r.z;
end

%seperate two balls
apart=0.5;% apart distance between two ball center
for i=1:length(mol)
   X2(i)=mol(i).r.x+apart+R+R2;
   Y2(i)=mol(i).r.y;
   Z2(i)=mol(i).r.z;
end

%get the origin coordinates
origin=[(max(X)+min(X))/2 (max(Y)+min(Y))/2 (max(Z)+min(Z))/2;
apart+R+R2+(max(X)+min(X))/2 (max(Y)+min(Y))/2
(max(Z)+min(Z))/2 ];


%cut within R
k=1;
for i=1:length(mol)
    dd(i)=((X(i)-origin(1,1))^2+(Y(i)-origin(1,2))^2+(Z(i)-
origin(1,3))^2)-R^2;
    if dd(i)<=0
        ind(k)=i;
        k=k+1;
    end
end

k=1;
for i=1:length(mol)
```

```
    dd2(i)=((X2(i)-origin(2,1))^2+(Y2(i)-
origin(2,2))^2+(Z2(i)-origin(2,3))^2)-R2^2;
    if dd2(i)<=0
        ind2(k)=i;
        k=k+1;
    end
end

XR1=X(ind)';
YR1=Y(ind)';
ZR1=Z(ind)';
rR1=[XR1 YR1 ZR1];

XR2=X2(ind2)';
YR2=Y2(ind2)';
ZR2=Z2(ind2)';
rR2=[XR2 YR2 ZR2];

ID2=(1:length(XR2))';
TYPE2=ones(length(XR2),1);
rR2=[XR2 YR2 ZR2];
PP2=[ID2 TYPE2 rR2];

PP=[PP1;
    PP2];
% xlswrite('Ni2BALLSxyz',PP,'A2113:E2388');

fid=fopen('xyz.txt','w');
fprintf(fid,'%1d  %1d  %11.8f  %11.8f  %11.8f\n',PP');

fid=fopen('small.in','w');
fprintf(fid,'%1d  %1d  %11.8f  %11.8f  %11.8f\n',PP2');


%transfer atom index into core/neck context for LAMMPS
grouping


%get number of the lattice layers


for i=1:length(XR1)
    if (XR1(i)-origin(1)-2*gap(1))>=0
        neckAtomID(i)=i;

   end
end

nlayer2=R2/gap(1);%radius layers, the x limit of x*gap
for i=1:length(XR2)
    if ((origin(2,1)-XR2(i)-gap(1))>=0)
        neckAtomID2(i)=i;

    end
end
```

```
neckID=find(neckAtomID);% only matrix index used for plotting,
not the IDs for lammps
neckID2=find(neckAtomID2);
figure
scatter(XR1(neckID), ZR1(neckID));
hold on
scatter(XR2(neckID2), ZR2(neckID2));

%get number of the lattice layers
%radius layers, the x limit of x*gap
strip1=max(XR1)-origin(1,1);
for i=1:length(XR1)
    if ((XR1(i)-origin(1,1))^2==(strip1)^2)| ((YR1(i)-
origin(1,2))^2==(strip1)^2)|((ZR1(i)-
origin(1,3))^2==(strip1)^2)
        surfAtomID1(i)=i;%Id should be extracted from this
variable

    end
end

surfID1=find(surfAtomID1);% only matrix index used for
plotting, not the IDs for lammps

strip2=0.95*(max(XR2)-origin(2,1));
for i=1:length(XR2)
    if ((XR2(i)-origin(2,1))^2>=(strip2)^2)| ((YR2(i)-
origin(2,2))^2>=(strip2)^2)|((ZR2(i)-
origin(2,3))^2>=(strip2)^2)
        surfAtomID2(i)=i;

    end
end

surfID2=find(surfAtomID2);

%get number of the lattice layers
nlayer=0.7*(max(XR1)-origin(1,1));%radius layers, the x limit
of x*gap
for i=1:length(XR1)
    if ((XR1(i)-origin(1,1))^2>=(nlayer)^2)| ((YR1(i)-
origin(1,2))^2>=(nlayer)^2)|((ZR1(i)-
origin(1,3))^2>=(nlayer)^2)
        outAtomID1(i)=i;%Id should be extracted from this
variable

    end
end

outID1=find(outAtomID1);% only matrix index used for plotting,
not the IDs for lammps

nlayer2=0.7*(max(XR2)-origin(2,1));
for i=1:length(XR2)
```

```
    if ((XR2(i)-origin(2,1))^2>=(nlayer2)^2)| ((YR2(i)-
origin(2,2))^2>=(nlayer2)^2)|((ZR2(i)-
origin(2,3))^2>=(nlayer2)^2)
        outAtomID2(i)=i;

    end
end

outID2=find(outAtomID2);

%output atom IDs

%MEAN-SQUARE-DISPLACEMENT DATA PROCESSING FOR LAMMPS
clear;

Data_b_ball={'msd_b_ball_1000K.out','msd_b_ball_1100K.out',...

'msd_b_ball_1200K.out','msd_b_ball_1300K.out','msd_b_ball_140
0K.out','msd_b_ball_1500K.out'};
Data_b_surf={'msd_b_surf_1000K.out','msd_b_surf_1100K.out',...

'msd_b_surf_1200K.out','msd_b_surf_1300K.out','msd_b_surf_140
0K.out','msd_b_surf_1500K.out'};
Data_b_outl={'msd_b_outl_1000K.out','msd_b_outl_1100K.out',...

'msd_b_outl_1200K.out','msd_b_outl_1300K.out','msd_b_outl_140
0K.out','msd_b_outl_1500K.out'};
Data_b_neck={'msd_b_neck_1000K.out','msd_b_neck_1100K.out',...

'msd_b_neck_1200K.out','msd_b_neck_1300K.out','msd_b_neck_140
0K.out','msd_b_neck_1500K.out'};
Data_b_core={'msd_b_core_1000K.out','msd_b_core_1100K.out',...

'msd_b_core_1200K.out','msd_b_core_1300K.out','msd_b_core_140
0K.out','msd_b_core_1500K.out'};

Data_s_ball={'msd_s_ball_1000K.out','msd_s_ball_1100K.out',...
             'msd_s_ball_1200K.out', 'msd_s_ball_1300K.out',
'msd_s_ball_1400K.out', 'msd_s_ball_1500K.out'};
Data_s_surf={'msd_s_surf_1000K.out','msd_s_surf_1100K.out',...

'msd_s_surf_1200K.out','msd_s_surf_1300K.out','msd_s_surf_140
0K.out','msd_s_surf_1500K.out'};
Data_s_outl={'msd_s_outl_1000K.out','msd_s_outl_1100K.out',...

'msd_s_outl_1200K.out','msd_s_outl_1300K.out','msd_s_outl_140
0K.out','msd_s_outl_1500K.out'};
Data_s_neck={'msd_s_neck_1000K.out','msd_s_neck_1100K.out',...

'msd_s_neck_1200K.out','msd_s_neck_1300K.out','msd_s_neck_140
0K.out','msd_s_neck_1500K.out'};
Data_s_core={'msd_s_core_1000K.out','msd_s_core_1100K.out',...

'msd_s_core_1200K.out','msd_s_core_1300K.out','msd_s_core_140
0K.out','msd_s_core_1500K.out'};

%preallocating arrays
```

```
Ndata=length(Data_b_ball);


for i=1:Ndata
[b_ball_step(:,i),b_ball_x(:,i),
b_ball_y(:,i),b_ball_z(:,i),b_ball_sum(:,i)]=textread(Data_b_
ball{i},'%f %f %f %f %f','headerlines',2);
[b_surf_step(:,i),b_surf_x(:,i),
b_surf_y(:,i),b_surf_z(:,i),b_surf_sum(:,i)]=textread(Data_b_
surf{i},'%f %f %f %f %f','headerlines',2);
[b_outl_step(:,i),b_outl_x(:,i),
b_outl_y(:,i),b_outl_z(:,i),b_outl_sum(:,i)]=textread(Data_b_
outl{i},'%f %f %f %f %f','headerlines',2);
[b_neck_step(:,i),b_neck_x(:,i),
b_neck_y(:,i),b_neck_z(:,i),b_neck_sum(:,i)]=textread(Data_b_
neck{i},'%f %f %f %f %f','headerlines',2);
[b_core_step(:,i),b_core_x(:,i),
b_core_y(:,i),b_core_z(:,i),b_core_sum(:,i)]=textread(Data_b_
core{i},'%f %f %f %f %f','headerlines',2);

[s_ball_step(:,i),s_ball_x(:,i),
s_ball_y(:,i),s_ball_z(:,i),s_ball_sum(:,i)]=textread(Data_s_
ball{i},'%f %f %f %f %f','headerlines',2);
[s_surf_step(:,i),s_surf_x(:,i),
s_surf_y(:,i),s_surf_z(:,i),s_surf_sum(:,i)]=textread(Data_s_
surf{i},'%f %f %f %f %f','headerlines',2);
[s_outl_step(:,i),s_outl_x(:,i),
s_outl_y(:,i),s_outl_z(:,i),s_outl_sum(:,i)]=textread(Data_s_
outl{i},'%f %f %f %f %f','headerlines',2);
[s_neck_step(:,i),s_neck_x(:,i),
s_neck_y(:,i),s_neck_z(:,i),s_neck_sum(:,i)]=textread(Data_s_
neck{i},'%f %f %f %f %f','headerlines',2);
[s_core_step(:,i),s_core_x(:,i),
s_core_y(:,i),s_core_z(:,i),s_core_sum(:,i)]=textread(Data_s_
core{i},'%f %f %f %f %f','headerlines',2);

end


%diffusion
time=(b_ball_step-1000)*0.001;%in unit of ps
T=[1000,1100,1200,1300,1400,1500];
Nend=2001;
R=8.314472; % J ¡¤ K-1 ¡¤ mol-1
eV=1.60217653e-19; %J.
NA=6.02214179e23;

RMSD_b_ball=b_ball_sum.^(0.5);
RMSD_b_neck=b_neck_sum.^(0.5);
RMSD_b_outl=b_outl_sum.^(0.5);
RMSD_b_core=b_core_sum.^(0.5);
RMSD_b_surf=b_surf_sum.^(0.5);

RMSD_s_ball=s_ball_sum.^(0.5);
RMSD_s_neck=s_neck_sum.^(0.5);
RMSD_s_outl=s_outl_sum.^(0.5);
RMSD_s_core=s_core_sum.^(0.5);
```

```
RMSD_s_surf=s_surf_sum.^(0.5);

DT_b_ball=b_ball_sum./(6*time);
DT_b_neck=b_neck_sum./(6*time);
DT_b_outl=b_outl_sum./(6*time);
DT_b_core=b_core_sum./(6*time);
DT_b_surf=b_surf_sum./(6*time);

DT_s_ball=s_ball_sum./(6*time);
DT_s_neck=s_neck_sum./(6*time);
DT_s_outl=s_outl_sum./(6*time);
DT_s_core=s_core_sum./(6*time);
DT_s_surf=s_surf_sum./(6*time);

for i=1:6
logD_b_ball(i)=log(mean(DT_b_ball(11:Nend,i)));
logD_b_neck(i)=log(mean(DT_b_neck(11:Nend,i)));
logD_b_outl(i)=log(mean(DT_b_outl(11:Nend,i)));
logD_b_core(i)=log(mean(DT_b_core(11:Nend,i)));
logD_b_surf(i)=log(mean(DT_b_surf(11:Nend,i)));

logD_s_ball(i)=log(mean(DT_s_ball(11:Nend,i)));
logD_s_neck(i)=log(mean(DT_s_neck(11:Nend,i)));
logD_s_outl(i)=log(mean(DT_s_outl(11:Nend,i)));
logD_s_core(i)=log(mean(DT_s_core(11:Nend,i)));
logD_s_surf(i)=log(mean(DT_s_surf(11:Nend,i)));
end

%MEAN-SQUARE-DISPLACEMENT DATA PROCESSING FOR LAMMPS

clear;

Data_lay1={'msd_layer1_1000K.out','msd_layer1_1100K.out',...

'msd_layer1_1200K.out','msd_layer1_1300K.out','msd_layer1_140
0K.out','msd_layer1_1500K.out'};
Data_lay2={'msd_layer2_1000K.out','msd_layer2_1100K.out',...

'msd_layer2_1200K.out','msd_layer2_1300K.out','msd_layer2_140
0K.out','msd_layer2_1500K.out'};
Data_lay3={'msd_layer3_1000K.out','msd_layer3_1100K.out',...

'msd_layer3_1200K.out','msd_layer3_1300K.out','msd_layer3_140
0K.out','msd_layer3_1500K.out'};
Data_lay4={'msd_layer4_1000K.out','msd_layer4_1100K.out',...

'msd_layer4_1200K.out','msd_layer4_1300K.out','msd_layer4_140
0K.out','msd_layer4_1500K.out'};
Data_lay5={'msd_layer5_1000K.out','msd_layer5_1100K.out',...

'msd_layer5_1200K.out','msd_layer5_1300K.out','msd_layer5_140
0K.out','msd_layer5_1500K.out'};

Data_lay6={'msd_layer6_1000K.out','msd_layer6_1100K.out',...
             'msd_layer6_1200K.out', 'msd_layer6_1300K.out',
'msd_layer6_1400K.out', 'msd_layer6_1500K.out'};
Data_lay7={'msd_layer7_1000K.out','msd_layer7_1100K.out',...
```

```
'msd_layer7_1200K.out','msd_layer7_1300K.out','msd_layer7_140
0K.out','msd_layer7_1500K.out'};
Data_lay8={'msd_layer8_1000K.out','msd_layer8_1100K.out',...

'msd_layer8_1200K.out','msd_layer8_1300K.out','msd_layer8_140
0K.out','msd_layer8_1500K.out'};
Data_lay9={'msd_layer9_1000K.out','msd_layer9_1100K.out',...

'msd_layer9_1200K.out','msd_layer9_1300K.out','msd_layer9_140
0K.out','msd_layer9_1500K.out'};
Data_lay10={'msd_layer10_1000K.out','msd_layer10_1100K.out',.
..

'msd_layer10_1200K.out','msd_layer10_1300K.out','msd_layer10_
1400K.out','msd_layer10_1500K.out'};

Data_core1={'msd_core1_1000K.out','msd_core1_1100K.out',...

'msd_core1_1200K.out','msd_core1_1300K.out','msd_core1_1400K.
out','msd_core1_1500K.out'};
Data_core2={'msd_core2_1000K.out','msd_core2_1100K.out',...

'msd_core2_1200K.out','msd_core2_1300K.out','msd_core2_1400K.
out','msd_core2_1500K.out'};
Data_core3={'msd_core3_1000K.out','msd_core3_1100K.out',...

'msd_core3_1200K.out','msd_core3_1300K.out','msd_core3_1400K.
out','msd_core3_1500K.out'};


Ndata=length(Data_lay1);
for i=1:Ndata
[b_lay1_step(:,i),b_lay1_x(:,i),
b_lay1_y(:,i),b_lay1_z(:,i),b_lay1_sum(:,i)]=textread(Data_la
y1{i},'%f %f %f %f %f','headerlines',2);
[b_lay2_step(:,i),b_lay2_x(:,i),
b_lay2_y(:,i),b_lay2_z(:,i),b_lay2_sum(:,i)]=textread(Data_la
y2{i},'%f %f %f %f %f','headerlines',2);
[b_lay3_step(:,i),b_lay3_x(:,i),
b_lay3_y(:,i),b_lay3_z(:,i),b_lay3_sum(:,i)]=textread(Data_la
y3{i},'%f %f %f %f %f','headerlines',2);
[b_lay4_step(:,i),b_lay4_x(:,i),
b_lay4_y(:,i),b_lay4_z(:,i),b_lay4_sum(:,i)]=textread(Data_la
y4{i},'%f %f %f %f %f','headerlines',2);
[b_lay5_step(:,i),b_lay5_x(:,i),
b_lay5_y(:,i),b_lay5_z(:,i),b_lay5_sum(:,i)]=textread(Data_la
y5{i},'%f %f %f %f %f','headerlines',2);
[b_lay6_step(:,i),b_lay6_x(:,i),
b_lay6_y(:,i),b_lay6_z(:,i),b_lay6_sum(:,i)]=textread(Data_la
y6{i},'%f %f %f %f %f','headerlines',2);
[b_lay7_step(:,i),b_lay7_x(:,i),
b_lay7_y(:,i),b_lay7_z(:,i),b_lay7_sum(:,i)]=textread(Data_la
y7{i},'%f %f %f %f %f','headerlines',2);
[b_lay8_step(:,i),b_lay8_x(:,i),
b_lay8_y(:,i),b_lay8_z(:,i),b_lay8_sum(:,i)]=textread(Data_la
y8{i},'%f %f %f %f %f','headerlines',2);
```

```
[b_lay9_step(:,i),b_lay9_x(:,i),
b_lay9_y(:,i),b_lay9_z(:,i),b_lay9_sum(:,i)]=textread(Data_la
y9{i},'%f %f %f %f %f','headerlines',2);
[b_lay10_step(:,i),b_lay10_x(:,i),
b_lay10_y(:,i),b_lay10_z(:,i),b_lay10_sum(:,i)]=textread(Data
_lay10{i},'%f %f %f %f %f','headerlines',2);

[b_core1_step(:,i),b_core1_x(:,i),
b_core1_y(:,i),b_core1_z(:,i),b_core1_sum(:,i)]=textread(Data
_core1{i},'%f %f %f %f %f','headerlines',2);
[b_core2_step(:,i),b_core2_x(:,i),
b_core2_y(:,i),b_core2_z(:,i),b_core2_sum(:,i)]=textread(Data
_core2{i},'%f %f %f %f %f','headerlines',2);
[b_core3_step(:,i),b_core3_x(:,i),
b_core3_y(:,i),b_core3_z(:,i),b_core3_sum(:,i)]=textread(Data
_core3{i},'%f %f %f %f %f','headerlines',2);
end

%diffusion
time=(b_lay1_step-2000)*0.001;%in unit of ps
T=[1000,1100,1200,1300,1400,1500];


Nend=2001;
R=8.314472; % J ¡¤ K-1 ¡¤ mol-1
eV=1.60217653e-19; %J.
NA=6.02214179e23;


for i=1:6
DT_b_lay1(:,i)=b_lay1_sum(2:Nend,i)./(6*time(2:Nend,i));
DT_b_lay2(:,i)=b_lay2_sum(2:Nend,i)./(6*time(2:Nend,i));
DT_b_lay3(:,i)=b_lay3_sum(2:Nend,i)./(6*time(2:Nend,i));
DT_b_lay4(:,i)=b_lay4_sum(2:Nend,i)./(6*time(2:Nend,i));
DT_b_lay5(:,i)=b_lay5_sum(2:Nend,i)./(6*time(2:Nend,i));

DT_b_lay6(:,i)=b_lay6_sum(2:Nend,i)./(6*time(2:Nend,i));
DT_b_lay7(:,i)=b_lay7_sum(2:Nend,i)./(6*time(2:Nend,i));
DT_b_lay8(:,i)=b_lay8_sum(2:Nend,i)./(6*time(2:Nend,i));
DT_b_lay9(:,i)=b_lay9_sum(2:Nend,i)./(6*time(2:Nend,i));
DT_b_lay10(:,i)=b_lay10_sum(2:Nend,i)./(6*time(2:Nend,i));

DT_b_core1(:,i)=b_core1_sum(2:Nend,i)./(6*time(2:Nend,i));
DT_b_core2(:,i)=b_core2_sum(2:Nend,i)./(6*time(2:Nend,i));
DT_b_core3(:,i)=b_core3_sum(2:Nend,i)./(6*time(2:Nend,i));

end

for i=1:6

D_b_lay1(i)=(mean(DT_b_lay1(:,i)));
D_b_lay2(i)=(mean(DT_b_lay2(:,i)));
D_b_lay3(i)=(mean(DT_b_lay3(:,i)));
D_b_lay4(i)=(mean(DT_b_lay4(:,i)));
D_b_lay5(i)=(mean(DT_b_lay5(:,i)));
```

```
D_b_lay6(i)=(mean(DT_b_lay6(:,i)));
D_b_lay7(i)=(mean(DT_b_lay7(:,i)));
D_b_lay8(i)=(mean(DT_b_lay8(:,i)));
D_b_lay9(i)=(mean(DT_b_lay9(:,i)));
D_b_lay10(i)=(mean(DT_b_lay10(:,i)));

D_b_core1(i)=(mean(DT_b_core1(:,i)));
D_b_core2(i)=(mean(DT_b_core2(:,i)));
D_b_core3(i)=(mean(DT_b_core3(:,i)));
end


for i=1:6

logD_b_lay1(i)=log(mean(DT_b_lay1(:,i)));
logD_b_lay2(i)=log(mean(DT_b_lay2(:,i)));
logD_b_lay3(i)=log(mean(DT_b_lay3(:,i)));
logD_b_lay4(i)=log(mean(DT_b_lay4(:,i)));
logD_b_lay5(i)=log(mean(DT_b_lay5(:,i)));
logD_b_lay6(i)=log(mean(DT_b_lay6(:,i)));
logD_b_lay7(i)=log(mean(DT_b_lay7(:,i)));
logD_b_lay8(i)=log(mean(DT_b_lay8(:,i)));
logD_b_lay9(i)=log(mean(DT_b_lay9(:,i)));
logD_b_lay10(i)=log(mean(DT_b_lay10(:,i)));

logD_b_core1(i)=log(mean(DT_b_core1(:,i)));
logD_b_core2(i)=log(mean(DT_b_core2(:,i)));
logD_b_core3(i)=log(mean(DT_b_core3(:,i)));
end


t=T.^(-1);
p_b_lay1=polyfit(t(1:6), logD_b_lay1(1:6),1);
p_b_lay2=polyfit(t(1:6), logD_b_lay2(1:6),1);
p_b_lay3=polyfit(t(1:6), logD_b_lay3(1:6),1);
p_b_lay4=polyfit(t(1:6), logD_b_lay4(1:6),1);
p_b_lay5=polyfit(t(1:6), logD_b_lay5(1:6),1);
p_b_lay6=polyfit(t(1:6), logD_b_lay6(1:6),1);
p_b_lay7=polyfit(t(1:6), logD_b_lay7(1:6),1);
p_b_lay8=polyfit(t(1:6), logD_b_lay8(1:6),1);
p_b_lay9=polyfit(t(1:6), logD_b_lay9(1:6),1);
p_b_lay10=polyfit(t(1:6), logD_b_lay10(1:6),1);

p_b_core1=polyfit(t(1:6), logD_b_core1(1:6),1);
p_b_core2=polyfit(t(1:6), logD_b_core2(1:6),1);
p_b_core3=polyfit(t(1:6), logD_b_core3(1:6),1);

N1=4;
N2=12;
N3=52;
N4=72;
N5=136;
N6=180;
N7=280;
N8=352;
N9=468;
N10=556;
```

```
A=R/eV/NA;

E_b_core1=-p_b_core1(1)*A;
E_b_core2=-p_b_core2(1)*A;
E_b_core3=-p_b_core3(1)*A;

E_b_lay1=-p_b_lay1(1)*A;
E_b_lay2=-p_b_lay2(1)*A;
E_b_lay3=-p_b_lay3(1)*A;
E_b_lay4=-p_b_lay4(1)*A;
E_b_lay5=-p_b_lay5(1)*A;
E_b_lay6=-p_b_lay6(1)*A;
E_b_lay7=-p_b_lay7(1)*A;
E_b_lay8=-p_b_lay8(1)*A;
E_b_lay9=-p_b_lay9(1)*A;
E_b_lay10=-p_b_lay10(1)*A;

E_core1=E_b_lay1;
E_core2=(E_b_lay1*N1+E_b_lay2*N2)/(N1+N2);
E_core3=(E_b_lay1*N1+E_b_lay2*N2+E_b_lay3*N3)/(N1+N2+N3);
E_core4=(E_b_lay1*N1+E_b_lay2*N2+E_b_lay3*N3+E_b_lay4*N4)/(N1
+N2+N3+N4);
E_core5=(E_b_lay1*N1+E_b_lay2*N2+E_b_lay3*N3+E_b_lay4*N4+E_b_
lay5*N5)/(N1+N2+N3+N4+N5);
E_core6=(E_b_lay1*N1+E_b_lay2*N2+E_b_lay3*N3+E_b_lay4*N4+E_b_
lay5*N5+E_b_lay6*N6)/(N1+N2+N3+N4+N5+N6);
E_core7=(E_b_lay1*N1+E_b_lay2*N2+E_b_lay3*N3+E_b_lay4*N4+E_b_
lay5*N5+E_b_lay6*N6+E_b_lay7*N7)/(N1+N2+N3+N4+N5+N6+N7);
E_core8=(E_b_lay1*N1+E_b_lay2*N2+E_b_lay3*N3+E_b_lay4*N4+E_b_
lay5*N5+E_b_lay6*N6+E_b_lay7*N7+E_b_lay8*N8)/(N1+N2+N3+N4+N5+
N6+N7+N8);
E_core9=(E_b_lay1*N1+E_b_lay2*N2+E_b_lay3*N3+E_b_lay4*N4+E_b_
lay5*N5+E_b_lay6*N6+E_b_lay7*N7+E_b_lay8*N8+E_b_lay9*N9)/(N1+
N2+N3+N4+N5+N6+N7+N8+N9);
E_core10=(E_b_lay1*N1+E_b_lay2*N2+E_b_lay3*N3+E_b_lay4*N4+E_b
_lay5*N5+E_b_lay6*N6+E_b_lay7*N7+E_b_lay8*N8+E_b_lay9*N9+E_b_
lay10*N10)/(N1+N2+N3+N4+N5+N6+N7+N8+N9+N10);

E_LAY=[E_b_lay1,E_b_lay2,E_b_lay3,E_b_lay4,E_b_lay5,E_b_lay6,
E_b_lay7,E_b_lay8,E_b_lay9,E_b_lay10];
E_CORE=[E_b_core1,E_b_core2,E_b_core3];
```

Ni-Al alloy analysis

```
coords={'all200000','all1200000','all2200000','all3200000','a
ll4200000','all5200000',...

'all6200000','all7200000','all8200000','all9200000','all10200
000'};

for i=1:11
pe{i}=struct2cell(readdump_all(coords{i}));
end
```

```
NT=11;
NL=10;
NA=5636;
PI=3.1415926;

mol=zeros(NT,NA,4);
for i=1:NT
mol(i,:,1)=pe{i}{3,1}(1)+(pe{i}{3,1}(2)-
pe{i}{3,1}(1))*pe{i}{6,1}(:,3);
mol(i,:,2)=pe{i}{4,1}(1)+(pe{i}{4,1}(2)-
pe{i}{4,1}(1))*pe{i}{6,1}(:,4);
mol(i,:,3)=pe{i}{5,1}(1)+(pe{i}{5,1}(2)-
pe{i}{5,1}(1))*pe{i}{6,1}(:,5);
mol(i,:,4)=pe{i}{6,1}(:,2);
end

Nal=zeros(NT,NL);
Nni=zeros(NT,NL);


Rv_s=[28.6092,28.3764,28.3665,28.2049,28.1074,27.9783,27.7375
,27.6101,27.5552,27.4819,27.4243];
R=Rv_s;
for i=1:NT
    for j=1:NL
V_ring(i,j)=(4/3)*PI*R(i)*((j)^3-(j-1)^3)/(NL*3);
    end
end


for i=1:NT %number of configuration
    for j=1:NL %number of layers
        for k=1:NA
        if
((mol(i,k,1)*mol(i,k,1)+mol(i,k,2)*mol(i,k,2)+mol(i,k,3)*mol(
i,k,3)-(j-1)*(j-1)*(R(i))^2/(NL*NL))>0.0)...

&&((mol(i,k,1)*mol(i,k,1)+mol(i,k,2)*mol(i,k,2)+mol(i,k,3)*mo
l(i,k,3)-(j)*(j)*(R(i))^2/(NL*NL))<=0)
            if mol(i,k,4)==1
                Nal(i,j)=Nal(i,j)+1;
            elseif mol(i,k,4)==2
                Nni(i,j)=Nni(i,j)+1;
            end
        end
        end
    end
end

for i=1:NT
    for j=1:NL
rho_al(i,j)=Nal(i,j)/V_ring(i,j);
rho_ni(i,j)=Nni(i,j)/V_ring(i,j);
    end
end
```

```
clear;
PE_al_1={'all10200000'};

pe_al_1 = readdump_all(PE_al_1{1});

stepRdf=1;
for i=1:stepRdf
molall=pe_al_1.atom_data(:,3:5,i);
end

mol(:,1)=-24.3908+49.1205*molall(:,1);
mol(:,2)=-25.8673+50.9905*molall(:,2);
mol(:,3)=-24.4475+48.9048*molall(:,3);

NA=5636;
NV=64170.208;
rangeRdf=51.2379;
pi=3.1415926;
sizeHistRdf=200;
countRdf=1;
limitRdf=500;
deltaR=rangeRdf/sizeHistRdf;

histRdf=zeros(sizeHistRdf,1);

dr=zeros(NA*NA,3);


for j1=1:(NA-1)
    for j2=(j1+1):NA
        dr=mol(j1,:)-mol(j2,:);
        rr=dr.^2;
        if (sum(rr)<(rangeRdf^2))
            n=fix(sum(rr)^0.5/deltaR);
            histRdf(n)=histRdf(n)+1;
        end
    end
end

    normFac=NV/(2*pi*deltaR^3*NA^2*limitRdf);
    for n=1:sizeHistRdf
        histRdf(n)=histRdf(n)*(normFac/(n-0.5)^2);
%         countRdf=1;
    end


% fid = fopen('rdfww','a');
for n=1:sizeHistRdf
    rb(n)=(n+0.5)*rangeRdf/sizeHistRdf;
%     fprintf(fid,'%9.5f  %9.5f\n',rb(n), histRdf(n));

end

coords={'all_h2040000'};

for i=1:1
```

```
pe{i}=struct2cell(readdump_all(coords{i}));
end

NT=1;
NL=10;
NA=5636;
PI=3.1415926;

mol=zeros(NT,NA,4);
for i=1:NT
mol(i,:,1)=pe{i}{3,1}(1)+(pe{i}{3,1}(2)-
pe{i}{3,1}(1))*pe{i}{6,1}(:,3);
mol(i,:,2)=pe{i}{4,1}(1)+(pe{i}{4,1}(2)-
pe{i}{4,1}(1))*pe{i}{6,1}(:,4);
mol(i,:,3)=pe{i}{5,1}(1)+(pe{i}{5,1}(2)-
pe{i}{5,1}(1))*pe{i}{6,1}(:,5);
mol(i,:,4)=pe{i}{6,1}(:,2);
end

Nal=zeros(NT,NL);
Nni=zeros(NT,NL);


Rv_s=[28.6092,28.3764,28.3665,28.2049,28.1074,27.9783,27.7375
,27.6101,27.5552,27.4819,27.4243];
R=26.95005;
for i=1:NT
    for j=1:NL
V_ring(i,j)=(4/3)*PI*R(i)*((j)^3-(j-1)^3)/(NL*3);
    end
end


for i=1:NT %number of configuration
    for j=1:NL %number of layers
        for k=1:NA
        if
((mol(i,k,1)*mol(i,k,1)+mol(i,k,2)*mol(i,k,2)+mol(i,k,3)*mol(
i,k,3)-(j-1)*(j-1)*(R(i))^2/(NL*NL))>0.0)...

&&((mol(i,k,1)*mol(i,k,1)+mol(i,k,2)*mol(i,k,2)+mol(i,k,3)*mo
l(i,k,3)-(j)*(j)*(R(i))^2/(NL*NL))<=0)
            if mol(i,k,4)==1
                Nal(i,j)=Nal(i,j)+1;
            elseif mol(i,k,4)==2
                Nni(i,j)=Nni(i,j)+1;
            end
        end
        end
    end
end

for i=1:NT
    for j=1:NL
rho_al(i,j)=Nal(i,j)/V_ring(i,j);
rho_ni(i,j)=Nni(i,j)/V_ring(i,j);
    end
```

```
end

ST_al_1={'Allay1_st1100K.dump'};
ST_al_2={'Allay2_st1100K.dump'};
ST_al_3={'Allay3_st1100K.dump'};
ST_al_4={'Allay4_st1100K.dump'};

ST_ni_1={'Nilay1_st1100K.dump'};
ST_ni_2={'Nilay2_st1100K.dump'};
ST_ni_3={'Nilay3_st1100K.dump'};
ST_ni_4={'Nilay4_st1100K.dump'};
ST_ni_5={'Nilay5_st1100K.dump'};


st_al_1 = readdump_all(ST_al_1{1});
st_al_2 = readdump_all(ST_al_2{1});
st_al_3 = readdump_all(ST_al_3{1});
st_al_4 = readdump_all(ST_al_4{1});

st_ni_1 = readdump_all(ST_ni_1{1});
st_ni_2 = readdump_all(ST_ni_2{1});
st_ni_3 = readdump_all(ST_ni_3{1});
st_ni_4 = readdump_all(ST_ni_4{1});
st_ni_5 = readdump_all(ST_ni_5{1});


time=st_al_1(1).timestep*0.001;%unit of ps
T=[300:5.220883534:1600];


    for j=1:250

a1_st_atom(:,j)=(st_al_1.atom_data(:,1,j)+st_al_1.atom_data(:
,2,j)+st_al_1.atom_data(:,3,j));

a2_st_atom(:,j)=(st_al_2.atom_data(:,1,j)+st_al_2.atom_data(:
,2,j)+st_al_2.atom_data(:,3,j));

a3_st_atom(:,j)=(st_al_3.atom_data(:,1,j)+st_al_3.atom_data(:
,2,j)+st_al_3.atom_data(:,3,j));

a4_st_atom(:,j)=(st_al_4.atom_data(:,1,j)+st_al_4.atom_data(:
,2,j)+st_al_4.atom_data(:,3,j));


n1_st_atom(:,j)=(st_ni_1.atom_data(:,1,j)+st_ni_1.atom_data(:
,2,j)+st_ni_1.atom_data(:,3,j));

n2_st_atom(:,j)=(st_ni_2.atom_data(:,1,j)+st_ni_2.atom_data(:
,2,j)+st_ni_2.atom_data(:,3,j));

n3_st_atom(:,j)=(st_ni_3.atom_data(:,1,j)+st_ni_3.atom_data(:
,2,j)+st_ni_3.atom_data(:,3,j));

n4_st_atom(:,j)=(st_ni_4.atom_data(:,1,j)+st_ni_4.atom_data(:
,2,j)+st_ni_4.atom_data(:,3,j));
```

```
n5_st_atom(:,j)=(st_ni_5.atom_data(:,1,j)+st_ni_5.atom_data(:
,2,j)+st_ni_5.atom_data(:,3,j));
    end



    a1_st_sum=sum(a1_st_atom,1);
    a2_st_sum=sum(a2_st_atom,1);
    a3_st_sum=sum(a3_st_atom,1);
    a4_st_sum=sum(a4_st_atom,1);

    n1_st_sum=sum(n1_st_atom,1);
    n2_st_sum=sum(n2_st_atom,1);
    n3_st_sum=sum(n3_st_atom,1);
    n4_st_sum=sum(n4_st_atom,1);
    n5_st_sum=sum(n5_st_atom,1);



    pi=3.1415926;
    al_lay_sum=[a1_st_sum;a2_st_sum; a3_st_sum; a4_st_sum];
    ni_lay_sum=[n1_st_sum;n2_st_sum; n3_st_sum;
n4_st_sum;n5_st_sum];
    V_al_lay=[4/3*pi*0.5^3; 4/3*pi*(1-0.5^3);4/3*pi*(1.5^3-
1);4/3*pi*(2^3-1.5^3)];



clear;
load molallfast;
load BONDfast;
R=3.5;
NA=5636;
%N=10,N=12,N=14 should be considered as duplicates of N=5,N=6
and N=7
%===clear count
for i=1:11
    for j=1:NA
       BONDfast{i}(j).id(15)=0;
       BONDfast{i}(j).id(16)=0;
       BONDfast{i}(j).id(17)=0;
       BONDfast{i}(j).id(18)=0;
       BONDfast{i}(j).id(19)=0;
       BONDfast{i}(j).id(20)=0;
    end
end

%check enviromental bond

for i=1:11
    for j=1:NA

     moz{i}=squeeze(mol(i,nonzeros(BONDfast{i}(j).id)',1:3));

     if (BONDfast{i}(j).count==5);
     for j1=1:4
         for j2=(j1+1):5
         r1=moz{i}(j1,:)-moz{i}(j2,:);
         r1r1=r1.^2;
```

```
        if (sum(r1r1)<=R*R)
            BONDfast{i}(j).id(18)=BONDfast{i}(j).id(18)+1;
        end
        end
    end

elseif (BONDfast{i}(j).count==6);
        for j1=1:5
        for j2=(j1+1):6
        r2=moz{i}(j1,:)-moz{i}(j2,:);
        r2r2=r2.^2;
        if (sum(r2r2)<=R*R)
            BONDfast{i}(j).id(19)=BONDfast{i}(j).id(19)+1;
        end
        end
    end

    elseif (BONDfast{i}(j).count==7);
        for j1=1:6
        for j2=(j1+1):7
        r3=moz{i}(j1,:)-moz{i}(j2,:);
        r3r3=r3.^2;
        if (sum(r3r3)<=R*R)
            BONDfast{i}(j).id(20)=BONDfast{i}(j).id(20)+1;
        end
        end
        end
     elseif (BONDfast{i}(j).count==10);
        for j1=1:9
        for j2=(j1+1):10
        r4=moz{i}(j1,:)-moz{i}(j2,:);
        r4r4=r4.^2;
        if (sum(r4r4)<=R*R)
            BONDfast{i}(j).id(15)=BONDfast{i}(j).id(15)+1;
        end
        end
        end
     elseif (BONDfast{i}(j).count==12);
        for j1=1:11
        for j2=(j1+1):12
        r5=moz{i}(j1,:)-moz{i}(j2,:);
        r5r5=r5.^2;
        if (sum(r5r5)<=R*R)
            BONDfast{i}(j).id(16)=BONDfast{i}(j).id(16)+1;
        end
        end
        end
     elseif (BONDfast{i}(j).count==14);
        for j1=1:13
        for j2=(j1+1):14
        r6=moz{i}(j1,:)-moz{i}(j2,:);
        r6r6=r6.^2;
        if (sum(r6r6)<=R*R)
            BONDfast{i}(j).id(17)=BONDfast{i}(j).id(17)+1;
        end
        end
     end
    end
```

```
   end
end


for i=1:11
    for j=1:NA
    b5(i,j)=BONDfast{1,i}(1,j).id(18);
    b6(i,j)=BONDfast{1,i}(1,j).id(19);
    b7(i,j)=BONDfast{1,i}(1,j).id(20);
    b10(i,j)=BONDfast{1,i}(1,j).id(15);
    b12(i,j)=BONDfast{1,i}(1,j).id(16);
    b14(i,j)=BONDfast{1,i}(1,j).id(17);
    end
end

for i=1:11
B5{i}=(nonzeros(b5(i,:)));
B6{i}=(nonzeros(b6(i,:)));
B7{i}=(nonzeros(b7(i,:)));
B10{i}=(nonzeros(b10(i,:)));
B12{i}=(nonzeros(b12(i,:)));
B14{i}=(nonzeros(b14(i,:)));
end

for i=1:11
n5(i)=length(nonzeros(b5(i,:)));
n6(i)=length(nonzeros(b6(i,:)));
n7(i)=length(nonzeros(b7(i,:)));
n10(i)=length(nonzeros(b10(i,:)));
n12(i)=length(nonzeros(b12(i,:)));
n14(i)=length(nonzeros(b14(i,:)));
end

for i=1:11
N1421(i)=(length(find(B5{1,i}==6))+length(find(B10{1,i}==12))
)/(n5(i)+n10(i));%POSSIBLE 1422
N1431(i)=(length(find(B5{1,i}==7))+length(find(B10{1,i}==14))
)/(n5(i)+n10(i));
N1441(i)=(length(find(B5{1,i}==8))+length(find(B10{1,i}==16))
)/(n5(i)+n10(i));

N1541(i)=(length(find(B6{1,i}==9))+length(find(B12{1,i}==18))
)/(n6(i)+n12(i));
N1551(i)=(length(find(B6{1,i}==10))+length(find(B10{1,i}==20)
))/(n6(i)+n12(i));

N1661(i)=(length(find(B7{1,i}==7))+length(find(B14{1,i}==14))
)/(n7(i)+n14(i));
end


clear;
load molslow;
load BONDslow11;
R=3.2;
NA=5636;
NT=11;
```

```
%N=10,N=12,N=14 should be considered as duplicates of N=5,N=6
and N=7
%clear count
for i=1:NT
    for j=1:NA
       BONDslow11{i}(j).id(15)=0;
       BONDslow11{i}(j).id(16)=0;
       BONDslow11{i}(j).id(17)=0;
       BONDslow11{i}(j).id(18)=0;
       BONDslow11{i}(j).id(19)=0;
       BONDslow11{i}(j).id(20)=0;
    end
end

%check enviromental bond

for i=1:NT
    for j=1:NA


moz{i}=squeeze(mol(i,nonzeros(BONDslow11{i}(j).id)',1:3));

     if (BONDslow11{i}(j).count==5);
     for j1=1:4
         for j2=(j1+1):5
         r1=moz{i}(j1,:)-moz{i}(j2,:);
         r1r1=r1.^2;
         if (sum(r1r1)<=R*R)

BONDslow11{i}(j).id(18)=BONDslow11{i}(j).id(18)+1;
         end
         end
     end

 elseif (BONDslow11{i}(j).count==6);
         for j1=1:5
         for j2=(j1+1):6
         r2=moz{i}(j1,:)-moz{i}(j2,:);
         r2r2=r2.^2;
         if (sum(r2r2)<=R*R)

BONDslow11{i}(j).id(19)=BONDslow11{i}(j).id(19)+1;
         end
         end
     end

     elseif (BONDslow11{i}(j).count==7);
         for j1=1:6
         for j2=(j1+1):7
         r3=moz{i}(j1,:)-moz{i}(j2,:);
         r3r3=r3.^2;
         if (sum(r3r3)<=R*R)

BONDslow11{i}(j).id(20)=BONDslow11{i}(j).id(20)+1;
         end
         end
         end
      elseif (BONDslow11{i}(j).count==10);
```

```
         for j1=1:9
         for j2=(j1+1):10
         r4=moz{i}(j1,:)-moz{i}(j2,:);
         r4r4=r4.^2;
         if (sum(r4r4)<=R*R)

BONDslow11{i}(j).id(15)=BONDslow11{i}(j).id(15)+1;
         end
         end
         end
      elseif (BONDslow11{i}(j).count==12);
         for j1=1:11
         for j2=(j1+1):12
         r5=moz{i}(j1,:)-moz{i}(j2,:);
         r5r5=r5.^2;
         if (sum(r5r5)<=R*R)

BONDslow11{i}(j).id(16)=BONDslow11{i}(j).id(16)+1;
         end
         end
         end
      elseif (BONDslow11{i}(j).count==14);
         for j1=1:13
         for j2=(j1+1):14
         r6=moz{i}(j1,:)-moz{i}(j2,:);
         r6r6=r6.^2;
         if (sum(r6r6)<=R*R)

BONDslow11{i}(j).id(17)=BONDslow11{i}(j).id(17)+1;
         end
         end
      end
     end
   end
end



for i=1:NT
    for j=1:NA
    b5(i,j)=BONDslow11{1,i}(1,j).id(18);
    b6(i,j)=BONDslow11{1,i}(1,j).id(19);
    b7(i,j)=BONDslow11{1,i}(1,j).id(20);
    b10(i,j)=BONDslow11{1,i}(1,j).id(15);
    b12(i,j)=BONDslow11{1,i}(1,j).id(16);
    b14(i,j)=BONDslow11{1,i}(1,j).id(17);
    end
end

for i=1:NT
B5{i}=(nonzeros(b5(i,:)));
B6{i}=(nonzeros(b6(i,:)));
B7{i}=(nonzeros(b7(i,:)));
B10{i}=(nonzeros(b10(i,:)));
B12{i}=(nonzeros(b12(i,:)));
B14{i}=(nonzeros(b14(i,:)));
end

for i=1:NT
```

```
n5(i)=length(nonzeros(b5(i,:)));
n6(i)=length(nonzeros(b6(i,:)));
n7(i)=length(nonzeros(b7(i,:)));
n10(i)=length(nonzeros(b10(i,:)));
n12(i)=length(nonzeros(b12(i,:)));
n14(i)=length(nonzeros(b14(i,:)));
end

for i=1:NT
N1421(i)=(length(find(B5{1,i}==6))+length(find(B10{1,i}==12))
)/(n5(i)+n10(i));%POSSIBLE 1422
N1431(i)=(length(find(B5{1,i}==7))+length(find(B10{1,i}==14))
)/(n5(i)+n10(i));
N1441(i)=(length(find(B5{1,i}==8))+length(find(B10{1,i}==16))
)/(n5(i)+n10(i));

N1541(i)=(length(find(B6{1,i}==9))+length(find(B12{1,i}==18))
)/(n6(i)+n12(i));
N1551(i)=(length(find(B6{1,i}==10))+length(find(B10{1,i}==20)
))/(n6(i)+n12(i));

N1661(i)=(length(find(B7{1,i}==7))+length(find(B14{1,i}==14))
)/(n7(i)+n14(i));
end
```

Silicon Oxidation Analysis

```
clear;
load si1000;
X=54.309298175*si1000(:,1);
Y=54.309298175*si1000(:,2);
Z=54.309298175*si1000(:,3);
R=10;

origin_al=[(max(X)+min(X))/2 (max(Y)+min(Y))/2
(max(Z)+min(Z))/2];
X=X-origin_al(1);
Y=Y-origin_al(2);
Z=Z-origin_al(3);
origin_si=[(max(X)+min(X))/2 (max(Y)+min(Y))/2
(max(Z)+min(Z))/2];

k2=1;
for n=1:length(X)
if (((X(n)-origin_si(1))^2+(Y(n)-origin_si(2))^2+(Z(n)-
origin_si(3))^2)<=(0.95*R)^2)
X_si(k2)=X(n);
Y_si(k2)=Y(n);
Z_si(k2)=Z(n);
k2=k2+1;
end
end



kB=1.3806505E-23;
Na=6.0221418E23;
```

```
nmol=216;
dOO=1.21;% unit of angstrom
Am=32;
rho=3.8;%7.6; %g
count=1;
origin=[0 0 0];


        mass=nmol*Am/(Na);% mass unit of g

        n=fix(nmol^(1/3));           % number of particles in
each direction
        box=(mass/rho*10e24)^(1/3);         % length of box
in each dimension
        del=box/n;                % displacement between
neighbouring particles
        dx=-del*0.5;
        for i=1:n
                dx=dx+del;
                dy=-del*0.5;
                for j=1:n
                        dy=dy+del;
                        dz=-del*0.5;
                        for k=1:n
                                dz=dz+del;
                                count=count+1;
                                mol(count,1,1)=dx;
                                mol(count,1,2)=dy-0.5*dOO;
                                mol(count,1,3)=dz;
                                mol(count,2,1)=dx;
                                mol(count,2,2)=dy+0.5*dOO;
                                mol(count,2,3)=dz;
                                 end
                        end
        end
        mol(1,:,:)=[];%delete the first molecule since it's
overlapped due to loop from '1' ,leaving the first mol
unassigned


vec=[(max((mol(:,1,1)+mol(:,2,1))/2)+min((mol(:,1,1)+mol(:,2,
1))/2))/2;(max((mol(:,1,2)+mol(:,2,2))/2)+min((mol(:,1,1)+mol
(:,2,1))/2))/2;...

(max((mol(:,1,3)+mol(:,2,3))/2)+min((mol(:,1,3)+mol(:,2,3))/2
))/2];


    %tranlate to one space
    Mol(:,1,1)=mol(:,1,1)-vec(1);
    Mol(:,1,2)=mol(:,1,2)-vec(2);
    Mol(:,1,3)=mol(:,1,3)-vec(3);
    Mol(:,2,1)=mol(:,2,1)-vec(1);
    Mol(:,2,2)=mol(:,2,2)-vec(2);
    Mol(:,2,3)=mol(:,2,3)-vec(3);
```

```
originO2=[(max((Mol(:,1,1)+Mol(:,2,1))/2)+min((Mol(:,1,1)+Mol
(:,2,1))/2))/2;(max((Mol(:,1,2)+Mol(:,2,2))/2)+min((Mol(:,1,1
)+Mol(:,2,1))/2))/2;...

(max((Mol(:,1,3)+Mol(:,2,3))/2)+min((Mol(:,1,3)+Mol(:,2,3))/2
))/2];



k=1;
for i=1:length(Mol)

    CUTCRT(i)=(((Mol(i,1,1)+Mol(i,2,1))/2-
origin(1))^2+((Mol(i,1,2)+Mol(i,2,2))/2-
origin(2))^2+((Mol(i,1,3)+Mol(i,2,3))/2-origin(3))^2)-R^2;
    if(CUTCRT(i)>=0)
       indO2(k)=i;
        k=k+1;
    end
end

mO2=Mol(indO2,:,:);

figure
scatter3(X_si,Y_si,Z_si,'r');
hold on
scatter3(mO2(:,1,1),mO2(:,1,2),mO2(:,1,3),'g');
hold on
scatter3(mO2(:,2,1),mO2(:,2,2),mO2(:,2,3),'b');


INX1=1:2:(2*length(mO2)-1);
INX2=2:2:2*length(mO2);
mmO2(INX1,:)=mO2(:,1,:);
mmO2(INX2,:)=mO2(:,2,:);

NM=length(mmO2)/2;
NA=length(X_si);


PmID(1:2:(2*NM-1),1)=1:1:NM;
PmID(2:2:2*NM,1)=1:1:NM;

load xyzSi;
si_x=xyzSi(:,5);
si_y=xyzSi(:,6);
si_z=xyzSi(:,7);

PM=[((2*NM+1):(2*NM+NA))' ((NM+1):(NA+NM))' X_si' Y_si'
Z_si'];
PMSi=[((1):(NA))' ((1):(NA))' X_si' Y_si' Z_si'];
% PM0Chg=[((3*NM+1):(3*NM+NA))' ((NM+1):(NA+NM))'  zeros(NA,1)
X_al' Y_al' Z_al'];
PB1=[((NA+1):(NA+NM))' ones(NM,1) ((NA+1):2:(NA+2*NM-1))'
((NA+2):2:(NA+2*NM))'];
```

```
% PB2=[((1+NM):(2*NM))' ones(NM,1) (3:3:3*NM)' (1:3:3*NM-2)'];
% PA=[(1:NM)' ones(NM,1)  (2:3:3*NM-1)' (1:3:3*NM-2)'
(3:3:3*NM)'];
PO2=[((NA+1):(NA+2*NM))' NA+PmID  mmO2(:,1) mmO2(:,2)
mmO2(:,3)];
POO=[((NA+1):(NA+2*NM))' ((NA+1):(NA+2*NM))' mmO2(:,1)
mmO2(:,2) mmO2(:,3)];

fid = fopen('oxgas','a');
fprintf(fid,'LAMMPS 3d silicon oxidation data file produced
by P.Song 03/03/09\n ');
fprintf(fid,'       \n ');
fprintf(fid,'184   atoms\n ');
fprintf(fid,'0 bonds\n ');
fprintf(fid,'0 angles\n ');
fprintf(fid,'0 dihedrals\n ');
fprintf(fid,'0 impropers\n ');
fprintf(fid,'       \n ');
fprintf(fid,'1 atom types\n ');
fprintf(fid,'0 bond types\n ');
fprintf(fid,'0 angle types\n ');
fprintf(fid,'0 dihedral types\n ');
fprintf(fid,'0 improper types\n ');
fprintf(fid,'       \n ');
fprintf(fid,' -15.0000 15.0000 xlo xhi\n ');
fprintf(fid,' -15.0000 15.0000 ylo yhi\n ');
fprintf(fid,' -15.0000 15.0000 zlo zhi\n ');
fprintf(fid,'       \n ');
fprintf(fid,'Masses\n ');
fprintf(fid,'       \n ');
fprintf(fid,' 1 28.0855\n ');
fprintf(fid,'       \n ');
fprintf(fid,'Atoms\n ');
fprintf(fid,'       \n ');
fprintf(fid,'%4d  %4d   2  0  %9.5f  %9.5f  %9.5f\n ',PO2');
fprintf(fid,'Bonds\n ');
fprintf(fid,'       \n ');
fprintf(fid,'%4d   %4d  %4d  %4d\n ',PB1');

fclose(fid);



fid = fopen('oxgasNB','a');
fprintf(fid,'LAMMPS 3d silicon oxidation data file produced
by P.Song 18/03/09\n ');
fprintf(fid,'       \n ');
fprintf(fid,'368   atoms\n ');
fprintf(fid,'0 bonds\n ');
fprintf(fid,'0 angles\n ');
fprintf(fid,'0 dihedrals\n ');
fprintf(fid,'0 impropers\n ');
fprintf(fid,'       \n ');
fprintf(fid,'1 atom types\n ');
fprintf(fid,'0 bond types\n ');
fprintf(fid,'0 angle types\n ');
fprintf(fid,'0 dihedral types\n ');
```

```
fprintf(fid,'0 improper types\n ');
fprintf(fid,'       \n ');
fprintf(fid,' -15.0000 15.0000 xlo xhi\n ');
fprintf(fid,' -15.0000 15.0000 ylo yhi\n ');
fprintf(fid,' -15.0000 15.0000 zlo zhi\n ');
fprintf(fid,'       \n ');
fprintf(fid,'Masses\n ');
fprintf(fid,'       \n ');
fprintf(fid,'2 15.9994\n ');
fprintf(fid,'       \n ');
fprintf(fid,'Atoms\n ');
fprintf(fid,'       \n ');
fprintf(fid,'%4d  2  0  %9.5f  %9.5f  %9.5f\n ',POO');

fclose(fid);

fid = fopen('sioxNB.data','a');
fprintf(fid,'LAMMPS 3d silicon oxidation data file produced
by P.Song 18/03/09\n ');
fprintf(fid,'       \n ');
fprintf(fid,'552   atoms\n ');
fprintf(fid,'184 bonds\n ');
fprintf(fid,'0 angles\n ');
fprintf(fid,'0 dihedrals\n ');
fprintf(fid,'0 impropers\n ');
fprintf(fid,'       \n ');
fprintf(fid,'2 atom types\n ');
fprintf(fid,'1 bond types\n ');
fprintf(fid,'0 angle types\n ');
fprintf(fid,'0 dihedral types\n ');
fprintf(fid,'0 improper types\n ');
fprintf(fid,'       \n ');
fprintf(fid,' -16.0000 16.0000 xlo xhi\n ');
fprintf(fid,' -16.0000 16.0000 ylo yhi\n ');
fprintf(fid,' -16.0000 16.0000 zlo zhi\n ');
fprintf(fid,'       \n ');
fprintf(fid,'Masses\n ');
fprintf(fid,'       \n ');
fprintf(fid,' 1 28.0855\n ');
fprintf(fid,' 2 15.9994\n ');
fprintf(fid,'       \n ');
fprintf(fid,'Atoms\n ');
fprintf(fid,'       \n ');
fprintf(fid,'%4d  %4d  1  0.0  %9.5f  %9.5f  %9.5f\n ',PMSi');
fprintf(fid,'%4d  %4d  2  0.0  %9.5f  %9.5f  %9.5f\n ',POO');

fclose(fid);

clear;
dump = fopen('sibond','r');

i=1;
k1=1;
k2=1;
k3=1;
k4=1;
k5=1;
k6=1;
```

```
while feof(dump) == 0
    a = fgetl(dump);
    if length(a) > 4 && strcmp(a(3:10),'Timestep')
            atomdata(i).timestep = str2num(a(11:(length(a)-
1)));

    else if length(a) > 4 && (strcmp(a(1),' '))
            alldl = str2num(fgetl(dump));
            atom_id(i)=alldl(1);
            atom_type(i)=alldl(2);
        else if alldl(3)==1
               atomdata(i).bond1(k1,:)=str2num(fgetl(dump));
               k1=k1+1;
            else if alldl(3)==2
               atomdata(i).bond2(k2,:)=str2num(fgetl(dump));
               k2=k2+1;
                else if alldl(3)==3
               atomdata(i).bond3(k3,:)=str2num(fgetl(dump));
               k3=k3+1;
                    else if alldl(3)==4
              atomdata(i). bond4(k4,:)=str2num(fgetl(dump));
               k4=k4+1;
                        else if alldl(3)==5
               atomdata(i).bond5(k5,:)=str2num(fgetl(dump));
               k5=k5+1;
                            else if alldl(3)==6
               atomdata(i).bond6(k6,:)=str2num(fgetl(dump));
               k6=k6+1;
               end
               end
               end
            end
            end
           end
        end
        i=i+1;
end
end



clear;
%silicon id <=184; 616> oxygen >184;
dump = fopen('sibond1000_2000K','r');
t=[0:0.25/10:0.25];
bondSicount(1:11)=0;
time=[0:0.5/20:0.5];
T=[300:2700/20:3000];
i=1;
j=1;
k1=1;
k2=1;
k3=1;
k4=1;
k5=1;
k6=1;
while feof(dump) == 0
    a = fgetl(dump);
```

```
    if length(a) > 10 && strcmp(a(3:10),'Timestep')
            timestep(j) =str2num(a(12:(length(a))));
            j=j+1;
    else if length(a) > 30 && ~(strcmp(a(1),'#'))
            alldl{i} = str2num(a);
            atom_id(i)=alldl{i}(1);
            atom_type(i)=alldl{i}(2);
        if alldl{i}(3)==1
               list(j-1).bond1(k1,:)=str2num(a);
               k1=k1+1;
            else if alldl{i}(3)==2
               list(j-1).bond2(k2,:)=str2num(a);
               k2=k2+1;
                else if alldl{i}(3)==3
               list(j-1).bond3(k3,:)=str2num(a);
               k3=k3+1;
                    else if alldl{i}(3)==4
              list(j-1).bond4(k4,:)=str2num(a);
               k4=k4+1;
                        else if alldl{i}(3)==5
               list(j-1).bond5(k5,:)=str2num(a);
               k5=k5+1;
                            else if alldl{i}(3)==6
               list(j-1).bond6(k6,:)=str2num(a);
               k6=k6+1;
               end
               end
               end
            end
            end
        end
           i=i+1;
        end

    end

end



%GET NON-ZERO ROWs OF LIST, WRITE TO CELLS

for i=1:11
B1{i}=list(i).bond1(find(list(i).bond1(:,1)~=0),:);
B2{i}=list(i).bond2(find(list(i).bond2(:,1)~=0),:);
B3{i}=list(i).bond3(find(list(i).bond3(:,1)~=0),:);
B4{i}=list(i).bond4(find(list(i).bond4(:,1)~=0),:);
B5{i}=list(i).bond5(find(list(i).bond5(:,1)~=0),:);
B6{i}=list(i).bond6(find(list(i).bond6(:,1)~=0),:);
end

BOND={B1,B2,B3,B4,B5,B6};
for i=1:11
N1(i)=length(B1{i});
N2(i)=length(B2{i});
N3(i)=length(B3{i});
N4(i)=length(B4{i});
```

```
N5(i)=length(B5{i});
N6(i)=length(B6{i});
end

for i=1:11
    for j=1:6
    OxBond{i,j}=BOND{j}{i}(find(BOND{j}{i}(:,1)>184),:);
    SiBond{i,j}=BOND{j}{i}(find(BOND{j}{i}(:,1)<185),:);
end
end

for i=1:11
    NO2(i)=length(OxBond{i,1});
end


%GENERATE BOND MAP

for j=2:6
for i=1:11

        for k=1:length(SiBond{i,j}(:,1))
            for m=4:(j+3)
        if ((SiBond{i,j}(k,1)~=0) &&(SiBond{i,j}(k,m)<185))
            MAP{i,j}(k,1)=SiBond{i,j}(k,1);
            MAP{i,j}(k,m)=1;
            MAP{i,j}(k,2)=MAP{i,j}(k,2)+1;%count Si-Si number

        else
            MAP{i,j}(k,1)=SiBond{i,j}(k,1);
            MAP{i,j}(k,m)=0;
            MAP{i,j}(k,3)=MAP{i,j}(k,3)+1;%count Si-O number

end
                            end
                            end
end

end


%BOND MAPS
j=3;% 3 bonds in Si BONDLIST
m1=1;
for i=1:11

        for k=1:length(SiBond{i,j}(:,1))


BO_3X{i}(m1,:)=SiBond{i,j}(k,4)*SiBond{i,j}(k,5)*SiBond{i,j}(
k,6);

BO_3T{i}(m1,:)=SiBond{i,j}(k,4)+SiBond{i,j}(k,5)+SiBond{i,j}(
k,6);
            m1=m1+1;
```

```
        end
end
for k=1:11
B_3X{k}=BO_3X{k}((find(BO_3X{k}(:,1)~=0)),:);
B_3T{k}=BO_3T{k}((find(BO_3T{k}(:,1)~=0)),:);
End

%BOND MAPS
j=4;% 4 bonds in Si BONDLIST
m1=1;

for i=1:11

        for k=1:length(SiBond{i,j}(:,1))

BO_4X{i}(m1,:)=SiBond{i,j}(k,4)*SiBond{i,j}(k,5)*SiBond{i,j}(
k,6)*SiBond{i,j}(k,7);

BO_4T{i}(m1,:)=SiBond{i,j}(k,4)+SiBond{i,j}(k,5)+SiBond{i,j}(
k,6)+SiBond{i,j}(k,7);
             m1=m1+1;
    end
end
for k=1:11
B_4X{k}=BO_4X{k}((find(BO_4X{k}(:,1)~=0)),:);
B_4T{k}=BO_4T{k}((find(BO_4T{k}(:,1)~=0)),:);
End

%BOND MAPS

j=5;% 5 bonds in Si BONDLIST
m1=1;
for i=1:11

        for k=1:length(SiBond{i,j}(:,1))

BO_5X{i}(m1,:)=SiBond{i,j}(k,4)*SiBond{i,j}(k,5)*SiBond{i,j}(
k,6)*SiBond{i,j}(k,7)*SiBond{i,j}(k,8);

BO_5T{i}(m1,:)=SiBond{i,j}(k,4)+SiBond{i,j}(k,5)+SiBond{i,j}(
k,6)+SiBond{i,j}(k,7)+SiBond{i,j}(k,8);
         m1=m1+1;
        end
    end
     for k=1:11
B_5X{k}=BO_5X{k}((find(BO_5X{k}(:,1)~=0)),:);
B_5T{k}=BO_5T{k}((find(BO_5T{k}(:,1)~=0)),:);
end

%Silicon BOND MAPS

j=6;% 5 bonds in Si BONDLIST
m1=1;
for i=1:11

        for k=1:length(SiBond{i,j}(:,1))
```

```
BO_6X{i}(m1,:)=SiBond{i,j}(k,4)*SiBond{i,j}(k,5)*SiBond{i,j}(
k,6)*SiBond{i,j}(k,7)*SiBond{i,j}(k,8)*SiBond{i,j}(k,8)*SiBon
d{i,j}(k,9);

BO_6T{i}(m1,:)=SiBond{i,j}(k,4)+SiBond{i,j}(k,5)+SiBond{i,j}(
k,6)+SiBond{i,j}(k,7)+SiBond{i,j}(k,8)+SiBond{i,j}(k,8)+SiBon
d{i,j}(k,9);
         m1=m1+1;
    end
end
for k=1:11
B_6X{k}=BO_6X{k}((find(BO_6X{k}(:,1)~=0)),:);
B_6T{k}=BO_6T{k}((find(BO_6T{k}(:,1)~=0)),:);
end

for i=1:11
    for k=1:length(B_3T{i}(:))
BTmat(1,i,k)=B_3T{i}(k);
    end
end

for i=1:11
    for k=1:length(B_4T{i}(:))
BTmat(2,i,k)=B_4T{i}(k);
    end
end

for i=1:11
    for k=1:length(B_5T{i}(:))
BTmat(3,i,k)=B_5T{i}(k);
    end
end

for i=1:11
    for k=1:length(B_6T{i}(:))
BTmat(4,i,k)=B_6T{i}(k);
    end
end


for i=1:11
    for k=1:length(B_3X{i}(:))
BXmat(1,i,k)=B_3X{i}(k);
    end
end

for i=1:11
    for k=1:length(B_4X{i}(:))
BXmat(2,i,k)=B_4X{i}(k);
    end
end

for i=1:11
    for k=1:length(B_5X{i}(:))
BXmat(3,i,k)=B_5X{i}(k);
    end
end
```

```
for i=1:11
    for k=1:length(B_6X{i}(:))
BXmat(4,i,k)=B_6X{i}(k);
    end
end

for i=1:4
    for j=1:11
BT{i,j}=sort(BTmat(find(BTmat(i,j,:)~=0)));
BX{i,j}=sort(BXmat(find(BXmat(i,j,:)~=0))/1000);
    end
end


Nex=zeros(4,11);
for i=1:4
    for j=1:11
        for k=1:(length(BT{i,j})-1)

    if
((BT{i,j}(k)==BT{i,j}(k+1))&&(BX{i,j}(k)==BX{i,j}(k+1)))
        Nex(i,j)=Nex(i,j)+1;
    end
        end
    end
end

for i=1:11
NexT(i)=sum(Nex(:,i));
end


clear;
%silicon id <=184; 616> oxygen >184;
dump = fopen('sibond1000_2000K','r');
t=[0:0.25/10:0.25];
i=1;
j=1;
k1=1;
k2=1;
k3=1;
k4=1;
k5=1;
k6=1;
while feof(dump) == 0
    a = fgetl(dump);
    if length(a) > 10 && strcmp(a(3:10),'Timestep')
            timestep(j) =str2num(a(12:(length(a))));
            j=j+1;
    else if length(a) > 30 && ~(strcmp(a(1),'#'))
            alldl{i} = str2num(a);
            atom_id(i)=alldl{i}(1);
            atom_type(i)=alldl{i}(2);
        if alldl{i}(3)==1
               list(j-1).bond1(k1,:)=str2num(a);
               k1=k1+1;
```

```
            else if alldl{i}(3)==2
               list(j-1).bond2(k2,:)=str2num(a);
               k2=k2+1;
                else if alldl{i}(3)==3
               list(j-1).bond3(k3,:)=str2num(a);
               k3=k3+1;
                    else if alldl{i}(3)==4
              list(j-1).bond4(k4,:)=str2num(a);
               k4=k4+1;
                        else if alldl{i}(3)==5
               list(j-1).bond5(k5,:)=str2num(a);
               k5=k5+1;
                            else if alldl{i}(3)==6
               list(j-1).bond6(k6,:)=str2num(a);
               k6=k6+1;
               end
               end
               end
            end
            end
        end
           i=i+1;
        end

    end

end


%GET NON-ZERO ROWs OF LIST, WRITE TO CELLS
for i=1:11
B1{i}=list(i).bond1(find(list(i).bond1(:,1)~=0),:);
B2{i}=list(i).bond2(find(list(i).bond2(:,1)~=0),:);
B3{i}=list(i).bond3(find(list(i).bond3(:,1)~=0),:);
B4{i}=list(i).bond4(find(list(i).bond4(:,1)~=0),:);
B5{i}=list(i).bond5(find(list(i).bond5(:,1)~=0),:);
B6{i}=list(i).bond6(find(list(i).bond6(:,1)~=0),:);
end

BOND={B1,B2,B3,B4,B5,B6};

for i=1:11
N1(i)=length(B1{i});
N2(i)=length(B2{i});
N3(i)=length(B3{i});
N4(i)=length(B4{i});
N5(i)=length(B5{i});
N6(i)=length(B6{i});
end

figure
plot(1:11,N1,'-o', 1:11,N2,'-v',1:11,N3,'-^',1:11,N4,'-
<',1:11,N5,'->',1:11,N6,'-s');
legend('Single','Dual Bond','Tri Bond','4
Bond','5Bond','6Bond');

for i=1:11
```

```
    for j=1:6
    OxBond{i,j}=BOND{j}{i}(find(BOND{j}{i}(:,1)>184),:);
    SiBond{i,j}=BOND{j}{i}(find(BOND{j}{i}(:,1)<185),:);
end
end

%GENERATE BOND MAP

for j=2:6
for i=1:11

        for k=1:length(SiBond{i,j}(:,1))
            for m=4:(j+3)
        if ((SiBond{i,j}(k,1)~=0) &&(SiBond{i,j}(k,m)<185))
            MAP{i,j}(k,1)=SiBond{i,j}(k,1);
            MAP{i,j}(k,m)=1;
            MAP{i,j}(k,2)=MAP{i,j}(k,2)+1;%count Si-Si number

        else
            MAP{i,j}(k,1)=SiBond{i,j}(k,1);
            MAP{i,j}(k,m)=0;
            MAP{i,j}(k,3)=MAP{i,j}(k,3)+1;%count Si-O number

end
                            end
                            end
end

end

%BOND MAPS
j=3;% 3 bonds in Si BONDLIST
m1=1;
m2=1;
m3=1;
m4=1;
for i=1:11

        for k=1:length(SiBond{i,j}(:,1))
        if (MAP{i,j}(k,2)==3)
            Si_3{i,j}(m1,:)=SiBond{i,j}(k,:);
            m1=m1+1;
        elseif (MAP{i,j}(k,2)==2)
                O_2Si{i,j}(m2,:)=SiBond{i,j}(k,:);
                m2=m2+1;
        elseif (MAP{i,j}(k,2)==1)
                        Si_2O{i,j}(m3,:)=SiBond{i,j}(k,:);
                        m3=m3+1;
        elseif (MAP{i,j}(k,3)==3)
                        O3{i,j}(m4,:)=SiBond{i,j}(k,:);
                        m4=m4+1;

        end
    end
end
```

```
for k=1:11
Si3{k}=Si_3{k,3}((find(Si_3{k,3}(:,1)~=0)),:);
end

for k=[8:11]
Ox2Si{k}=O_2Si{k,3}((find(O_2Si{k,3}(:,1)~=0)),:);
end

%BOND MAPS
j=4;% 4 bonds in Si BONDLIST
m1=1;
m2=1;
m3=1;
m4=1;
m5=1;
for i=1:11

        for k=1:length(SiBond{i,j}(:,1))
        if (MAP{i,j}(k,2)==4)
            Si_4{i,j}(m1,:)=SiBond{i,j}(k,:);
            m1=m1+1;
        elseif (MAP{i,j}(k,2)==3)
                Si3_O{i,j}(m2,:)=SiBond{i,j}(k,:);
                m2=m2+1;
        elseif (MAP{i,j}(k,2)==2)
                        Si2_2O{i,j}(m3,:)=SiBond{i,j}(k,:);
                        m3=m3+1;
        elseif (MAP{i,j}(k,2)==1)
                        Si_3O{i,j}(m4,:)=SiBond{i,j}(k,:);
                        m4=m4+1;
        else
                        O4{i,j}(m5,:)=SiBond{i,j}(k,:);
                        m5=m5+1;
        end
    end
end

for k=1:11
Si4{k}=Si_4{k,4}((find(Si_4{k,4}(:,1)~=0)),:);
Ox3Si{k}=Si3_O{k,4}((find(Si3_O{k,4}(:,1)~=0)),:);
O2x2Si{k}=Si2_2O{k,4}((find(Si2_2O{k,4}(:,1)~=0)),:);
O3xSi{k}=Si_3O{k,4}((find(Si_3O{k,4}(:,1)~=0)),:);
end

%BOND MAPS
j=5;% 5 bonds in Si BONDLIST
m1=1;
m2=1;
m3=1;
m4=1;
m5=1;
m6=1;
for i=1:11

        for k=1:length(SiBond{i,j}(:,1))
        if (MAP{i,j}(k,2)==5)
            Si_5{i,j}(m1,:)=SiBond{i,j}(k,:);
            m1=m1+1;
```

```
        elseif (MAP{i,j}(k,2)==4)
                Si4_O{i,j}(m2,:)=SiBond{i,j}(k,:);
                m2=m2+1;
        elseif (MAP{i,j}(k,2)==3)
                        Si3_2O{i,j}(m3,:)=SiBond{i,j}(k,:);
                        m3=m3+1;
        elseif (MAP{i,j}(k,2)==2)
                        Si2_3O{i,j}(m4,:)=SiBond{i,j}(k,:);
                        m4=m4+1;
         elseif (MAP{i,j}(k,2)==1)
                        Si_4O{i,j}(m5,:)=SiBond{i,j}(k,:);
                        m5=m5+1;
        else
            O5{i,j}(m6,:)=SiBond{i,j}(k,:);
                        m6=m6+1;
        end
    end
end

for k=1:11
Si5{k}=Si_5{k,j}((find(Si_5{k,j}(:,1)~=0)),:);
Ox4Si{k}=Si4_O{k,j}((find(Si4_O{k,j}(:,1)~=0)),:);
O3x2Si{k}= Si3_2O{k,j}((find(Si3_2O{k,j}(:,1)~=0)),:);
End

%BOND MAPS
j=6;% 5 bonds in Si BONDLIST
m1=1;
m2=1;
m3=1;
m4=1;
m5=1;
m6=1;
m7=1;
for i=1:11

        for k=1:length(SiBond{i,j}(:,1))
        if (MAP{i,j}(k,2)==6)
            Si_6{i,j}(m1,:)=SiBond{i,j}(k,:);
            m1=m1+1;
        elseif (MAP{i,j}(k,2)==5)
                Si5_O{i,j}(m2,:)=SiBond{i,j}(k,:);
                m2=m2+1;
        elseif (MAP{i,j}(k,2)==4)
                        Si4_2O{i,j}(m3,:)=SiBond{i,j}(k,:);
                        m3=m3+1;
        elseif (MAP{i,j}(k,2)==3)
                        Si3_3O{i,j}(m4,:)=SiBond{i,j}(k,:);
                        m4=m4+1;
         elseif (MAP{i,j}(k,2)==2)
                        Si2_4O{i,j}(m5,:)=SiBond{i,j}(k,:);
                        m5=m5+1;
        elseif (MAP{i,j}(k,2)==1)
            Si_5O{i,j}(m6,:)=SiBond{i,j}(k,:);
                        m6=m6+1;
        else
            O6{i,j}(m7,:)=SiBond{i,j}(k,:);
                        m7=m7+1;
```

```
        end
    end
end

clear;
%silicon id <=184; 616> oxygen >184;
dump = fopen('sibond300_1000K','r');
t=[0:0.25/10:0.25];
bondSicount(1:11)=0;
time=[0:0.5/20:0.5];
T=[300:2700/20:3000];
i=1;
j=1;
k1=1;
k2=1;
k3=1;
k4=1;
k5=1;
k6=1;
while feof(dump) == 0
    a = fgetl(dump);
    if length(a) > 10 && strcmp(a(3:10),'Timestep')
            timestep(j) =str2num(a(12:(length(a))));
            j=j+1;
    else if length(a) > 30 && ~(strcmp(a(1),'#'))
            alldl{i} = str2num(a);
            atom_id(i)=alldl{i}(1);
            atom_type(i)=alldl{i}(2);
        if alldl{i}(3)==1
               list(j-1).bond1(k1,:)=str2num(a);
               k1=k1+1;
            else if alldl{i}(3)==2
               list(j-1).bond2(k2,:)=str2num(a);
               k2=k2+1;
                else if alldl{i}(3)==3
               list(j-1).bond3(k3,:)=str2num(a);
               k3=k3+1;
                    else if alldl{i}(3)==4
              list(j-1).bond4(k4,:)=str2num(a);
               k4=k4+1;
                        else if alldl{i}(3)==5
               list(j-1).bond5(k5,:)=str2num(a);
               k5=k5+1;
                            else if alldl{i}(3)==6
               list(j-1).bond6(k6,:)=str2num(a);
               k6=k6+1;
               end
               end
               end
            end
            end
        end
           i=i+1;
        end

    end

end
```

```
%GET NON-ZERO ROWs OF LIST, WRITE TO CELLS

for i=1:11
B1{i}=list(i).bond1(find(list(i).bond1(:,1)~=0),:);
B2{i}=list(i).bond2(find(list(i).bond2(:,1)~=0),:);
B3{i}=list(i).bond3(find(list(i).bond3(:,1)~=0),:);
B4{i}=list(i).bond4(find(list(i).bond4(:,1)~=0),:);
B5{i}=list(i).bond5(find(list(i).bond5(:,1)~=0),:);
B6{i}=list(i).bond6(find(list(i).bond6(:,1)~=0),:);
end

BOND={B1,B2,B3,B4,B5,B6};

for i=1:11
N1(i)=length(B1{i});
N2(i)=length(B2{i});
N3(i)=length(B3{i});
N4(i)=length(B4{i});
N5(i)=length(B5{i});
N6(i)=length(B6{i});
end

for i=1:11
    for j=1:6
    OxBond{i,j}=BOND{j}{i}(find(BOND{j}{i}(:,1)>184),:);
    SiBond{i,j}=BOND{j}{i}(find(BOND{j}{i}(:,1)<185),:);
end
end

for i=1:11
    NO2(i)=length(OxBond{i,1});
end


%GENERATE BOND MAP
for j=2:6
for i=1:11

        for k=1:length(SiBond{i,j}(:,1))
            for m=4:(j+3)
        if ((SiBond{i,j}(k,1)~=0) &&(SiBond{i,j}(k,m)<185))
            MAP{i,j}(k,1)=SiBond{i,j}(k,1);
            MAP{i,j}(k,m)=1;
            MAP{i,j}(k,2)=MAP{i,j}(k,2)+1;%count Si-Si number

        else
            MAP{i,j}(k,1)=SiBond{i,j}(k,1);
            MAP{i,j}(k,m)=0;
            MAP{i,j}(k,3)=MAP{i,j}(k,3)+1;%count Si-O number

end
                            end
                            end
end

end
```

```
%BOND MAPS
j=3;% 3 bonds in Si BONDLIST
m1=1;
for i=1:11

        for k=1:length(SiBond{i,j}(:,1))


BO_3X{i}(m1,:)=SiBond{i,j}(k,4)*SiBond{i,j}(k,5)*SiBond{i,j}(
k,6);

BO_3T{i}(m1,:)=SiBond{i,j}(k,4)+SiBond{i,j}(k,5)+SiBond{i,j}(
k,6);
            m1=m1+1;

        end
end
for k=1:11
B_3X{k}=BO_3X{k}((find(BO_3X{k}(:,1)~=0)),:);
B_3T{k}=BO_3T{k}((find(BO_3T{k}(:,1)~=0)),:);
end

%BOND MAPS
j=4;% 4 bonds in Si BONDLIST
m1=1;

for i=1:11

        for k=1:length(SiBond{i,j}(:,1))

BO_4X{i}(m1,:)=SiBond{i,j}(k,4)*SiBond{i,j}(k,5)*SiBond{i,j}(
k,6)*SiBond{i,j}(k,7);

BO_4T{i}(m1,:)=SiBond{i,j}(k,4)+SiBond{i,j}(k,5)+SiBond{i,j}(
k,6)+SiBond{i,j}(k,7);
             m1=m1+1;
    end
end
for k=1:11
B_4X{k}=BO_4X{k}((find(BO_4X{k}(:,1)~=0)),:);
B_4T{k}=BO_4T{k}((find(BO_4T{k}(:,1)~=0)),:);
end


%BOND MAPS

j=5;% 5 bonds in Si BONDLIST
m1=1;
for i=1:11

        for k=1:length(SiBond{i,j}(:,1))

BO_5X{i}(m1,:)=SiBond{i,j}(k,4)*SiBond{i,j}(k,5)*SiBond{i,j}(
k,6)*SiBond{i,j}(k,7)*SiBond{i,j}(k,8);
```

```
BO_5T{i}(m1,:)=SiBond{i,j}(k,4)+SiBond{i,j}(k,5)+SiBond{i,j}(
k,6)+SiBond{i,j}(k,7)+SiBond{i,j}(k,8);
         m1=m1+1;
        end
    end
     for k=1:11
B_5X{k}=BO_5X{k}((find(BO_5X{k}(:,1)~=0)),:);
B_5T{k}=BO_5T{k}((find(BO_5T{k}(:,1)~=0)),:);
end

%Silicon BOND MAPS

j=6;% 5 bonds in Si BONDLIST
m1=1;
for i=1:11

        for k=1:length(SiBond{i,j}(:,1))

BO_6X{i}(m1,:)=SiBond{i,j}(k,4)*SiBond{i,j}(k,5)*SiBond{i,j}(
k,6)*SiBond{i,j}(k,7)*SiBond{i,j}(k,8)*SiBond{i,j}(k,8)*SiBon
d{i,j}(k,9);

BO_6T{i}(m1,:)=SiBond{i,j}(k,4)+SiBond{i,j}(k,5)+SiBond{i,j}(
k,6)+SiBond{i,j}(k,7)+SiBond{i,j}(k,8)+SiBond{i,j}(k,8)+SiBon
d{i,j}(k,9);
         m1=m1+1;
    end
end
for k=1:11
B_6X{k}=BO_6X{k}((find(BO_6X{k}(:,1)~=0)),:);
B_6T{k}=BO_6T{k}((find(BO_6T{k}(:,1)~=0)),:);
end

for i=1:11
    for k=1:length(B_3T{i}(:))
BTmat(1,i,k)=B_3T{i}(k);
    end
end

for i=1:11
    for k=1:length(B_4T{i}(:))
BTmat(2,i,k)=B_4T{i}(k);
    end
end

for i=1:11
    for k=1:length(B_5T{i}(:))
BTmat(3,i,k)=B_5T{i}(k);
    end
end

for i=1:11
    for k=1:length(B_6T{i}(:))
BTmat(4,i,k)=B_6T{i}(k);
    end
end
```

```
for i=1:11
    for k=1:length(B_3X{i}(:))
BXmat(1,i,k)=B_3X{i}(k);
    end
end

for i=1:11
    for k=1:length(B_4X{i}(:))
BXmat(2,i,k)=B_4X{i}(k);
    end
end

for i=1:11
    for k=1:length(B_5X{i}(:))
BXmat(3,i,k)=B_5X{i}(k);
    end
end

for i=1:11
    for k=1:length(B_6X{i}(:))
BXmat(4,i,k)=B_6X{i}(k);
    end
end

for i=1:4
    for j=1:11
BT{i,j}=sort(BTmat(find(BTmat(i,j,:)~=0)));
BX{i,j}=sort(BXmat(find(BXmat(i,j,:)~=0))/1000);
    end
end


Nex=zeros(4,11);
for i=1:4
    for j=1:11
        for k=1:(length(BT{i,j})-1)

    if
((BT{i,j}(k)==BT{i,j}(k+1))&&(BX{i,j}(k)==BX{i,j}(k+1)))
        Nex(i,j)=Nex(i,j)+1;
    end
        end
    end
end

for i=1:11
NexT(i)=sum(Nex(:,i));
end


%Si-O bond length and bond angle

clear;
%silicon id <=184; 616> oxygen >184;oxibond correspond to
300-2000K bond
%infor
dump = fopen('oxibond','r');
```

```
%in dump file order is: id, type, q, x, y,z
trjfile={'trjallfix100000','trjallfix200000','trjallfix300000
','trjallfix400000','trjallfix500000',...

'trjallfix600000','trjallfix700000','trjallfix800000','trjall
fix900000','trjallfix1000000','trjallfix1100000'};
for i=1:11
trjdata{i} = load(trjfile{i});
end

for i=1:11
orderdata{i} = sortrows(trjdata{i});
end


t=[0:0.25/10:0.25];
i=1;
j=1;
k1=1;
k2=1;
k3=1;
k4=1;
k5=1;
k6=1;
while feof(dump) == 0
    a = fgetl(dump);
    if length(a) > 10 && strcmp(a(3:10),'Timestep')
            timestep(j) =str2num(a(12:(length(a))));
            j=j+1;
    else if length(a) > 30 && ~(strcmp(a(1),'#'))
            alldl{i} = str2num(a);
            atom_id(i)=alldl{i}(1);
            atom_type(i)=alldl{i}(2);
        if alldl{i}(3)==1
               list(j-1).bond1(k1,:)=str2num(a);
               k1=k1+1;
            else if alldl{i}(3)==2
               list(j-1).bond2(k2,:)=str2num(a);
               k2=k2+1;
                else if alldl{i}(3)==3
               list(j-1).bond3(k3,:)=str2num(a);
               k3=k3+1;
                     else if alldl{i}(3)==4
              list(j-1).bond4(k4,:)=str2num(a);
               k4=k4+1;
                         else if alldl{i}(3)==5
               list(j-1).bond5(k5,:)=str2num(a);
               k5=k5+1;
                             else if alldl{i}(3)==6
               list(j-1).bond6(k6,:)=str2num(a);
               k6=k6+1;
               end
               end
               end
            end
            end
        end
           i=i+1;
```

```
        end

    end

end



%GET NON-ZERO ROWs OF LIST, WRITE TO CELLS

for i=1:11
B1{i}=list(i).bond1(find(list(i).bond1(:,1)~=0),:);
B2{i}=list(i).bond2(find(list(i).bond2(:,1)~=0),:);
B3{i}=list(i).bond3(find(list(i).bond3(:,1)~=0),:);
B4{i}=list(i).bond4(find(list(i).bond4(:,1)~=0),:);
B5{i}=list(i).bond5(find(list(i).bond5(:,1)~=0),:);
B6{i}=list(i).bond6(find(list(i).bond6(:,1)~=0),:);
end

BOND={B1,B2,B3,B4,B5,B6};

for i=1:11
N1(i)=length(B1{i});
N2(i)=length(B2{i});
N3(i)=length(B3{i});
N4(i)=length(B4{i});
N5(i)=length(B5{i});
N6(i)=length(B6{i});
end

for i=1:11
    for j=1:6
    OxBond{i,j}=BOND{j}{i}(find(BOND{j}{i}(:,1)>184),:);
    SiBond{i,j}=BOND{j}{i}(find(BOND{j}{i}(:,1)<185),:);
end
end



for i=1:11

ang_SiOSi{i}=[OxBond{i,2}(:,1),OxBond{i,2}(:,4),OxBond{i,2}(:
,5)];
end

%A(x1,y1,z1),B(x2,y2,z2),C(x3,y3,z3)
%AB=(x2-x1,y2-y1,z2-z1);AC=(x3-x1,y3-y1,z3-z1)
%cos<A=AB*AC/(|AB|*|AC|)
%=[(x2-x1)*(x3-x1)+(y2-y1)*(y3-y1)+(z2-z1)*(z3-z1)]/{[(x2-
x1)^2+(y2-y1)^2+(z2-z1)^2]^0.5+[(x3-x1)^2+(y3-y1)^2+(z2-
z1)^2]^0.5}

for i=1:11
BondDist{i}=((orderdata{i}(ang_SiOSi{i}(:,1),4)-
orderdata{i}(ang_SiOSi{i}(:,2),4)).^2+...
    (orderdata{i}(ang_SiOSi{i}(:,1),5)-
orderdata{i}(ang_SiOSi{i}(:,2),5)).^2+...
```

```
    (orderdata{i}(ang_SiOSi{i}(:,1),6)-
orderdata{i}(ang_SiOSi{i}(:,2),6)).^2).^0.5;
end

for i=1:11
CosAngl{i}=((orderdata{i}(ang_SiOSi{i}(:,2),4)-
orderdata{i}(ang_SiOSi{i}(:,1),4)).*((orderdata{i}(ang_SiOSi{
i}(:,3),4)-orderdata{i}(ang_SiOSi{i}(:,1),4)))+...
    (orderdata{i}(ang_SiOSi{i}(:,2),5)-
orderdata{i}(ang_SiOSi{i}(:,1),5)).*((orderdata{i}(ang_SiOSi{
i}(:,3),5)-orderdata{i}(ang_SiOSi{i}(:,1),5)))+...
    (orderdata{i}(ang_SiOSi{i}(:,2),6)-
orderdata{i}(ang_SiOSi{i}(:,1),6)).*((orderdata{i}(ang_SiOSi{
i}(:,3),6)-orderdata{i}(ang_SiOSi{i}(:,1),6)))./...
    (((orderdata{i}(ang_SiOSi{i}(:,1),4)-
orderdata{i}(ang_SiOSi{i}(:,2),4)).^2+(orderdata{i}(ang_SiOSi
{i}(:,1),5)-orderdata{i}(ang_SiOSi{i}(:,2),5)).^2+...
    (orderdata{i}(ang_SiOSi{i}(:,1),6)-
orderdata{i}(ang_SiOSi{i}(:,2),6)).^2).^0.5+...
    ((orderdata{i}(ang_SiOSi{i}(:,1),4)-
orderdata{i}(ang_SiOSi{i}(:,3),4)).^2+(orderdata{i}(ang_SiOSi
{i}(:,1),5)-orderdata{i}(ang_SiOSi{i}(:,3),5)).^2+...
    (orderdata{i}(ang_SiOSi{i}(:,1),6)-
orderdata{i}(ang_SiOSi{i}(:,3),6)).^2).^0.5);
end

for i=1:11
BondAngl{i}=acos(CosAngl{i})*180/3.1415926;
end

for i=1:11
avgBD(i)=mean(BondDist{i});
avgBA(i)=mean(BondAngl{i});
end
```

Bibliography

Adams, D. M., Christy, A. G., Haines, J. and Clark, S. M. (1992). Second-order phase transition in PbO and SnO at high pressure: Implications for the litharge-massicot phase transformation, *Phys. Rev. B*, **46**: 11358-11367.

Adanez, J., de Diego, L. F., Garcia-Labiano, F., Gayan, P., Abad, A., and Palacios, J. M. (2004). Selection of oxygen carriers for Chemical-Looping Combustion, *Energy & Fuels,* **18**: 371-377.

Åkermark, T., Gosset, L., Ganem, J. J., Trimaille, I. and Rigo, S. (1999a). Loss of oxygen at the Si-SiO_2 interface during dry oxidation of silicon, *J. Electrochem. Soc.,* **146**: 3389-3392.

Åkermark, T., Ganem, J. J., Trimaille, I., Vickridge, I. and Rigo, S. (1999b). Temperature and pressure dependence of the oxygen exchange at the SiO_2-Si interface, $O_2 \leftrightarrow SiO_2$ during dry thermal oxidation of silicon, *J. Phys. Chem. B,* **103**: 9910-9914.

Alavi, S. and Thompson, D. L. (2006). Molecular dynamics simulations of the melting of aluminum nanoparticles, *J. Phys. Chem. A*, **110**: 1518-1523.

Alder, B. J. and Wainwright, T. E. (1957). Phase transition for a hard sphere system, *J. Chem. Phys.*, **27(5)**: 1208-1209.

Allen, M. P. and Tildesley, D. J. (1989). Computer simulation of liquids, Oxford University Press, Oxford.

Allouti, F., Manceron, L. and Alikhani, M. E. (2006). The Ni_2+O_2 reaction: the IR spectrum and structure of Ni_2O_2: A combined IR matrix isolation and theoretical study, *Physical Chemistry Chemical Physics*, **8**: 3715-3725.

Andersen, O. K. and Jepsen, O. (1984). Explicit, first-principle Tight-Binding theory, *Phys. Rev. Lett.*, **53**: 2571-2574.

Anderson, H. C. (1980). Molecular dynamics simulations at constant pressure and/or temperature, *J. Chem. Phys.*, **72**: 2384.

Anderson, P. W. (1997). Basic notions of condensed matter physics, Perseus Publishing.

Andrzejak, T. A., Shafirovich, E. and Varma, A. (2007). Ignition mechanism of nickel-coated aluminum particles, *Combustion and Flame*, **150**: 60-70.

Angelo, J. E., Moody, N. R. and Baskes, M. I. (1995). Trapping of hydrogen to lattice defects in nickel, *Modelling and Simulation in Materials Sciences & Engineering*, **3**: 289-307.

Arcidiacono, S., Bieri, N. R., Poulikakos, D. and Grigoropoulos, C. P. (2004). On the coalescence of gold nanoparticles, *International Journal of Multiphase Flow*, **30**: 979-994.

Aste, T., Beruto, D., Botter, R., Ciccarelli, C., Giordani, M. and Pozzolini, P. (1994). Microstructural development during the oxidation process in SnO_2 thin films for gas sensors, *Sens. Actuators B*, **19**: 637-641.

ASTM standard E698-79 (reapproved 1984).

Atkinson, A., Taylor, R. I. and Goode, P. D. (1979). Transport processes in the oxidation of Ni studied using tracers in growing NiO scales, *Oxid. Met.*, **13**: 519-543.

Atkinson, A. and Taylor, R. I. (1981). The diffusion of ^{63}Ni along grain boundaries in nickel oxide, *Philosophical Magazine A*, **43**: 979 -998.

Atkinson, A. (1985), Transport processes during the growth of oxide films at elevated temperature, *Reviews of Modern Physics*, **57**: 437-470.

Avrami, M. (1939). Kinetics of phase change. I. General theory, *J. Chem. Phys.,* **7**: 1103-1112.

Avrami, M. (1940). Kinetics of phase change. II. Transformation-time relations for random distribution of nuclei, *J. Chem. Phys.*, **8**: 212-224.

Avrami, M. (1941). Kinetics of phase change. III. Granulation, phase change, and microstructure, *J. Chem. Phys.*, **9**: 177-184.

Aylward, G. H. and Findlay, T. J. V. (1974). SI Chemical Data, John Wiley & Sons, Hong Kong.

Babuk, V. A., Vassiliev, V. A. and Sviridov, V. V. (2001). Propellant formulation factors and metal agglomeration in combustion of aluminized solid rocket propellant, *Combust. Sci. Technol.*, **163**: 261-289.

Baer, M. R. (2002). Modeling heterogeneous energetic materials at the mesoscale, *Thermochimica Acta*, **384**: 351-367.

Baletto, F. and Ferrando, R. (2005). Structural properties of nanoclusters: Energetic, thermodynamic, and kinetic effects, *Rev. Mod. Phys.,* **77**: 371-423.

Berendsen, B. J. (1982). Biological molecules and membranes, Molecular Dynamics of rigid system in Cartesian coordinates: A general formulation, in G. Ciccotti and W.G. Hoover (eds), *Mol. Phys.*, Taylor and Francis Limited, Abingdon, UK.

Bezjak, A., Kurajica, S. and Sipusic, J. (2002). A new approach to solid-state reactions kinetics analysis: the application of assisting functions to basic equations for isothermal conditions, *Thermochimica Acta,* **386**: 81-90.

Boswell, P. G. (1980). On the calculation of activation-energies using a modified Kissinger method, *Journal of Thermal Analysis*, **18**: 353-358.

Bottani, C. E., Li, A., Bassi, A., Stella, P., Cheyssac, R. and Kofman, R. (2001). Investigation of confined acoustic phonons of tin nanoparticles during melting, *Europhys. Lett.*, **56**: 386-392.

Bongiorno, A. and Pasquarello, A. (2004). Multiscale modeling of oxygen diffusion through the oxide during silicon oxidation, *Physical Review B*, **70**: 195312.

Bongiorno, A. and Pasquarello, A. (2005). Atomic-scale modelling of kinetic processes occurring during silicon oxidation, *J. Phys.*: *Condens. Matter*, **17**: S2051-S2063.

Breiter, A. L., Maltsev, V. M. and Popov, E. I. (1990). Means of modifying metallic fuel in condensed systems, *Combust. Explos. Shock Waves*, **26**: 86-92.

Brenner, D. W. (1990). Empirical potential for hydrocarbons for use in simulating the chemical vapor deposition of diamond films, *Phys. Rev. B*, **42(5)**: 9458-9471.

Brooks, B. R., Bruccoleri, R. E., Olafson, B. D., States, D. J., Swaminathan, S. and Karplus, M. (1983). CHARMM: A program for macromolecular energy, minimization, and dynamics calculations, *J. Comp. Chem.,* **4**: 187-217.

Buehler, M. J., Dodson, J., Meulbroek, P., van Duin, A. C. T. and Goddard III, W. A. (2006a). The Computational Materials Design Facility (CMDF): A powerful framework for multiparadigm multi-scale simulations, *Mat. Res. Soc. Proceedings*, 0894-LL03-03.

Buehler, M. J., van Duin A. C. T. and Goddard III, W. A. (2006b). Multi-paradigm modelling of dynamical crack propagation in silicon using the ReaxFF reactive force field, *Physical Review Letters*, **96**: 095505.

Cabrera, N. and Mott N. F. (1948-1949). Theory of the oxidation of metals, *Rep. Progr. Phys.*, **12**: 163.

Cahen, S., David, N., Fiorani, J. M., Maitre, A. and Vilasi, M. (2003). Thermodynamic modelling of the O-Sn system, *Thermochimica Acta,* **403**: 275-285.

Campbell, T., Kalia, R. K., Nakano, A., Vashishta, P., Ogata, S. and Rodgers, S. (1999). Dynamics of oxidation of aluminum nanoclusters using variable charge molecular-dynamics simulations on parallel computers, *Physical Review Letters*, **82**: 4866-4869.

Campbell, T. J., Aral, G., Ogata, S., Kalia, R. K., Nakano, A. and Vashishta, P. (2005). Oxidation of aluminum nanoclusters, *Physical Review B*, **71**: 205413.

Cao, L. F., Xu, G. F., Xie, D., Guo, M. X., Luo, L., Li, Z. and Wang, M. P. (2006). Thermal stability of Fe, Co, Ni metal nanoparticles, *Phys. Stat. Sol.* (*b*), **243**: 2745-2755.

Carter, R. E. (1960). Kinetic model for solid-state reactions, *J. Chem. Phys.*, **34**: 2010.

Catchart, J. V., Petersen, G. F. and Sparks, C. J. (1969). The Structure of thin oxide films formed on nickel crystals, *J. Electrochem. Soc.,* **116**: 664-668.

Charvin, P., Abanades, S., Lemont, F. and Flamant, G. (2008). Experimental study of SnO_2/SnO/Sn thermochemical systems for solar production of hydrogen, *The American Institute of Chemical Engineers Journal*, **54(10)**: 2759-2767.

Chen, C. H., Yamaguchi, T., Sugawara, K. and Koga, K. (2005). Role of stress in the self-limiting oxidation of copper nanoparticles, *J. Phys. Chem. B,* **109(44)**: 20669-20672.

Chenoweth, K., van Duin, A. C. T., Persson, P., Cheng, M. J., Oxgaard, J. and Goddard III, W. A. (2008). Development and application of a ReaxFF reactive force field for oxidative dehydrogenation on vanadium oxide catalysts, *J. Phys. Chem. C*, **112**: 14645-14654.

Chiang, Y. M., Birnie, D., Kingery, P. and David, W. (1996). Physical ceramics: Principles for ceramic science and engineering, John Wiley & Sons, New York.

Chien, F. S. S., Chou, Y. C., Chen, T. T., Hsieh, W. F., Chao, T. S. and Gwo, S. (2001). Nano-oxidation of silicon nitride films with an atomic force microscope: Chemical mapping, kinetics, and applications, *Journal of Applied Physics*, **89(4)**: 2465-2472.

Cho, P., Mattissonb, T. and Lyngfelt, A. (2004). Comparison of iron-, nickel-, copper- and manganese-based oxygen carriers for chemical-looping combustion, *Fuel*, **83**: 1215-1225.

Cho, S., Yu, J., Kang, S. K. and Shih, D. Y. (2005) An oxidation study of pure Tin and its alloys via electrochemical reduction analysis, *Journal of Electronic Materials*, **34(5)**: 635-642.

Choi, W. K., Sung, H., Kim, K. H., Cho, J. S., Choi, S. C., Jung, H. J., Koh, S. K., Lee, C. M. and Jeong, K. (1997). Oxidation process from SnO to SnO_2, *J. Mater. Sci. Lett.,* **16**: 1551-1554.

Chushak, Y. G. and Bartell, L. S. (2003). Freezing of Ni-Al bimetallic nanoclusters in computer simulations, *J. Phys. Chem. B*, **107**: 3747-3751.

Coble, R. L. (1961). Sintering crystalline solids II. Experimental test of diffusion models in powder compacts, *J. Appl. Phys.*, **32**: 793-799.

Cornell, W. D., Cieplak, P., Bayly, C. I., Gould, I. R., Merz, K. M. Jr., Ferguson, D. M., Spellmeyer, D. C., Fox, T., Caldwell, J. W. and Kollman, P. A. (1995). A second generation force field for the simulation of proteins, nucleic acids, and organic molecules, *J. Am. Chem. Soc.,* **117**: 5179-5197.

Daw, M. S. and Baskes, M. I. (1984). Embedded-atom method: Derivation and application to impurities, surfaces, and other defects in metals, *Physical Review B,* **29 (12)**: 6443-6453.

Deal, B. E. and Grove, A. S. (1965).General relationship for the thermal oxidation of silicon, *J. Appl. Phys*., **36(12)**: 3770.

Debiaggi, S. R. de, Campillo, J. M. and Caro, A. (1999). Phase stability of Ni-Al nanoparticles, *J. Mater. Res.*, **14:** 2849-2854.

Deligoz, E., Colakoglu, K. and Ciftci, Y. O. (2008). The structural, elastic, and electronic properties of the pyrite-type phase for SnO_2, *Journal of Physics and Chemistry of Solids*, **69**: 859-864.

Delogu, F. (2007a). Numerical simulation of the thermal response of Al core/Ni shell nanometer-sized particles, *Nanotechnology*, **18**: 505702-505708.

Delogu, F. (2007b). Demixing phenomena in NiAl nanometre-sized particles, *Nanotechnology*, **18**: 065708-065714.

Demkov, A. A. and Sankey, O. F. (1999). Growth study and theoretical investigation of the ultrathin oxide SiO_2-Si heterojunction, *Physical Review Letters*, **83(10)**: 2038-2041.

Ding, L., Davidchack, R. L. and Pan, J. (2009). A molecular dynamics study of sintering between nanoparticles, *Computational Materials Science,* **45**: 247-256.

Dosbaeva, G. K., Veldhuis, S. C., Yamamoto, K., Wilkinson, D. S. , Beake, B. D., Jenkins, N., Elfizy, A. and Fox-Rabinovich, G. S. (2010). Oxide scales formation in nano-crystalline TiAlCrSiYN PVD coatings at elevated temperature, *Int. Journal of Refractory Metals & Hard Materials,* **28**: 133-141.

Dreizin, E. L. and Trunov, M. A. (1995). Surface phenomena in aluminum combustion, *Combustion and Flame*, **101(3)**: 378-382.

Ducati, C., Alexandrou, I., Chhowalla, M., Robertson, J. and Amaratunge, G. (2004). The role of the catalytic particle in the growth of carbon nanotubes by plasma enhanced chemical vapor deposition, *Journal of Applied Physics*, **95**: 6387-6391.

Dybkov, V. I. (2002). Reaction diffusion and solid state chemical kinetics, The IPMS Publications, Kyiv.

Eckert, J., Holzer, J. C., Ahn, C. C., Fu, Z. and Johnson, W. L. (1993). Melting behavior of nanocrystalline aluminum powders, *Nanostructured Materials*, **2(4)**: 407-413.

Eisenreich, N., Fietzek, H., Juez-Lorenzo, M., Kolarik, V., Koleczko, A. and Weiser, V. (2004). On the mechanism of low temperature oxidation for aluminum particles down to the nano-scale, *Propellants, Explosives, Pyrotechnics,* **29(3)**: 137-145.

Eisenreich, N., Fietzek, H., Juez-Lorenzo, M., Kolarik, V., Weiser, V. and Koleczko, A. (2005). Influence of nano-particle size on the oxidation behaviour of Al, Fe and Cu, *Materials at High Temperatures*, **22(3-4)**: 329-333.

Erofeev, B. V. (1960). Reactivity of solids, in De Boer, J. H. (eds), Proc. 4th. Int. Symp. on Reactivity of Solids, Elsevier, Amsterdam.

Evans, U. R. (1960). The Corrosion and oxidation of metals: Scientific principles and practical applications, St. Martin Press, New York.

Finnis, M. and Sinclair, E. (1984). A simple empirical *N*-body potential for transition metals, *Phil. Mag. A.,* **5**: 45-55.

Flynn, J. H. and Wall, L. A. (1966). A quick, direct method for the determination of activation energy from thermogravimetric data, *Polymer Letters*, **4**: 323-328.

Foiles, S. M. (1985). Application of embedded-atom method to liquid transition metals, *Physical Review B*, **32**: 3409-3415.

Foiles, S. M. and Daw, M. S. (1987). Application of the embedded atom method to Ni_3Al, *J. Mater. Res.,* **2**: 5-15.

Foley, T. J., Johnson, C. E. and Higa, K. T. (2005). Inhibition of oxide formation on aluminum nanoparticles by transition metal coating, *Chemistry of Materials*, **17(16)**: 4086-4091.

Franchy, R. (2000). Growth of thin, crystalline oxide, nitride and oxynitride films on metal and metal alloy surfaces, *Surface Science Reports,* **38**: 195-294.

Friedman, H. L. (1969). New methods for evaluating kinetic parameters from thermal analysis data, *Journal of Polymer Science Part B: Polymer Letters*, **7**: 41-46.

Fromhold Jr., A. T. (1976). Theory of metal oxidation, volume I - Fundamentals, series in Defects in crystalline solids, North-Holland, Oxford.

Fromhold Jr., A. T. (1980). Theory of metal oxidation, volume II - Space charge, series in defects in solids, North-Holland, Oxford.

Fromhold Jr., A. T. (1988). Growth rate of low-space-charge oxides on spherical metal particles, *Journal of Physics and Chemistry of Solids*, **49**: 1159-1166.

Gallego, L. J., Garcia-Rodeja, J., Alonso, J. A., Neal, C. M., Atarace, A. K. and Jarrold, M. F. (2007). Heat capacity of a model system with two non-degenerate states, *Phys. Rev. B,* **76**: 54113.

Galwey, A. K. (2004). Is the science of thermal analysis kinetics based on solid foundations? A literature appraisal, *Thermochimica Acta*, **413**: 139-183.

Galwey, A. K. and Mortimer, M. (2006). Compensation effects and compensation defects in kinetic and mechanistic interpretations of heterogeneous chemical reactions, *International Journal of Chemical Kinetics*, **38(7)**: 464-473.

García-Méndez, M., Valles-Villarreal, N., Hirata-Flores, G. A. and Farías, M. H. (1999). Study of thermal diffusion between Al_2O_3 and Al thin films, *Applied Surface Science*, **151**: 139-147.

Geurts, J., Rau, S., Richter, W. and Schmitte, F. J. (1984). SnO films and their oxidation to SnO_2: Raman scattering, IR reflectivity and X-ray diffraction studies, *Thin Solid Films*, **121**: 217-225.

Giefers, H., Porsch, F. and Wortmann, G. (2005). Kinetics of the disproportionation of SnO, *Solid State Ionics*, **176**: 199-207.

Giefers, H., Porsch, F. and Wortmann, G. (2006). Structural Study of SnO at high pressure, *Physica B*, **373**: 376-381.

Giesen, B., Orthner, H. R., Kowalik, A. and Roth, P. (2004). On the interaction of coagulation and coalescence during gas-phase synthesis of Fe-nanoparticle agglomerates, *Chemical Engineering Science*, **59**: 2201-2211.

Ginstling, A. M. and Brounshtein, B. I. (1950). Concerning the diffusion kinetics of reactions in spherical particles, *J. Appl. Chem. USSR*, **23**: 1327-1338.

Giri, S., Ganguli, S. and Bhattacharya, M. (2001). Surface oxidation of iron nanoparticles, *Applied Surface Science*, **182(3-4)**: 345-349.

Goddard, W. A., van Duin, A. C. T., Chenoweth, K., Cheng, M., Pudar, S., Oxgaard, J., Merinov, B., Jang, Y. H. and Persson, P. (2006). Development of the ReaxFF reactive force field for mechanistic studies of catalytic selective oxidation processes on $BiMoO_x$, *Topics in Catalysis*, **38(1-3)**: 93-103.

Graham, M. J., Caplan, D., and Cohen, M. (1972) .Growth via leakage paths of nickel oxide on nickel at high temperatures, *Journal of Electrochemistry Society*, **119**: 1265-1267.

Graham, M. J. and Cohen, M. (1972). On the mechanism of low-temperature oxidation (23-450°C) of polycrystalline nickel, *J. Electrochem. Soc.,* **119**: 879-882.

Granier, J. J. and Pantoya, M. L. (2004). The effect of size distribution on burn rate in nanocomposite thermites: A probability density function study, *Combustion Theory and Modelling*, **8(3)**: 555-565.

Graydon, J. W., Thorpe, S. J. and Kirk, D. W. (1994) Interpretation of activation energies calculated from non-isothermal transformations of amorphous metals, *Acta Metallurgica et Materialia*, **42**: 3163-3166.

Gromov, A. A., Il'in, A. P., Foerter-Barth, U. and Teipel, U. (2006). Effect of the passivating coating type, particle size, and storage time on oxidation and nitridation of aluminium powders, *Combustion, Explosion, and Shock Waves,* **42(2)**: 177-184.

Graydon, J. W., Thorpe, S. J. and Kirk, D. W. (1994). Interpretation of activation energies calculated from non-isothermal transformations of amorphous metals, *Acta Metallurg. Mater.*, **42**: 3163-3166.

Guczi, L. (2005).Bimetallic nano-particles: featuring structure and reactivity, *Catalysis Today*, **101**: 53-64.

Gupta, A. K. and Curtis, A. S. G. (2004). Lactoferrin and ceruloplasmin derivatized superparamagnetic iron oxide nanoparticles for targeting cell surface receptors, *Biomaterials*, **25(15)**: 3029-3040.

Gwinn, M. R. and Vallyathan, V. (2006). Nanoparticles: Health Effects-Pros and Cons., *Environ. Health Perspect.*, **114(12)**: 1818-1825.

Han, Z., Guo, N., Li, F., Zhang, W., Zhao, H. and Qian, Y. (2001). Solvothermal preparation and morphological evolution of stannous oxide powders, *Mater. Lett.,* **48**: 99-103.

Han, S., Chen, H., Chen, C., Yuan, T., and Shih, H. C. (2007). Characterization of Ni nanowires after annealing, *Materials Letters,* **61**: 1105-1108.

Hanszen, K. J. (1960). Theoretische Untersuchungen über den Schmelzpunkt kleiner Kugelchen-Ein Beitrag zur Thermodynamik der Grenzflächen, *Z. Phys.*, **157 (5)**: 523-553.

Hauffe, K. (1965). Oxidation of metals, Plenum Press, New York.

Hawa, T. and Zachariah, M. R. (2004). Molecular dynamics study of particle-particle collision between hydrogen-passivated silicon nanoparticles, *Physical Review B*, **69**: 035417.

Hawa, T. and Zachariah, M. R. (2006). Coalescence kinetics of unequal sized nanoparticles, *Aerosol Science*, **37**: 1-15.

Hawa, T. and Zachariah, M. R. (2007). Molecular dynamics simulation and continuum modelling of straight-chain aggregate sintering: Development of a phenomenological scaling law, *Physical Review B*, **76**: 054109.

Hémeryck, A., Estève, A., Richard, N., Rouhani, M. D. and Chabal, Y. J. (2009). Fundamental steps towards interface amorphization during silicon oxidation: Density functional theory calculations, *Physical Review B*, **79**: 035317.

Hémeryck, A., Estève, A., Richard, N., Rouhani, M. D. and Landa, G. (2009). A kinetic Monte Carlo study of the initial stage of silicon oxidation: Basic mechanisms-induced partial ordering of the oxide interfacial layer, *Surface Science*, **603**: 2132-2137.

Hendy, S., Brown, S. A. and Hyslop, M. (2003). Coalescence of nanoscale metal clusters: Molecular dynamics study, *Physical Review B*, **68**: 241403.

Henz, B. J., Hawa, T. and Zachariah, M. (2009). Molecular dynamics simulation of the energetic reaction between Ni and Al nanoparticles, *Journal of Applied Physics*, **105(12)**: 124310.

Hillman, D. D. and Chumbley, L. S. (2006). Characterization of tin oxidation products using sequential electrochemical reduction analysis, *Soldering & Surface Mount Technology*, **18**: 31-41.

Honeycutt, J. D. and Andersen, H. C. (1987). Molecular dynamics study of melting and freezing of small Lennard-Jones clusters, *J. Phys. Chem.,* **91**: 4950-4963.

Hoover, W. G. (1985). Canonical dynamics: equilibrium phase-space distributions, *Phys. Rev. A*, **31**: 1695.

Hu, J. Q., Ma, X. L., Shang, N. G., Xie, Z. Y., Wong, N. B., Lee, C. S., and Lee, S. T. (2002). Large-scale rapid oxidation synthesis of SnO_2 nanoribbons*, J. Phys. Chem. B*, **106**: 3823-3826.

Hu, Z., Boiadjiev, V. and Thundat, T. (2005). Nanocatalytic spontaneous ignition and self-supporting room-temperature combustion, *Energy and Fuels*, **19(3)**: 855-858.

Huh, M., Kim, S., Ahn, J., Park, J. and Kim, B. (1999). Oxidation of nanophase tin particles, *Nano Structured Materials*, **11**: 211-220.

Hunt, E. M. and Pantoya, M. L. (2005). Ignition dynamics and activation energies of metallic thermites: From nano- to micron-scale particulate composites, *Journal of Applied Physics*, **98(3)**: 034909.

Hwang, I. S., Lo, R. L. and Tsong, T. T. (1998). Mechanisms and energetics of site hopping and chemical reactions of O_2 molecules at Si(111)-7×7 surfaces, *Surface Science*, **399**: 173-189.

Ilyin, A., Gromov, A., Vladimir, A., Faubert, F., de Izarra, C., Espagnacq, A. and Brunet, L. (2002). Characterization of aluminum powders I. parameters of reactivity of aluminum powders, *Propellants, Explosives, Pyrotechnics,* **27**: 361-364.

James Baker III Institute for Public Policy (2005). Energy and Nanotechnology**:** Strategy for the future, *Conference Report of Rice Energy Program initiative on Energy Policy and Nanoscience*, Rice University, USA.

Jander, W. (1927). Reaktionen im festen Zustande bei höheren Temperaturen. Reaktionsgeschwindigkeiten endotherm verlaufender Umsetzungen, *Z. Anorg. Allgem. Chem.,* **163(1)**: 1-30.

Jiang, Q., Yang, C. C. and Li, J. C. (2002). Melting enthalpy depression of nanocrystals, *Material Letter,* **56**: 1019-1021.

Jin, Z. H. and Lu, K. (1998). Melting of surface-free bulk single crystals. *Philosophical Magazine Letters*, **78**: 29-35.

Johnson, W. A. and Mehl, P. A. (1939) Transition reaction kinetics in processes of nucleation and growth, *AIME*, **135**: 416.

Jose-Yacaman, M., Gutierrez-Wing, C., Miki, M., Yang, D. Q., Piyakis, K. N. and Sacher, E. (2005). Surface diffusion and coalescence of mobile metla nanoparticles, *J. Phys.Chem. B*, **109**: 9703-9711.

Jun, S., Zhang, H. and Bechhoefer, J. (2005). Nucleation and growth in one dimension. I. the generalized Kolmogorov-Johnson-Mehl-Avrami model, *Physical Review E,* **71**: 011908.

Kadau, K., Germann, T. C. and Lomdahl, P. S. (2006). Molecular dynamics comes of age: 320 billion atom simulation on BlueGene/L, *International Journal of Modern Physics C*, **17(3)**: 279-291.

Kageshima, H., Uematsu, M., Akagi, K., Tsuneyuki, S., Akiyama, T. and Shiraishi, K. (2006). Mechanism of oxide deformation during silicon thermal oxidation, *Physica B*, **376-377**: 407-410.

Karmhag, R., Niklasson, G. A. and Nygren, M. (1999a). Oxidation kinetics of small nickel particles, *Journal of Applied Physics*, **85(2)**: 1186.

Karmhag, R., Niklasson, G. A. and Nygren, M. (1999b). Oxidation kinetics of large nickel particles, *Journal of Materials Research*, **14(7)**: 3051-3058.

Karmhag, R., Tesfamichael, T., Wäckelgård, E., Niklasson, G. A. and Nygren, M. (2000). Oxidation kinetics of nickel particles: Comparison between free particles and particles in an oxide matrix, *Solar Energy*, **68(4)**: 329-333.

Karmhag, R. (2001). Oxidation kinetics of nickel solar absorber nanoparticles, *Journal of Applied Physics D*: *Applied Physics,* **34**: 400-406.

Karmhag, R., Niklasson, G. A. and Nygren, M. (2001). Oxidation kinetics of nickel nanoparticles, *J. of Appl. Phys.,* **89(5)**: 3012-3017.

Karmhag, R. and Niklasson, G. A. (2003). Oxidation kinetics of metallic nanoparticles, *Surface Science*, **532-535**: 324-327.

Kazanc, S. and Tatar, C. (2008). Investigation of the effect of pressure on some physical parameters and thermoelastic phase transformation of NiAl alloy, *International Journal of Solids and Structures*, **45**: 3282-3289.

Kelzenberg, S., Weiser, V. and Eisenreich, N. (2007). Influence of the particle size on reactions of metal oxidation including nano-scale, *Proceedings of the European Combustion Meeting*, Third European Combustion Meeting.

Khawan, A. and Flanagan, D. R. (2005). Basics and applications of solid-state kinetics: A pharmaceutical perspective, *Journal of Pharmaceutical Sciences*, **95(3)**: 472-498.

Khoi, N. N., Smeltzer, W. W. and Embury, J. D. (1975). Growth and structure of nickel oxide on nickel crystal faces, *J. Electrochem. Soc.,* **122**: 1495-1503.

Kim, S. H., Oh, M. H. and Wee, D. M. (2003). Effects of ternary additions on the thermoelastic martensitic transformation of NiAl, *Metallurgical and Materials Transactions*, **34A**: 2089-2095.

Kim, S. H., Oh, M. H., Kishida, K., Hirano, T. and Wee, D. M. (2005). Deposition of NiAl coating for improvement of oxidation resistance of cold-rolled Ni3Al foils, *Intermetallics*, **13**: 129-136.

Kissinger, H. E. (1957). Reaction kinetics in differential thermal analysis, *Analytical Chemistry*, **29**: 1702-1706.

Koch, W. and Friedlander, S. K. (1990). The effect of particle coalescence on the surface area of a coagulating aerosol, *J. Colloid and Interface Science*, **140**: 419-217.

Kofstad, P. (1966). High temperature oxidation of metals, John Wiley & Sons, New York.

Kolarik, V., Engel, W. and Eisenreich, N. (1993). Kinetics of growing oxide layers studied by means of X-ray diffraction, *Proceedings of the 2nd European Powder Diffraction Conference*, **133-136**: 563-568.

Kolmakov, A., Zhang, Y. and Moskovits, M. (2003). Topotactic thermal oxidation of Sn nanowires: intermediate suboxides and core-shell metastable structures, *Nano Lett.*, **3**: 1125-1129.

Kolmogorov, A. N. (1937). Izv. Akad. Nauk SSSR, *Ser. Fiz.*, **1**: 335.

Koparde, V. and Cummings, P. (2005). Molecular dynamics simulation of titanium dioxide nanoparticle sintering, *J. Phys. Chem.*, **109**: 24280-24287.

Koparde, V. and Cummings, P. (2007). Sintering of titanium dioxide nanoparticles: a comparision between molecular dynamics and phenomenological modelling, *Journal of Nanoparticle Research,* **10**: 11069-1182.

Kuczynski, G. C. (1980). Sintering processes, Plenum Press, New York.

Kwok, Q. S. M., Fouchard, R. C., Turcotte, A., Lightfoot, P. D., Bowes, R. and Jones, D. E. G. (2002). Characterization of aluminum nanopowder compositions, *Propellants, Explosives, Pyrotechnics*, **27(4)**: 229-240.

Lai, S. L., Guo, J. Y., Petrova, V., Ramanath, G. and Allen, L. H. (1996). Size-dependent melting properties of small Tin particles: nanocalorimetric measurements, *Physical Review Letters*, **77**: 99-102.

Lawson, F. (1967). Tin oxide-Sn_3O_4, *Nature*, **215**: 955-956.

Le Claire, A. D. (1975). In treatise of solid state chemistry, Plenum Press, New York.

Lebrat, J. P. and Varma, A. (1994). Mechanistic studies in combustion synthesis of Ni_3Al and Ni_3Al-matrix composites, *Combust. Sci. Technol.*, **88**: 1184-1192.

Lee, W. H. (2002). Oxidation and sulfidation of Ni_3Al, *Materials Chemistry and Physics*, **76**: 26-37.

Leite, E. R., Cerri, J. A., Longo, E., Varela, J. A. and Paskocima, C. A. (2001). Sintering of ultrafine undoped SnO_2 powder, *J. Eur. Ceram. Soc.*, **21**: 669-675.

Lennard-Jones, J. E. (1924). On the determination of molecular fields. II. From the equation of a state of a gas, *Proc. Roy. Soc.*, **A(106)**: 463-477.

Lewis, L. J., Jensen, P. and Barrat, J. L. (1997). Melting, freezing and coalescence of gold nanoclusters, *Physical Review B*, **56**: 2248-2257.

Lim, D. C., Lopez-Salido, I., Dietsche, R., Bubek, M. and Kim, Y. D. (2006). Oxidation of Au nanoparticles on HOPG using atomic oxygen, *Surface Science*, **600(3)**: 507-513.

Lyubartsev, A., Tu, Y. Q. and Laaksonen, A. (2009). Hierarchical multiscale modelling scheme from first principles to mesoscale, *Journal of Computational and Theoritical Nanoscience*, **6(5)**: 955-959.

Ma, E. (2005). Alloys created between immiscible elements, *Progress in Materials Science*, **50**: 413-509.

Mahadevan, R., Lee, D., Sakurai, H. and Zachariah, M. R. (2002). Measurement of condensed-phase reaction kinetics in the aerosol phase using single particle mass spectrometry, *J. Phys. Chem. A,* **106**: 11083-11092.

Metals Handbook: Properties and Selection: Nonferrous Alloys and Pure Metals, American Society for Metals Handbook, 9th Edition (1979). ASM International, Ohio, USA.

Mitchell, J. W. (eds) (1969). Reactivity of solids, John Wiley & Sons, New York.

Mahadevan, R., Lee, D., Sakurai, H. and Zachariah, M. R. (2002). Measurement of condensed-phase reaction kinetics in the aerosol phase using single particle mass spectrometry, *Journal of Physical Chemistry A,* **106**: 11083-11092.

Maitra, S., Pal, A. J., Bandyopadhyay, N., Das, S. and Pal, J. (2007). Use of genetic algorithm to determine the kinetic model of solid-state reactions, *Journal of the American Ceramic Society*, **90(5)**: 1611-1614.

Mallikaa, C., Edwin, A. M., Raj, S, Nagaraja, K. S. and Sreedharana, O. M. (2001). Use of SnO for the determination of standard Gibbs energy of formation of SnO_2 by oxide electrolyte e.m.f. measurements, *Thermochimica Acta*, **371**: 95-101.

Mayo, S. L., Olafson, B. D. and Goddard III, W. A. (1990). DREIDING: A Generic Force Field for Molecular Simulations, *J. Phys. Chem*., **94**: 8897-8909.

Mazzone, A. M. (2000). Coalesence of metallic clusters: a study by molecular dynamics, *Philosophical Magazine B*, **80**: 95-111.

McCallum, J. R. (1970). Tanner, Derivation of Rate Equations used in thermogravimetry, *Nature*, **225**: 1127-1128.

Mei, Q. S. and Lu, K. (2007). Melting and superheating of crystalline solids: From bulk to nanocrystals, *Progress in Materials Science*, **52**: 1175-1262.

Miracle, D. B. (1993). Overview No. 104: The physical and mechanical properties of NiAl, *Acta Metallurgica et Materialia*, **41(3)**: 649-684.

Mittemeijer, E. J. (1992). Analysis of the kinetics of phase transformations, *Journal of Materials Science*, **27**: 3977-3987.

Mitra, S., Tatti, S. R. and Stark, J. P. (1989). A spectroscopic study of nickel oxide films on polycrystalline nickel, *Thin Solid Films*, **177**: 171-180.

Morse, P. M. (1929). Diatomic molecules according to the wave mechanics. II. Vibrational levels, *Phys. Rev.*, **34**: 57-64.

Mott, N. F. (1947). The theory of the formation of protective oxide films on metals. III, *Trans. Faraday Soc.,* **43**: 429-434.

Moreno, M. S., Punte, G., Rigotti, G., Mercader, R. C., Weisz, A. D. and Blesa, M. A. (2001). Kinetic study of the disproportionation of tin monoxide, *Solid State Ionics*, **144**: 81-86.

Muto, S., Schryvers, D., Merk, N. and Tanner, L. E. (1993). High-resolution electron microscopy and electron diffraction study of the displacive transformation of the Ni_2Al phase in a $Ni_{65}Al_{35}$ alloy and associated with the martensitic transformation, *Acta Metall. Mater.*, **41**: 2377-2383.

Nakano, A., Kalia, R. K., Nomura, K. , Sharma, A., Vashista, P., Shimojo, F., van Duin, A. C. T., Goddard, W. A., Biswas, R. Srivastava, D. and Yang, L. H. (2008). De Novo Ultrascale Atomistic Simulations on high-end parallel supercomputers, *International Journal for High Performance Computing Applications*, **22**: 113-128.

Nanda, K. K., Kruis, F. E. and Fissan, H. (2002). Evaporation of free PbS nanoparticles: evidence of the Kelvin effect, *Phys. Rev. Lett*., **89**: 256103.

Neeft, J. P. A., Makkee, M. and Moulijn, J. A. (1996). Diesel particulate emission control, *Fuel Processing Technology*, **47(1)**: 1-69.

Niklasson, G. and Karmhag, R. (2003). Oxidation kinetics of metallic nanoparticles, *Surface Science*, **532-535**: 324-327.

Ning, N., Calvo, F., van Duin, A. C. T., Wales, D. J. and Vach, H. (2008). Sponaneous self-assembly of silica nanocages into inorganic framework materials, *Journal of Physical Chemistry C*, **113(2)**: 518-523.

Nomora, K., Kalia, R. K., Nakano, A., Vashista, P., van Duin, A. C. T. and Goddard III, W. A. (2007). Dynamic transition in the shock structure of an energetic crystal, *Physical Review Letters*, **99**: 148303.

Nosé, S. (1984). A molecular dynamics method for simulations in the canonical ensemble, *Mol. Phys.*, **52**: 255.

Ojwang, J. G. O., van Santen, R., Kramer, G. J., van Duin, A. C. T. and Goddard III, W. A. (2008). Predictions on melting, crystallization and local atomic arrangements of aluminium clusters using a reactive force field, *Journal of Chemistry and Physics*, **129(24)**: 244506.

Ono, S., Ito, E., Katsura, T., Yoneda, A., Walter, M. J., Urakawa, S., Utsumi, W. and Funakoshi, K. (2000). Thermoelastic properties of the high-pressure phase of SnO_2 determined by in situ X-ray observations up to 30 GPa and 1400 K, *Physics and Chemistry of Minerals*, **27**: 618-622.

Opfermann, J. (2000). Kinetic analysis using multivariate non-linear regression, I. basic concepts, *Journal of Thermal Analysis and Calorimetry*, **60**: 641-658.

Ortega, A. (2001). The kinetics of solid-state reactions toward consensus - Part I: Uncertainties, failures, and successes of conventional methods, *International Journal of Chemical Kinetics*, **33(6)**: 343-353.

Ozawa, T. (1992). Estimation of activation-energy by isoconversion methods, *Thermochima Acta*, **203**:159-165.

Pabi, S. K. and Murty, B. S. (1996). Mechanism of mechanical alloying in Ni-Al and Cu-Zn systems, *Mater. Sci. Eng.*, **A214**: 146-152.

Pan, H., Ko, S. H. and Grigoropoulos, C. (2008). The solid-state neck growth mechanisms in low energy laser sintering of gold nanoparticles: a

molecular dynamics simulation study, *Transactions of ASME Journal of Heat Transfer*, **130**: 092404.

Pan, X. Q. and Fu, L. (2001). Oxidation and phase transitions of epitaxial tin oxide thin films on sapphire, *Journal of Applied Physics*, **89**: 6049-6055.

Panigrahi, B. B. (2007). Sintering and grain growth kinetics of ball milled nanocrystalline nickel powder, *Materials Science and Engineering A*, **460-461**: 7-13.

Pantelides, S. T. and Ramamoorthy, M. (1999). Atomic-scale dynamics during silicon oxidation and the properties of defects at the Si-SiO2 interface, *Journal of Non-Crystalline Solids*, **254**: 38-46.

Pantoya, M. L. and Granier, J. J. (2005). Combustion behavior of highly energetic thermites: Nano versus micron composites, *Propellants, Explosives, Pyrotechnics,* **30(1)**: 53-62.

Pantoya, M. L. and Granier, J. J. (2006). The effect of slow heating rates on the reaction mechanisms of nano and micron composite thermite reactions, *Journal of Thermal Analysis and Calorimetry*, **85(1)**: 37-43.

Park, K., Lee, D., Rai, A., Mukherjee, D. and Zachariah, M. R. (2005). Size-resolved kinetic measurements of aluminum nanoparticle oxidation with single particle mass spectrometry, *Journal of Physical Chemistry B*, **109(15)**: 7290-7299.

Park, K., Rai, A. and Zachariah, M. R. (2006). Characterizing the coating and size-resolved oxidative stability of carbon-coated aluminum nanoparticles by single-particle mass-spectrometry, *Journal of Nanoparticle Research*, **8(3-4)**: 455-464.

Parrinello, M. and Rahman, A. (1980). Crystal structure and pair potentials: A molecular dynamics study, *Phys. Rev.Lett.,* **45**: 1196.

Pasquarello, A., Hybertsen, M. S. and Car, R. (1998). Interface structure between silicon and its oxide by first principles molecular dynamics, *Nature*, **396**: 58-60.

Patterson, R. I. A. and Kraft, M. (2007). Models for the aggregate structure of soot particles, *Combust. Flame,* **151**: 160-172.

Pauling, L. (1947). Atomic radii and interatomic distances in metals, *J. Am. Chem. Soc.*, **69**: 542.

Pawluk, T. and Wang, L. (2007). Molecular dynamics simulations of the coalescence of iridium clusters, *J. Phys. Chem. C*, **111**: 6713-6719.

Peraldi, R., Monceau, D. and Pieraggi, B. (2002). Correlations between growth kinetics and microstructure for scales formed by high-temperature oxidation of pure nickel, *Oxidation of Metals,* **58**: 249-273.

Pilling, M. J. and Seakins, P. W. (1995). Reaction kinetics, Oxford University Press, Oxford.

Pina, G., Louis, C. and Keane, M. (2003). Nickel particle size effects in catalytic hydrogenation and hydrodechlorination: phenolic transformations over nickel/silica, *Phys. Chem. Chem. Phys.,* **5**: 1924-1931.

Plimpton, S., Crozier, P. and Thompson, A. (2010). User Manual of LAMMPS, http://lammps.sandia.gov/doc/Manual.pdf.

Potapov, P. L., Ochin, P., Pons, J. and Schryvers, D. (2000). Nanoscale inhomogeneities in melt-spun Ni-Al, *Acta Mater.*, **48**: 3833-3845.

Powder Diffraction File (1991). Card No. 47-1049, International Center for Diffraction Data.

Price, E. W., Sigman, R. K., Yang, V., Brill, T. B. and Ren, W. Z. (eds) (2000). Solid propellant chemistry, combustion and motor ballistics: Progress in astronautics and aeronautics, *AIAA*, **185**.

Qi, Y., Cagin, T., Johnson, W. L. and Goddard III, W. A. (2001). Melting and crystallization in Ni nanoclusters: The mesoscale regime, *Journal of Chemical Physics*, **115**: 385-394.

Raghavan, V. and Cohen, M. (1975). In treatise of solid state chemistry, volume 5, Plenum Press, New York.

Rai, A., Lee, D., Park, K. and Zachariah, M. R. (2002). Measurement of condensed-phase reaction kinetics in the aerosol phase using single particle mass spectrometry, *Journal of Physical Chemistry B,* **106(46)**: 11083-11092.

Rai, A., Lee, D., Park, K. and Zachariah, M. R. (2004). Importance of phase change of aluminum in oxidation of aluminum nanoparticles, *Journal of Physical Chemistry B*, **108(39)**: 14793-14795.

Rai, A., Park, K., Zhou, L. and Zachariah, M. R. (2006). Understanding the mechanism of aluminium nanoparticle oxidation, *Combustion Theory and Modelling*, **10(5)**: 843-859.

Rapaport, D. C. (2004). The Art of molecular dynamics simulation, 2nd Edition, Cambridge University Press, Cambridge.

Rappe, A. K. and Goddard III, W. A. (1991). Charge Equilibration for Molecular Dynamics Simulations, *J. Phys. Chem.*, **95**: 3358-3363.

Raut, J. S., Bhagat, R. B. and Fichthorn, K. A. (1998). Sintering of aluminum nanoparticles: A molecular dynamics study, *Nanostructured Materials*, **10**: 837-851.

Rogak, S. N. (1997). Modeling small cluster deposition on the primary particles of aerosol agglomerates, *Aerosol Sci. Tech.*, **26**: 127-140.

Sales, B. C. and Maple, M. B. (1977). Oxidation of nickel in the vicinity of its Curie temperature, *Physical Review Letters*, **39**: 1636-1639.

Sangaletti, L., Depero, L. E., Allieri, B., Pioselli, F., Comini, E., Sberveglier, G. and Zocchi, M. (1998). Oxidation of Sn thin films to SnO_2, micro-ramam mapping and X-ray diffraction studies, *Journal of Materials Research*, **13**: 2457-2460.

Sankaranarayanan, S. K. R. S. and Ramanathan, S. (2008). Molecular dynamics simulation study of nanoscale passive oxide growth on Ni-Al alloy surfaces at low temperatures, *Physical Review B*, **78**: 085420.

Sasi, B. and Gopchandran, K. G. (2007). Nanostructured mesoporous nickel oxide thin films, *Nanotechnology*, **18**: 115613-115621.

Sberveglieri, G., Faglia, G., Groppelli, S., Nelli, P. and Camanzi, A. (1990). A new technique from growing large surface SnO_2 thin film (RGTO technique), *Semicond. Sci. Technol.*, **5**: 1231-1233.

Schlogl, R. and Abd Hamid, S. B. (2004). Nanocatalysis: Mature science revisited or something really new? *Angewandte Chemie. Int. Ed.,* **43(13)**: 1628-1637.

Schmidt, M. and Haberland, H. (2002). Phase transitions in clusters, *C. R. Phys.,* **3**: 327-340.

Schbert, B., Avouris, P. and Hoffmann, R. (1993). A theoretical study of the initial stages of Si(111)-7×7 oxidation. I. The molecular precursor, *J. Chem. Phys.*, **98(9)**: 7593-7605.

Seko, A., Togo, A., Oba, F. and Tanaka, I. (2008). Structure and stability of a homologous series of Tin oxides, *Physical Review Letters*, **100**: 045702.

Shi, F. G. (1994). Size dependent thermal vibration and melting in nanocrystals. *Journal of Materials Research*, **9**: 1307-1313.

Smit, B. and Frenkel, D. (2001). Understanding molecular simulation, Academic Press, San Diego.

Song, P. and Wen, D. (2009). Heating and oxidation investigation of iron nanoparticles as potential oxygen carriers for chemical-looping combustion, *11th UK Heat Transfer Conference*, London.

Starink, M. J. (1996). A new method for the derivation of activation energies from experiments performed at constant heating rate, *Thermochimica Acta,* **288**: 97-104.

Strachan, A., Kober, E. M., van Duin, A. C. T., Oxgaard, J. and Goddard III, W. A. (2005). Thermal decomposition of RDX from reactive molecular dynamics, *J. Chem. Phys.*, **122**: 054502.

Su, H., Nielsen, R. J., van Duin, A. C. T. and Goddard III, W. A. (2007). Simulations on the effects of confinement and Ni-catalysis on the formation of tubular fullerene structures from peapod structures, *Phys. Rev. B.*, **75**: 134107.

Subramanian, K. N. (2007). Role of anisotropic behaviour of Sn on thermomechanical fatigue and fracture of Sn-based solder joints under thermal excursions, *Fatigue & Fracture of Engineering Materials & Structures*, **30**: 420-431.

Sun, J., Pantoya, M. L. and Simon, S. L. (2006). Dependence of size and size distribution on reactivity of aluminum nanoparticles in reactions with oxygen and MoO_3, *Thermochimica Acta*, **444(2)**: 117-127.

ten Wolde, P. R., Ruiz-Montero, M. J. and Frenkel, D. (1996). Numerical calculation of the rate of crystal nucleation in a Lennard-Jones system at moderate undercooling, *J. Chem. Phys.*, **104**: 9932-9947.

Teraishi, K., Endou, A., Gunji, I., Kubo, M., Miyamoto, A. and Kitajima, M. (1999). Use of umbrella sampling in the calculation of the potential of the mean force for silicon surface oxidation, *Surface Science*, **426**: 290-297.

Tersoff, J. (1986). New empirical model for the structural properties of silicon, *Phys. Rev. Lett.,* **56**: 632.

Tersoff, J. (1988). New empirical approach for the structure and energy of covalent systems, *Phys. Rev. Lett.*, **61**: 2879.

Thiers, L., Mukasyan, A. S. and Varma, A. (2002). Thermal explosion in Ni-Al system: influence of reaction medium microstructure, *Combust. Flame*, **131**: 198-209.

Titova, Z. P., Savina, E. V. and Klushin, D. N. (1964). *J. Appl. Chem. USSR*, **37**: 2129.

Trunov, M. A., Schoenitz, M. and Dreizin, E. L. (2005a). Ignition of aluminum powders under different experimental conditions, *Propellants,*

Explosives, Pyrotechnics, **30(1)**: 36-43.

Trunov, M. A., Schoenitz, M., Zhou, X. and Dreizin, E. L. (2005b). Effect of polymorphic phase transformations in Al_2O_3 film on oxidation kinetics of aluminum powders, *Combustion and Flame*, **140(4)**: 310-318.

Trunov, M. A., Schoenitz, M. and Dreizin, E. L. (2006a). Effect of polymorphic phase transformations in alumina layer on ignition of aluminium particles, *Combustion Theory and Modelling*, **10(4)**: 603-623.

Trunov, M. A., Umbrajkar, S. M., Schoenitz, M., Joseph, T. M. and Dreizin, E. L. (2006b). Oxidation and melting of aluminum nanopowders, *Journal of Physical Chemistry B*, **110(26)**: 13094-13099.

Torre, J. D., Bocquet, J. L., Limoge, Y., Crocombette, J. P., Adam, E., Martin, G., Baron, T., Rivallin, P. and Mur, P. (2002). Study of self-limiting oxidation of silicon nanoclusters by atomistic simulations, *Journal of Applied Physics*, **92(2)**: 1084-1094.

Tsantilis, S. and Pratsinis, S. E. (2000). Evolution of primary and aggregate particle-size distributions by coagulation and sintering, *AIChE,* **46**: 407-415.

Tseng, W., Hsu, C., Chi, C. and Teng, K. (2002). Thermal and microstructural characterizations of nickel nanoparticles at elevated temperatures, *Material Letters*, **52**: 313-318.

Tseng, W. and Chen, C. (2006). Dispersion and rheology of nickel nanoparticle inks, *Journal of Materials Science,* **41**: 1213-1219.

Tsumuraya, K., Watanabe, M. S. and Ikeda, S. K. (1988). Molecular dynamics study of homogeneous nucleation and growth in a metal liquid, *Transactions of the Iron and Steel Institute of Japan,* **28**: 869-875.

Tsyganov, S., Kastner, J., Rellinghaus, B. and Kauffeldt, T. (2007). Analysis of Ni nanoparticle gas phase sintering, *Physical Review B*, **75**: 045421.

Tu, Y. and Tersoff, J. (2002). Microscopic dynamics of silicon oxidation, *Physical Review Letters*, **89(8)**: 086102.

Uchikoshi, T., Sakka, Y., Yoshitake, M., and Yoshihara, K. (1994). A study of the passivating oxide layer on fine nickel particles, *Nanostructure Material*, **4**: 199-206.

Urban, J., Sack-Kongehl, H. and Weiss, K. (1997). Study of partial oxidation of Cu clusters by HRTEM, *Catalysis Letters*, **49**: 101-108.

Utgikar, V. P., Lattin, W. and Jacobsen, T. (2006). Nanometallic fuels for transportation: a well-to-wheels analysis, *International Journal of Energy Research*, **31(1)**: 99-108.

Van, D. S. D., Lindahl, E., Hess, B., Groenhof, G., Mark, A. E. and Berendsen, H. J. (2005). GROMACS: fast, flexible, and free, *J. Comput. Chem.,* **26 (16)**: 1701-1718.

van Duin, A. C. T. (2009). User Manual of ReaxFF, http://www.wag.caltech.edu/-home/duin/reax_um.pdf.

van Duin, A. C. T., Dasgupta, S., Lorant, F. and Goddard III, W. A. (2001). ReaxFF: A reactive force field for hydrocarbons, *J. Phys. Chem. A*, **105(41)**: 9396-9409.

van Duin, A. C. T., Strachan, A., Stewman, S., Zhang, Q. and Goddard III, W. A. (2003). $ReaxFF_{SiO}$ reactive force field for silicon and silicon oxide systems, *J. Phys. Chem. A,* **107**: 3803-3811.

van Duin, A. C. T., Merinov, B. and Goddard III, W. A. (2008a). The ReaxFF Reactive Force Field for Solid Oxide Fuel Cell Systems with Application to Oxygen Ion Transport in Yttria-Stabilized Zirconia, *Journal of Physical Chemistry A,* **112**: 3133-3140.

van Duin, A. C. T., Merinov, B., Han, S. S., Dorso, C. and Goddard III, W. A. (2008b). ReaxFF reactive force field study of grain and grain boundary proton diffusion in Y-doped BaZrO3, *Journal of Physical Chemistry A*, **112(45)**: 11414-11422.

Varma, A., Mukasyan, A. S. , Borisov, A. A. , De Luca, L. and Merzhanov, A. (eds.) (2002). Self-propagating high-temperature synthesis of materials, Combustion science and technology book series, volume 5, Taylor & Francis, New York.

Vashishta, P., Kalia, R. K. and Nakano, A. (2003). Multimillion atom molecular dynamics simulations of nanostructures on parallel computers, *Journal of Nanoparticle Research,* **5**: 119-135.

Verlet, L. (1967). Computer 'experiment' on classical fluids. I. Thermodynamical properties of Lennard-Jones molecules, *Phys. Rev.,* **159**: 98.

Vyazovkin, S. and Wight, C. A. (1997). Isothermal and nonisothermal reaction kinetics in solids: in search of ways toward consensus, *J. Phys. Chem. A,* **101**: 8279-8284.

Wagner, C. (1933). Beitrag zur Theorie des Anlaufvorgangs, *Z. Phys. Chem.,* **21(B)**: 25.

Wang, X., Zhang, F. X., Loa, I., Syassen, K., Hanfland, M. and Mathis, Y. L. (2004). Structural properties, infrared reflectivity, and Raman modes of SnO at high pressure, *Phys. Stat. Sol.* (*B*)*,* **241**: 3168-3178.

Wakai, F. (2006). Modelling and simulation of elementrary processes in ideal sintering, *J. Am. Cerm. Soc*., **89**: 1471-1484.

Wakuda, D., Kim, K. S. and Suganuma, K. (2008). Room temperature sintering of Ag nano-scale particles with drying of the solvent. *IEEE Conference on Polymers and Adhesives in Microelectronics and Photonics and 2008 IEEE Interdisciplinary Conference on Portable Information Devices,* 215-220.

Ward, T. S., Trunov, M. A., Schoenitz, M. and Dreizin, E. L. (2006). Experimental methodology and heat transfer model for identification of ignition kinetics of powdered fuels, *International Journal of Heat and Mass Transfer,* **49(25-26)**: 4943-4954.

Weingarten, N. S., Mattson, W. D. and Rice, B. M. (2009). Determination of the pressure dependent melting temperatures of Al and Ni using molecular dynamics, *Journal of Applied Physics*, **106(6)**: 063524.

Weiser, V., Kelzenberg, S. and Eisenreich, N. (2001). Influence of the metal particle size on the ignition of energetic materials, *Propellants, Explosives, Pyrotechnics,* **26(6)**: 284-289.

Wen, D., Alexander, T., Crookes, R. J., Guo, Z. X. and Lawn, C. (2007). Nanofuel as Future Energy Vectors, EPRSC reference: EP/F027281/1, URL: (http://gow.epsrc.ac.uk/ViewGrant.aspx?GrantRef=EP/F027281/1).

Wendt, H. R. and Abraham, F. F. (1978). Empirical criterion for the glass transition region based on the Monte Carlo simulations, *Physical Review Letters*, **41**: 1244-1246.

West, R. H., Celnik, M. S., Inderwildi, O. R., Kraft, M., Beran, G. J. O. and Green, W. H. (2007). Towards a comprehensive model of the synthesis of TiO_2 particles from $TiCl_4$, *Ind. Eng. Chem. Res*., **46(19)**: 6147-6156.

Witusiewicz, V. T., Arpshofen, I., Seifert, H. J., Sommer, F. and Aldinger, F. (2000). Thermodynamics of liquid and undercooled liquid Al-Ni-Si alloys, *Journal of Alloys and Compounds*, **305**: 157-171.

Wu, G., Wang, J., Tang, X., Gu, M., Chen, L. and Shen, J. (2000). Isothermal oxidation of Tin films, *Acta Physica Sinica*, **49**: 1015-1018.

Xing, Y. and Rosner, D. (1999). Predication of spherule size in gas phase nanoparticle synthesis, *Journal of Nanoparticle Research*, **1**: 277-291.

Xun, Y. W. and Mohamed, F. A. (2004). Superplastic behavior of Zn-22%Al containing nano-scale dispersion particles, *Acta Materialia*, **52(15)**: 4401-4412.

Yagodnikov, D. A. and Voronetskii, A. V. (1997). Experimental and theoretical study of the ignition and combustion of an aerosol of encapsulated aluminium particles, *Combust. Explos. Shock Waves*, **33**: 49-55.

Yetter, R. A., Risha, G. A. and Son, S. F. (2009). Metal particle combustion and nanotechnology, *Proceedings of the Combustion Institute,* **32**: 1819-1838.

Zachariah, M. and Carrier, M. (1999). Molecular dynamics computation of gas-phase nanoparticle sintering: a comparion with phenomenological models, *Journal of Aerosol Science,* **30**: 1139-1151.

Zeng, P., Zajac, S., Clapp, P. and Rifkin, J. A. (1998). Nanoparticle sintering simulations, *Materials Science and Engineering A,* **252**: 301-306.

Zhang, L., Gu, F. X., Chan, J. M., Wang, A. Z., Langer, R. S. and Farokhzad, O. C. (2008). Nanoparticles in medicine: therapeutic applications and developments, *Clin. Pharmacol. Ther.*, **83**: 761-769.

Zhao, S., Germann, T. C. and Strachan, A. (2006). Atomistic simulations of shock-induced alloying reactions in Ni/Al nanolaminates, *Journal of Chemical Physics*, **125**: 164707.

Zhao, S., Germann, T. C. and Strachan, A. (2007a). Melting and alloying of Ni/Al nanolaminates induced by shock loading: A molecular dynamics Simulation study, *Physical Review B*, **76**: 104105.

Zhao, S., Germann, T. C. and Strachan, A. (2007b). Molecular dynamics characterization of the response of Ni/Al nanolaminates under dynamic loading, *Journal of Propulsion and Power*, **23(4)**: 693-697.

Zheng, Y. and Geer, R. E. (2004). Nanomechanical imaging and nanoscale elastic modulus measurements of SnO_2 nanobelts, *Materials Research Society Symposium Proceedings*, **821**: 175-180.

Zhou, Y., Gu, D., Geng, Y. and Gan, F. (2006). Thermal, structural and optical properties of NiO*x* thin films deposited by reactive DC-magnetron sputtering, *Materials Science and Engineering B,* **135**: 125-128.

Zhu, H. L. and Averback, R. S. (1996a). Sintering of nano-particle powders: simulations and experiments, *Materials and Manufacturing Processes*, **11**: 905-923.

Zhu, H. L. and Averback, R. S. (1996b). Sintering process of two nanoprticles: a study by moleculr-dynamics, *Philosophical Magazine Letters*, **73**: 27-33.

Zhurkin, E. E. and Hou, M. (2000). Structural and thermodynamic properties of elemental and bimetallic nanoclusters: an atomic scale study, *J. Phys.*: *Condens. Matter*, **12**: 6735-6754.

Zhurkin, E. E., Hautier, G. and Hou, M. (2006b). Stress distribution and mechanical properties of free and assembled Ni_3Al nanoclusters, *Physical Review B*, **73**: 094108.